THE DEVELOPMENT OF ANTIBACTERIAL AND WEAR- RESISTANT TI6AL4V SURFACES BY SILVER DOPING, SELECTIVE LASER MELTING AND THERMAL OXIDATION.

By

Tatiana Mukinay

A thesis submitted to

The University of Birmingham

for the degree of

DOCTOR OF PHILOSOPHY

School of Metallurgy and Materials

College of Engineering and Physical Sciences

The University of Birmingham

September 2019

ABSTRACT

Ti6Al4V is the most popular titanium alloy employed in the medical industry for orthopaedic applications, due to its antimicrobial behaviour, biocompatibility, superior mechanical properties. However, the alloy demonstrates poor tribology and implant failure due to device –related infections (DRIs) and aseptic loosening. The aim of this study was two fold. Firstly, to improve the antimicrobial resistance of the alloy by selective laser melting (SLM) doped Ti6Al4V with Ag on the surface of Ti6Al4V substrate layer via solid solution strengthening. SLM was employed in an attempt to permanently incorporate Ag into Ti6Al4V. Secondly, the alloy underwent thermal oxidation treatment to improve its wear performance.

SLM of various process parameters, thus various energy densities were employed to implement a single layer thickness scan over pre-cut Ti6Al4V discs. This SLM layer consisted of varying weight percentages of Ag, 0.2, 1 and 5 wt.%, mixed with Ti6Al4V gas atomised powders. These samples underwent thermal oxidation treatment at 600 °C for 4 h. All treated samples were compared against a control that was ground to 400 SiC paper surface finish.

The result demonstrated that SLM process increased the surface roughness (R_a) due to the formed laser track grooves. This increase in surface area resulted in the substrate surface demonstrating hydrophobic behaviour, and so resulted in greater bacterial (*S. aureus* and *E. coli*) attachment, and biofilm formation. On the contrary the SLM process, resulted in greater surface area thus more space for cell attachment in comparison to the control. SLM also improved the corrosion behaviours of the substrates. But the surface configuration negatively impacted the CoF and wear behaviour of the substrate surfaces when tested with 15 and 30 N

load in both air and Ringers solution, at a speed of 5 mms^{-1} using a 12 mm in diameter tungsten carbide ball.

The addition of Ag displayed no difference in roughness (R_a) due to the relatively low weight percentages the element alloyed in. The inclusion of Ag SLM was not homogenous through out the SLM layer. However, increasing wt. % of Ag led to an increase in SLM layer hardness as a result of solid solution strengthening. The increase in SLM layer hardness reflected in the increased CoF. However, the roughness of the SLM surface resulted in its higher wear rate, as adhesive and abrasive wear were apparent. Additionally, with increasing Ag, there was an increase in antifouling character of Ti6Al4V and a decrease in biofilm formation. Ag had negligible effect on promoting metabolic activity of SOAS-2 cell compared to the control. Ag was also found to accelerate the growth of titanium oxide (TiO_2) layer, during thermal oxidation.

The thermal oxidation process resulted in the growth of TiO_2 anatase and rutile phased layer that exhibited double the hardness in comparison to the SLM layer, it remedied the reduction in corrosion resistance after Ag doping; and considerably enhanced the wear rates of all treated samples. The treatment also led to superior antimicrobial properties in reducing biofilm growth.

This study has expanded the understanding of melting Ag into the SLM single scan layer on bulk pre-cut Ti6Al4V discs. The limiting factors of the M2 SLM machines in unevenly spreading the powder and difficulties in repeatability of samples rendered the investigation of SLM process parameters insignificant. However, the results obtained provide basis on the investigating for optimal SLM process parameters with optimal Ag wt. % in combination with ideal thermal oxidation temperature and time, for future work.

ACKNOWLEDGEMENTS

Firstly I would like to thank Yahweh for everything He has done for me. His unrelenting support, strength, and love poured into me, has been my Ebenezer. My sincerest gratitude to my supervisors, Prof. Hanshan Dong, Dr. Rachel Sammons and Dr. Xiaoying Li, for their continued guidance throughout. My supervisors have been patient, thoughtful, given very essential suggestions and advice that has structured and been a road map to my research. I would like to also take this opportunity to thank my loving parents, Jean-Marcel Mukinay and Esperance Nkunzi, whom without I would not have made it thus far.

I would like to thank the entire Surface Engineering cohort, especially, Dr. Zhenxue Zhang, Dr. Shaojun Qi, Mr Behnam Dashtbozorg and Mr James Alexander, who have all supported, offered solutions and made the office a wonderful environment to work in. I would also like to acknowledge Prof. Moataz Attallah and the Netshape group for their devoted help and willingness to work with me. Thank you very much Ekoh.

Jerusalem Ministry Church has been instrumental to my growth as an individual, which has helped me with my research. I would like to give a special thanks to Rev. Anderson Ongono, for his scarifies, prayers and ample words of wisdom. Thank you to all my friends that have unremittingly encouraged and supported me, especially Toyosi Bello, Benedicte Ngoma, Alice Diowo, Kechikamma Omehia and Michael Kamumvu.

Finally, I wish to acknowledge the EPSRC and IMPaCT CDT for their financial supervision and support. I would like to acknowledge Dr. Val Franklin at the University of Aston and Centre for Electron Microscopy for their training and expertise and use of machines. I acknowledge the Henry Royce Institute for the Royce PhD Equipment Access Scheme, which enable me to have access to XPS.

TABLE OF CONTENTS

LIST OF FIGURES

LIST OF TABLES

CHAPTER 1: INTRODUCTION

1.1 The driver for the research

Dating back to ancient times, the limited understanding in scientific and philosophical knowledge resulted in high mortality and morbidity rates. The natural shift of human evolution from a Paleolithic to a Neolithic Age of agrarian societies led to more humans living in more permanent proximities. Consequently, this altered their surrounding ecosystems and environments leading to an improvement in standards of living. However, it also granted countless pathogens a new thriving ecological system birthing the way to end-, epi-, and pandemics (1). Generally, public health evolved based on trial and error - usually as a consequence to war or natural disasters. The approaches to overcoming health-threats were highly influenced by religious and societal beliefs. However, by the 19th century public health activists produced a health reform derived from observations and systematic testing of ideas (2). In the last century there has been a progressive decline in mortality caused by infectious diseases and bettered healthcare quality due to improvements in documentation, sanitation, sterilization, education and technology (2,3)**.** However, in spite of the knowledge acquired, the fight against pathogens continues due to various reasons explained in more detail in chapter 2 of the thesis.

Firstly, microbes are microorganisms that can be found populating the air, water, soil, plants and animals. More specifically, there is an intimate and dependent relationship between the human body and microbes. There are five basic groups of microorganisms, which are: bacteria, fungi, viruses, protozoa and algae. Those that coexist on and in the human body without causing harm are called the “normal flora” or “normal microbiota.” The normal flora is a necessary prevention to pathogens (organisms that are capable of invading the body and causing diseases) from attaching and colonization onto or in the human body. Generally, the body is a flourishing ecosystem that houses tens of thousands of microbe and human cells (4). There are numerous portals of entry that pathogens use to gain access into the body for example, broken skin, hair follicles or the mucous membrane (e.g. respiratory tract) (5). Once entry has been attained, pathogens must then colonise the host (either locally or systemically) by avoiding, evading or compromising its defense systems to finally form a biofilm (polysaccharide-based matrix). The formation of a biofilm can result in the damage of the host's associated tissues causing a disease. The process described of disease-causing organisms invading a host is known as infection (4–6).

The plight of infection faced today, despite the advancements achieved in the medical sector, can be partly attributed due to the evolution of antimicrobial resistance (AMR) (7). The resistance to antibiotics have posed a problem, especially in hospital settings, and contribute to healthcare-associated infections (HAIs) (8–10) HAIs describe any infection contracted 48 hours or more after receiving hospitalisation or 30 days after receiving healthcare (10)**.** Upon the understanding and application of the principles of hygiene and antiseptics, HAIs were significantly reduced. However, as of yet no institution or country can claim to have eradicated HAIs (11,12). The growth in our ageing population, i.e. it has been estimated that by 2050 around 50% of working age individuals will be aged ≥ 65 per hundred people has led to a demand in more Long-term care facilities (LTCFs). Despite the need for more LTCFs thus less intensive medical care, HAIs rates are still proving threatening; this is attributed to the evolution of AMR (7,13)**.** In England, the National Institute for Health and Care Excellence (NICE) has estimated that around 300,000 patients under National Health Service (NHS) acquire HAIs. This is costing the NHS around £1 billion per year, and out of the

300,000 patients there are approximately 5,000 deaths (14,15). HAIs have made a resurgence becoming a major problem for the NHS as they prolong patient stays in hospitals and in worst cases cause permanent disability or death (10). AMR has been estimated to cause around 50,000 deaths annually in the US and Europe alone (15). The causes of HAIs include, cross contamination between individuals, clinical sepsis, pneumonia, urinary tract infections, surgical site infections with many being credited to implants and prostheses etc. (10,11). The current developments of AMR means regimens administered to treat infections fail to work as efficiently (16,17). This loss in efficacy will abate progression in certain medical fields; more specifically, proving difficult to overcome in joint replacement and/or organ transplants as it relies on the ability of antimicrobial prophylaxis to reduce infection rates (17,18).

Alongside the evolution of healthcare, there were advancements in the use of materials in the body i.e. biomaterials. A biomaterial is a natural or synthetic (i.e. metal, ceramic and/or polymer) material implemented for medical and aesthetic reasons, in the replacement or restoration of bodily function(s); once placed in the body it is known as an 'implant' (19,20). There are three types classes of synthetic biomaterials employed today which are: metal, polymers and ceramics. Each class can further be classified into either and/or of the three types of biomaterials governed by tissue responses. These are: (i) bio-inert, which elicits minimal tissue response; (ii) bioactive, whereby the biomaterial promotes bonding to surrounding tissues; or (iii) biodegradable, that degrades over time (19,21). The demand for biomaterials has increased over the years due to: (i) an increasing geriatric population, (ii) more physically active individuals, (iii) a rise in cardiovascular diseases (e.g. due to prevalence in obesity), (iv) advancements in medical innovation & technology, and (v) cosmetic surgery demands. The collaborative effects of these factors, with the rise in antibiotic-resistant pathogenic strains are the major drives behind the need for better performing durable implants (16,22,23).

This thesis will focus on a Ti-6Al-4V (Ti64) as a biomaterial used for orthopeadic applications. Biomaterials employed orthopeadic applications are required to restore or replace the function of damaged or diseased bones and/or joints (24,25). After the use of stainless steel and cobalt-based alloys, titanium and its alloys were introduced as the newest of the three metallic biomaterials to be employed for orthopeadic application (26). Ti64 is the most widely used titanium alloy for implant applications due to its many advantageous behaviour such as, high biocompatibility, antibacterial-resistant and superior mechanical properties which are discussed further in chapter 2 (25,27). However, one of its major limitations is that it exhibits poor tribology (28). Tribology can be broken down into the Greek work 'tribos' which means 'to rub' and the suffix 'ology' which means 'the study of' (29). It is one of the oldest engineering disciplines. Thus, the word is defined as the science and technology of interacting surfaces in relative motion, and the subsequent use of the knowledge and information attained, to advise surface engineering advancements in given applications (29). Tribology is characterized by the nature and consequence of friction, wear and lubrication behaviours between interfacial interactions of materials (29). During tribological interactions, there is a conversion of mechanical energy, mass transfer and the surface transformation of the physical and chemical natures of the interacting materials. Due to tribology being interdisciplinary, as its understanding necessitates knowledge from an array of subjects (such as, physics, material science, mechanical engineering etc.), it is one of the least developed classical sciences to date (29,30). Titanium's major limitation in its use in load-bearing articulating surfaces has encouraged research and developments in surface engineering modification techniques. These techniques are employed to improve the metals surface hardness and/or lower its friction coefficient, with the aim to better its wear performance (31).

In summary, in spite of the medical knowledge attained over decades resulting in the waning of infection, it is a problem that is still currently occurring. In addition to infection, implanted devices are also at risk of bacterial adherence leading to device-related infection(s) (DRIs)-a topic explored in more detail in chapter 2 (32,33). Thus with an increasing demand for implants there is also an increase in DRIs (34). Furthermore, the current mechanical performance limitations of titanium as an implant also need to be addressed and improved. Infection and wear are the two factors being explored in this thesis. To tackle infection, the uses of silver (Ag) as an anti-microbial agent is employed; the use of thermal oxidation as a surface modification technique is implemented to tackle wear. Selective laser melting (SLM) is an additive manufacturing 3-D modification technique also used to melt and fuse the Ag and Ti-6Al-4V particles together using varying process parameters (i.e. varying the laser power, laser speed and hatch spacing)- more detail in chapter 2. The use of the different process parameters employed could influence surface topography, which has been reported in numerous papers to influence the adhesion and alignment of both human and bacteria cells (35,36).

1.2 Aims and objectives

The overall aim of this project was to deepen understanding in the performance of Ti-6Al-4V after thermal oxidation, selective laser melting (SLM) along with the synergetic and independent antimicrobial and wear performance of the substrates after 0.2, 1 and 5 weight percentages (wt. %) Ag doping. Various process parameters were also implemented to determine the effects of topography (i.e. roughness and surface patterns) on its cellular performance.

The objectives of this project were to:

- To investigate the microbiological behaviours, e.g. bacteria attachment (*Staphylococci aureus* and *Escherichia coli*) and MTT (SOAS-2) cell metabolic activity assays, of Ag-doped SLM and thermally oxidized Ti-6Al-4V substrates.
- To evaluate the influences of selective laser melting (SLM), by comparing the resultant effects of the use of the varying process parameters have on cell attachment or surface physical and chemical properties of Ti6Al4V substrates.
- To investigate the synergetic effects of Ag and SLM with thermal oxidation on Ti-6Al-4V's wear performance.

1.3 Thesis overview

Chapter 2- presents a literature overview of: infection; physical metallurgy and titanium & its alloys; surface engineering techniques; and additive manufacturing. This chapter will compare and explore in detail the current findings, mechanisms and evolutions in research and those implemented throughout science, citing its advantages and disadvantages where applicable.

Chapter 3- Provides detail on the experimental procedures used. Details on how powder and sample preparation were conducted, alongside the different surface characteristics analyses completed by scanning electron microcopy (SEM) and energy dispersive spectroscopy (EDS). Details how other analyses such as, X-ray diffraction (XRD), wear test, wettability, hardness and roughness measurements were done will also be included. It will also contain the methods on how the microbiological experiments were accomplished regarding antibacterial attachment tests, biofilm formation analyses and MTT assays using the Soas-2 cell line.

Chapter 4- Contains results on the surface morphology, topography and roughness measurements of substrate surfaces. Surface modifications and phases analytical results of

XRD, EDX and XPS will be shown alongside cross-sectional data. Surface physical and chemical properties including wettability, surface energy, and electrochemical corrosion are also included. Mechanical and tribological performance of the samples are also depicted, thus it includes results on its hardness measurements, wear-resistance and nano-indentation. Finally, also presented din this chapter are the microbiological behaviours of the samples after undergoing SLM, SLM with Ag and thermal oxidation. The Japanese spread plate method for bacterial attachment test results using *Staphylococci aureus* (*S. aureus*) and *Escherichia coli (E. Coli)*. Also biofilm formation results using *S. aureus* are recorded, with the addition of a biocompatibility test via MTT assay using the SAOS-2 cell line.

Chapter 5- Broken down into three sub-sections that discusses all the main findings of the results. The first section discusses the corrosion behaviour of the treatments, the second investigates the tribological performance post-treatments and the last discusses the biological behaviour outcome.

Chapter 6- Summarises the main conclusions based on the results and discussions obtained in this study. This chapter will also provide a collective summary of future works.

Chapter 7 – References

1.4 Preliminary work

Prior to the work conducted within this research, the deposition of Ag via PVS, electroplating and active screen plasma silvering were conducted. These samples underwent thermal oxidation, and the addition of Ag resulted in a catalytic effect on the growth of TiO_2 layer, thus the thermal oxidation times of Ag treated samples were reduced from 50 h to 6 h at 600 °C. These finings are concluded in Figure 1.1. From these findings, Ag could easily be wiped off during contact, which could make practical handling of a hip or knee component difficult. The idea of doping Ag particles into the Ti6Al4V surface layer was birthed. Three scan strategies were created and underwent Japanese spread plate antibacterial attachment test (detailed in chapter 3). Based on the results, the island scan strategy was chosen. Twelve different SLM process parameters with this scan strategy, varying in laser power, scan speed, a1 (hatch spacing) therefore energy density (J/mm^3), were treated (refer to Table 1-1) and Figure 1.2. These samples underwent further antibacterial testing and based on the results, six parameters; two that performed well (low bacteria percentage survival), two mediocre and two worse (high percentage bacterial survival), were selected (Figure 1.3).

Furthermore, a tested SLMed Ti6Al4V discs doped with 0.2 wt. % Ag doped was thermally oxidised for 6 h at 600 °C. Cross-sectional analyses, demonstrated spallation and very thick oxide layer grown. Confirming the catalytic influence of Ag, thus the thermal oxidation time within this research was reduced to 4 h Figure 1.4.

Silver (Ag) was deposited using PVD and electro-plating methods, those samples subsequently underwent thermal oxidation. The SEM images demonstrated Ag spikey straw like structure while electroplating demonstrated Ag clumps.

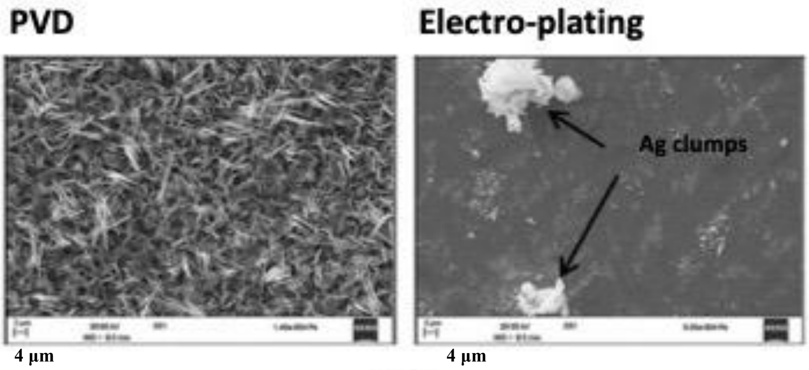

Cross-sections of oxide layer formed onto the surface of samples after thermal oxidation.

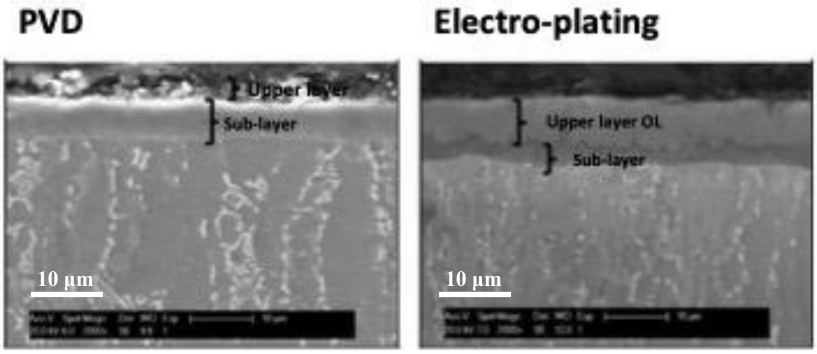

The PVD thermally oxidised sample demonstrated a thinner upper layer ~2.9µm, and a thicker sub-layer of ~5.9µm. On the other hand, the Ag-plated thermally oxidised sample demonstrated a oxide thicker upper layer and a thinner sub-layer of ~7.8 µm and ~2.71 µm, respectively.

Figure 1.1 Flowchart of the final year dissertation results demonstrating SEM surface and cross-sections of the effects of Ag addition has on Ti6Al4V surfaces via PVD and electroplating after thermal oxidation at 600 °C for 6 h.

Sample treatment process parameters

Table 1-1 The initial twelve randomised process parameters (PPs) created by the Design Expert software

Processing parameters	**Laser power (W)**	**Scan speed (mm/s)**	**Hatch spacing (a1)**	**Energy density (J/mm^3)**
1	**250**	**2750**	**0.5**	**60.60**
2	**250**	**2250**	**0.5**	**74.07**
3	**200**	**2750**	**0.5**	**48.48**
4	**250**	**2750**	**0.7**	**43.29**
5	**150**	**2750**	**0.5**	**36.36**
6	**250**	**2750**	**0.5**	**60.60**
7	**250**	**1750**	**0.5**	**95.24**
8	**250**	**2750**	**0.5**	**60.60**
9	**250**	**2750**	**0.3**	**101.01**
10	**300**	**2750**	**0.5**	**72.72**
11	**250**	**2750**	**0.1**	**303.03**
12	**250**	**3250**	**0.5**	**51.28**

Figure 1.2 Images of the twelve process parameters (PPs) created via SLM. The circled numbers were the chosen six further pursued in this research based on their antibacterial performances.

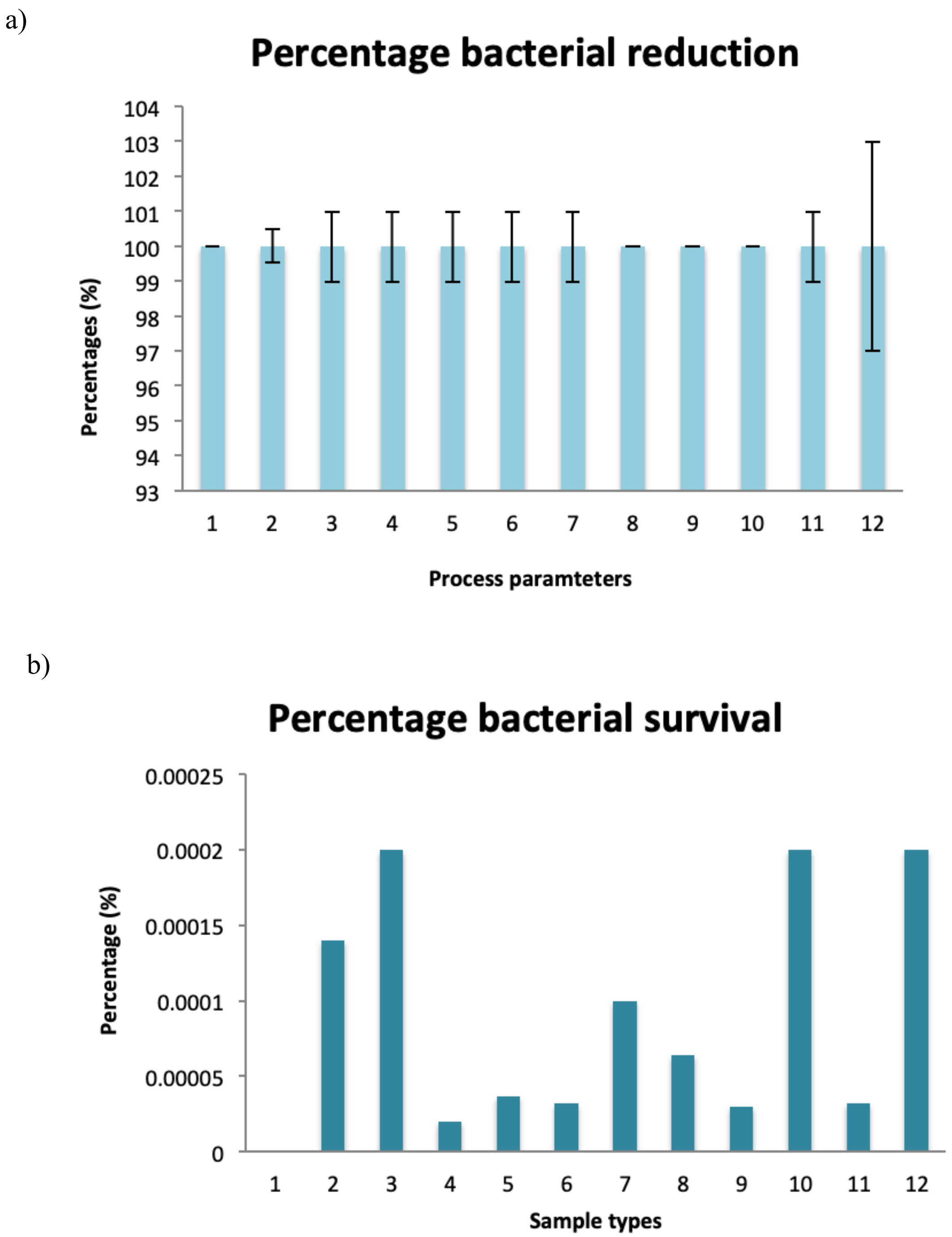

Figure 1.3 Bar graphs displaying (a) percentage bacterial reduction with the standard deviation, while graph (b) displays the results as percentage survival to better illustrate the differences between the twelve PPs. The standard deviations on graph (b) were not displayed.

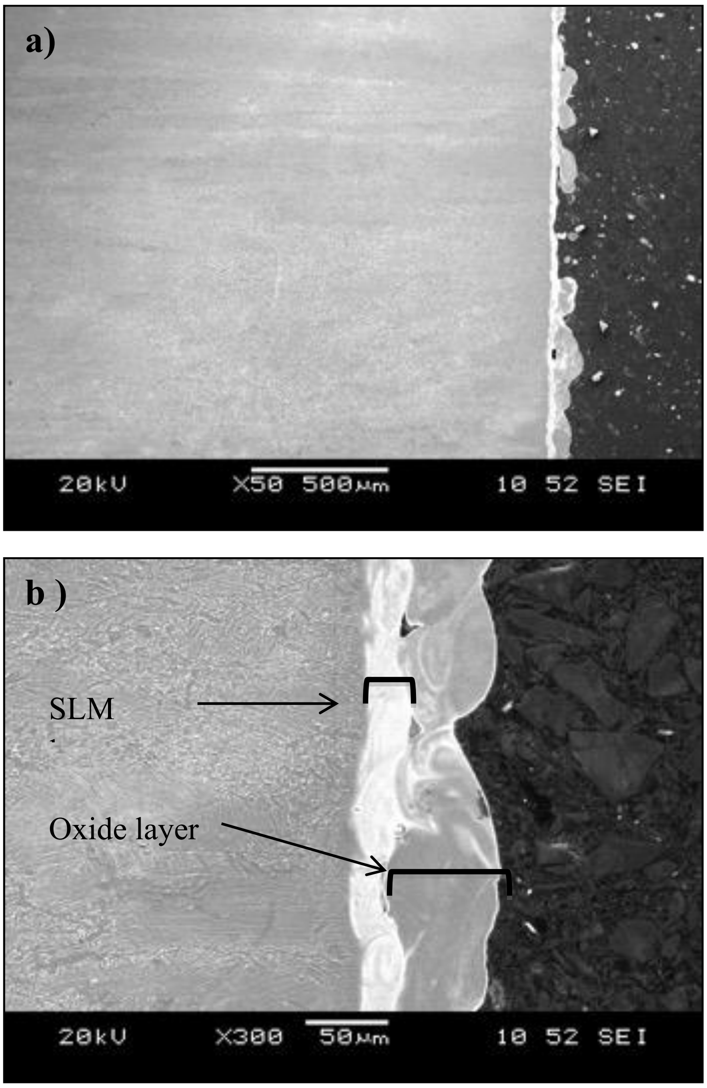

Figure 1.4 SEM cross-section of Ti6Al4V discs that underwent Ag 0.2 wt. % alloying via SLM, and thermal oxidation at 600 °C for 6 h resulting in an oxide layer formation.

2 LITERATURE REVIEW

2.1.1 Problems of Orthopeadic device-related infections (ODRIs)

In developed countries, over half of all chronic diseases occur in people over the age of 50, with bone and joint degeneration being one of the main problems. It has been estimated that by 2020 the percentage of people over 50 years of age suffering from bone disease will double. Patients are suffering from osteoporosis, scoliosis, bone fractures, musculoskeletal complications (37). Some of these issues require permanent, temporary or sometimes biodegradable biomaterial devices (37). Orthopaedic implants have become fundamental components in current medicine for the betterment of patient quality of life with over 50,000 total hip replacements being performed in the UK (38). Orthopaedic implants are used as substitution for different bone or joint functions (37).

However, each time a device is implanted, a phenomena known as 'race for the surface' occurs, whereby bacterial and human precursor cells compete to adhere to the implant surface micro-seconds from its implantation. Initially proteins adsorb onto the implant surface to form a conditioning film onto which cells adherence occurs. However, if pathogenic bacteria and native cells both are present, they compete and race for adherence to the surface (39). Native and bacterial cells are known to react differently to implant surfaces depending on their characteristics. However, even in the absence of a conditioning film, some bacterial strains are reported to have developed an advantageous mechanism that still enables proficient adhesion to the implants' surface. Conceptually, the bacterial adhesion process can be divided into reversible and irreversible implant surface-to-bacterial surface adhesion interactions; the former initial mechanism, is biologically and mechanically less stable than the latter. Once the latter (irreversible) interaction is reached, as the bacteria multiply a more stable biofilm layer (polysaccharide-based matrix) will form. Biofilm matrix necessitates an ecosystem and it strengthens the cluster of bacteria it harbours by strengthening its adherence to the implant surface (i.e. increasing shear force and electrostatic forces), through its use of fimbriae, pili and release of glycocalyx. It also allows bacteria to have motility via flagella (39,40). As the cell population within the biofilm grows, gene expression within bacterial cells will change to adapt and alter physiological processes that influence motility, sporulation and release of virulence factors essential for survival (40). Once infection is established, the implant's function can be adversely affected causing an array of symptoms. For example an infected joint replacement could result in edema, persistent local pains, erythema and/or sometimes loss of motions in the affected area; thus beginning the short or long-term failure of an implant (41–43).

S. aureus is one of the most prevalent microorganisms in ODRIs as it accounts for 20 to 30% of infections in fracture fixation and prosthetic joint infection cases, and is most commonly found amongst the normal flora of the skin (40,44**)**. Generally, *Staphylococci* accounts for about 50% of ODRIs cases (38). But aside from infection, implants can fail due to wear, corrosion, fracture, rejection or fibrous encapsulation (lack of bonding at the implant-body interface) (45). Device-related infections (DRIs) are accounting for substantial morbidity and mortality rates while also increasing healthcare cost due to the prolongment of in-patients (22,45**)**. Bacteria reside in many areas from being air born, residing on surgical equipments, scrubs, or being transferred through contact transmission during implantation (46,47). There is also a reservoir of bacteria situated on the patient's own skin or mucous membrane (44,46). Additionally, anaerobic gram-negative bacteria such as *E. coli* also causes device related infections (identified in chronic prosthetic hip infections and urinary catheters); the bacteria is becoming more prevalent in LTCFs (38,40,48). Around 1-2% of elective hip and knee replacements contribute to ODRIs (11). In Europe, at least 1.5% of orthopaedic implants lead to peri-prosthetic infections, which equates to 12,000 infections from 800,000 annually implanted devices. Furthermore, this infection rate does not include the rate of revision surgery infections which are not only more likely to occur in comparison to first time implantation; but there is a steady growth in the number of revision surgeries conducted (22).

With the increasing demand for geriatric medicine as a consequence of our ageing population and the general waning of infectious and acute illnesses, patients are increasingly suffering from chronic and degenerative diseases such as arthritis, osteoporosis and heart disease. These diseases have led to and increasing demand for biomaterials. However, during and post-implantation of a biomaterial there is a risk of acquiring infection. The combining effects of these consequences, with the increase in AMR are the major drives behind the search for more suitable methods to avoid infections. Hence the increasing need for longer-lasting and better performing biomaterials that promote the host's cell to win the race for the surface (22,23,45,46,49,50).

2.1.2 Current strategies against infection

Currently, there are gold standard hygienic procedures and guidelines provided by the NHS which provides comprehensive recommendations on tackling issues including hand hygiene, use of disinfectants and use of sterilised surgical equipments (51). However, infection rates are still proving problematic due to numerous reasons previously discussed (52). Thus other preventative strategies have to be adopted. Presently, the application of antibiotic prophylaxis can be administered either pre-surgery, in an attempt to either elevate the level of prophylactic antibiotics within the desired area, or post- to reduce the frequency of wound infections (53). Unfortunately, the therapy is not only costly but issues regarding patient toxicity/allergies can transpire. In addition the collaborative effects of biofilms with the dormant nature of certain bacterial strains can sometimes render antibiotic therapy ineffective (21,47).

The desired biological responses of implant devices are strictly associated with its surface topography and physiochemical characteristics. These characteristics play a key role on implant-tissue reactions, which consequently affects the efficacy of implant-integration, while demonstrating the desired pleiotropic effects on bacteria cells (54–56**).**

Generally, antimicrobial surface techniques involve the coatings of: organic substances, metals, non-metallic elements or their combinations. The use of antimicrobial metallic surface coatings on implants demonstrates far lower propensity to impel AMR than antibiotics (55,57). However, there are some reports of resistance to metallic coatings which creates concern (50,58). Metals with antimicrobial properties have been reported to impede biofilm growth, which is a quintessential phenotype for bacteria's AMR (58).

The use medicinal use of silver dates as far back as 100BC (59). Silver (Ag) can exist as a transitional ductile and malleable metal with no charge or as silver ions of various oxidation states (59–61). Throughout history silver has evolved from being used for the making of utensils, jewellery, currency and dental alloys, to its use in antibiotic therapy for open wounds and burns due to its demonstrated antiseptic activity (62). With better understanding of silver's expansive bactericidal, virucidal and fungicidal spectrum it is subsequently the most prevalent metal employed for antimicrobial function in biomedical applications (50,59–61). Generally, silver has been employed for coating coated biomaterials and has demonstrated a reduction in bacterial adhesion; additionally concentrations of silver ions can have great antimicrobial efficacy (22,62–64). Unfortunately on a clinical level, silver coated onto medical devices have worn off, thus the durability of its efficacy is necessary (62**).**

Ultimately its bactericidal mechanism has not yet been fully elucidated, but there have been suggestions on its effect on *E. Coli* (65). It has been reported that silver ions could bind to key functional groups (such as thiol) of enzymes situated on bacteria cytoplasmic cell membranes, altering the transportation and release of phosphate ions (K^+), as well as inactivating enzymic functions (64,66,67). Silver ions have also been reported to cause the inhibition of bacterial cell growth, replication, as well as causing irreversible changes in cell wall. These changes in the cell wall causes an increase in membrane permeability, thus the cell undergoes leakage of cellular contents such as ions, proteins etc. (64,65). Schreurs and Rosenberg (1982) reported silver ions inhibited the respiratory chain and impaired the uptake and release of K^+ in *E. coli* (68). More specifically, an experiment conducted by Raffi *et al.*, (2010) concluded that within a few minutes of *E. coli* cell contact exposure to Ag nanoparticles (AgNPs), *E. coli* cell membranes were "completely disrupted" (67). In support of these findings, results concluded by a proteomic data on AgNPs treated *E. coli,* discovered that the cells outer membrane were destabilised due to an accumulation of immature membrane precursor proteins. This study asserts that it was due the depletion and dissipation of cellular adenosine triphosphate (ATP) and proton motive forces, which are both necessary energy providers to the translocation of precursor proteins to bacteria cellular membranes (65,67). Yamanaka, Hara and Kudo (2005) concluded that silver ions not only infiltrated through *E. coli* cellular membranes, but also interacted with ribosomes subsequently suppressing the expression of ATP (69).

Silver's lower efficacy on gram-positive bacteria (e.g. *S. aureus*) as opposed to gram-negative bacteria (e.g. *E. coli)* is reportedly due to the thickness and composition (i.e. peptidoglycan) of the outside of cell wall (57). In the case of AgNPs, gram-negative bacteria are more susceptible as they have less negatively charged peptidoglycan (around 3 to 4 nm in thickness), compared to gram-positive bacteria (around 30 nm in thickness) which also has thicker cell wall. The thickness of the wall provides a greater barrier for silver ions to penetrate through (57,62,65). By decreasing the size of silver particles to a nano level there is an increase in surface-area-to-volume-ratio, which consequently increases the silvers antimicrobial efficacy (62,65). However, there are numerous reports on the cytotoxic and genotoxicity effects of AgNPs on human cells. AgNPs has been suggested to cause genotoxicity by penetrating the nucleus, inducing oxidative based damages and DNA mutation that lead to fibrosis and carcinogenesis (62,65).

The limitations of silver also include how expensive it is, and so other metallic agents are considered which tend to be transition metals and some metalloids, such as Copper (Cu) and Zinc (Zn), Gold (Au), Lead (Pb) etc. (58,70). Similarly, the subjects of mechanisms are not entirely clear (70). More specifically, Cu and Zn have been reported to demonstrate potent antibacterial effects due to their disruption of multiple enzymatic and cellular processes on an array of bacterial species (50**.** According to Noyce, Michels and Keevil (2006) copper demonstrated antifouling properties by killing 10^7 cfu/ml of MRSA population under an hour of exposure time (71). Coppers ability to be bactericidal is suggested to be attributed to its ability to alternate between Cu^+ and Cu^{2+} which was said to produce reactive oxygen species upon contact (72,73). On the other hand, McDevitt *et al.*, (2011) displayed zinc's toxicity on *Streptococcus pneumonia*, and attributed it to zinc ability to inhibit the bacteria's uptake of Mn^{+2} (74).

There is also the use of antibiotic releasing coatings, the likes of vancomycin or gentamicin which are antibiotics placed in bone cements for local delivery. The latter is commonly used due to its wide antibacterial spectrum and its heat-stable property. Titanium (Ti) implants can sometimes be coated with gentamicin carriers, which were shown to significantly reduce infection rates; even after infection the implant has demonstrated better recovery in comparison to administration of systemic gentamicin (75). Porous cementless implants have displayed an increased surface area for pathogenic bacteria adhesion, thus increased risk of infection compared to cemented ones (50). Vancomycin on the other hand, can be loaded into thin silica sol-gel coatings on Ti implants with the intention of averting and treating bone infections (75). A report by Radin and Ducheyne (2007) conducted in a rat osteomyelitis model revealed the sol-gel infused vancomycin significantly reduced the number of *S. aureus* cells. They also observed a degradation rate in the sol-gel film (76).

Anti-adhesion coatings have also been used on the surface of indwelling implants in hopes of reducing the attachment of pathogenic bacteria. These anti-adhesion coatings influence, surface energy, wettability, surface charge and roughness of implant surfaces. Contradicting results are reported on the wettability influence of implant surfaces on bacterial adhesion. Privett et al., (2011) reported a reduction in *S. aureus* attachment on glass treated with a super-hydrophobic coating (77). Contrarily, other anti-adhesives promote highly hydrated layers on implant surfaces by trapping free water molecules in its hydrophilic chains (62,78). The resultant effects of hydrophilic and negatively charged surfaces generally lead to a decrease in bacterial adhesion when compared to its hydrophobic-surface counterpart. Other factors which affect wettability of a surface include microstructural topography (35).

There are numerous reports of topographical modifications, such as: pits, nanotubes, grooves and protrusions which can be described as surface roughness, demonstrating significantly different biological cell behaviours (54). There have been reports on the different and combining effects of macro- (100 μm to mm), micro- (100 nm to 100 μm) and nano-roughness's (<100 nm) on implant surfaces. Roughness increases the surface area for cell-implant interactions, thus implants with roughened surfaces have proven to perform better than their smooth-surfaced equivalents (35,79). In a regular bone remodelling cycle, complex structural topographical micro- and nano- features support new bone formation after resorption; hence it is thought that these features can direct osteoblastic cell responses and tissue regeneration. Consequently, clinically available implants try to mimic the bone's hierarchical structures by integrating surface modification features (8,54,79). Cell response to topographical features depends on cell size and feature geometry; nano-topographical features may have more influence on smaller cells (≤100 nm) than features on a microscale, as protein entities can sometimes be too small to sense microscale features (35). There are many reports whereby micro-topography and nano-topography promoted osteoblastic-cell attachment, production of osteogenic proteins, improved micro-retention to increase an implants healing potential. There are approaches which use nanotechnology, which alters surface characteristics on an atomic scale, to produce nano-topographical features with modified chemistry (i.e. surface free energy and wettability) in the aspiration that it will offer greater specific control of adherent cells by influencing the initial protein adsorption (8,55,79,80).

Nano-topographical features can be assumed to either be isotropic (organised) or anisotropic (unorganised) patterns. For example, on dental implant fixtures they tend to be anisotropic as isotropic features, such as nanogrooves, are difficult to apply onto complex-screw designs. To ameliorate the performance of implants, a lot of research has gone into more suitable nano-topographical features which could offer improved performances, one of which is TiO_2 nanotubes (TNT) (79,81). TNTS offer a greater surface area by demonstrating a rougher surface; hence promote protein adsorption, which results in increased cell adhesion, and subsequent osseointegration. TNT with diameters in the range of 30-100 nm are reported to elongate adhered osteoblasts which increased filopodia attachment compared to smooth surfaced titanium substrates (82**).** Although, TNT increase the number of osteoblast cell adhering to its surface, it is difficult to determine the level of cellular adhesion as cells reach confluence. However, this increase is also attributed to an increase in the hydrophilic and surface energy of the TNT surface, as well as the space between nanotubes array, which provides a nutrient path for cells (82). A study conducted by S. *et al.*, (2012) concluded TNT ~100 nm in diameter are optimal for inducing extremely elongated cellular shapes which resulted in substantially enhanced bone-formation as a result of enhanced alkaline phosphatase activity (83). TNT can also be used for drug delivery; it can be used to carry osteogenic growth factors (e.g. bone morphogenetic protein-2) or metallic antimicrobial agents (e.g. Ag) (82). One of the most common causes of dental implant failure is due to peri-implantitis: an inflammatory reaction with the localised loss of the supporting bone around an implant (84,85). It is difficult to adequately eradicate adherent bacteria from dental implant surfaces, and this makes treating the infection arduous. A study was conducted whereby TNTs were used to carry gentamicin, and the results indicated that the drug–eluting nanotubes effectively reduced bacterial adhesion, while promoting osteoblast differentiation on its surface (82).

Alternatively, the choice of biomaterials, particularly those that possess antibacterial behaviour, is another strategy against infection (20). The focus in this study will be on Ti-6Al-4V, which is the most popular titanium alloy, due to its desired combination of high biocompatibility, antibacterial-resistant and superior mechanical properties compared to other bio-metals (57,86)**.**

2.2 Physical metallurgy of Titanium and its alloys

2.2.1 Introduction to titanium

Mineral extraction of commercially pure titanium (cp-Ti) and TiO_2

Titanium and its alloys are increasingly being researched and used in aerospace, automotive and medical industries amongst many others, mainly due to their relative high strength-to-weight ratio (specific strength), performance reliability, cost-effectiveness and osseointegration. (82). Titanium is generally extracted from ores via conventional mineral beneficiation techniques, with ilmenite ($FeTiO_3$) and rutile (TiO_2) the main ores used for primary production of the material. Approximately 90% of the world's titanium mineral demands have been estimated to be supplied by ilmenite (87), with ilmenite and rutile being processed separately (88).

Rutile is usually favourable due to its high titanium content as its ore usually consists of around 10% iron compared to ilmenite, thus resulting in better quality TiO_2 pigments (87,88). There are various methods employed for the production of titanium from rutile, but the chloride process is currently employed for the production of commercial titanium and it is preferred over the sulphate process as it produces less waste (87). The Figure 2.1 and Figure 2.2, below are schematics of the mineral extraction processes for both pure titanium and rutile (TiO_2).

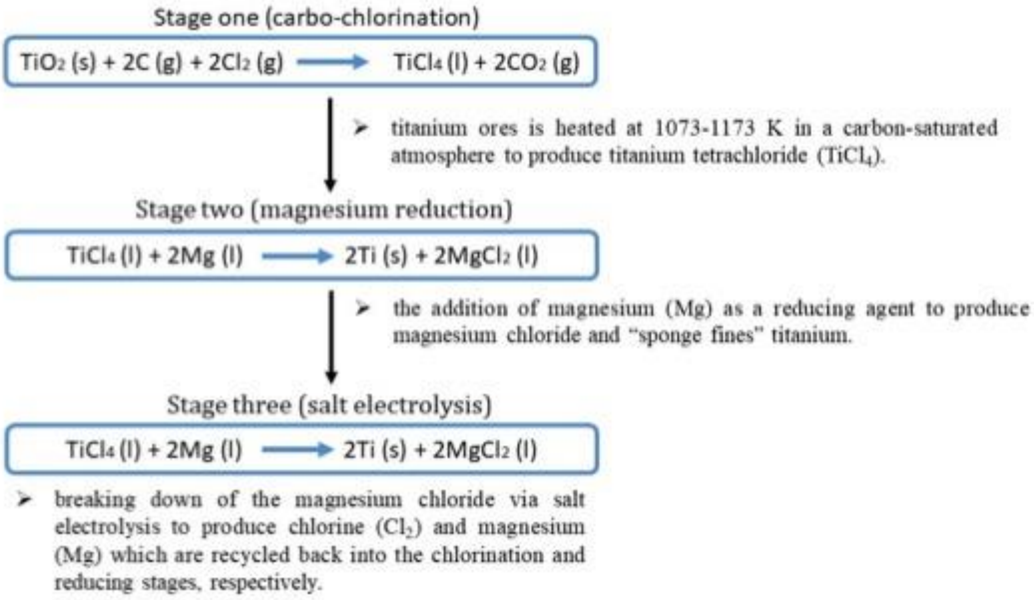

- titanium ores is heated at 1073-1173 K in a carbon-saturated atmosphere to produce titanium tetrachloride ($TiCl_4$).
- the addition of magnesium (Mg) as a reducing agent to produce magnesium chloride and "sponge fines" titanium.
- breaking down of the magnesium chloride via salt electrolysis to produce chlorine (Cl_2) and magnesium (Mg) which are recycled back into the chlorination and reducing stages, respectively.

Figure 2.1 Illustrates the mineral extraction of the titanium from ores

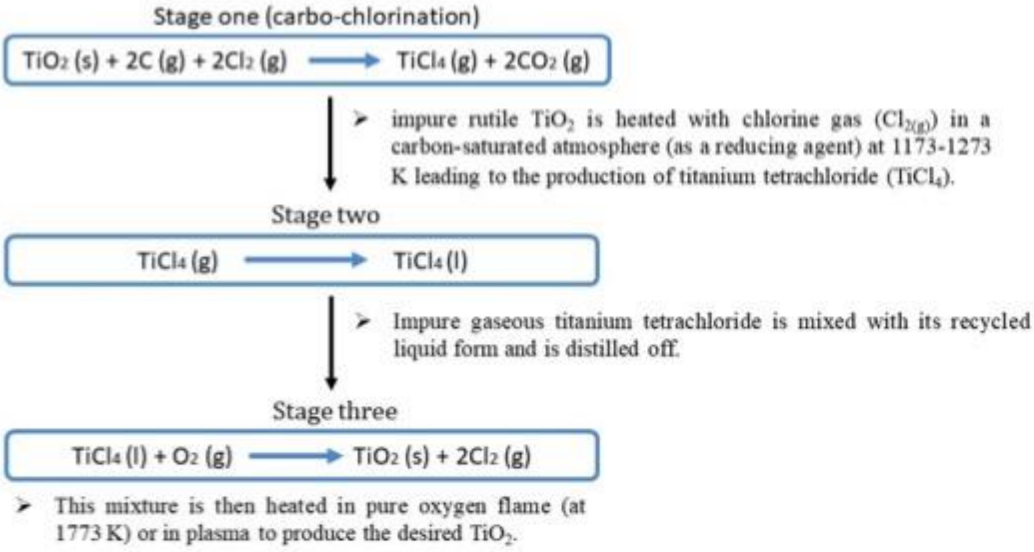

- impure rutile TiO_2 is heated with chlorine gas ($Cl_{2(g)}$) in a carbon-saturated atmosphere (as a reducing agent) at 1173-1273 K leading to the production of titanium tetrachloride ($TiCl_4$).
- Impure gaseous titanium tetrachloride is mixed with its recycled liquid form and is distilled off.
- This mixture is then heated in pure oxygen flame (at 1773 K) or in plasma to produce the desired TiO_2.

Figure 2.2 Illustrates the mineral extraction of the titanium dioxide from ores

TiO_2 (or otherwise known as titania) is a polymorph can exist in three crystalline forms: anatase and rutile and brookite as illustrated in Figure 2.3 (89). The differences in these are the crystal structures; anatase and rutile are both tetragonal structures consisting of octahedral TiO_6 sharing four corners or two edges, respectively (89,90). On the other hand, brookite exhibits an orthorhombic structure (90,91). From a thermodynamic point of view, anatase and brookite are metastable hence when heated they transform to a stable rutile structure (Allen *et al.*, 2018). Anatase and rutile are the most commonly researched; the former has been reported to demonstrate photocatalytic bactericidal behaviour under UV irradiation (91,92).

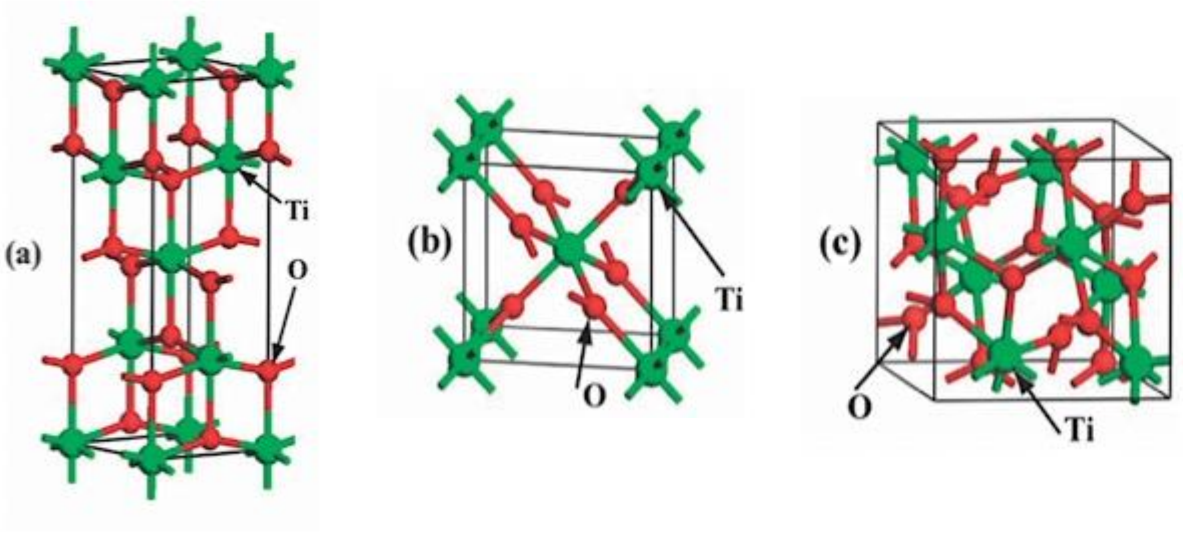

Figure 2.3 Schematic drawing of TiO_2 (a) anatase, (b) rutile, and (c) brookite (93)

2.2.2 Titanium and titanium alloy classifications

With regards to microstructure, titanium and its alloys can be classified into three main categories, namely; α-, α + β-, and β-crystalline phased alloys (94,95) The addition of interstitial alloying elements determines the crystalline phase titanium will exhibit, as it increases or decreases the metals transition temperature (β-transus). Below a β-transus of 883°C titanium exhibits a hexagonal-close-pack (hcp) crystal structure, and above this temperature titanium changes to β-phase body-centered-cubic (bcc). β-transus defines "*the lowest equilibrium temperature at which the material is 100% beta*" (96)**.** Thus the equilibrium temperature is vital to a metal alloy’s heat-treatment processing as the microstructure attained influences its mechanical behaviours (96,97).

Table 2-1 Displays information on examples of titanium and its alloys employed as biomaterials (98–100).

α- phase alloys and cpTi			
Common Name	**Alloy Composition (wt. %)**	**β- Transus (°C)**	**Applications**
Grade 2	cpTi (0.3Fe, 0.25O)	915	Orthodontics (i.e. Dental screws) and as dental prosthetics
Grade 4	cpTi (0.5Fe, 0.40O)	950	Employed in orthodontics.
α + β-phase alloys			
Common Name	**Alloy Composition (wt. %)**	**β- Transus (°C)**	**Applications**
Ti-6-4	Ti-6Al-4V (0.2O)	995	Used for Artificial hip joint (metallic cup and hip stem), as well as in the automotive and aerospace industries.
Ti-6-4 ELI	Ti-6Al-4V (0.13O)	975	For cryogenic applications
β-phase alloys			
Common Name	**Alloy Composition (wt. %)**	**β- Transus (°C)**	**Application**
TMA	Ti-11.5Mo-6Zr-4.5Sn	1000	Orthodontic wires

α-alloy:

α-alloys and commercially pure titanium (cpTi) exhibit hexagonal-closed-pack (hcp) crystal structures (Figure 2.4). However, the addition of alloying elements known as α-stabilisers results in an increase in the β-transus of which alpha can exist (90,100). Examples of α-stabilisers include aluminium (Al), oxygen (O) and nitrogen (N). Oxygen has been reported to increase titanium's yield and tensile strength but at the cost of reducing its ductility (90,100). Each element has its own level of solubility within α-titanium, with oxygen being used the greatest as it is easier and very effective in comparison to carbon and nitrogen (101). Additionally, the effects these elements depends on the other α-alloying elements present. For example, the addition of O and N to unalloyed Ti resulted in a greater increase in its yield strength as oppose to its additions in α- alloying Ti-5Al-2.5Sn (101).When some α-alloys contain a small volume percent of β-stabilising elements, they are known as near- α-alloys (99). Generally, α-alloys demonstrate poor formability, good weldability, and tensile strengths in the example of cpTi (240-255 MPa) used for low-load bearing dental implant applications-bone fixations and stents (31,45). Furthermore, cpTi can be found in four grades of varying weight percentage (wt. %) of interstitial elements (e.g. O, Fe) which affects the metals' tensile strength and β-transus (102). (Table 2-1). But cpTi is in danger of hydrogen embrittlement, if exposed to hydrogen-sensitive environments, due to the formation of brittle hydride (TiH_2) phases (Lutjering and Williams, 2007; Froes, 2015).

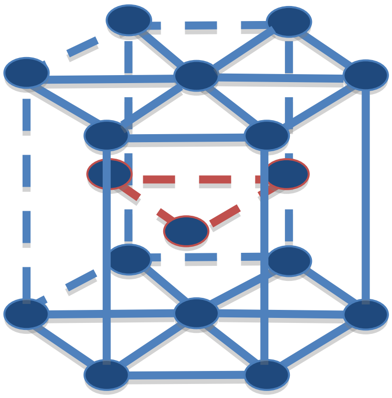

Figure 2.4 Unit cell of an α-phase

β-alloy :

Above the β-transus (>883°C), titanium exhibits a body-centered-cubic (bcc) crystal structure (Figure 2.5). The interstitial elements added to the metal to decrease its β-transus are known as β-stabilisers; these can be further divided into β-imorphous group and β-eutectic group. The former are elements such as Molybdenum (Mo), Vanadium (V), Niobium (Nb), which are soluble in the β-phase crystal structure (96,99). On the other hand, the latter group can form intermetallic compounds; these include elements such as Manganese (Mn), Iron (Fe), and Cobalt (Co) (96,99). Figure 2.6 below displays schematic representations of alloying elements and its effect on phase diagrams. To form β-alloys, the metals usually heated above its β-transus and then quenched without the occurrence of martensitic decomposition of the β-phase) (96,99). This retains 100% of the β-phase and usually > 10% of β-stabilisers are required for this to occur (99). β-alloys can further be classified into near β (lean) and metastable β-alloys. The difference is that near β-alloys are lean in α-stabilisers and rich in β-stabilisers; the α elements are added to strengthen the alloy (96,99,101). Metastable β-alloys are non-equilibrium phases that contain the minimum inhibitory percentage of β-stabilisers that guarantee to retain 100 vol. % of the bcc β-phase structure from a single β-phase field after quenching to room temperature (100,101). Once quenched, metastable β-alloys demonstrate low tensile strength and high ductility. To increase its strength thus decreasing its ductility, the alloy undergoes an isothermal aging process whereby it transforms into stable α and β-phases (100,101,103). At a given strength, both lean and metastable β-alloys usually demonstrate increased fracture toughness over α + β-alloys. Generally, these alloys exhibit good formability at room temperature and superior corrosion resistance, with high specific strength (100,101**).** The synergies of these properties, manipulated by alloying quantities, have led to the use of β-alloys as orthopeadic implants, and orthodontic wires (Table 2-1). However, β-alloys are at risk of embrittlement during the low temperature ageing process from the formation an intermediate metastable β'-phase (or omega ω-phase) (100,101).

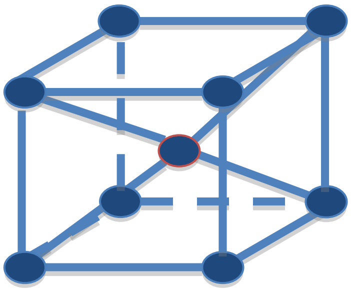

Figure 2.5 Unit cell of β-phase.

α+β-alloys:

Titanium alloys containing dual α and β-phases at room temperature are known as allotropic alloys, this is due to the presence of both α + β- stabilising elements (100,101). As previously explained, these interstitial elements influence the phase morphology of the alloy, and depending on the relative vol. % of each element, and its thermochemical treatment, varying mechanical properties can be attained (100). These alloys are most widely used due to their high strength to density ratio, good fatigue behaviour, excellent corrosion resistance and good toughness (100,101). One of the principle commonly used α-stabilisers is Al as it strengthens the α-phase; the addition of β-stabilisers to this alloy increases the α + β-phase field and this alloy is usually achieved via solution heat treatment and aging (94,101). The most commonly used and known allotropic titanium alloys is Ti-6Al-4V (101). This is not only due to its good balance of properties but also because it is the most researched, tested and developed titanium alloy –this is of great benefit as its greatest use is in the aerospace industry (99). The alloy is also used in the medical industry as bio-implant materials (99). Generally, these dual phased alloys are characterised by good formability, improved tensile strength for both cryogenic and elevated temperature applications (31).

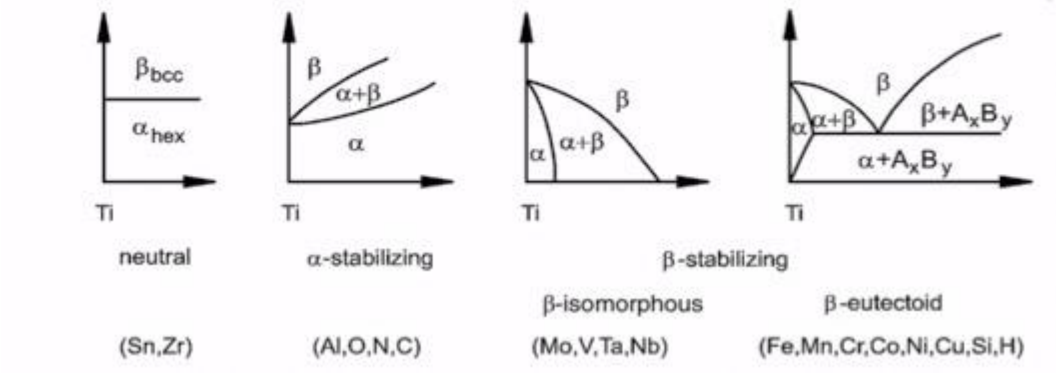

Figure 2.6 Schematic drawings on the influence of alloying elements on Ti and Ti alloys phase diagram (99).

2.2.3 The microstructure of Ti-6Al-4V

2.2.3.1 Alloying chemistry- Influence of alloying elements and phases

In the 1950's an allotropic (α + β-phase) alloy known as Ti-6Al-4V (Ti64) was discovered, and has since dominated other titanium alloys due to its superior balance of properties influenced by its microstructures (95,101,104). The nominal compositions of elements may vary. For example, oxygen contents can reach up to 0.2 wt. % while nitrogen can be altered to 0.05 wt. %, with aluminium and vanadium sometimes tailored to 6.75 and 4.5 wt. %, respectively. These increases in interstitial alloying elements ameliorate the strength of the alloy but at the cost of other properties behaviours such as depreciation in its ductility, and fracture toughness behaviours (105). Thus, Ti-6Al-4V ELI (extra low interstitial) grades composed of low O, and Fe have been developed. This grade exhibits increased fracture toughness and admirable damage tolerance properties, accordingly it also tends to be used in the aerospace and biomedical industry (94,101,105).

Table 2-2 The biomaterial densities and tensile strengths (45,103,106).

Metal	Density (ρ) (g/cm^3)	Ultimate Tensile strength, UTS (MPa)	Yield Strength, YS (MPa)	Elastic Modulus, E (GPa)	Elongation Modulus, EI (%)
Ti-6Al-4V (wrought)	4.5	900-1050	880-950	114	8.1-15
316 stainless steel	7.9	490	190	193	40
Co-Cr alloys	8.3	793-860	241-310	210-232	50
Bone (cortical)	-	-	-	4.4-28.8	-

Ti64 is available in different forms; wrought, cast, and powder metallurgy (PM). The properties of these differ depending on the varying vol. % of alloying elements and its thermochemical treatments. In saying this, wrought Ti64 is the most abundant type employed due to its extensive range of product forms, for example it can be produced as billets, sheets, tubes, wires, extrusions etc (105). There is also a preferential use of wrought Ti64 in the medical industry as bone screws, partial or total joint replacements; as it demonstrates good tensile and fatigue strength, good corrosion resistance, biocompatibility, excellent strength to density ratio, and low elastic modulus, closer to that of bone compared to other employed metallic counterparts (53,95,105). On the other hand, cast alloys are also employed for specific medical implant applications, although not as abundantly as wrought, as it exhibits poor fatigue resistance (105). They are extensively used in the turbine engine industry, for missile bodies, and space applications (105). As for PM, it is principally utilised for the production of near-net shaped components (105). This process will be discussed in further details in the surface engineering section.

2.2.3.2 Phase morphology and features

Depending on processing, Ti64 can exhibit a range of microstructures with a range of geometrical arrangement of α + β crystal phases (105). Lamellar, equiaxed, and bimodal (a mixture of equiaxed α' within lamellar α + β-matrix), are the three distinct microstructures that can be obtained from α + β-alloys. Succinctly, lamellar structures are created via nucleation and growth of the α-phase from β-grain boundaries after subsequent heating and slow cooling (99,105**).** The cooling rate categorically determines the final lamellae size, α-colony size, and the degree of α-layers at the β-grain boundaries (94). For example, air cooling result in fine needle-like acicular α-phases, while quenching from temperatures between 750 to 900°C forms soft orthorhombic martensite α'' (105). When the alloy is quenched from above 900°C, needle like hcp martensite α' is obtained which bears crystallographic parameters similar to the α-phase lattice (105). Equiaxed microstructures are obtained by a deformation process in the α + β phase field, that breaks up lamellar α into more reproducible equiaxed α grains, which undergo further heat treatments and slow cooling to produce recrystallised coarse α-grains (105). For bimodal microstructures the alloy would undergo 1 h of annealing, quenching or air cooling and finally an aging treatment is conducted to strengthen the alloy and relief stresses (99,105). Generally, lamellae structures demonstrate significantly better creep strength in comparison to equiaxed or bimodal structures (94,105). A study conducted by Park *et al.*, (2012) displayed pictures of equiaxed, lamellar and bimodal microstructures on Ti-6Al-4V ELI; this is shown in Figure 2.7 (27). The equiaxed structure was obtained as-received, while the lamellar structure was heated at 1040°C for 2 h before being heated again at 730°C for 4 h, both times after heating it was cooled at air cooled room temperature. As for the bimodal structures, the titanium alloy was heated to 950°C for 2 h, water quenched, reheated at 540°C for 4 h, before being air-cooled.

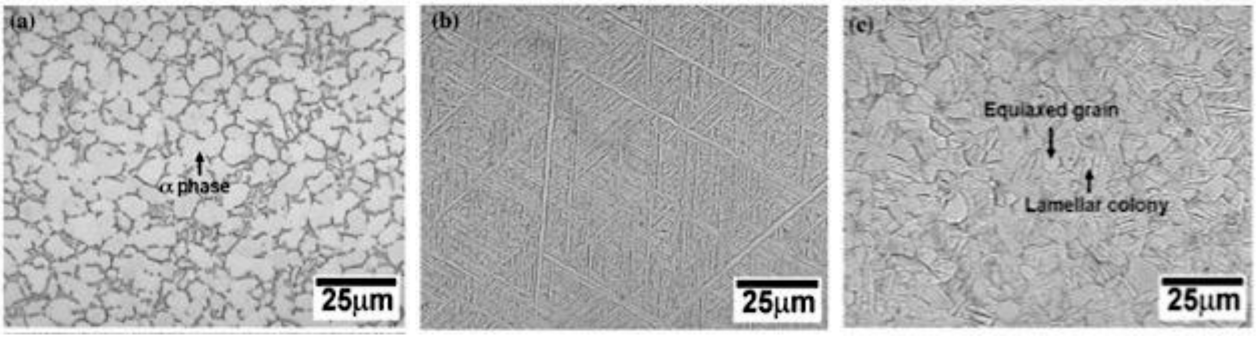

Figure 2.7 Optical micrographs of typical ELI Ti64's microstructure: a) equiaxed, b) lamellar and c) bimodal (27) .

Oxygen has a high solubility in unalloyed Ti, a maximum of around 14.3 wt. % (94). Thus when the metal is exposed to a O containing environment there is a passive 5-10nm thick TiO_2 oxide layer (OL) formed (94,107). Similarly, Ti64 demonstrates a high chemical affinity to an O, and when exposed it has a thin OL. However, with increasing temperature there is an increase in oxygen diffusion rates into the metal. As oxygen diffuses into the metal, it stabilises the α-phase of Ti surface changing its deformation behaviour resulting in an increase in surface hardness while decreasing ductility (94). Below ~500°C diffusion of oxygen into the metal is slow, however above this temperature, excess oxygen begins to diffuse past the surface layer and into the bulk material building a porous multi-layer (94,105). This causes surface embrittlement, which is not ideal for fatigue loading applications (i.e. joint replacements), as the surface will crack under tension loading (94,105). This titanium's oxide layer when controlled through thermochemical processing, could prove advantageous as it demonstrates increased hardness compared to the bulk material (97,108).

2.2.3.3 Weldability and machinability of Ti-6Al-4V

Welding is a process that uses heat to melt and fuse materials together, with the aim of repairing or building components (82). Generally, the process of welding increases the strength and hardness of a metal, but at the expense of its tensile and bend ductility (109). With regards to Ti64, its idyllic for welding to be conducted in certain environments/ process conditions as titanium has a high chemical reactivity e.g. it readily reacts with oxygen, grease, dirt etc. (109,110). Specifically, when interstitial impurities are present during high temperature welding, they get introduced resulting in dendritic microstructural growth, which essentially affects the final alloys properties (109). Titanium alloys is said to be prone to contaminants when temperatures are above 600°C (111). Successful high temperatures welding of Ti64 are conducted in an argon atmosphere, which shields the metal from contaminants, and it results in the material maintaining a level of ductility and corrosion resistance. However, when poorly conducted the welded area/joint demonstrate limited weld ductility and a lower corrosion resistance due to its dendritic microstructure (109). However, post-welding heat treatments can strengthen the metal (109). Additionally, when titanium is welded with dissimilar metals, as it is readily reactive, it usually forms brittle compounds (109)**.** For example, titanium and aluminium when molten together can form Ti-Al intermetallic phases, which demonstrate too low of a ductility and poor fatigue strength to be ideal for load-bearing applications. (111,112). To avoid this, the welding process needs to be overcome any precipitation of Ti-Al intermetallic phases (113). Additionally, when more than 0.1% of carbon is introduced into titanium during welding, titanium carbide formation may occur and carbon may also react with oxygen to form carbon oxide or dioxide gases that essentially form gaseous pores trapped within the weld zone (111).

Ti64's thermo-mechanical properties such as low thermal conductivity, low elastic modulus, high chemical reactivity, and its preservation of high hardness at elevated temperatures all contribute to the its poor machinability (114). During cutting, the metals poor thermal conductivity means that the dissipation of heat is slow, and so the heat and temperature builds up at the cutting zone (115). In addition to this, titanium demonstrates high chemical affinity to cobalt binders (found in cutting tool material), which causes rapid chemical wear by diffusion and titanium chipping (115,116). Thusly, due to titanium chipping at the cutting tool interface there is increased cutting zone stresses; which in turn degrades the surface integrity of the cutting tool ensuing premature failure (114–116). Moreover the chipped off titanium material could weld onto cutting tools due to the pressures applied during the cutting process

(115). All limiting factors have reduced the choice of cutting tool to carbide-based materials and at limited speeds of 60 m/min (115).

2.2.4 Advantages of Ti-6Al-4V

The manipulation of α + β-phases within this alloy means it exhibits lower modulus, closest to that of bone, compared to its competing metallic counterparts (Table 2-2) (25,26,45,106). However, although it has the lowest, its modulus is still significantly higher than that of bone, and this leads to issues discussed in the disadvantages of Ti-6Al-4V (45). The passive OL formed on Ti64's surface is attributed to the alloy's excellent biocompatibility, unique osseointegration and corrosion resistance behaviours (106,117,118). There are reports that the rutile TiO_2, which is favoured for biomedical application, exhibits a more inert behaviour, alongside decreased friction coefficient and higher hardness- all desired performance outcomes for its use in orthopaedic applications (25,117,118). Furthermore, Ti64 displays an excellent tensile strength of ~860MPa per 4.5g/cm^3 density ratio; its tensile strength is similar to that of stainless steel which is much heavier (7.9g/cm^3 density ratio) - thus Ti64 edges in advantage. Ti64 also displays good fatigue resistance (20,25,45).

2.2.5 Titanium and titanium alloys tribological limitation

2.2.6 Wear

Without surface modifications Ti64 exhibits poor tribological behaviour (28). This issue has greatly impeded the use of titanium in a span of applications (119). Tribology is noted by the nature and consequences of friction, wear and lubrication behaviours between interfacial interactions of materials; and is characterized by: its high friction coefficient, severe adhesive wear and low abrasion resistance with strong tendencies of seizing, which renders it unsuitable for load-bearing applications (28).

Wear is the removal of material from interacting surfaces in motion as a result of friction (120). Dry friction can be defined mechanically as the resistance to motion in a tangential direction of the contact and/or the result of energy dissipation at the (sliding) interface generating heat. Two mechanisms contribute to friction: physio-chemical or a mechanical interactions, termed adhesive or ploughing effects, respectively (121). Adhesive friction results in the formation of microwelds located at the interface of asperities when sufficient normal force (F_N) is applied to two apparent smooth surfaces. With the application of ample shear force (F_τ), fracture of the weaker surface should occur. Hence, the coefficient of friction (μ) can be calculated by (122):

$$\boldsymbol{\mu = \tau / \sigma_{YIELD}} \qquad \text{whereby } \tau = \text{shear stress}$$

$$\sigma_{YIELD} = \text{Yield stress}$$

In terms of ploughing, for ease of explanation asperities are assumed to be cone shaped, it is considered to be a plastic deformation process, whereby a displacement of asperities between two interlocking surfaces occurs (123). The μ of this form of friction mechanism can be represented by (122);

$$\boldsymbol{\mu = 2/\pi \tan(\theta)}$$

Whereby, θ is ½ the angle of the cone. μ depends on the tan (θ), which is proportional to θ.

Wear is characterised by irreversible change of surfaces and can materialise in various patterns such as: abrasion, fatigue, erosion and cavitation, with abrasive and adhesive wear being the most abundant wear mechanisms (120,124). Bowden and Tabor (1950) concluded that adhesive wear consequently occurs as a result of adhesive friction mechanism (125). The variation of adhesive wear can be attributed to the effects of metallurgical compatibility (MC); whereby if two elements have a high solubility to each other, they are likely to adhere together (126). As for abrasive wear, it occurs when as softer materials surface is removed by rubbing against a harder surface. The harder material has asperities that plough and cut into the surface of the opposing softer material under load. One of the best examples of abrasive wear is during grinding or polishing (121). An abrasive hardness over material hardness (Ha/Hm) ratio greater than 1.2 (hard abrasion) is usually desired as the abrasive effects on the material are significantly reduced (29,121).

Titanium and its alloys are ‘soft’ and so have a propensity to gall and eventually seize when employed for sliding applications, hence its poor fretting wear resistance (28,107). Galling occurs when two mating surfaces rub and get friction welded together resulting in gross surface damages (i.e. transfer, displacement of bits of material, and roughened surface) (127). This phenomenon is not aided by titanium’s mechanically unstable passive oxide layer (OL), which demonstrate low shear strength, and so can be breached and removed by opposing contacting asperities. Once the OL is removed (via oxidative wear), the bulk metal is exposed to Ti64 undergoes adhesive wear whereby there is material transfer from the Ti64 surface to its harder rubbing counterpart (127). These transfers of material results in a roughened material-to-material surface contact points, and the transferred material abrade the remaining Ti64 surface (127). As a consequence Ti64 can experience galling that could potentially foster catastrophic asperity junctions that are calamitous to the sliding system, eventuating in a seizure (106,107).

Kumar et al., (2018) reported a decrease in wear rate and coefficient of friction of Ti6Al4V substrates with increasing load (13.7 N to 109.9 N) and sliding speed (0.01 m/s to 1 ms), this was reported to have occurred as a result of the formation of a protective oxide layer (128). Moreover, there are reports that concluded that the wear resistance of the harder material Ti6Al4V was lower in comparison to the softer material CP-Ti, as hardness of a material is not the only contributing factor. Other influencing factors such as mechanical, microstructural and surface characteristics play an important role, within the sliding interface (129). Similarly, Feng and Khan (2008) and Hadke et al., (2015) reported on a supporting theory when comparing as-received Ti64 to quenched and aged Ti64. These outcomes have been linked to the ensuing effects of microstructure had shifting the wear mechanism. It has been suggested that the at low temperatures change in microstructures on the tribo-pair contacting asperity surfaces occurs a consequence of frictional heating (130,131). In addition, the increasing sliding speed and load can result in phase transformation, plastic deformation and loss of resistivity thus activating thermal softening (132,133). A study conducted by Collings (1984) reported that thermal softening enhanced wear rates (via delamination) as it decreased Ti-alloy's yield strength with increasing temperature (134). Delamination mechanism has been described to occur when there is continuous interaction of contact asperities leading to severe plastic deformation. This results in an accumulation of strains that eventually surpass the critical plastic strain, thus initiating nucleation or propagation of cracks from the subsurface regions of the substrate (135,136).

More specifically Ti64 demonstrates high friction coefficient, poor adhesive wear resistance, and when its employed for sliding applications, the alloy is prone to wear particle release, galling and seizing (25,137). For load-bearing articulating surface applications, Ti64's proclivity to wear, results in material degradation over time and subsequent aseptic loosening to sequential implant failure (28,138). Aside from infection, aseptic loosening is one of the major causes of implant failure that requires revision surgery (32,139,140). Furthermore, the host's bio-reactivity to wear debris varies depending on its characteristics which would require identifying its underlying mechanism (138,141). For example, under normal cyclic conditions of an articulating surface, the implant's protective OL could be worn away. This could result in the production of small wear particles, or in more severe cases greater number of irregularly shaped larger particles (141). These wear particles can lead to severe adverse bio-responses such as inflammation of affected area, periprosthetic osteolysis, cytotoxicity (due to the release of Vanadium), or even go as far as being linked to inducing malignant fibrous histiocytoma (106,121,138). The simultaneous reactions of adhesive, abrasive, oxidative wear during Ti alloys sliding mechanism can be grouped under the umbrella of fretting wear (127). The tendency for titanium and its alloys to wear, leads to aseptic loosening of the metal implant, which has been reported to be one of the main causes of implant failure. For example, its been reported that 56% of orthopeadic revision surgeries are due to loosening (142). Around 10 to 20% of titanium femoral head with a polymeric cup in an artificial hip joint will have to be replaced every 15-20 years due to aseptic loosening (106). Moreover, the wearing away of its thin OL layer due to its poor shear strength, renders titanium undesirable for torque applications such as bone screws (25,118)

Added blame to Ti64's poor thermal conductivity (17 W/mK) has also been reported. Reports state that flash temperatures generated, during sliding, by friction heating at the tribocontact asperities betters the diffusion, ductility and plastic deformation of asperities (127,143). This mechanism is supported by the research conducted by Basu *et al*., (2009) whereby pure titanium demonstrated lower friction coefficient when tested at liquid nitrogen temperatures (144). The thermal conductivity of a metal is linked to its deformation mode, and dislocation slips, hence the relation to its crystal structure (127). Generally, the understanding of titanium's tribological behaviour have not yet been fully grasped, it has been reported to be related to the alloy's electron configuration, crystal structure, and lubrication characteristics (107,117). The sections and Figure 2.8 below further illustrate these relationships for titanium and its alloys.

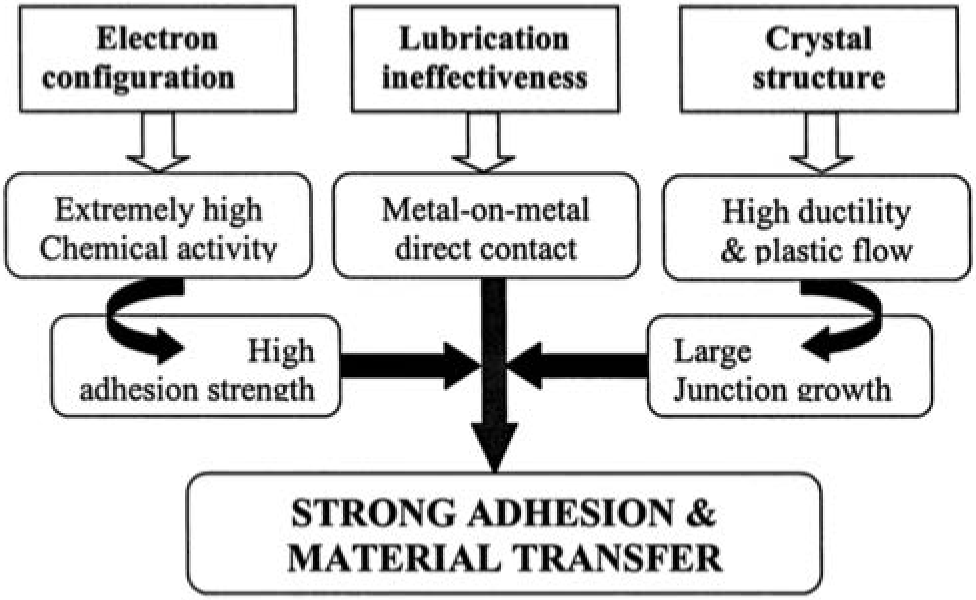

Figure 2.8 Schematic diagram of the three main factors that contribute to the tribological performance of titanium and its alloys (28).

2.2.7 Electron Configuration

Various transition metals possess differently unfilled valence bands (due to their oxidative states) based on their electron configurations; this determines its d-bond character. It is the filling of d-electron orbitals that influences a transition metals bulk and surface behavioural properties, such as adhesive energy, shear moduli and chemical stability (145,146). There is an opposing relation between d-bond character and the chemical affinity of transition metal surface. So the greater a metal's surface activity, the higher its friction coefficient and the lower its percentage d-bond character (145–147). For example, titanium is more chemically reactive (d-bond character of 27%) compared to rhodium when tested in sliding contact against diamond, as it demonstrated greater interfacial adhesion (145–147). Similarly, Rhodium demonstrated higher d-bond character and the lowest friction coefficient while titanium demonstrated the high friction coefficient when tested against silicon carbide (146). This relationships is expected on metal-metal and metal-ceramic contact, although the friction coefficient of metals on ceramic contact is lower (146,148,149).

2.2.8 Crystal structure

Titanium's plastic deformation and ductility leads to its poor adhesive wear performance; these are all birthed from the metals crystal structure (127). Usually β-phased bcc structures demonstrate lower friction and wear characteristics compared to α hcp crystal structures (127). At room temperature the deformation of hexagonal structures results in a slip along the basal plane (001) (127). This slip prevents further slips on other planes halting any further deformation; cubic structures differ as its deformation results in multiple slips systems. α-titanium exhibits an axial ratio c/a of 1.588, which is lower than the ideal ratio (1.633) required for the closest packing (127). Subsequently, titanium’s lattice is more compressed along the c-axis; hence its interplanar spacing and the planes atomic density are also reduced (127). These circumstances render the basal plane less favourable for slip and the slip can occur on other planes. Consequently, titanium now favours the behaviour of cubic crystal structured metals and demonstrates high ductility, easy deformation and poor tribology (127). Hence, Ti64 (being allotropic) exhibits better friction and wear characteristics when compared to cpTi (138).

2.2.9 Lubrication characteristics

Commonly, many sliding surfaces are lubricated to reduce adhesion, lower its friction coefficient, and insulate against the effects of wear (127). These lubricants can be in the form of gases, liquids and solids, for example, oxygen found in air can be considered a lubricant as it reduces adhesion, friction and wear of solid surfaces during contact (127). Unfortunately, all conventional lubricants have been infective when applied on titanium alloys (127). Sometimes, titanium and its alloys can experience boundary lubrication, but because the lubricating sheet is so thin, Ti asperities can still come into contact with opposing surface. In addition to this issue, titanium’s poor thermal conductivity results in the desorption of the all ready thin lubricant due to the flash temperatures produced at tribocontacting points (28,107).

Furthermore, although titanium demonstrates the closest Youngs modulus to bone (Table 2-1), it is still not close enough to avoid the phenomenon of stress shielding. The femoral bone consists of an outer cortical bone, which surrounds the central marrow cavity, however the proximal medullary femur bone of the femoral head is cancellous, which exhibits an even lower Youngs modulus. The mismatch in Youngs modulus, when a replacement metal femoral stem is placed, results in osteopenia. This occurs as the necessary stresses required by the femur (particularly osteoblasts) is mostly directed to the metal (Ti) implant and so the bone resorption ensues- this is stress shielding (19,45). This phenomenon is exacerbated by the use of 316 stainless steel, and cobalt-chromium implants due to their greater modulus mismatch (19,150,151).

Generally, Ti64's exhibits a great balance of desirable properties and behaviours for a vast array of applications (127). Nevertheless, its poor tribological behaviour is a serious detriment (127). Although, heat treatments are used to control its microstructure hence ameliorating its strength, or tailoring other properties to its optimum for specific applications, the nature of titanium still remains- thus adhesive wear is not necessarily improved (127). To overcome this lingering issue, surface engineering treatments are employed to create a hard protective surface layer onto the bulk Ti64 material that displays better lubrication behaviour, lower friction coefficient and improved fretting wear performance (108,152). In addition, there is a on going concern of bacterial adherence on titanium implant surfaces despite titanium's reported degree of antimicrobial behaviour attributed to its oxide layer (153). Both these main issues can be potentially be confronted by surface engineering techniques.

2.3 Surface engineering

2.3.1 Introduction

Presently, numerous surface engineering techniques can be used to enhance Ti64's poor tribological performance and better its antimicrobial behaviour. Surface engineering technologies ranging from surface modification to coating techniques have been employed to increasing its surface hardness and/or lowering its friction coefficient (97). Not only so, but titanium surface modifications can be optimised to elicit the desired biological response in its given function (108). The surface engineering of titanium and its alloy can be narrowed to two extensive groups of: surface coatings and thermochemical treatments (97). There are numerous surface thermochemical modification treatments adopted to improve Ti64's poor tribological performance, these include: nitriding, carburization and oxidation. However, these treatments are always almost conducted under high temperatures, which results in distortions within the metal substrate (108). Alternatively, there are thermochemical treatments employed for surface coatings, such as: physical vapour deposition (PVD) or chemical vapour deposition (CVP), to ameliorate the alloys surface properties. Unfortunately, the coating placed is at risk of interfacial separation, particularly under cyclic loading conditions (45,108).

2.3.2 Surface coatings

According to Arango *et al.*, 2012, coatings methods can be divided into thermal or chemical. The former includes methods such as thermal plasma spray (TPS), physical- and chemical-vapour deposition (PVD & CVD). The latter can be further subdivided into electrodeposition, electrophoresis and sol-gel methods (154). TPS method is based on a direct current arc providing a high temperature, which melts or semi-melts the coating material that is later plasma sprayed onto the bulk metal surface. The coating is plasma sprayed to ensure high deposition rates of around 80g/min, ensuring a thick deposit layer at low cost. Other materials have also been sprayed onto substrate surfaces by using a denotation gun, high velocity oxyfuel (97).

On the other hand, the coating material in PVD process as shown in Figure 2.9, which could be a metal alloy, compound or a metastable material, is sputtered or evaporated to form molecules or ions (from solid or liquid sources) that are deposited onto the surface of the substrate where it later condenses to form a film layer. This process is performed in a vacuum and it can occur via evaporation, sputtering or ion plating (108,154). PVD also provides wear-resistance and surface hardness of Ti64 (108,154,155). PVD provides a high coating densities ranging from angstroms to millimetres with strong interfacial adhesion (108). Briefly, chemical- vapour deposition process (CVD) illustrated in Figure 2.9, involves the dissociation of reactant gases (precursors) in a chamber to produce reactive species that are subsequently deposited onto the heated surface of the substrate to be coated (e.g. Ti64) (108,156). It occurs at temperatures ranging between ~200 to ~2000°C, which generally tend to be higher than the PVD process; thus any substrate that cannot undergo high temperature exposure required by the CVD process, may potentially be coated via PVD. Generally, CVD has good reproducibility and it results in uniform highly dense films with good adhesion due to the high deposition rates (156). However, the CVD process is somewhat limited to single components, due to its difficulty in depositing multicomponent materials because different materials possess different vaporisation rates (156).

Chemical conversion coatings such as electrochemical deposition can be employed to better the lubricity of titanium (108,154). This method has been utilised to reduce friction and better the corrosion resistance of certain metals (154). For example, copper plated titanium wires have improved surface lubricity, while the addition of platinum on titanium improved the surface electrochemical properties (31) . The sol-gel method is another chemical method, which consists of polymerising a solution to form a gelatinous network that is dried and made dense for its given application (154).

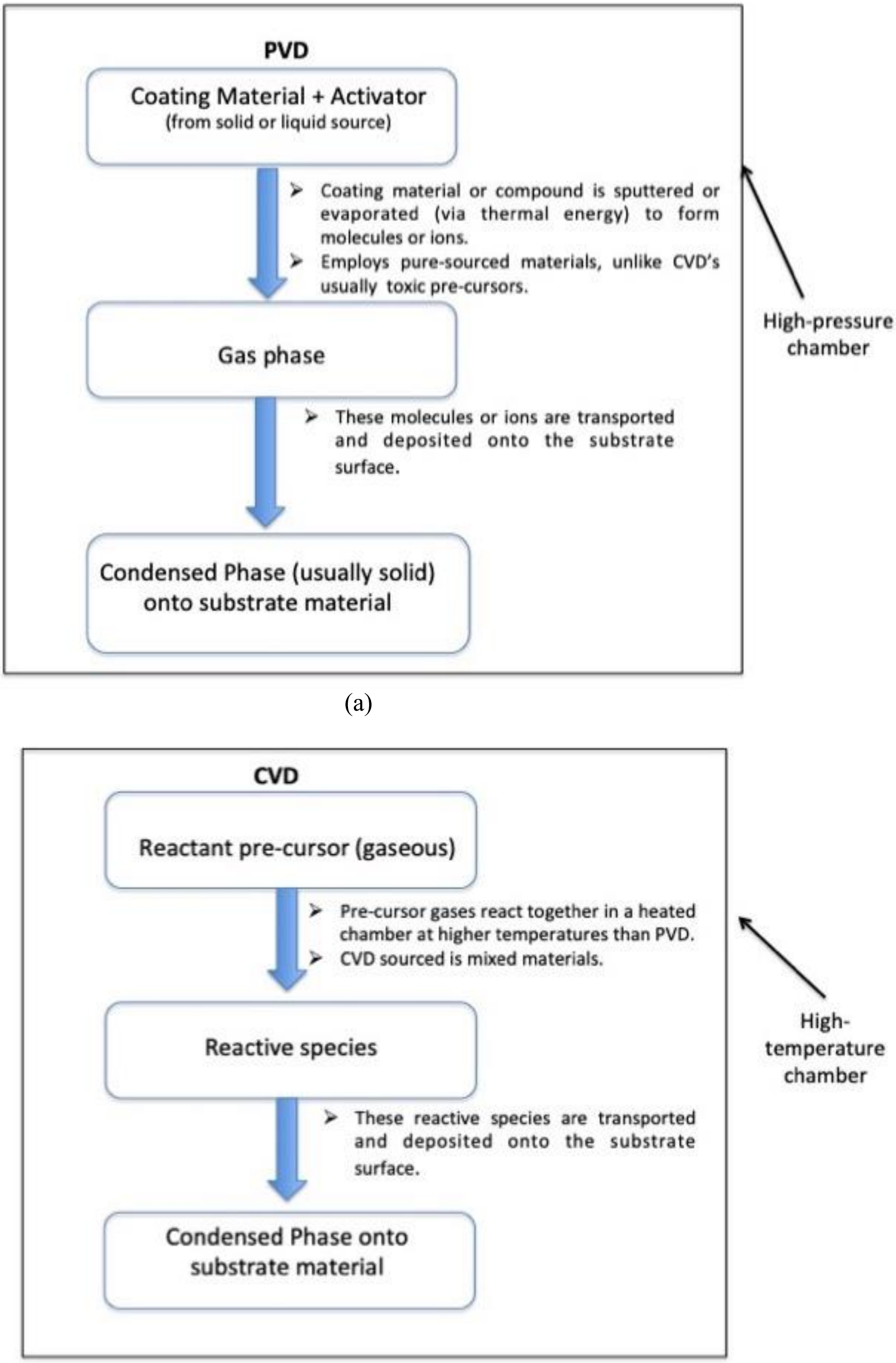

(a)

(b)

Figure 2.9 Schematic of the breakdown of: (a) PVD and (b) CVD process.

2.3.3 Thermochemical treatments

The three most popular thermochemical treatments that enhance the alloys tribological behaviour are carburisation, oxidation and nitriding; the latter can further be divided to plasma, gas, ion-beam and laser nitriding. Firstly, due to nitrogen's high solubility in α-Ti to form TiN surface layer with a sub-layer of Ti_2N which are higher in hardness; thus nitriding has been used for many years to enhance the surface hardness of titanium and its alloys used for orthopaedic implants (108,157,158). However, the process must partake in an oxygen depleted environment due to titanium tendency to react to oxygen to form TiO_2 (31). One of the main advantages of this process is the ability to control the phase formation alongside the depth of the nitride layer, as thicknesses of ~50 µm have been achieved. PVD and ion nitriding are the two main conventional nitriding processes used for titanium (31).

Secondly, carburisation of titanium and its alloys also occurs in oxygen-depleted environments. It is the formation of a hard TiC (cubic lattice) layer on the titanium surface (152). However, compared to nitriding and oxidation, carbon has the least solubility within titanium, thus thickness of 1 to 10 µm can be obtained with no underlying significant diffusion zone (31). This process can be further classified into solid, liquid or gas/plasma carburisation. Carburising has been reported to generate up to a two-fold hardening effect on the surface of Ti64, however excess carbon can have adverse effects (108).

Lastly, titanium naturally has a high affinity to oxygen, but also if this TiO_2 layer is controlled and grown to ideally 2-3 µm consistently thick layer can increase the hardness and corrosion resistance while reducing friction coefficient of Ti64 (117,152). Thermal oxidation and anodic oxidation are the different types of oxidations conducted. The former is the dissolution of oxygen molecules in an oxygen and nitrogen atmosphere in an furnace at an elevated temperature (28,152). Oxygen diffuses through the Ti64 to form TiO_2 forming an oxygen diffusion zone (ODZ), and as the process goes on more oxygen diffuses past the existing TiO_2 layer to the titanium-oxide layer interface where it reacts with titanium to form more TiO_2 (31,117,152). This OL can be porous or continuous depending on the rate of oxide formation, which is influenced by temperature and time (31,152). This thermal treatment otherwise known as thermal oxidation can result in the formation of anatase or rutile. Anatase structures exist at room temperature and can begin its irreversible transformation to rutile structures at temperatures above 600°C (31,117). Rutile structures are usually favoured for biomedical applications, as they are more thermodynamically stable and demonstrate more inert behaviour, higher hardness, lower friction co-efficient and antimicrobial behaviour (108,117). However, this OL can be quite brittle and so can easily be damaged (31). Anodic oxidation is an electrochemical reaction that drives oxygen ($2O^{2-}$) and titanium (Ti^{4+}) ions produced by redox reactions to the surface of the anodic titanium substrate, by the use of an externally applied electric field. Aside from also producing an OL, which demonstrates increased hardness, lower friction, it also exhibits improved adhesion and bonding (108). For the ions to continuously be driven through the existing OL formed on titanium, the electrical field needs to be strong enough. However, at high voltages there will be a build-up of oxygen gas (product of redox reaction), which could cause sparking (108). This sparking results in the formation of porous oxide films and this process is known as anodic spark oxidation (108).

Specifically with Ti64, temperatures >200°C result in a substantial diffusion of oxygen into alloy, and at even higher temperatures of approximately >400°C the ODZ develops (117). The optimal temperature of 600°C for 60 h has been reported as the idyllic parameters for OL formation supported by an ODZ to combat wear (117). This is because heat treatment at temperatures above 800°C results in a wider ODZ, and thicker OL which accentuates the mismatch in lattice structures between rutile TiO_2 and the bulk Ti64 (24,117). The differences in lattice structures means there are differences in thermal expansions and so during heating, the mismatch stresses result in the spallation of the oxide film from the bulk material (24,117).

2.4 Additive manufacturing

2.4.1 Introduction

Additive manufacturing (AM) is a comprehensive term for technologies that produce near-netshape or netshape three-dimensional component by successively joining material layer-by-layer from a computer-aided design (CAD) (24,159). Essentially it is the welding of materials in the hopes of creating near-netshape/ netshape components reduces cost significantly by getting rid of secondary processes i.e. machining or forging as these manufacturing methods result in large amount of material waste (159–161). This method can be employed for the fabrication of metal (e.g. titanium) implant parts that possess geometrical complexities (162).

In AM technology, the representative 3D CAD model of the manufacturing part to be produced is firstly created. This model undergoes various pre-processing steps, and combined with the desired processing parameters to produce the final component (163). This process is succinctly broken down in the Figure 2.10.

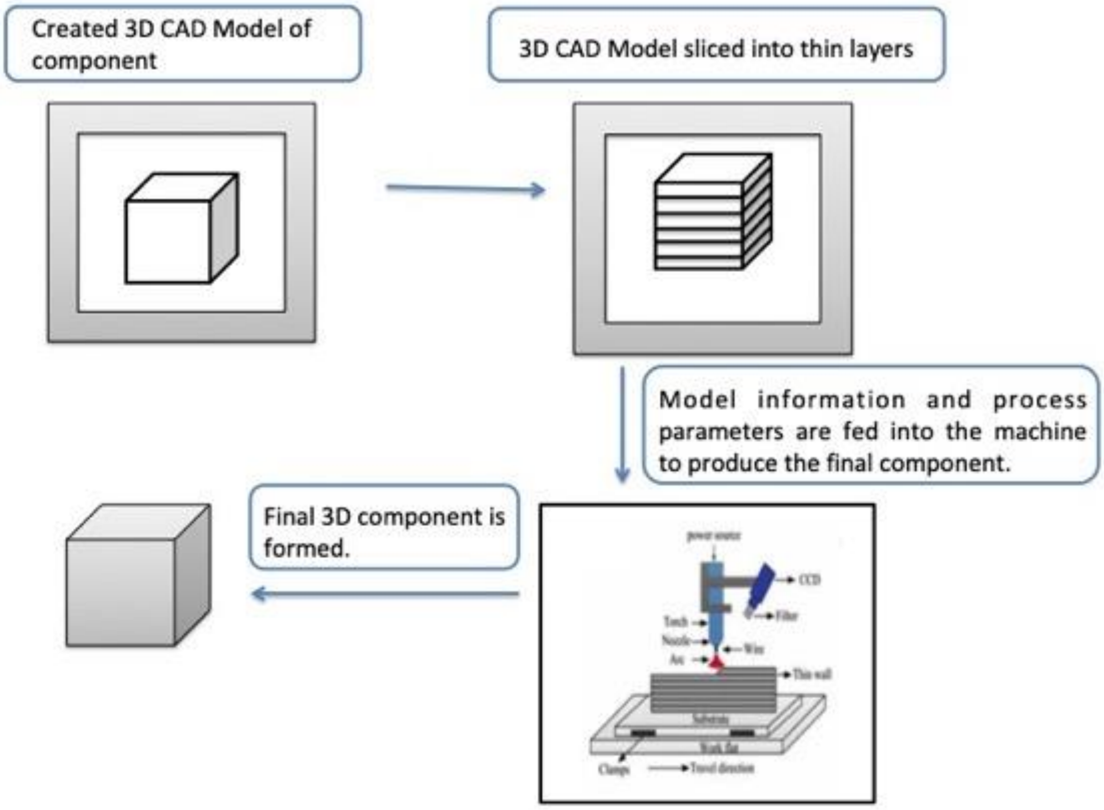

Figure 2.10 Illustration of the AM process (163).

Generally, according to the ASTM Standard F2792, the AM process can be divided into two main categories, which are Direct Energy Deposition (DED) and Powder Bed Fusion (PBF) (163)**.** The Figure 2.11 is a breakdown of the DED and PBF processes currently employed in various industries. The DED process is based on simultaneous coaxial powder feeding (using argon gas) along with laser melting (163). The argon gas is not only used to blow the powder into the melt pool but it also helps to protect the molten metal from oxidation (163). DED can also be conducted using an electron beam and can also melt commercial filler wires instead of fed power into the molten pool. This process is often used to generate large rough “blank” shapes, which require extensive machining (163). The latter is uses a laser or electron beam that scans/melts over a pre-spread metal powder on a powder bed. This process can further be broken down into selective laser sintering (SLS), Selective laser melting (SLM) and Electron beam melting (EBM) (163). SLS results in partial melting, that is sintering, of the pre-spread powder, whereas the aim of SLM and EBM is to completely melt the powder (163). This research will focus on the use of SLM. Generally, the processes result in rapid melting and re-solidification resulting in large temperature gradients and high cooling rates which can be as high as 10^6 K/s (160,162). Particularly in Ti64, this affects the microstructure and conduces high residual stresses (162). Other defects can also be created such as porosity, weld crack etc., which all depending on process parameters; these defects could significantly deteriorate the final product's mechanical and fatigue properties (160,162). These properties are important to Ti64 used for load-bearing applications, thus the understanding of the manufacturing process and its effect on specific mechanical properties are vital in deciding if AM is ideal (162). Post-welding heat treatments or machining can be conducted to relieve stresses and distortions defects however, defects such as porosity are trapped within the welded joints post-solidification (56). Porosity in titanium alloys has been attributed to the presence of oils, grease or moisture, which form gases on the surfaces being welded; as well as process parameters (e.g. scan speed, energy input, hatch spacing) (56).

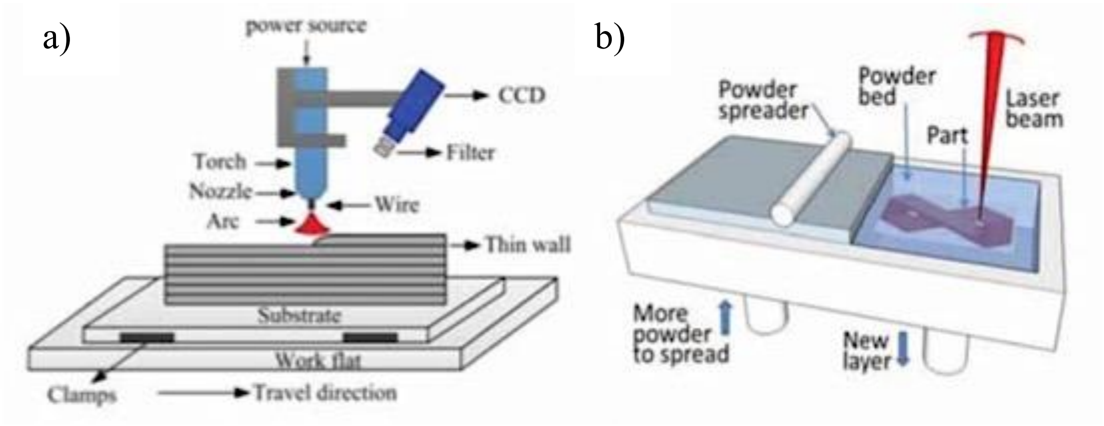

Figure 2.11 Illustration of the differences between: a) DED and b) SLM (163).

2.4.2 Advantages and limitations

Advantages:

- Allows for the formation of porous Ti64 structures to be created with the porosity of these structures has shown to reduce the Youngs modulus mismatch between bone and metal implant(s); it also promotes osseointergration and vascularisation on implant surfaces. Thus it allows for the process to be tailored to the final component function and complex geometry (151,164).
- Possible to create near-netshape products, thus minimising the machining and tooling employed by conventional methods; so it eliminates unnecessary process steps.
- Better lead-time (turn around) and limited waste as unused powder can be recycled (159,163).
- Cost- effective due to less waste, and no need for post-processing machining.

Limitations:

- Poor reproducibility and repeatability (microstructural inconsistencies) as a consequence of its complex nature due to its dependence on the various process parameters and phenomena
- High production and capital cost in purchasing to setting up the machine (159).
- Relatively high capital cost and purchase of the metallic powder feedstock (159).
- The process is restricted by its chamber size, thus only a certain number and certain size of components can be fabricated (159).
- There is still a lack of comprehensive understanding thermal impact has on microstructure development (56,160**)**.

2.4.3 Monitoring and Control Systems for AM Process

Due to the highly complex nature of the AM process, and lack of control of process parameter and understanding of underlying physics, research has been carried to help develop monitoring and control (feedback) systems to help provide dimensional accuracy during powder deposition. These include, infrared temperature signal system, CCD camera, pyrometer, photodiode, which monitors the thermal cycle/distribution, and the main scanning parameters such as power, speed and feed rate (165–167).

2.4.4 Selective laser melting (SLM)

2.4.4.1 Influence of Process Parameters and Phenomena

SLM technology is used for the production of filigree dental or human implant structures (168). Generally, the AM (SLM) process consists of numerous process parameters, with the main ones being power, atmosphere used, scan speed, scan strategy, layer height; when these parameters are altered, the energy input and thermal behaviours can also be affected (162,169)**.** Additionally, the size, shape, physical properties (e.g. flowability), and absorptivity of the powder also impacts the interaction with the laser and the final product quality (151,162). Anther factor, which majorly affects the quality of the final product, is the energy density (E, in J/m^3); it is the measure of the energy input (162,169). Energy density does not only determine the degree of consolidation of powder particles but also the formation of defects (170). Specifically for Ti64, the ideal energy density (E in J/m^3) currently researched at the university of Birmingham has been reported to be approximately 60 J/m^3; the expression for energy density is (162,169,171):

$E = P / v \bullet h \bullet t$ Whereby, P is the power (J/s),

v, Scan speed (mm/s)

h, Hatch spacing (mm)

t, Layer thickness (mm)

By achieving the optimal energy density, which varies with different powder material properties, the ultimate consolidation of powders with minimal porosity content can also be obtained. This process influenced by all the processing parameters mentioned in the equation above. Firstly, the amount of liquid phase found in the molten pool depends on the energy transferred and the melting temperature of the material itself; the major factor that influence this are laser power and scan speed (172). Dilip *et al.*, (2017) concluded that low laser power and high scan speed reduced the width of laser track on Ti64, and if these parameters are heightened the track became discontinued eventuating in balling (169). The authors also found the melt pool depth penetration increased with lower scan speed but with increasing power, it resulted in keyhole effects. Additionally, low scan speed and higher laser power can result in porosity defects and denudation of powder (171,173**.** Powder denudation is when the melt pool is large that it causes part solidification of surrounding powders and so there is insufficient powder to fill the gap between adjacent tracks (171). Moreover, high-energy input with low scan speed can form residual thermal stresses within the component after solidification (171).

On the other hand, hatch spacing is the distance between the centre of one scan vectors to its neighbouring vector; it is greatly influenced by the combination of laser power and speed

(174). Hatch spacing has been reported to be the least sensitive parameter with minimal effect on the mechanical properties of SLM parts (172,175). Layer thickness refers to the thickness of the layer deposited to be molten, this thickness ideally should be less than the molten pool depth (174). However, it must be noted that similar energy densities can still be obtained by various combinations of: laser power, scan speed, hatch spacing, scan strategy and layer thickness (175). For example, increasing the scan speed, while decreasing layer thickness and increasing laser power does not necessarily balance each other out to achieve similar results. Thusly a comparison by energy density only can be misleading as the relationship between processing parameters not linear (175). Hatch angle also affects the performance of the finished manufactured part; it is the angle between the laser scan directions of consecutive layers (172). However, when an unsuitable hatch angle is applied, anisotropy of the part's mechanical properties can manifest. Lastly, the acute angle between the vertical axis and the longitudinal axis of a given samples defines the build direction (172). This can impact the materials elongation potential, ductility and strength (172). Scan strategy also plays a role in final component properties, as towards the scan track the speed is reduced and the laser power is usually unstable resulting in defect formation. Furthermore, defects found within the material could be pushed along the molten pool to the end of the scan track forming a higher defect density area (169). To combat the formation of these defect density areas, the scan strategy has been employed as successive layers are displaced as each island is built randomly and continuously. This method also displaces thermal residual stresses reducing the initiation of cracks (171,176). Unfortunately, due to the limitations in the laser as it tends to be unstable; these defects are dissipated to the border of the small islands (171).

2.4.4.2 Powder characteristics and morphology

The quality of the final components is influenced by the characteristics of the feedstock powder such as; size distribution, shape, surface morphology, flowability, and composition (163). The manufacturing process of the powder then influences the characteristics of the powder particles (163). Currently, there are four employed methods of creating powder, which are: gas atomised (GA), rotatory atomisation (RA), plasma rotating electrode process (PREP), and high-pressure water jet process. Firstly, during the GA process, the molten alloy is placed within a container and it flows through the nozzle of the container into a chamber where it is automatically atomised by blowing high pressure argon and nitrogen gas onto it (177). GA is the most popular process utilised for the production of AM powders; this is because it ensures a spherical powder shapes, good powder density and good reproducibility of particle size distribution (177). Meanwhile in RA the molten alloy would be placed inside a rotatory disk which spins flinging fine droplets of molten metal out that solidify and as collected as powders (163). On the other hand, during the PREP process the end of a molten bar is rotated on its longitudinal axis and fed an electric arc or plasma, which centrifugally ejects the fine molten droplets that are collected as powders (163). Lastly, the high-pressure water jet uses a water atomisation mechanism to solidifies molten metal droplets (163).

As for the chemical composition of the powders, the presence of interstitial elements influences the melting temperature, mechanical properties, weldability and thermal properties etc. of the process (177). The finer powders produced by the GA process tend to exhibit higher oxygen content due its greater surface area (177). In the AM process particles distribution influences the surface roughness of the final component; the first is particles with a median of 50 µm are ideal for SLM processes, but sizes below 20 µm exhibit poor flowability. However, particles sizes greater than 50 µm is ideal for EBM (177).

The final powder morphology of the power particles affects the packing density of the layer thickness (177). Usually, spechical powder shapes are desired as it demonstrates good flowability and form uniform powder layers when spread onto the powder bed. But powder imperfections are not uncommon during power manufacturing, as irregular shaped powders, powders with satellites, powders stuck on powders, and hollow powder particles have been observed (177).

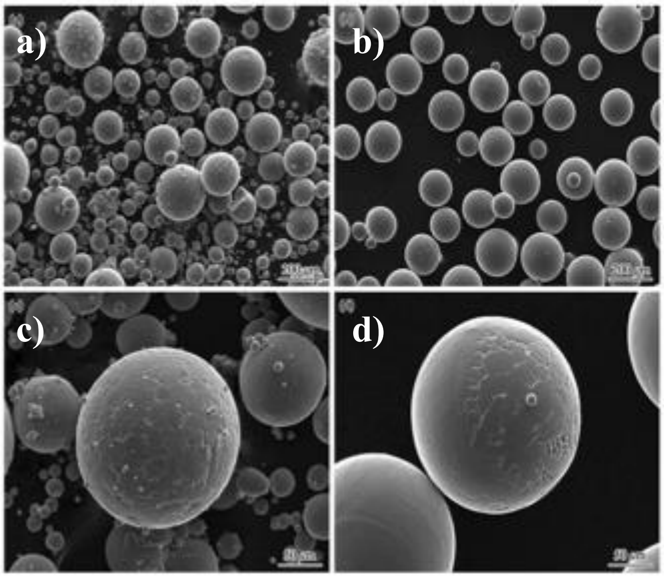

Figure 2.12 Displays SEM images of Ti6Al4V powder surfaces: a & c for electrode induction melting gas atomisation (EIGA) and b & d for plasma rotating electrode process (178).

2.4.4.3 Solidification Process and Heat transfer and Microstructure

Solidification in AM process is dependent on the liquid-metal interface, known as the melt pool, as it controls the heat transfers (162,176). Within the direct melting process, microstructure and solidification processes are dependent on the process parameters and phenomena; such as laser power, speed, scanning strategy and heat transfer modes (conduction – heat to substrate, convention-heat to gas, evaporation- ejection of liquid melt, and radiation) (176). So as the laser scans over the substrate powder, in its awake the fast cooling rates cause molten pool solidify quickly, and so dendritic structures are formed perpendicular to the melt pool/substrate surface (162,176).

The α +β allotropic phases found in Ti64 can only be present during slow solidification process, which is not the case in SLM (159). The fast cooling rates from heating above the β transus, β-phase will undergo martensitic decomposition, a diffusionless transformation to form extremely fine metastable α' (alpha-prime) (169). The α' martensite has been reported to form within a specific cooling ranges, cooling rates greater than 410°C/s form complete α', while only partial and incomplete transformation of α' can be noted between 20 to 410°C/s, and rates less than 20°C/s will produce no α' martensite (159). Some research have been made on the mechanics and formation of these α' grains, its been proposed that it grows roughly 40° from the build direction, and the grains grow within prior β columnar grains (179). The prior β columnar grains have a tendency to undergo intergranular failure, which decreases the ductility of the Ti64 SLMed part (179).

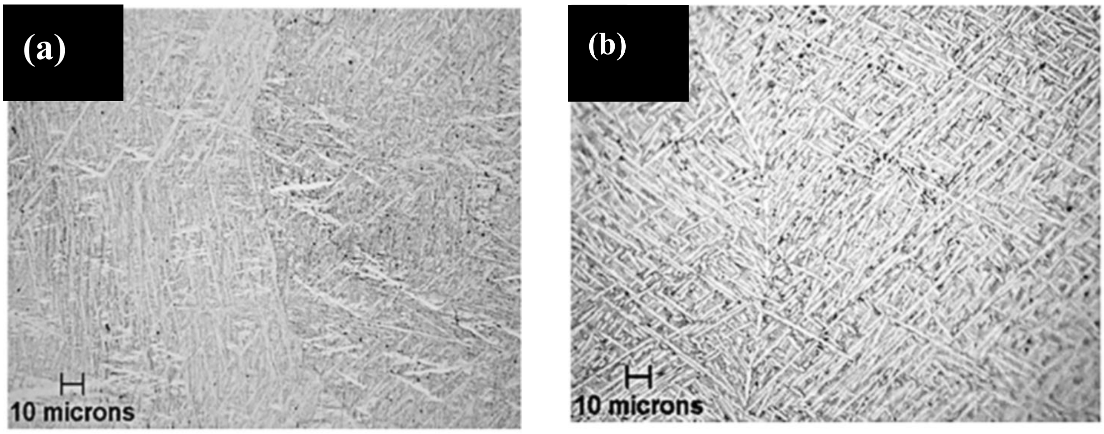

Figure 2.13 Optical microstructure of Ti6Al4V built by (a) Directed energy deposition producing fine needle-shaped α’ martensite phase and (b) annealed microstructure (940 °C/ 1 h/ air cooling) post directed energy deposition demonstrating α + β dual phase. Images of α’/ α phases are bright while β phase is dark (159).

Martensitic α’ has also been reported to mainly be acicular shaped when examinations on different processing and scanning parameters were conducted (179). This Martensitic α’ structure has been shown to demonstrate the higher tensile strength (MPa) compared to other Ti64 microstructures (i.e. equiaxed α +β, columnar α +β, and partially α’), but at the cost of exhibiting the lowest elongation percentage due its fine like needle shape and dislocations which results in low plastic strain (159). Generally, its strength is attributed to the non-equilibrium phase formed, which contains deformed lattice structures with lattice strains and dislocations- that ensue dislocation hardening (159). The features also help ameliorate the fatigue strength performance of SLMed Ti64 when compared to its EBMed counterpart (159). However, the SLM components demonstrate lower fatigue toughness, which can be resolved by implementing post-SLM processes such as annealing whereby the α’ martensite is decomposed, decreasing the size of the α phase there is a reduction of residual stresses (94,162).

2.4.4.4 Microstructural Features – Defects

Due to the SLM being a multi-physics process with transmission of energies, absorption, diffusion, evaporation of material etc, the process suffers from defective pores, cracks, incomplete fusion of material (balling) and impurities (171). These defects can greatly affect the mechanical performance of the final component with failure mechanism of surface and bulk defects performing differently (162,171). Broadly, SLM defects can be broken down into two major categories that are: process induced, and material induced.

The fast cooling rates of the SLM process creates a great temperature gradient, which in turn causes distortion, great thermal strains and residual stresses in the component that can also initiate crack and its propagation; this event is process-induced (163,171). During the scanning process there is a flow of heat via conduction, convection, radiation and evaporation. Conduction is the main path heat is dissipated into the platform, which holds the final component (159). But due to the platform being clamped, stiff and possessing a different thermal expansion coefficient, the fluctuating temperature gradient caused by laser melting and solidification, results in the expansion and compression of the platform and so an accumulation of thermal and residual stresses occurs. Thus, the platform is pre-heated prior to use in an attempt to alleviate these issues. Also, within a Ti64 specimen of zero defects, the decrease in the α phases from post-SLM heat treatment is essential in reducing the onset of crack nucleation phenomena. This is because without the presence of defects, crack initiation via plastic localisation occurs, and the α phases of the α + β microstructure of Ti64 impedes the localisation of plastic slips by its grain and phase boundaries. Thus α' martensite exhibiting its higher fatigue strength becomes the weakest link for crack initiation (162,180).

Defects due to porosity come under all three categories. Porosity is formed if gases present between or in the powder particles get trapped into the molten pool failing to be released due to the high solidification rates (171,173). With material induced-porosity, powder material during its initially preparation, for example GA powders, already contain trapped gasses, impurities and contamination elements, imperfections etc, hence pores within its powder particle. During the melting process these gases may also get trapped once the particle melts and solidifies into the component (171). To overcome this defect, PREP process is becoming widely recognised for the production of powder particles with high purity and near perfect spherical shapes (181). Melt induced porosity/voids occurs when the powder has a low packing density thus trapping gases (usually conducted in an argon atmosphere) between the powders when its laid on the powder bed (171). Therefore when the laser beam scans over the layer thickness of powder, argon gases between are trapped and forming pores; these gases can sometimes combine with the gases already present within the particles and so create bigger pores or cavities (171). Melt induced porosity/voids can further be broken down into: inter-layer, intra-track and inter-track. Hot isostatic pressing (HIP) is a post- AM treatment, which has proven effective in reducing porous defects (that serve as crack initiation points) in Ti64 to effectively improve the components fatigue strength and toughness. But components with complex geometries are at risk of losing its lattice structures (159). Also, the formation of pores have been controlled to produce porous structures tailored to reduce the phenomenon of stress-shielding in load-bearing applications (159).

Another process-induced phenomenon is the keyhole effect (182). It occurs when the energy density is high enough to cause evaporation of the molten metal, which is splattered; forming a keyhole shaped vapour cavity, which is later filled due to vapour pressure that cause the surrounding molten metal to collapse closing up the keyhole (56,182). King *et al.*, (2014) concluded that there is a threshold for the transition from conduction mode of the laser melting to the keyhole mode effect which is dependant on laser power, speed, beam size and layer thickness (182). If these parameters are optimised than the keyhole can be avoided as it results in the formation of voids. These voids or porous defects are created at the tip of the keyhole as the temperature is so high it causes the molten metal to bubble and the fast solidification rate and the collapsing in of surrounding molten metal traps gases (171,174). These inclusions are difficult to effectively eliminate (171). In the contrary, a process induced defect known as lack-of-fusion (LOF) occurs because there is not enough energy input to fully melt the metal powders. Hence, LOF defects consist of un-melted and/or poorly bonded powders (171). With low energy input, the width and depth of the melt pool is narrowed resulting in insufficient overlap between scanning tracks; when new layer of material is spread on top, it is even more difficult for the powder to be completely re-melted consequently birthing poor interlayer bonding (171). Additionally, LOF defects can sometimes be characterised by the affected area demonstrating a roughened surface as the defect area hinders the flow of molten metal forming interlayer defects that build up as the component is formed (171). Also, if a material such as titanium that has a high affinity for oxygen forms an OL on its surface, the wettability of the surface will decrease impeding on the flow of the molten metal. This consequently causes poor bonding between layers eventuating in incomplete fusion defects (171). Furthermore, the presence of contaminants such as oxygen or nitrogen gases (α-stabilisers) during the SLM process of Ti64 will result in slight increases in tensile and yield strength of the component as contaminants will pin dislocations (159). But despite the increase in strength, the presence of oxygen builds a brittle "*quasi-cleavage*" morphology, which resultantly reduces the plastic deformation of Ti64 (159). Additionally, the presence of oxygen results in the final Ti64 product will display a blue tint instead of being silver (159).

3 MATERIALS AND METHODS

3.1 Substrate preparation and treatments

Ti6Al4V rod was sourced from Baoki Tongrun Metal Material Limited Compnay. The specifications of the material is detailed in Table 3-1.

Table 3-1 Specification of Ti6Al4V rod cut by EDM.

Baoji Tongrun Metal Material Limited Company							
Commodity: GR 5 TITANIUM BAR				Finish: ANNEALED			
Specification: AM 4928/BS3 TA11/ASTM B348/ASTM B381/ISO5832 PT3/NACE MR0175				OrderNo: TT03315 TI-TEK (UK) Limited			
Chemical Composition (WT%)							
Ti	Al	V	Fe	C	N	O	H
Balance	5.5-6.75	3.5-4.5	0.30	0.08	0.05	0.20	0.0125

3.1.1 Cutting

Grade 5 Ti-6Al-4V annealed rod was cut using an electrical discharge machine (EDM), into 10 mm in height and 13 mm in diameter discs.

For characterisation, cross-sections were prepared by cutting the necessary samples in half using the Struers Accutom-5 (Version 2.1) cut-off machine. These samples were also polished and etched with 2%HF + 98% H_2O for 5-10 seconds to reveal their microstructure, before being rinsed with acetone and hot-dried under a hood dryer.

3.1.2 SLM

The SLM'ed discs in this research used for physical and chemical property evaluations, as well as microbiological testing were created using the Cusingў SLM system (Concept Laser, Germany) in the Netshape Lab of Met. And Mat. at the University of Birmingham by Parastoo Jamshidi. The M2 system employs a Nd:YAG laser with a wavelength of 1075 nm, spot size of 60 µm with a maximum laser output of 400 W. The samples created exhibited three different surface finishes using Ti-6Al-4V gas atomised powder (TLS Technik, Germany) sized 20-50 µm, at 150 W laser power, 1750 mm/s scanning speed, 20 µm slice thickness, and hatch spacing of 75 µm. Support structures were built between the substrate base and each individual disc to provide stability during the build. These samples were 20mm in diameter and 6mm in thickness. They underwent a Japanese JIS spread plate method (referred to in more detail under section 3.3.). Based on the results attained one pattern was chosen for further investigation in the PhD research.

To efficiently produce the samples required for the PhD research, pre-EDM'ed cut discs were placed inside a tailored aluminium build plate within the SLM chamber. A single SLM'ed layer approximately 20 µm thick using the 'island strategy' were created onto the pre-cut discs. The machine employs a Nd:YAG laser with a wavelength of 1075 nm, spot size of 60 µm. Different process parameters, which are power, scan speed, and a1 were employed and it resulted in various energy density outputs. Twelve different sample types with variations in process parameters including laser scan speed and power (thus energy densities), were selected at random using the Design Expert software in the Netshape lab a the University of

Birmingham. The twelve sample types were further tested using the Japanese JIS spread plate method (referred to in more detail under section 3.5.). Based on these results, six sample types were chosen; that is, two selected samples from the best performed, two from the average and two worst. The chosen samples were then replicated, but with some replicated with the addition of different weight percentages of silver (detailed in section 3.3).

3.1.3 Selected process parameters

After undergoing a Japanese spread plate method analyses (detailed in section 3.5), the chosen six a parameters are detailed below. Two parameters were chosen that performed the best (in reducing bacteria colony units), two that demonstrated an average performance and two that performed the worst. The detailed chosen process parameters are displayed in Table 3-2.

Table 3-2 The chosen six process parameters.

Processing parameters	Laser power (W)	Scan speed (mm/s)	Hatch spacing (a1)	Energy Density (J/mm^3)
1	200	2750	0.5	48.48
2	250	2750	0.7	43.29
3	250	1750	0.5	95.24
4	250	2750	0.5	60.60
5	250	2750	0.3	101.01
6	250	2750	0.1	303.03

Table 3-3 Displays sample ID from the chosen process parameters. The ID's with " underwent thermal oxidation.

Process parameters						
SLM treatment types	**1**	**2**	**3**	**4**	**5**	**6**
Ti64	Ti64_1	Ti64_2	Ti64_3	Ti64_4	Ti64_5	Ti64_6
	Ti64_1”	Ti64_2”	Ti64_3”	Ti64_4”	Ti64_5”	Ti64_6”
Ag0.2%	Ag0.2%_1	Ag0.2%_2	Ag0.2%_3	Ag0.2%_4	Ag0.2%_5	Ag0.2%_6
	Ag0.2%_1”	Ag0.2%_2”	Ag0.2%_3”	Ag0.2%_4”	Ag0.2%_5”	Ag0.2%_6”
Ag1%	Ag1%_1	Ag1%_2	Ag1%_3	Ag1%_4	Ag1%_5	Ag1%_6
	Ag1%_1”	Ag1%_2”	Ag1%_3’	Ag1%_4”	Ag1%_5”	Ag1%_6”
Ag5%	Ag5%_1	Ag5%_2	Ag5%_3	Ag5%_4	Ag5%_5	Ag5%_6
	Ag5%”_1”	Ag5%_2”	Ag5%_3”	Ag5%_4”	Ag5%_5”	Ag5%_6”

The 'island strategy' employed by the M2 for one layers thickness can be described as follows:

- After powder deposition, the laser scans the substrate surface creating the 'island strategy' at a 45° angle to the X-axis.
- In each island, laser scan vectors scan back and forth.
- The adjacent islands will have scan vectors running in a perpendicular direction.
- The M2 laser system employs a randomised order in which the islands are melted with the aim of reducing residual stresses within the final built component (refer to Figure 3.1).

The scan spacing (a1) parameters can be defined as:

$$a1 \quad = \quad \textit{scan spacing (h) / laser track width constant } (150\ \mu m)$$

The 'island scan strategy' was employed for all SLM'ed samples except for the control.

All the pre-cut discs to be SLM'ed were placed within a tailored aluminium plate with 15 holes cut to fit the Ti-6Al-4V discs. This was conducted to make the SLM process more efficient.

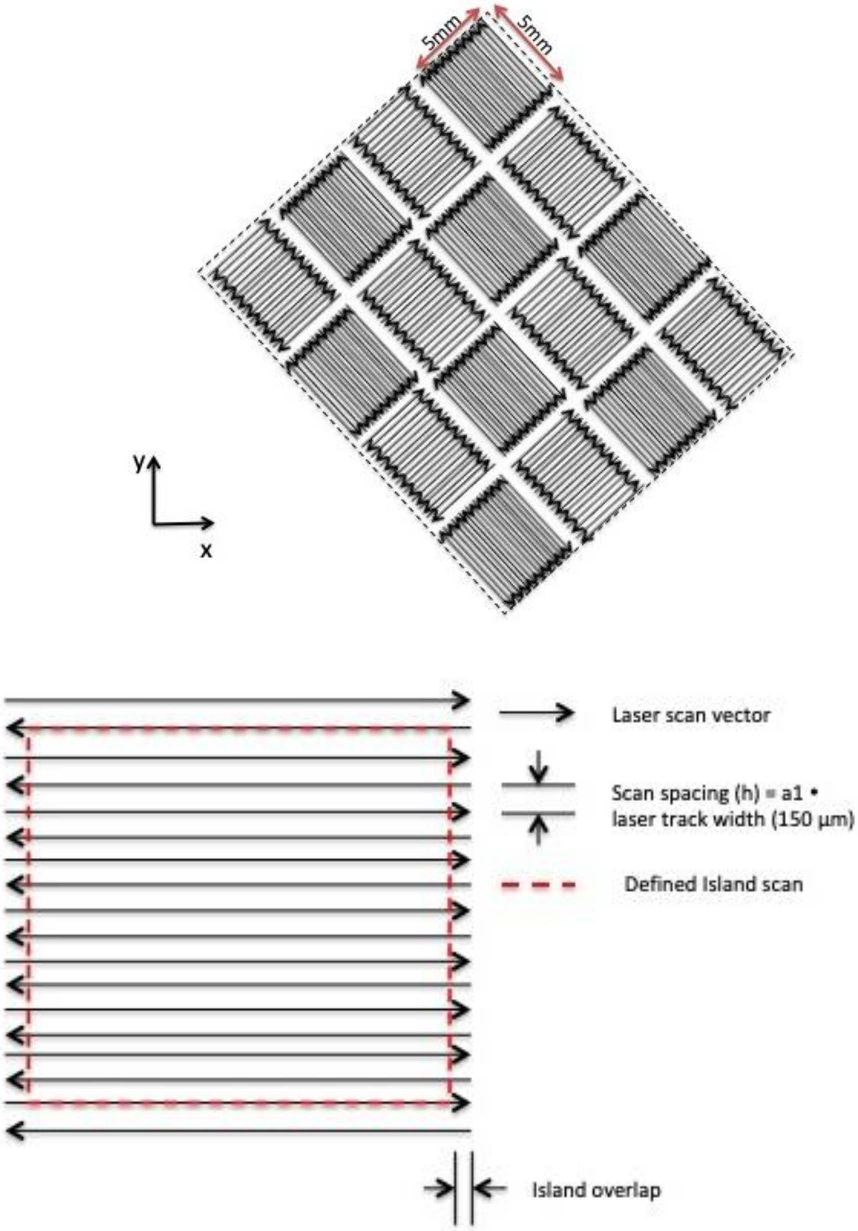

Figure 3.1 The 'Island scan strategy' of the SLM M2 system.

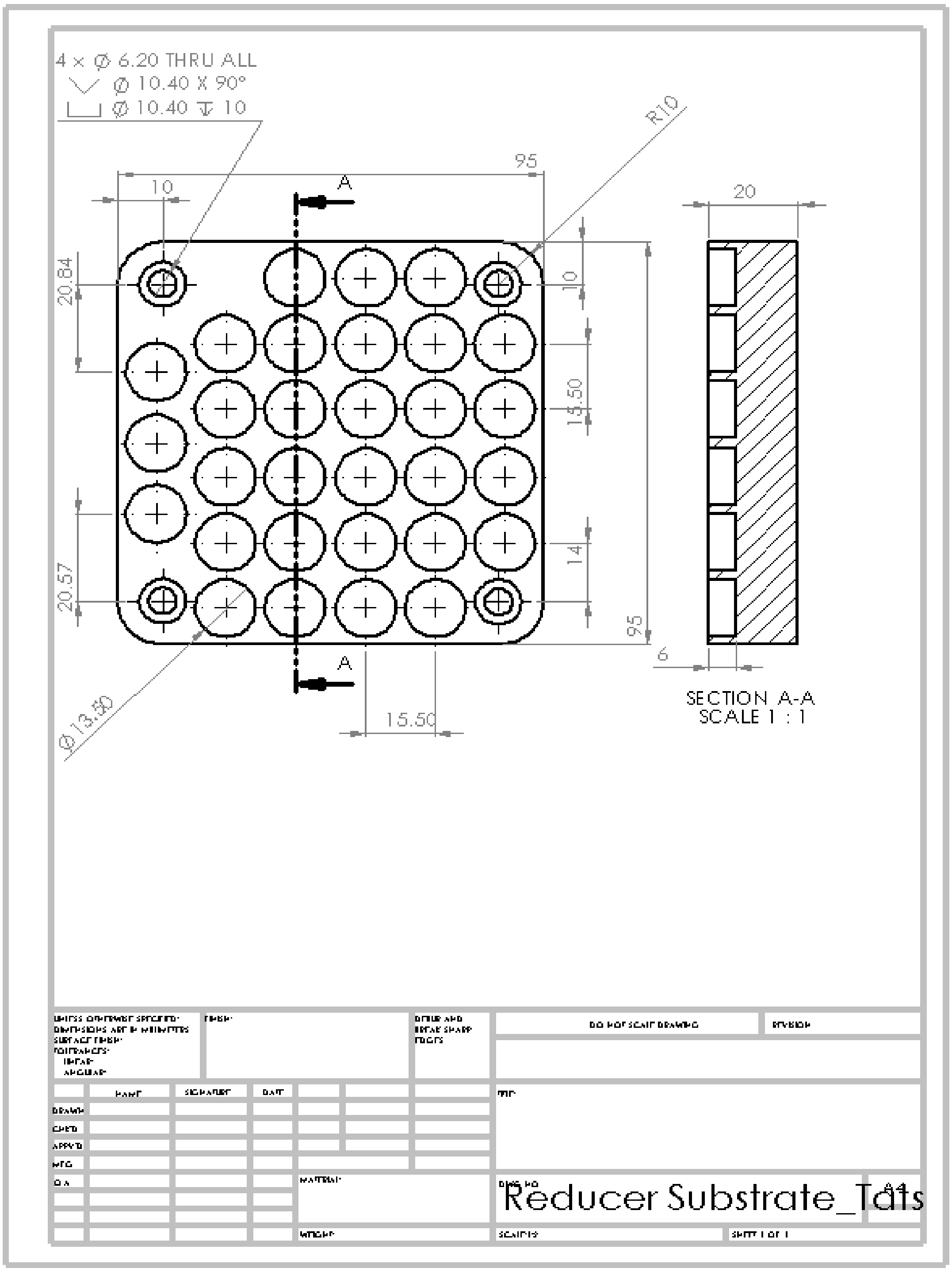

Figure 3.2 Sketch of the aluminium plate design.

The SLM layer, melted onto the surface of Ti-6Al-4V was conducted in four main batches;

Table 3-4 Details the various batch types and the different weight percentages doping of Ag conducted.

Batch I	Batch II	Batch III	Batch IV
Purely Ti6Al4V powder	Ti6Al4V powder doped with 0.2 wt% Ag powder	Ti6Al4V powder doped with 1 wt% Ag powder	Ti6Al4V powder doped with 05 wt% Ag powder

3.2 Thermal oxidation

Thermal oxidation (TO) treatments were carried out under normal atmosphere conditions for all sample batches that underwent SLM and untreated controls, in a large-scale laboratory furnace (Elite Thermal Systems Limited). TO was carried out at 600 °C for 4 h Table 3-3. Samples treated have a sample ID with " at the end.

3.3 Powder preparation

For the powder preparation, Ti-6Al-4V atomised powders were used. Batch I which contained purely Ti-6Al-4V powders were pre-deposited directly into the SLM powder chamber. However, pertaining to Batches II to IV, different weight percentages of Ag were added. Therefore, both powder batches were weighed inside a vacuum hood, due to titanium's high affinity for oxygen. Once the correct ratio of grade 5 titanium to silver was attained, the powders were placed inside four metallic cylinders with varying sized grinding balls and sealed to avoid the influx of air. The cylinders were placed inside a HMK-1901 planetary ball mill at 448 rpm for 12 h. These parameters were employed to mix the powders together.

Figure 3.3 The HMK-1901 planetary ball mill machine is displayed. The big red arrow demonstrates the clockwise direction at which the plate was spinning and the smaller red arrow.

3.4 Experimental methods

3.4.1 Scanning electron microscopy (SEM)

The surface morphologies of each sample were observed using a scanning electron microscope: JOEL JSM-6060LV (Japan) and the JOEL 7000F (Japan). There were conducted at an accelerated voltage of 15-20 kV.

In addition, some samples underwent analyses under Focused Ion Beam (FIB) milling SEM (FEI Quanta 3D). This was conducted to get a sample's cross-section on a site-specific area. Before 'milling' using the ion beam, the site of interest was covered in a protective platinum coating to shield from the potential damages the beam could cause on the surface and subsurface layers of the site of interest to be analysed.

3.4.2 Energy-dispersive spectroscopy (EDS)

EDS analyses conducted on the JOEL 6060 (Oxford Instruments Inca) demonstrated the chemical composition-depth and distribution of elements in the different modified and unmodified layers of samples.

3.4.3 X-ray diffraction (XRD)

XRD was performed within the diffraction angles of 20° to 90° (2Θ), normal coupled scans with a Cu Kα radiation (λ= 0.154 nm) and a dwell time of 2 s/step. The phase constituents of all the surfaces were tested using the XRD Powder Diffractometer Proto AXRD (Canada) at 30 kV accelerating voltage and 30 mA filament current. Subsequently, the X'pert High Score software was employed to identify the crystalline phases obtained from the XRD analyses.

The X'pert High Score software with PCPDFWIN database was used to identify and index the presence of crystalline phases on sample surfaces.

3.4.4 X –ray photospectroscopy (XPS)

XPS analyses was conducted at the Maxwell Center at the University of Cambridge on one as-SLMed sample with 1 wt.% doped Ag.

3.4.5 Surface roughness measurements

Surface roughness (R_a) was measured along and against (perpendicular to) laser build direction (BD). The substrates depth profile was also recorded in the form of colorimetric optical surface topography using the Alicona (of Mechanical Engineering department at the University of Birmingham). The measurements carried out were conducted along and perpendicular to the build direction in three different area's of the substrate surface. The Measure Suite Software of the Alicona was used to study the data collected and results are expressed as mean ± standard deviation (SD).

3.4.6 Contact angle measurements: surface energy and wettability analyses

Sample surface hydrophobicity was determined by water contact angle (WCA) measurements, using the sessile drop-instrument GBX Digidrop (Aston University). Distilled water (Υ= 72.8 mNm^{-1})(183) droplets of approximately 2 µl were deposited onto each sample surface at room temperature; and were analysed using a GBX Visodrop Software. Additionally, surface energy (SE) and wetting envelope measurements were also calculated using the GBX Visodrop software that employed the Owens-Wendt-2 equation by the use of approximately 1 µl diiodomethane (CAS: 75-11-6). All Results are expressed as mean ± standard deviation (SD) of the measurements.

3.4.7 Hardness measurements

Surface hardness was measured using a Mitutoyo (1996) MVK-H1 micro-hardness tester with a Vickers indenter at load of 50 gf at five different areas on sample cross-sections. The load applied was chosen to ensure it covers the SLM layer.

Nanoindentation measurements were conducted using the NanotTest Vantage instrument (Micro Materials Ltd. UK) equipped with a Berkovich tip pod indenter. The load applied onto the samples was 5 mN, with loading and unloading time being 30 seconds. The data was analysed using the built-in software provided by Micro Materials Ltd.

All sample cross-sections were polished to a mirror-like finish before the any hardness tests were conducted.

3.4.8 Wear testing

Wear resistance of the control and treated samples were analysed using a ball-on-disc TE79 multi-axis tribology machine under a load of 15 N and 30 N, at a scan speed of 5 mm/s, and ambient temperature of 25 °C for 1000 cycles and 5 mm wear tracks along the y-axis. The ball: Tungsten cobalt (WC/Co) ball was 12 mm in diameter. Results are expressed as means ± SD of the measurements. The limitations in this experiment, i.e. time, sample availability for testing, and the very rough surfaces of the SLMed substrates meant that only 15 N and 30 N could be tested and compared.

For coefficient of friction (CoF) measurements, the WC ball was 8 mmm in diameter. The tests were conducted in room temperature, in air and Ringer's solution (made with reference to Saji and Choe (2009)) (184)**,** at a scan speed of 5 mm/s, for 1000 cycles and 3 mm wear track. Ringer's solution was employed to mimic bodily fluids, as the substrate is used for implant application sliding in lubricated conditions. These tests were conducted along and against (perpendicular) to the build direction. The CoF were recorded.

After wear tracks were formed, the samples wear tracks were measured using the XP200 Plus Stylus Profilometer (USA). The wear track measurements were taken at two different points of the wear track for each track and the profilometer calculated the wear scar area.

3.4.9 Electrochemical corrosion testing

The corrosion behaviour of the surface treatments were investigated by means of potentiodynamic polarisation using the Gamry Interface 1000 potentiostat USA. Prior to testing the samples were cold mounted using a 2 part powder to 1 part liquid by volume by VARI-SET 20 cold mounting powder (Ref 11 10 28) (Batch 13022) and VARI-SET 10/20 cold mounting liquid (Ref 11 10 29) (Batch 13226). These was done to simply test the surface of the sample that underwent treatments, without other areas of the sample effecting the results. Each sample was connected to a conductive wire using copper conductive tape. The sample was submerged in a container part filled with Ringer solution (to mimic bodily fluids) (184). A platinum counter electrode and a saturated calomel reference electrode (SCE) were used. Prior to the polarisation measurements being recorded, open circuit potential (OCP) of the sample was recorded for 1 h. The polarisation measurements were performed at room temperature, in the range of -0.2 to + 1.2 V (versus the finishing OCP) at a scan rate of 1 mV/s, sample period 1 s, with each sample demonstrating an assumed surface area of 1.33 cm^2. The scan rate was chosen as the standard employed in our laboratory during testing. Due to the limitations in samples and time, other testing parameters could not be tested.

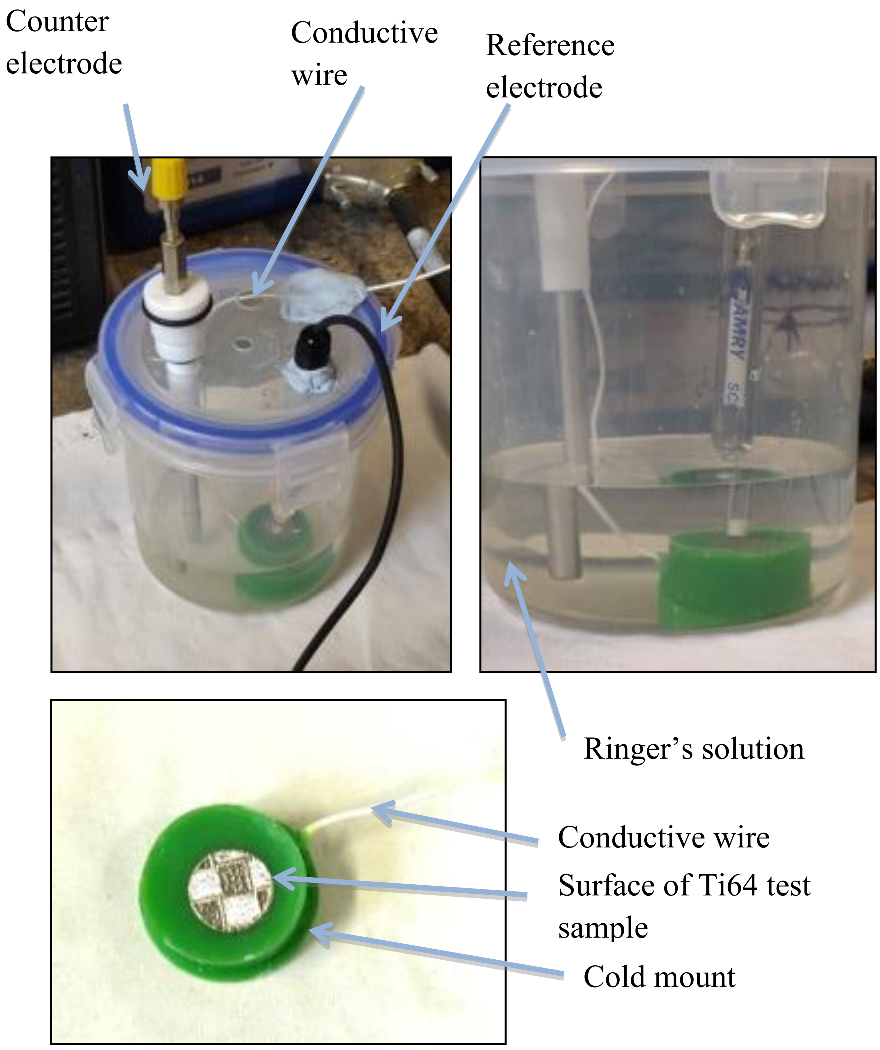

Figure 3.4 Demonstrates the set up for the electrochemical testing.

3.5 Microbiological experiments

3.5.1 Antibacterial susceptibility evaluation

Bacterial survival

The antibacterial activity of the four types of sample groups and control were tested using the standard Japanese JIS Z 2801:2000 spread plate method employed by Suzuki et al, 2006 (185). Gram-positive *Staphylococcus aureus (S. aureus)* NCTC 6571 and *Escherichia coli* (*E. coli*) NCTC 10418 were used. The bacteria were cultured in sterile tryptone soya broth (TSB) (Oxoid, UK) overnight at 37°C in a shaking incubator at 100 rpm. Serial dilutions were made to achieve a bacterial suspension of 10^3 colony-forming units per ml (cfu/ml) in a sterile Trypton Soya Broth (TSB). Subsequently, 5 µl of this bacterial suspension were placed onto the sterile samples which were then incubated at 37°C for 4 h without shaking.

After incubation, the samples were transferred into an MD falcon tube containing 10 ml of sterile phosphate-buffered saline (PBS), the contents were vortexed for 20 s to detach any surface adherent bacteria. 0.1 ml aliquots were plated on TSA to determine the viable counts of the recovered bacteria. The results are expressed as percentages with mean ± standard deviation (SD).

Percentage reductions were measured using the equation:

Reduction (%) (mean CFUs) = $[X0 – Xy]/X0$ x 100

where X0 is mean CFUs of control and Xy is mean CFUs of treated samples, both after 5 h. This test was conducted on *E. coli* and *S. aureus*. Results are expressed as means ± SD of the measurements.

3.5.2 Live /Dead staining

The LIVE/DEAD staining Bacteria Viability BackLight Kit (ThermoFisher Ltd.. UK), that contained SYTO9 and red fluorescent nucleic acid strain propidium iodide (PI). The SYTO9 stain generally labels all microorganisms in a population, those with intact and damaged membranes, while PI only penetrates microorganisms with damaged membranes reducing the SYTO 9 fluorescence. Thus microorganisms with intact membranes (i.e. live) stain fluorescent green, while those with damaged membranes (i.e. dead) stain fluorescent red. Once these samples underwent antibacterial test with *S. aureus* and the live/dead staining was carried out and the fluorescent analyses were carried out in a dark room using a ZEISS confocal microscope. Green light was used, as white light would not be able to penetrate the sample, to collect images using a B-front mounted camera (Nikon D5100).

3.5.3 Biofilm formation

Biofilm formation was conducted on *S. aureus* because it can undergo crystal violet staining and be dehydrated without compromising its shape. The method employed was modified from Christensen et al. (1985) (186).

Succinctly, S. aureus was cultured in sterile TSB (Oxoid, UK) overnight at 37°C in a shaking incubator at 100 rpm. Serial dilutions were made to achieve a bacterial suspension of 10^3 colony-forming units per ml (cfu/ml) in a sterile TSB were conducted. Subsequently, 4 ml of the diluted culture were placed inside 12 well plates containing Ti64 test substrates (the samples have to be completely immersed in culture media. The well plates were then placed into a shaking incubator of 37°C 40 rpm for 72 h. Every 24 h, the current culture media were pipetted out of each well, disposed of, and 4ml of fresh sterile TSB were poured in. While fresh media was being poured, care was taken not to directly make contact with the surface of the test substrates as to not dislodge forming biofilms. After 72 h, the TSB was gently pipetted off and the samples within the wells were rinsed gently by carefully pipetting in PBS. This rinse was conducted twice while care was taken not to dislodge the formed biofilm. The samples were then carefully taken out of wells and placed into new sterile well plates. Briefly, glutaraldehyde was added to the surface of samples for 5 min. before being pipetted off.

Crystal violet

After the removal of glutaraldehyde, the samples were immersed in 4 ml of (0.1%) crystal violet stain (Prolab-diagnostics) which was poured into each well containing samples and remained there for 5 minutes so to stain the biofilm. Then the stain was removed using a pipette and samples were rinsed with PBS twice before being placed inside an incubator at 37°C for 2 h to dry. After 2 h, 4 ml of methanol was placed onto the dried sample surfaces and those well plates were placed inside a shaking 37°C incubator for 2 h (speed 3) at 40 rpm. These steps are conducted being careful not to dislodge the biofilm, by pipetting in the solutions directly onto the walls of the wells, avoiding direct contact to the biofilm on the sample surfaces. Finally, the samples were removed form the well plates, and 100 µl from the 4 ml of methanol/crystal violet stain that remained were placed into cuvettes, and mixed with 900 µl of distilled water. Then the optical densities using the Jenway 7315 spectrophotometer at an absorbance of 590 nm was measured. The optical density (OD) measurements were recorded.

One sample in each batch type underwent fixation & dehydration for SEM observational images to attain qualitative results.

Dehydration & fixation

The samples undergoing dehydration and fixation were immersed in 20% ethanol for 10 min. This step was repeated for 40, 60, 70, 90, 95 and 100% ethanol, respectively. The samples immersed in 95% ethanol was repeated twice, each for 10 min. making sure to immerse in fresh ethanol, before immersing in 100% ethanol twice.

Finally, HMDS (Hexamethyldisilazane) was generously poured directly onto samples surfaces immediately after removing the 100% ethanol to avoid sample surfaces drying. The HMDS was poured using a fume hood and the samples were left overnight to completely dry.

Due to the low conductivity of cells under SEM analyses the samples were lightly sputter coated with gold (Au) for 1 min. with a deposition rate of 25 mA using an Emscope SC 500 (Agar scientific).

3.5.4 Biocompatibility test

SAOS-2 Culture

Retrieval of SAOS-2 cells from liquid nitrogen

A warm bath of 37°C was prepared to thaw media containing 200 ml of McCoy’s Media, 20 ml of Foetal calf serum (FCS) (Biosera), 5 ml of Hepes buffer and 2 ml of Penicillin & streptomycin (P/S). Enough media was made for the number of cryovials revived, that is 15 ml per vial/T75 flask and this was made prior to cell retrieval from liquid nitrogen store. The vials containing the cells were thawed for 1-2 min and the cells were retrieved and transferred to a sterile centrifuge tube containing 1 ml of fresh media. The tube was centrifuged at 800 rpm for 4 min. and the supernatant was carefully pipetted off. The cells were re-suspended in 1 ml of media before placing into a flask containing 14 ml of media. The flask was incubated in a humidified incubator at 37°C/5% CO_2 for 24 h.

The growths of the cells were checked daily under the inverted microscope for any potential infections and cell differentiation.

Once the cells were safely retrieved from the vials, they were thawed for 1-2 min.

Approximately, 15 ml of the prepared media was placed inside a flask and the cells retrieved from liquid nitrogen

Feeding cells.

The cells were fed every 48 h, by removing the old media in the flask and replacing it with new fresh media. The flask was returned to the humidified incubator at 37°C/5% CO_2.

Sub-culturing cells

Once the cells were confluent, the media was removed from the flask and disposed of into a bleach bottle. 10 ml of thawed trypsin-EDTA (Sigma T4049) was placed inside the flask containing the cells and the flask was placed inside the humidified incubator at 37°C/5% CO_2 for cell detachment. The flask was checked every 2 min under the inverted microscope to check the cell detachment process, if not completely detached, 6 ml of trypsin-EDTA was removed and the flask replaced back into the incubator for another 2 min.. The cells were checked again under the inverted microscope and were mechanically dislodged by tapping the flask until cells are completely dislodged from the base of the flask.

Subsequently, 10 ml of media were added to the flask and were pipetting out and back into the flask, repeatedly making sure to the media washes over the base of the flask were the cells were attached. This process was conducted to ensure the cells were completely dislodged and suspended in the media. The media was then placed into a universal bottle and 6 ml of extra media was added to make the total volume 20 ml. The universal tube was centrifuged at 1000 rpm for 5 min. Once complete the supernatant was removed and the cell pellet was re-suspended in 2 ml of media and gently agitated (by tapping the flask).

Following, a drop of the cell suspension media was placed onto the corner of the cover slip of the haemocytometer. The cells were then counted under the inverted microscope and the 2 ml cell suspension was diluted accordingly to 10^3 by adding the required amount of media.

The Ti64 samples to be tested were placed into 6 well plates and 5.5 ml of the 10^3 concentration of the cell suspension were placed inside wells, making sure to immerse the samples. The samples were incubated for 120 h in a humidified incubator at 37°C/5% CO_2. The media was changed to fresh sterile media every 48 h, and cell growth and attachment were checked everyday under the inverted microscope.

After 120 h, the cells underwent an MTT viability assay.

3.5.5 MTT viability assay

This assay measures the cell numbers based on its metabolic activity by measuring formazan (the metabolic product of MTT).

The required amount of MMT solution (5 mg/ml in PBS) was created. The MTT solution to media ratio within the well should be mixed to a ratio of 0.06 ml to 1 ml, respectively. Thus 4 ml of the mixed MTT and media immersed the Ti64 substrates after the removal and disposal of the old media. The well plates were then incubated in a humidified incubator at 37°C/5% CO_2 for 3-4 h for the MTT to metabolise. After incubation the formazan is re-suspended in 400 µl of DMSO (Dimethyl sulfoxide) and placed on a shaking platform for 5 min.. Then the samples are removed from the wells and placed into new sterile well plates (to avoid taking into account cell that grew on the surfaces surrounding the substrates within the well). The remaining solutions 100 µl of each were placed within cuvettes and optical density (OD) measurements were carried out at absorbance of 570 nm and 600 nm. These readings were carried out using the ELx 800 Universal microplate reader and the Gen5.1.11 software.

One sample in each batch type underwent fixation & dehydration for SEM observational images to attain qualitative results. These samples were then lightly sputter coated with gold (Au) for 1 min. with a deposition rate of 25 mA using an Emscope SC 500 (Agar scientific).

3.5.6 Statistical analyses

Data collected from the tests conducted were evaluated using a One-Way analysis of variance (ANOVA). This included the mean and standard deviation values used to calculate the significance difference at a 95% confidence level.

4 RESULTS

4.1 Powder characterisation

4.1.1 SEM and EDS surface morphology and cross-section

Micrograph images of the powders employed within this research of Ti6Al4V (gas atomised) and Ag powders.

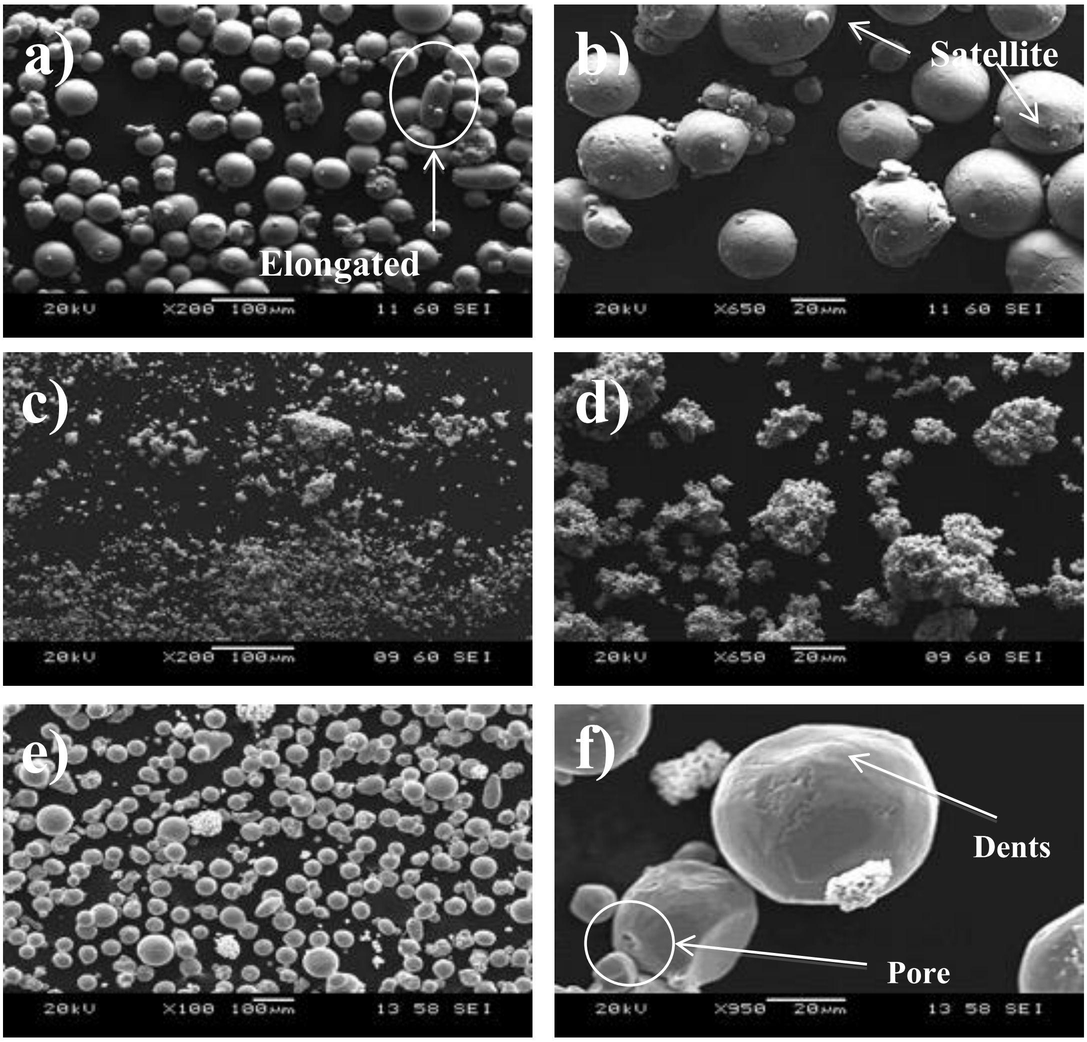

Figure 4.1 (a) and (b) display SEM images of gas atomised Ti6Al4V powders with irregularities, while (c) and (d) show agglomerated silver powders. Images (e) and (f) display mixed Ti6Al4V with Ag powder.

Images below are SEM cross-sectional images of powders used in this research.

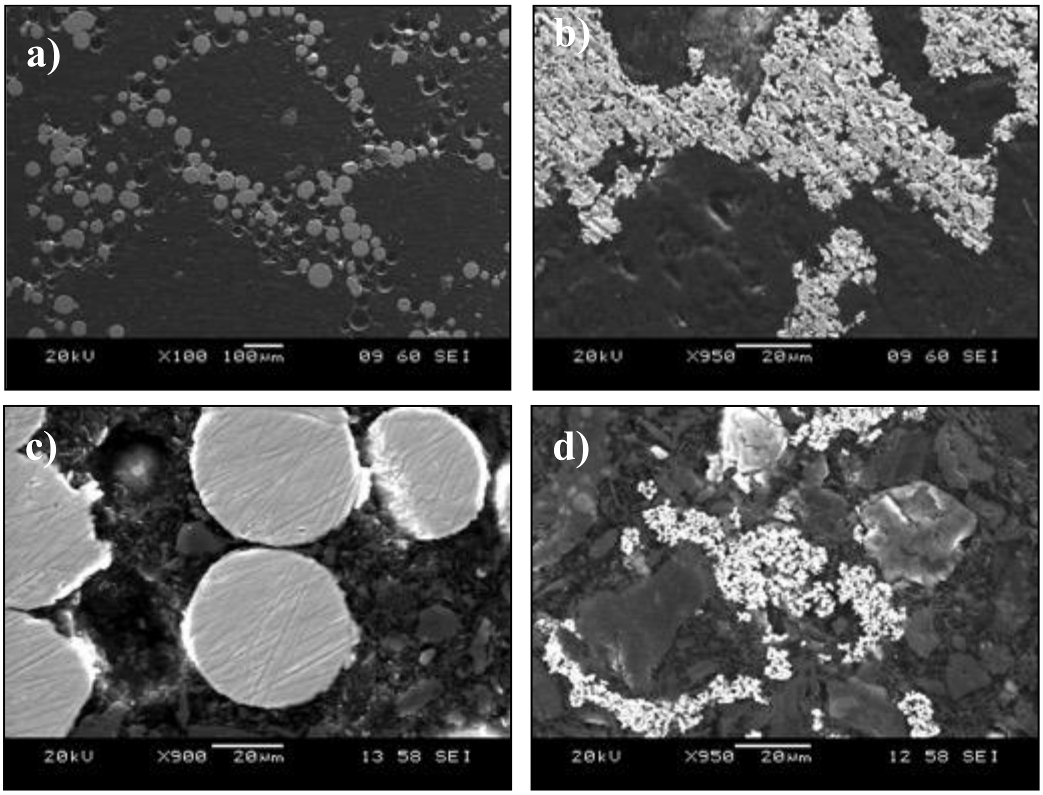

Figure 4.2 SEM cross-section (a) and (c) of Ti6Al4V gas atomised powder and (b) and (d) Ag powder

<u>**EDS analysis of powders**</u>

Table 4-1 EDS analysis of Ti6Al4V powder

Elements	**Ti6Al4V powder (wt.%)**
Ti	89.73
Al	4.10
V	3.96

Table 4-2 EDS analysis of Ag powder

Elements	Ag powder (Wt.%)
Ag	27.37
O	3.39

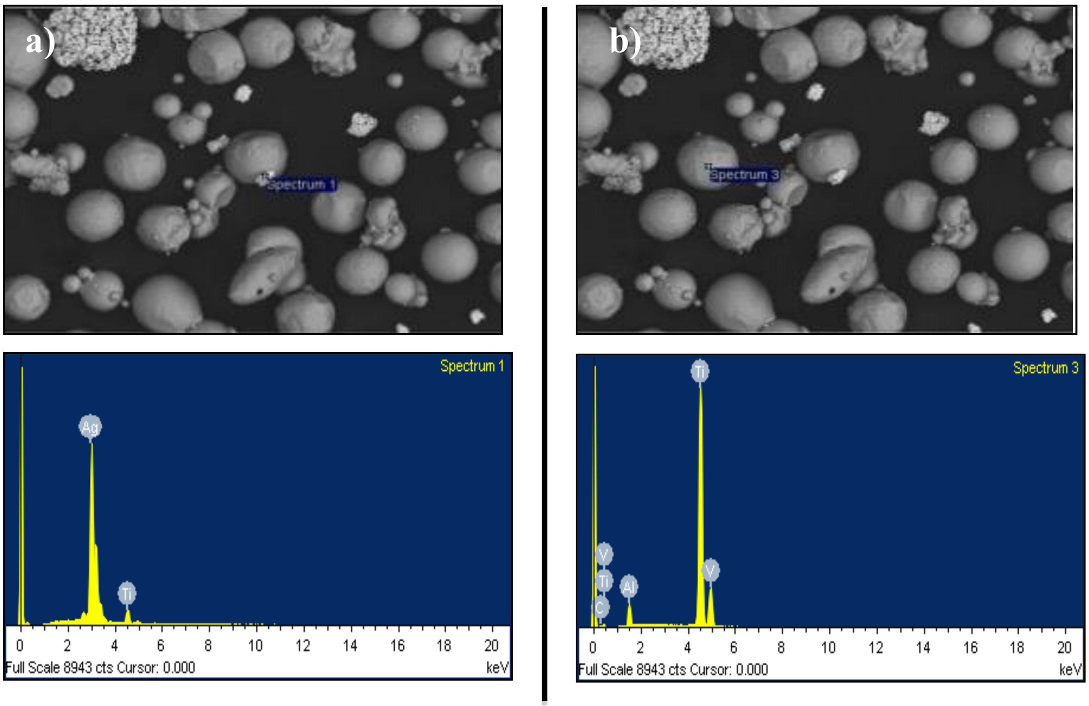

Figure 4.3 SEM and EDS analyses of a) Ag gas atomised powder and b) Ti6Al4V powder.

Micrographs for Ti6Al4V and Ag powder used in this experiment are shown in Figure 4.1 (a-f) at varying magnifications. These images display Ti6Al4V gas atomised powders. Figure 4.1 (b and f) used in this research during SLM. Some surface irregularities such as satellites and elongated-shaped powders can be seen. The irregularities found were a consequence of the powders manufacturing process most probably when liquid droplets collided with a solid surfaces. Specifically, Figure 4.1 (f) highlights powders with ‘dents’, thus not being completely spherical. From the SEM images, silver powders agglomerated and clumped together. Figure 4.1 (e) displays doped Ti6Al4V powders with Ag after mixing in an HMK-1901 planetary ball mill at 449 rpm for 12 h.

The SEM cross-section is Figure 4.2 shows little porosity in the gas atomised Ti6Al4V powders. Closed pores, suggested entrapment of argon gas as the powder particle solidified during the atomisation process. On the other hand, Ag powders agglomerated together, so single powders particles could not be seen. Table 4-1 displays the elemental weight percent analyses of Ti6Al4V powders with 89.73 wt. % Ti detection Al and V were also detected confirming the powders to be Ti6Al4V. Similarly, the Ag powder particles revealed 27.72 wt. % detection Table 4-2. The silver powder batch demonstrated oxygen content under EDS the oxygen and carbon detected are resultant of the conductive resin.

Figure 4.3 displays an EDS graph with spectrum point scans for Ti6Al4V and Ag mixed powder. Accordingly, the EDS graph demonstrates intense peaks of Ti and Ag.

4.1.2 Powder distribution

The table below displays the particle distribution of Ti64 powders employed in this research.

Titanium powder distribution

	Size (µm)		
	D10	**D50**	**D90**
Ti6Al4V	27.71 ± 2.45	46.42 ± 6.65	57.75 ± 4.35
Ag	10.53 ± 015	22.32 ± 0.11	37.05 ± 0.01

Table 4-3 Powder particle distribution of gas atomised Ti6Al4V and Ag

Ti6Al4V powder distribution

Powder distribution curves, which plots the density distribution Vs particle size.

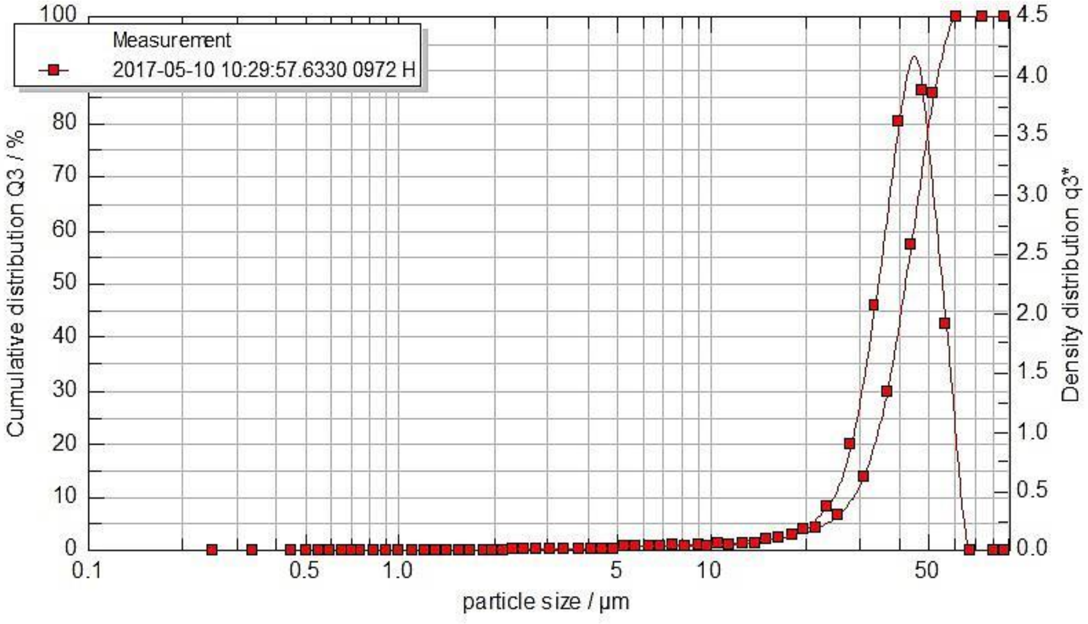

Figure 4.4 Powder distribution of Ti6Al4V gas atomised particles.

Ag powder distribution

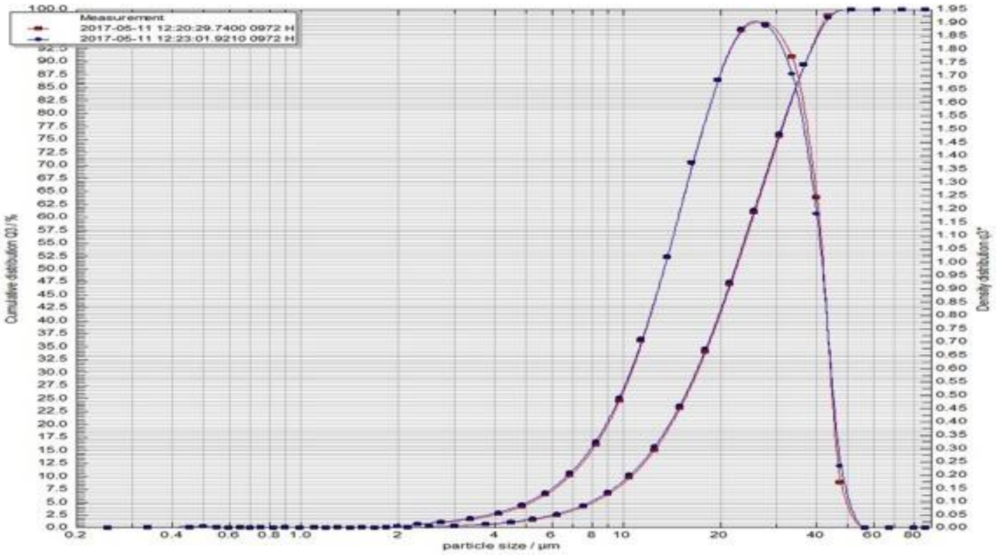

Figure 4.5 Powder distribution of Ag particles

The particle size distribution (PSD) of the two powders were conducted and shown in Figure 4.4 and Figure 4.5. The average size distribution (D50) of 46.42 ± 6.65 µm and 22.32 ± 0.11 µm were recorded for Ti6Al4V and Ag powders, respectively.

Table 4-3 includes the values of D10, D50 and D90 of the samples with standard deviations. The D50 of Ag powder is higher than the expected bought powder particle of 2 µm due to its clumping and agglomeration. The D values represent the midpoint and range of the particle sizes of a given sample.

4.2 Surface morphologies and microstructure

4.2.1 Morphology, topography and roughness

The images below are of the initial samples created using varying SLM scan strategies.

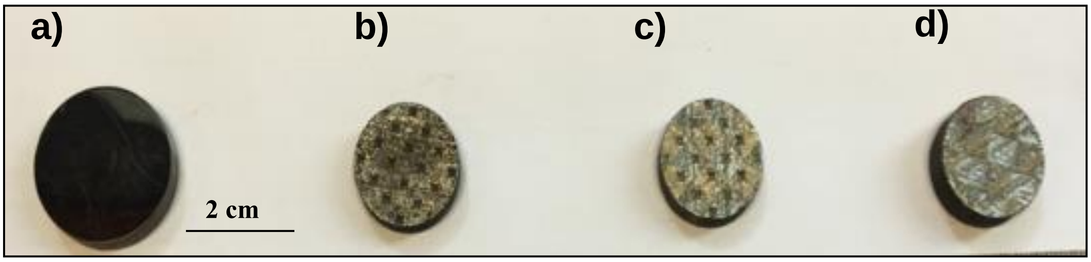

Figure 4.6 Visual surface appearances of samples: a) as-polished control, b) pattern 1, c) pattern 2 and d) pattern 3. Patterns 1-3 were created via SLM.

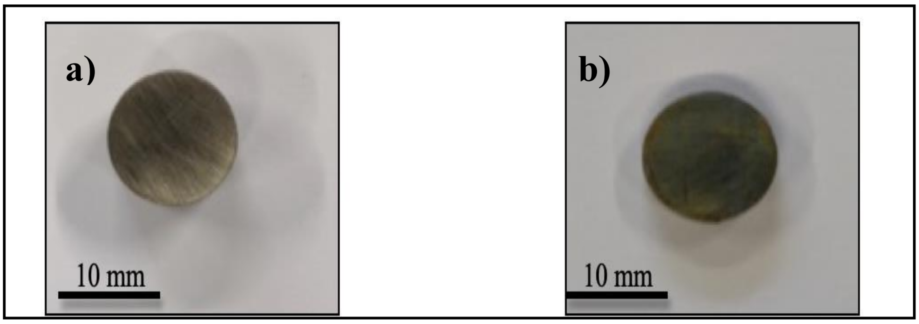

Figure 4.7 Visual surface appearance of the a) the control as ground, and b) the control post-thermal oxidation.

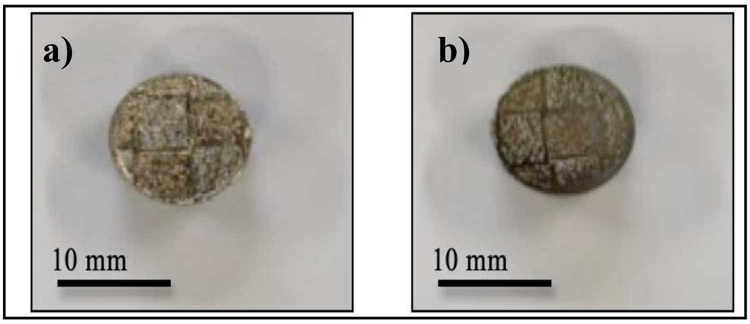

Figure 4.8 Surface appearances of a) a sample post- SLM treatment, b) SLM sample after being ground.

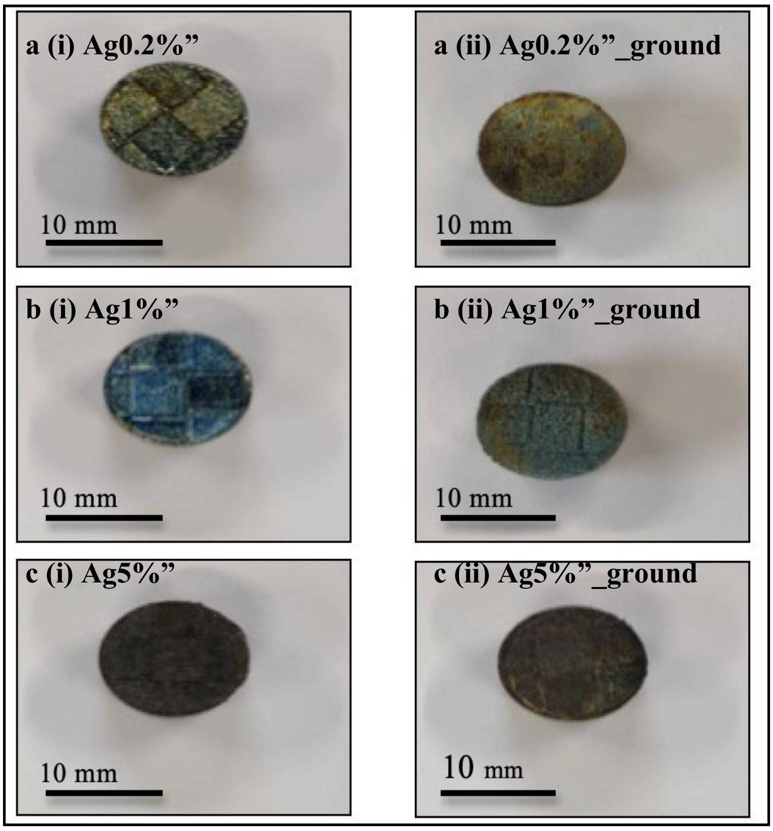

Figure 4.9 Surface appearances of a Ti6Al4V substrates alloyed with different weight percentages of Ag post-thermal oxidation, a (i) substrate doped with Ag 0.2 wt. %, a (ii) and after the sample was ground, b (i) sample doped with Ag 1 wt. % and b (ii) after being ground, and c (i) sample doped with Ag 5 wt. % and c (ii) was ground.

Figure 4.6 displays the visual surface appearance of samples before undergoing surface characterisation tests. Figure 4.6a is the control sample which has a mirror-like surface finish, Figure 4.6b-d are Pattern 1, 2 and Pattern 3, respectively manufactured via SLP. Figure 4.6b demonstrates a very rough surface with a pronounced regular pattern. Figure 4.6c displays a mixture of pronounced regular patterns with the addition of island scanning strategy patterns, while Figure 4.6 d) only demonstrates patterns from the island scan strategy. Ti64Al4V rod was cut into 13 mm diameter and 10 mm in height discs which were ground to 400 silicon carbide (SiC) paper. This condition was the basis of the as-ground control. It can be seen that the sample is silver with wear lines, evidence that the sample was ground is shown in Figure 4.7, Figure 4.8 and Figure 4.9. Once all the samples were ground, a single SLM layers thickness was deposited onto the disc surfaces. The as-SLMed samples can be seen with a different visual morphology, that of a rough surface pattern as a result of the island scan strategy employed. With further treatment, i.e. thermal oxidation at 600°C for 4 h, the samples demonstrated more of a changed appearance with the four batches of varying Ag wt.% diffracting in different colours. The control sample resulted in slightly green / yellow/ brown colour-finish, while SLM'ed samples such as Ti64 (not shown) diffracted in green/yellow, similar to Ag0.2% samples. However, the Ag1% samples were blue, while Ag5% were dark brown. After grinding to remove the effects of SLM roughness, the samples demonstrated similar but less intense colours to their non-ground equivalents.

SEM images of the initial samples tested that underwent varying SLM scan strategies.

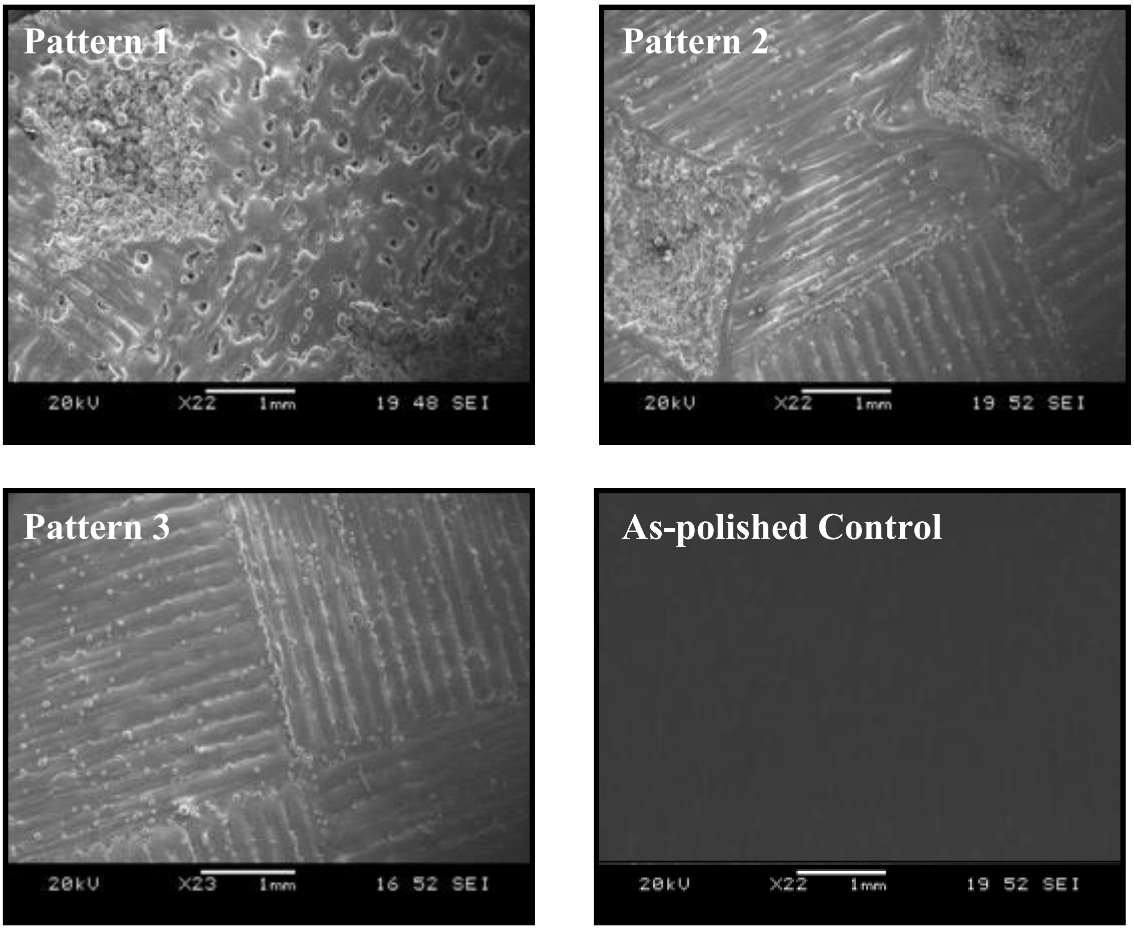

Figure 4.10 Surface morphology of pattern 1-3 displaying SLM scan strategy outcomes, compared to the as-polished control

SEM images of varying magnifications displaying the surface morphology of the samples created using varying scan strategies.

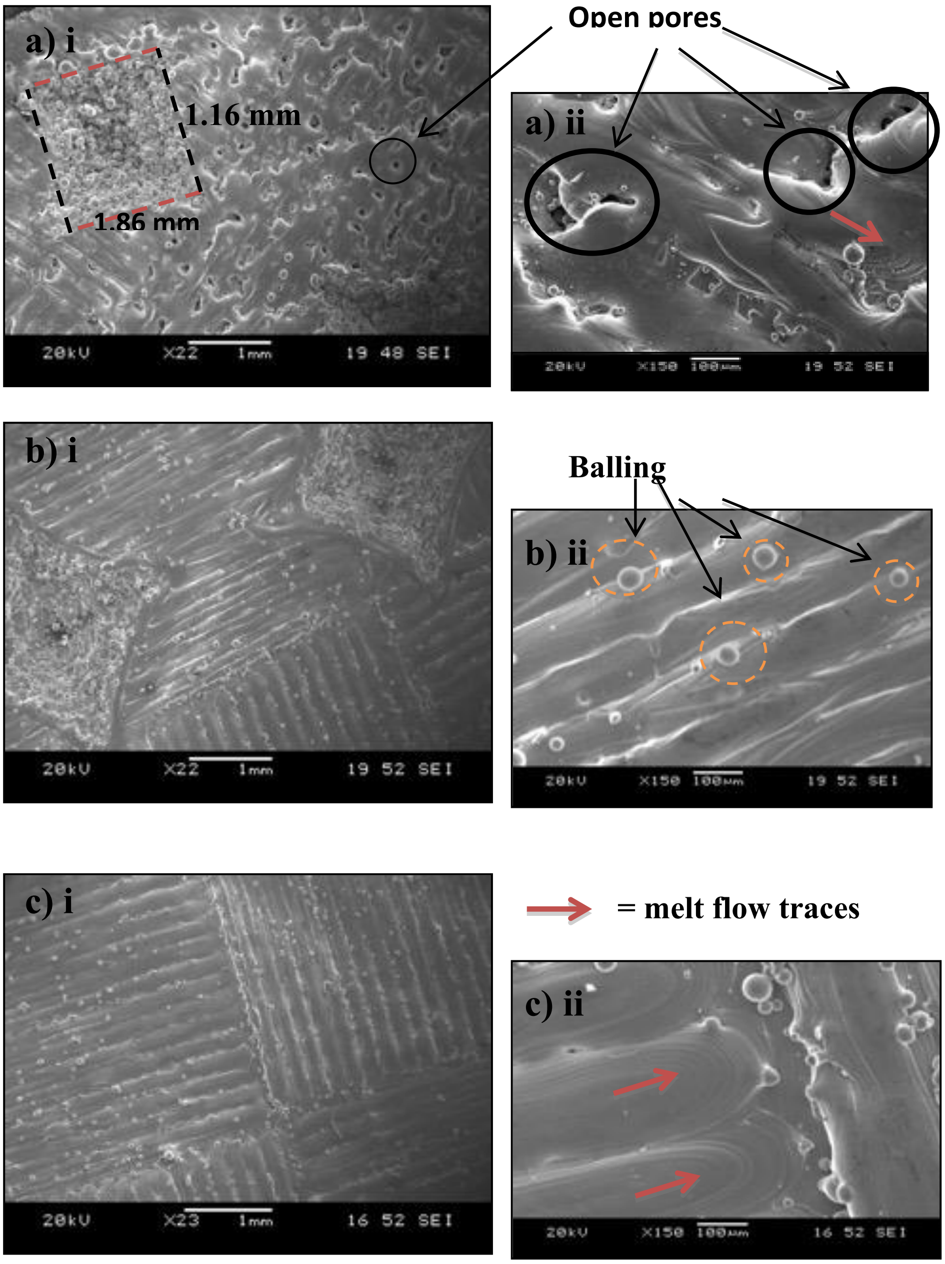

Figure 4.11 SEM micrographs showing the variation of top surface structures of as-SLMed Ti6Al4V samples. (a) Displays the porosity created by the SLM chosen parameters for pattern 1 with the size of the irregularities, balling effects resultant from the process can be seen in (b) pattern 2 and (c) pattern 3. The red arrows indicate the melt flow direction.

Higher magnification SEM images of the samples created using various SLM scan strategies, demonstrating the porosity of the surfaces.

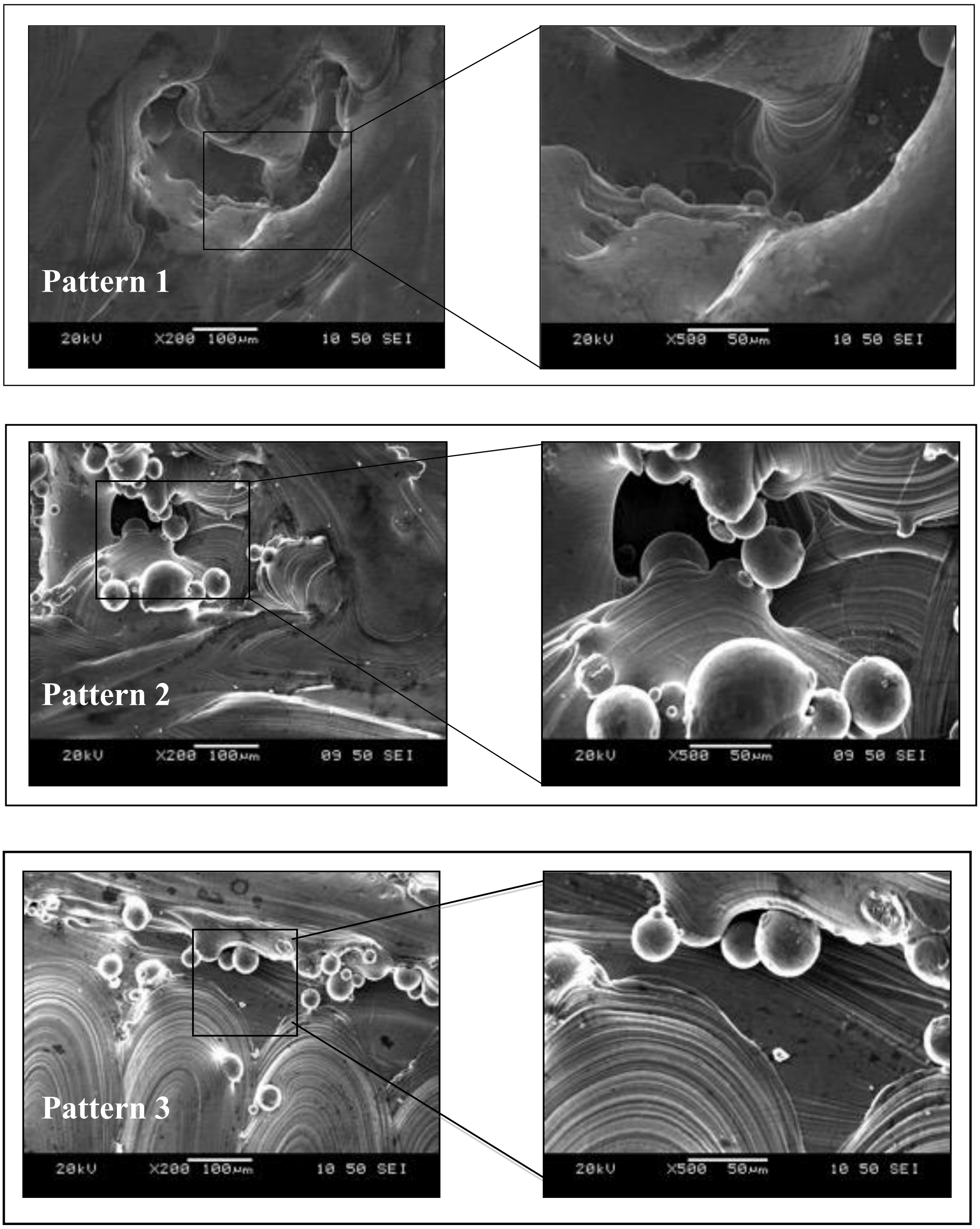

Figure 4.12 Higher magnification SEM of the surface features of the SLMed built parts..

Surface SEM images of SLMed samples made with different scan strategies. Images demonstrate the different morphologies.

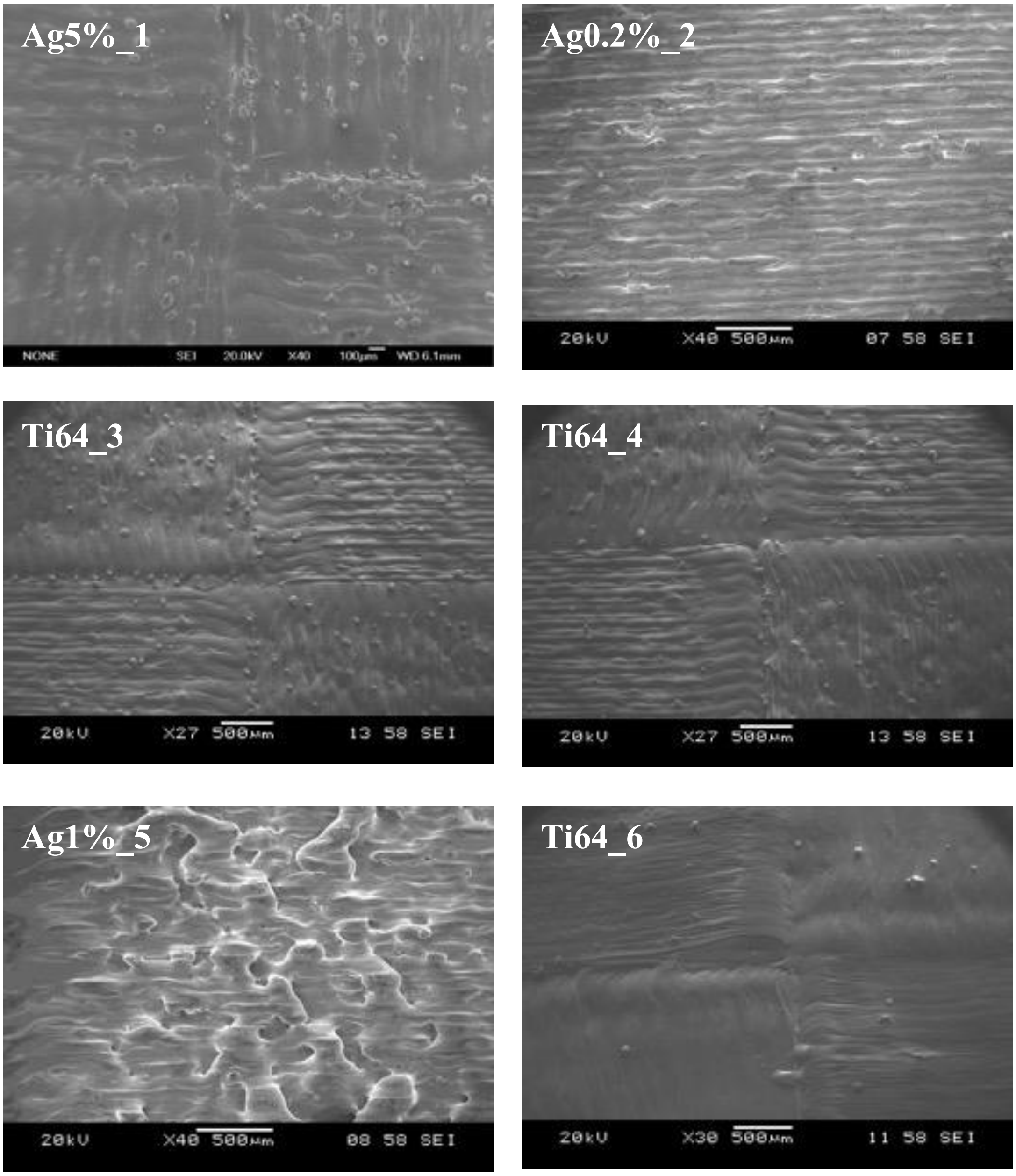

Figure 4.13 SEM morphological images of the surface of SLMed Ti6Al4V discs at the six chosen process parameters (PPs) with some being Ag doped a different wt.%.

SEM images of the SLMed samples surfaces that were created using varying process parameters post-thermal oxidation.

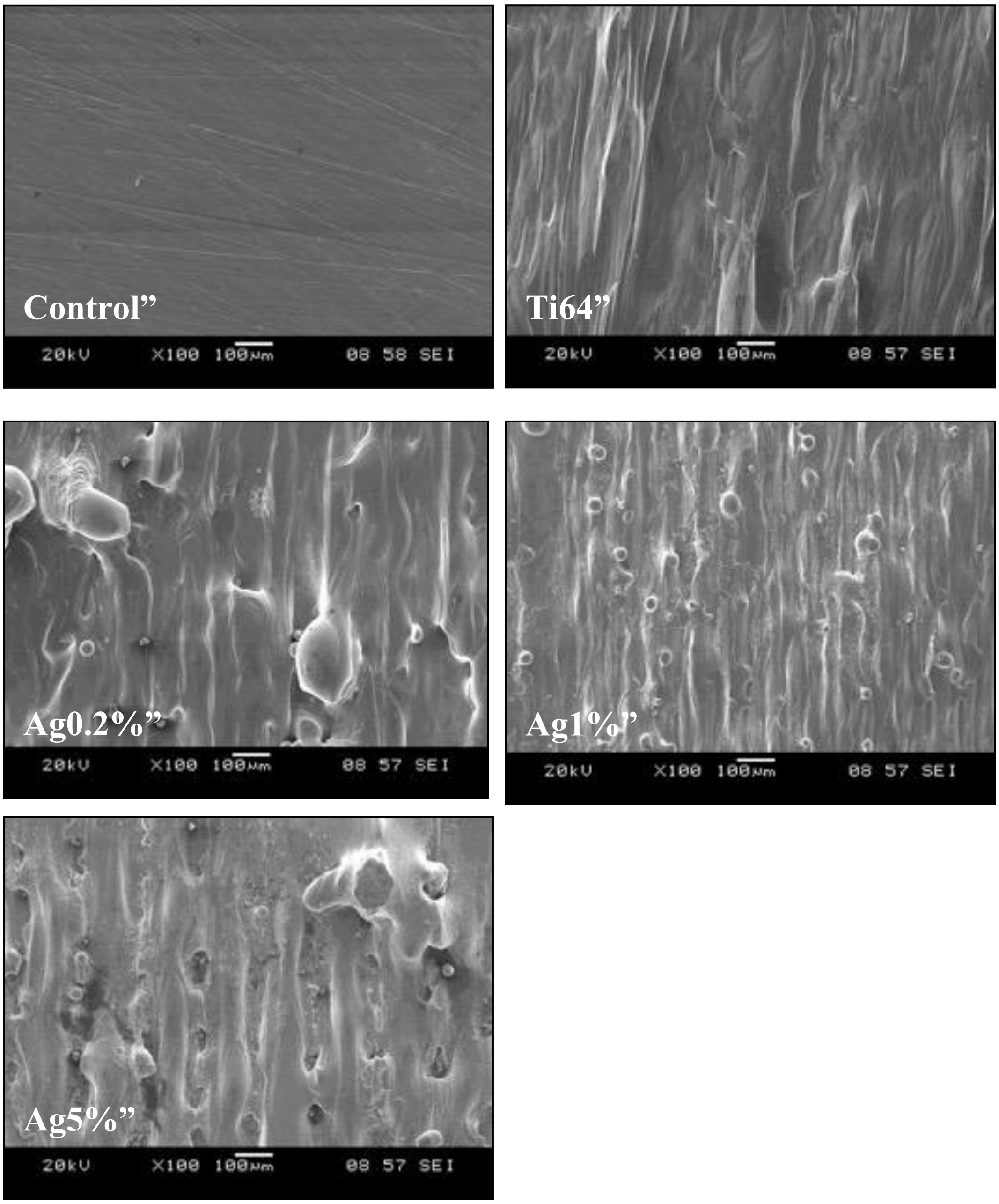

Figure 4.14 SEM images of surface features of as-ground control and SLMed samples post-thermal oxidation treatment.

Higher magnifications images of oxide ‘blisters’ and ‘scales’ formed post-thermal oxidation.

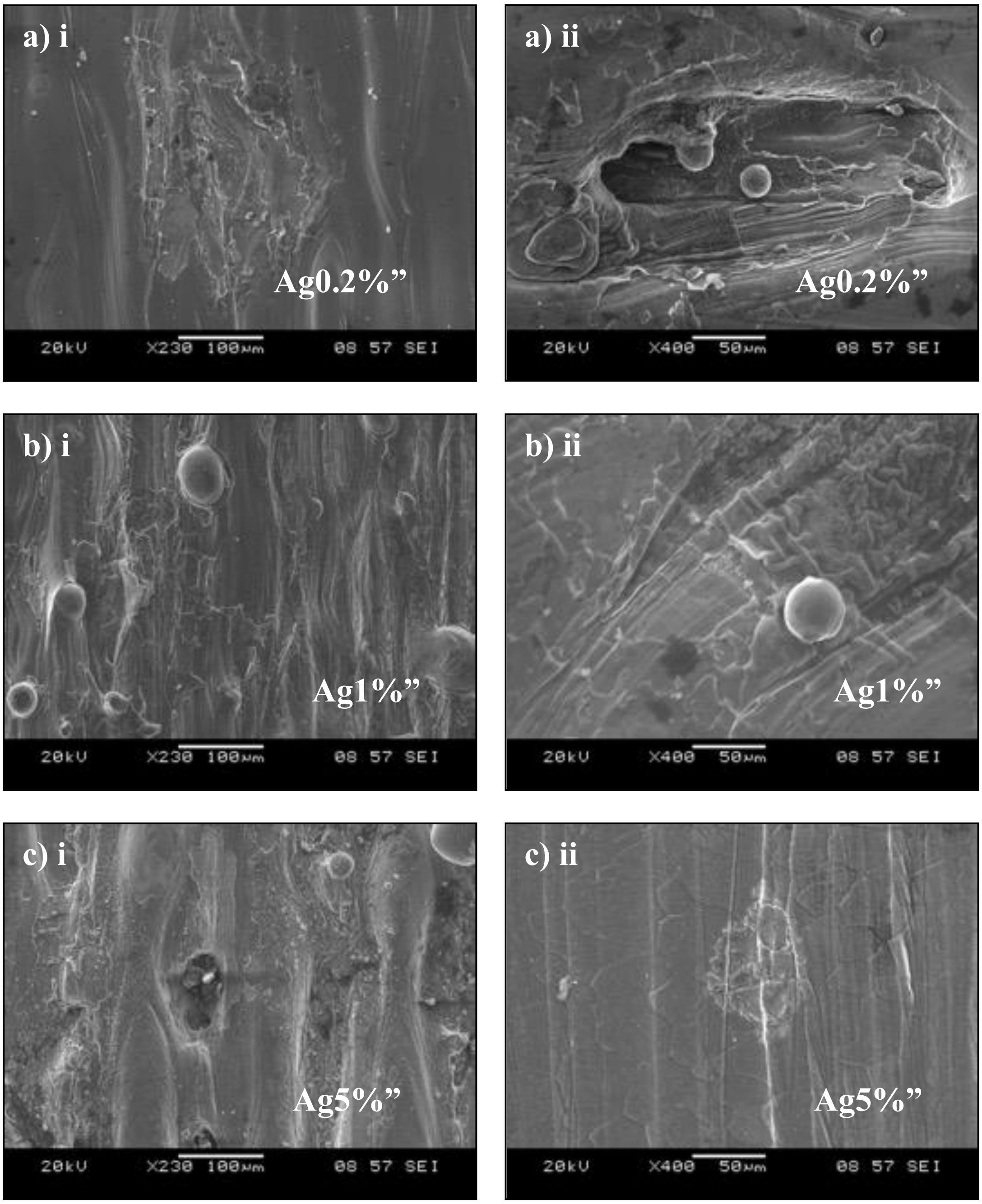

Figure 4.15 SEM image of thermally oxidised SLMed samples, displaying oxide 'blisters'.

Exemplary SEM images of demonstrating chipped oxide layer, blisters and scales.

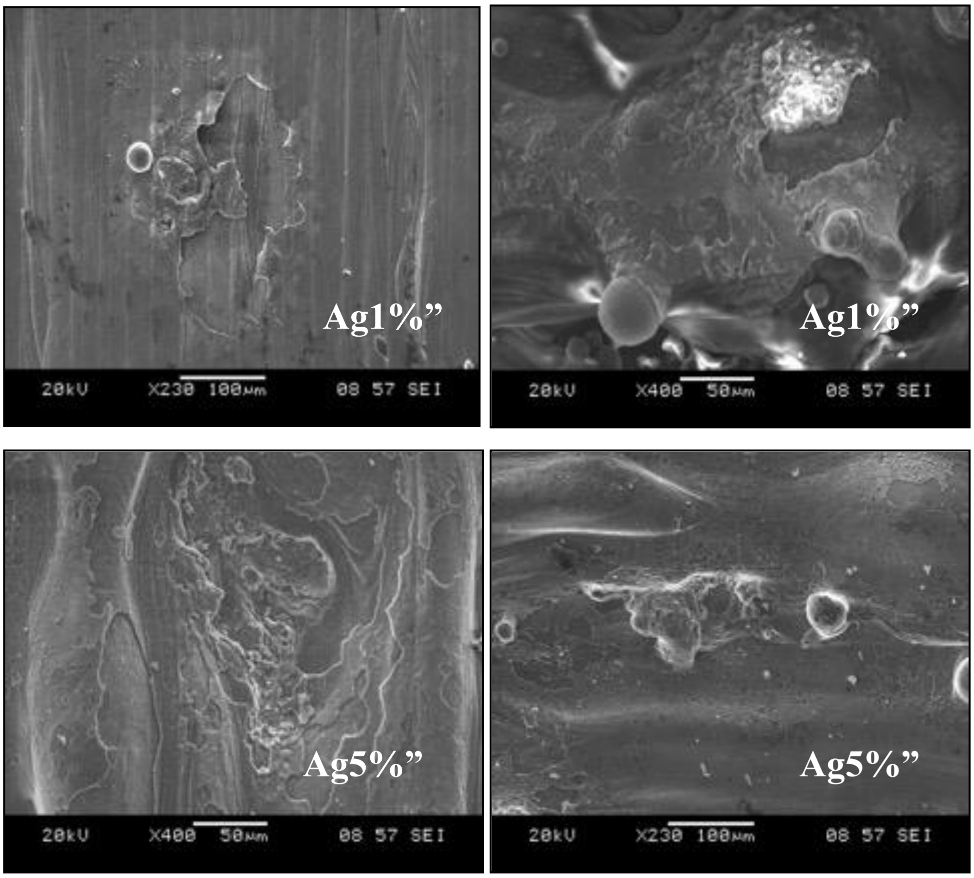

Figure 4.16 SEM images displaying the chipped oxide scale of Ag1%" and Ag5%"

Figure 4.10 displays the micro-morphology of all four sample types from preliminary tests: as-polished control, Pattern 1, Pattern 2, Pattern 3, obtained using SEM. The surface of the discs created by SLM, Figure 4.10, looked relatively rougher than the control sample. The pronounced irregular micro-morphological diamond-shaped dips can be more easily seen in on Pattern 1; while the macro-morphological island scanning strategy can be better seen in

Figure 4.10 Pattern 3, while Pattern 2 demonstrates both of the micro-and macro- features. Figure 4.11 demonstrates porosity and defects created by the SLM process. Figure 4.11(a) i displays the open pores found on the surface of Pattern 1 with (a) ii demonstrating the melt flow direction. Pattern 2 and 3, Figure 4.11 (b) and (c) presents balling effects of powders created on the surface of the discs.

Figure 4.12 displays the same sample's micro-morphology, at a higher magnification. These images focus on the porosity of the samples. The internal interconnecting porous channels of Pattern 1 and 2 can be seen a) and b). However, although theoretically created with the intentions of not having pores. Figure 4.12 c) revealed random pores on its surfaces most probably due to the SLM process. The control demonstrated to be without pores.

In Figure 4.13 different surface finishes based on the different PP's applied resulted in surface morphologies that were either rougher or smoother in appearance to each other. The grooves formed by the laser island scanning strategy can be seen accompanied balling effects from the application of high energy density. Specifically, process parameter (PP) 5 has demonstrated a very rough surface features compared to the other PPs. PP 6 has demonstrated fine laser scan tracks due to the combined effects of having the smallest a1 spacing of 0.1 with the highest energy density. No significant morphological differences can be seen based on the variations of weight percentages of Ag in the SLMed layer.

Post-thermal oxidation, the surface of the samples display an obvious changes as a scaly oxide layer evidently begins to forms. Figure 4.14 reveals examples from different batches, from Ti64, Ag0.2%, Ag1%, to Ag5%. A comparison between Figure 4.13 to Figure 4.14 it can be seen that post-thermal oxidation, the samples exhibit oxide scales and develop 'blisters,' Figure 4.15 a) ii, b) ii, and c) ii, but not completely covering the surface. There is also an increase in oxide scale with increasing weight percentage of Ag within the SLMed batches.

The surface is not completely covered by the oxide scales because the thermally oxidation time is short (4 h). The following, Figure 4.16, reveals the chipping found in the samples doped with 1 and 5 weight percent Ag, whereby an oxide layer is found but with random bits of the layer missing. These patchy oxide layer formed, gives the impression the layer has been chipped away.

The average surface roughness (R_a) of the initial samples tested using various scan strategies are displayed below.

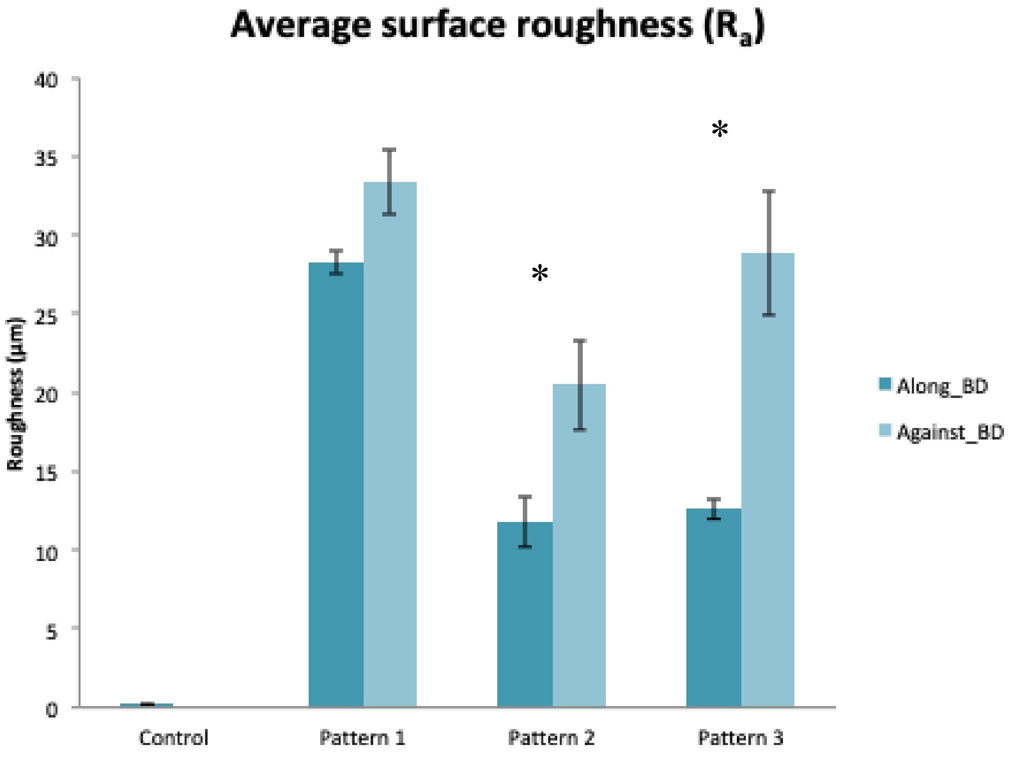

Figure 4.17 Roughness R_a measurements of as-polished, and SLMed patterns 1, 2 and 3. * P value <0.05.

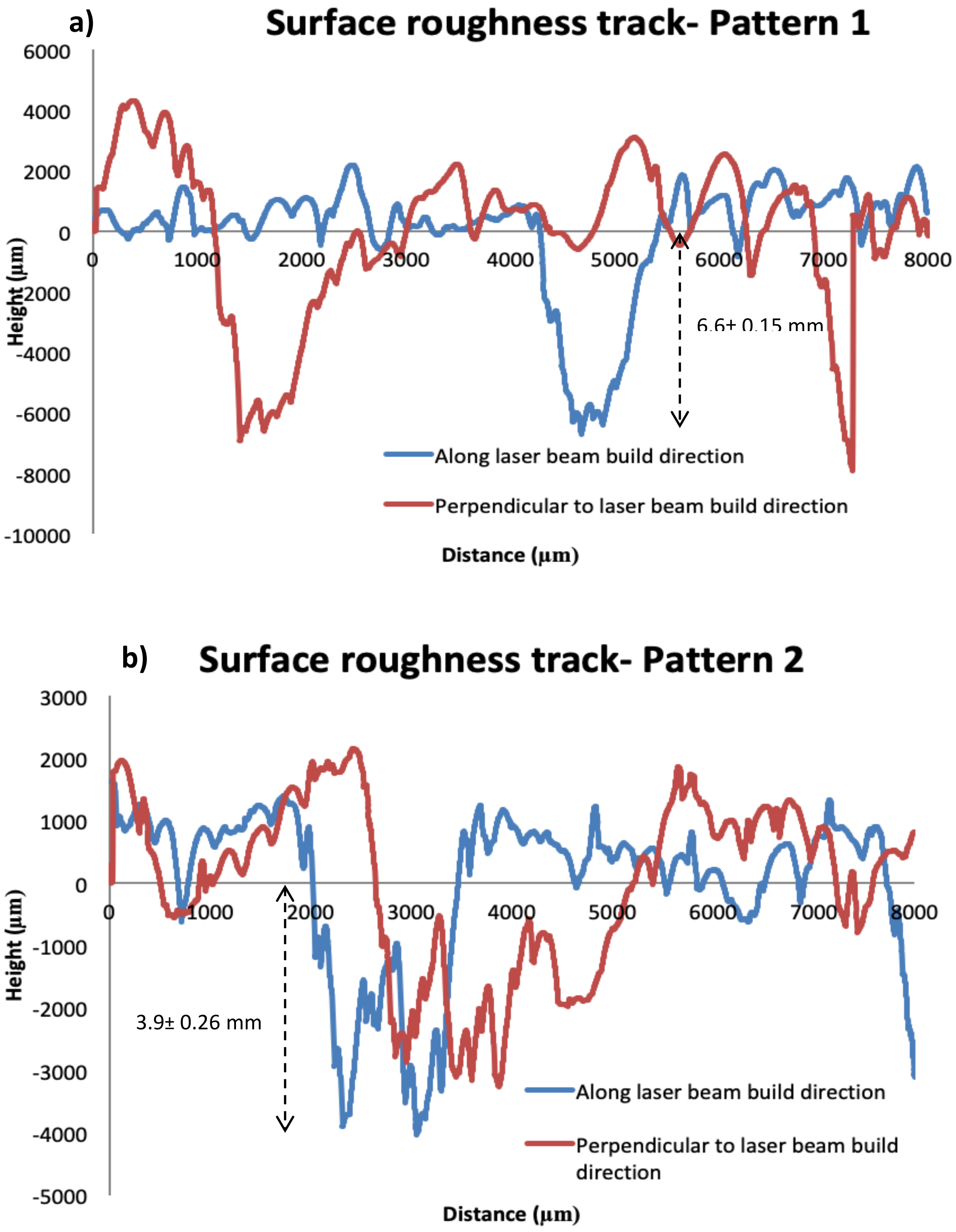

Figure 4.18 demonstrates surface roughness track lines for a) Pattern 1 and b) Pattern 2 along and perpendicular to the laser build direction (BD).

The average surface roughness (R_a) in microns is displayed in the figure below for all samples tested using various SLM process parameters.

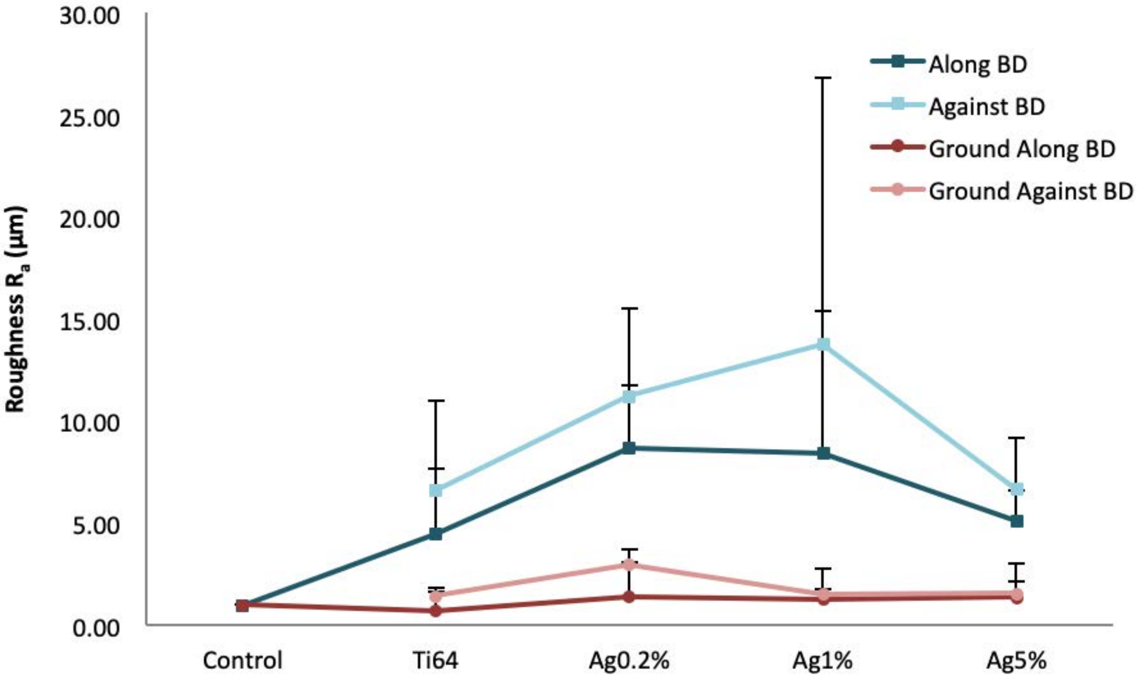

Figure 4.19 Surface roughness (R_a) measurements of the as-ground control, and the SLMed Ti6Al4V, Ag0.2%, Ag1% and Ag5%, as well as each sample types ground counterpart, along and against (perpendicular) to the laser BD. The lines are connected to better display the relationship between the different batches of Ti6Al4V.

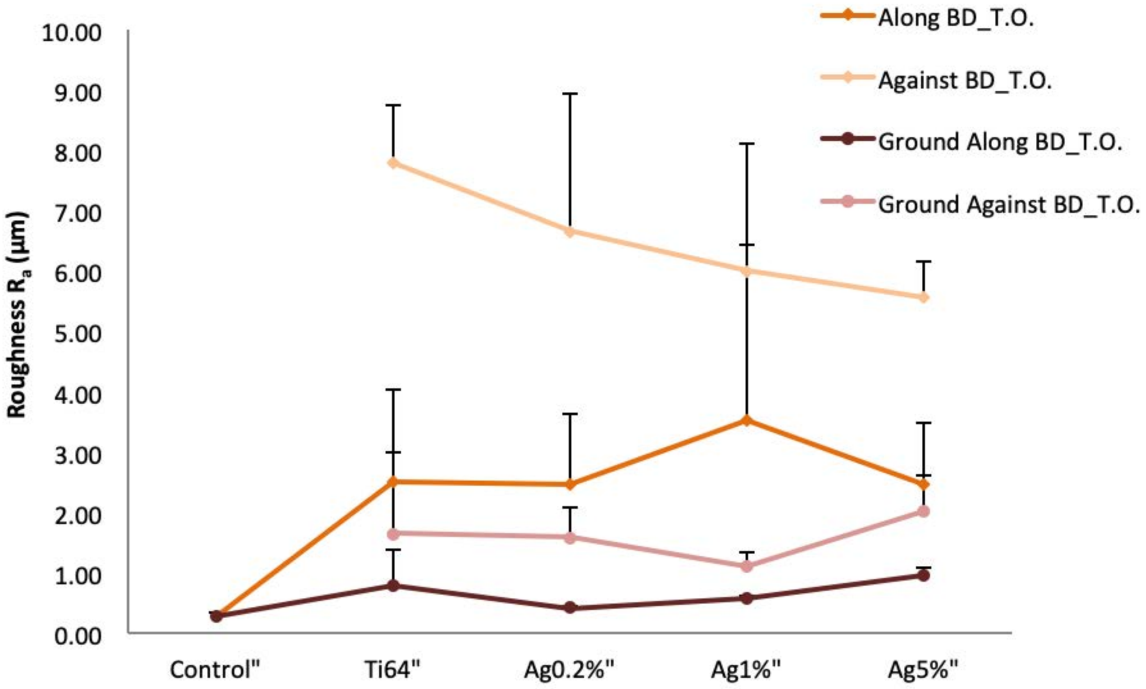

Figure 4.20 Surface roughness (R_a) measurements of post-thermal oxidation treatment of the control”, and the SLMed Ti64”, Ag0.2%,” Ag1%” and Ag5%”, as well as each sample types ground counterpart, along and against (perpendicular) to the laser BD. The lines are connected to better display the relationship between the different batches of Ti6Al4V.

Roughness depth profile

Colour depth profile surface images demonstrating the morphology and roughness profile, pre and post-thermal oxidation.

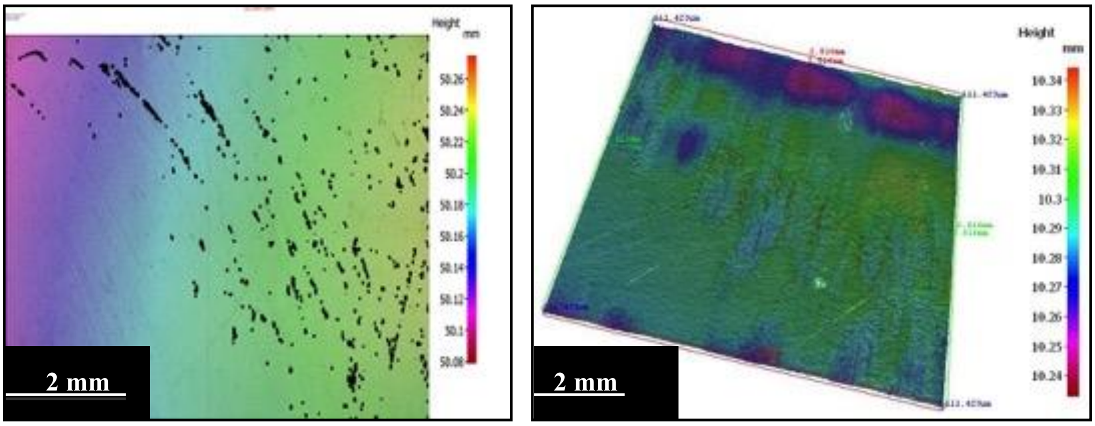
Control **Control”**

Figure 4.21 Depth profile displaying the surface texture of the control in 2D and control" in 3D.

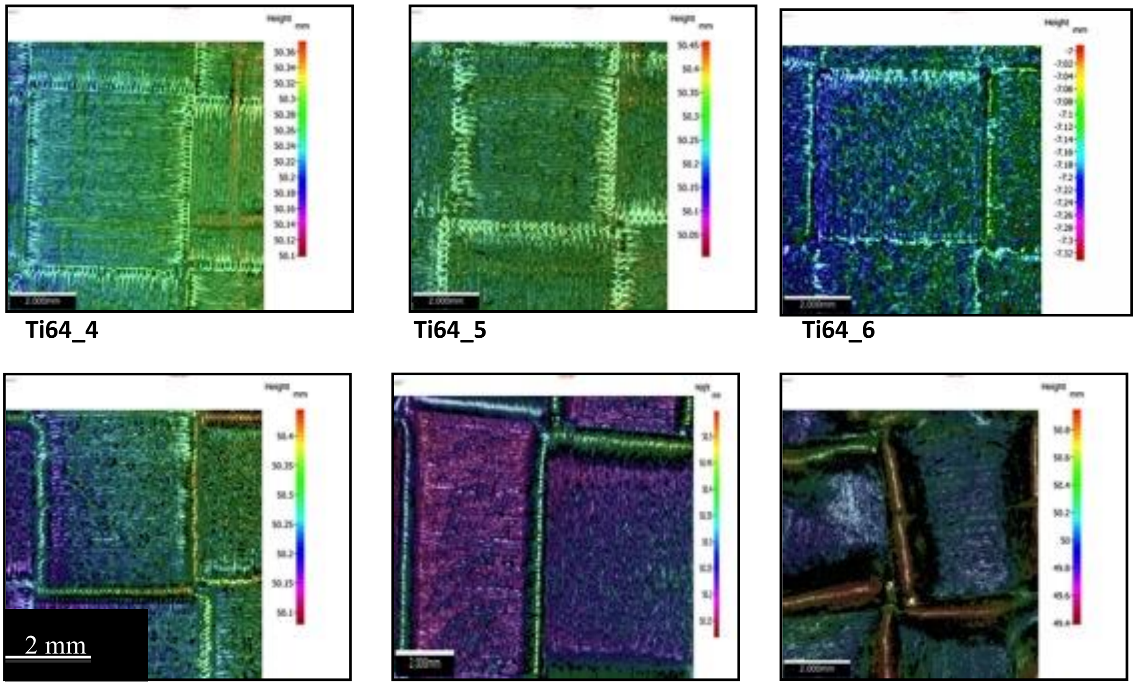
Ti64_1 **Ti64_2** **Ti64_3** **Ti64_4** **Ti64_5** **Ti64_6**

Figure 4.22 Depth profile of Ti64 SLMed samples with the six PPs.

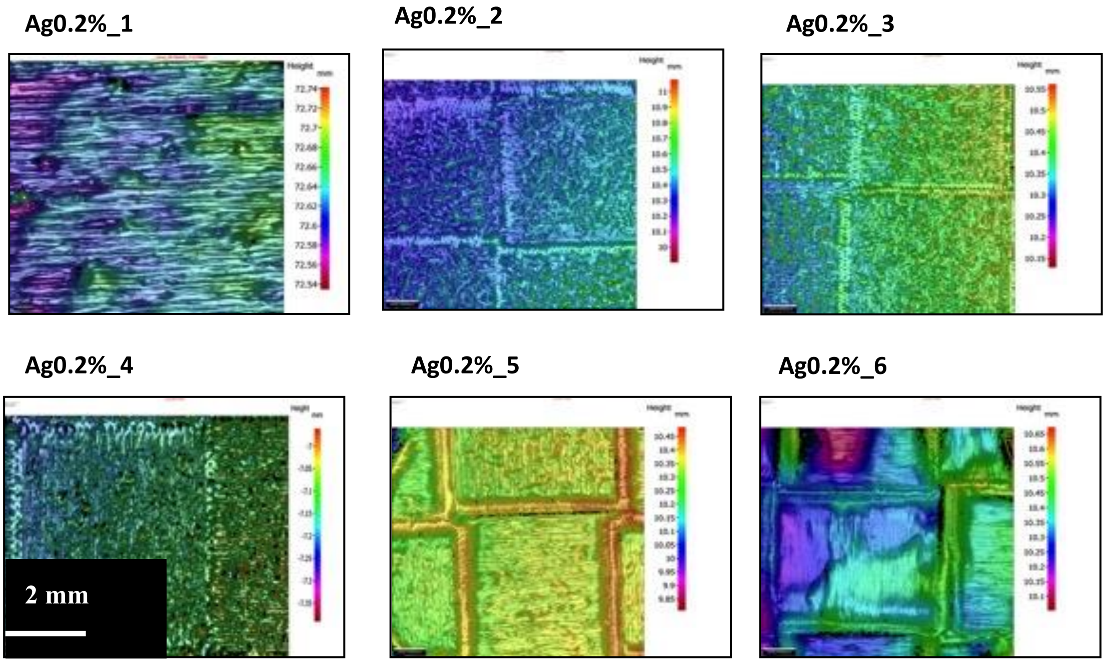
Ag0.2%_1
Ag0.2%_2
Ag0.2%_3
Ag0.2%_4
Ag0.2%_5
Ag0.2%_6

Figure 4.23 Depth profile of Ag0.2% samples created with the six PPs.

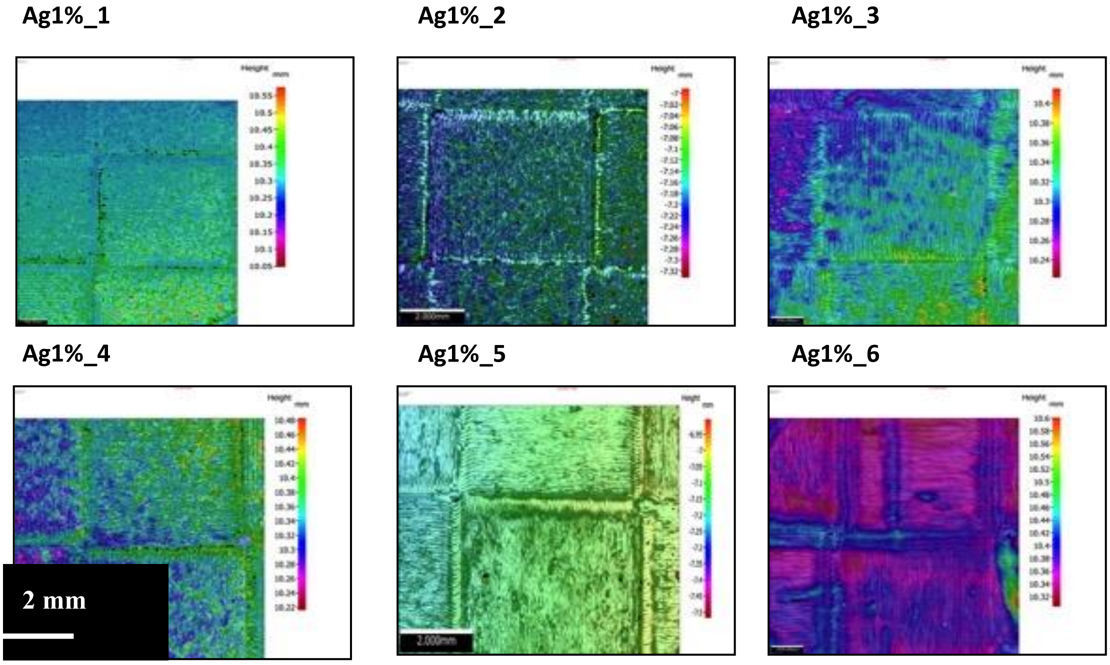
Ag1%_1
Ag1%_2
Ag1%_3
Ag1%_4
Ag1%_5
Ag1%_6

Figure 4.24 Depth profile of Ag1% samples created with the six PPs.

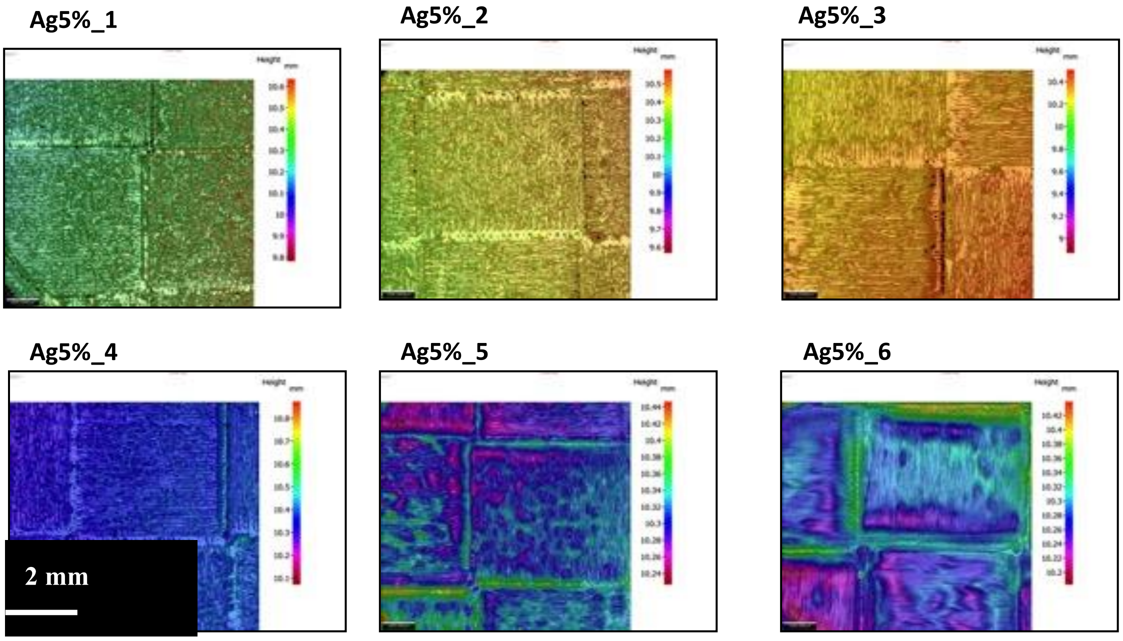

Figure 4.25 Depth profile of Ag5% samples created with the six PPs.

Exemplary 3D surface depth profile of different batches after being ground, pre-thermal oxidation.

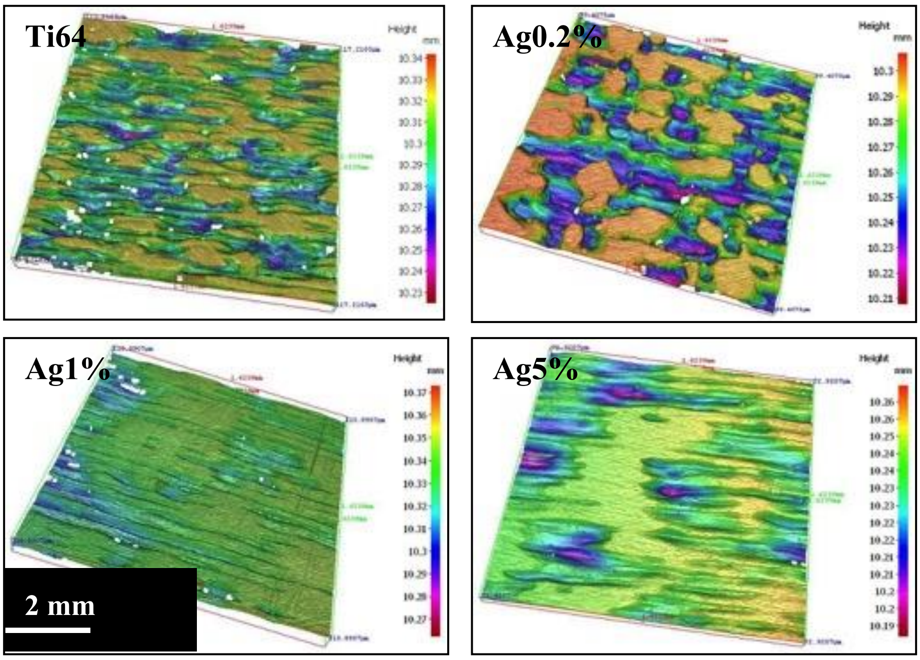

Figure 4.26 Height profile examples of the SLMed ground samples.

Roughness depth profile of samples post-thermal oxidation

Exemplary 3D Colour depth profiles of samples after being ground and undergoing post-thermal oxidation

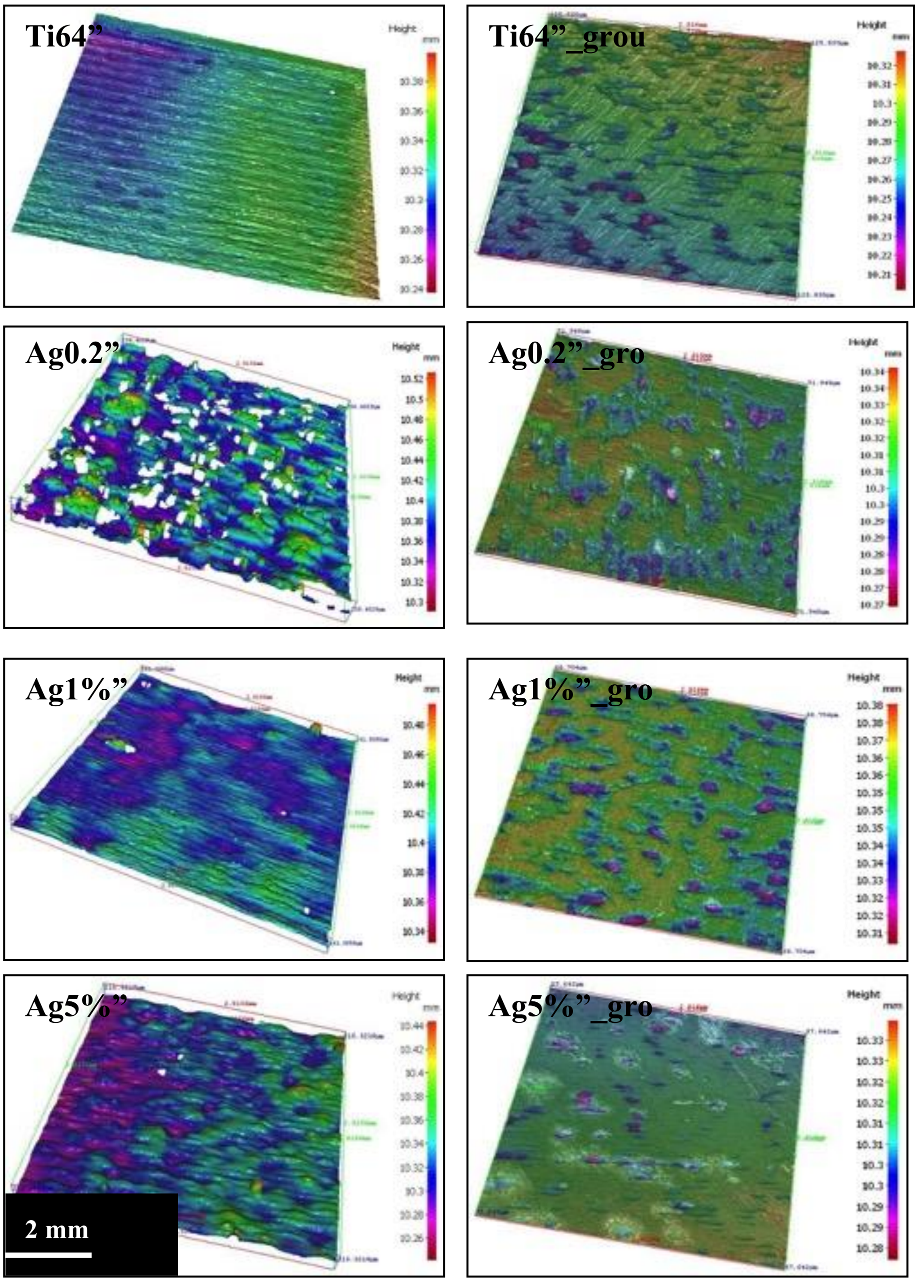

Figure 4.27 Height profile examples of samples post-thermal oxidation before and after being ground.

Figure 4.17 displays the surface roughness (R_a) of all four specimen types from the earlier work, which were measured along and perpendicular to the laser build direction (BD) avoiding the pronounced patterns in Pattern 1 and 2. Generally, R_a measurements perpendicular to the build direction were higher than those along for all specimen created by SLM. The as-polished control demonstrated the lowest R_a value of 0.171 ± 0.04. The R_a (μm) of samples progressively increased from Pattern 2 with: 11.76 ± 1.57, 20.48 ± 2.85, to 3 with: 12.62 ± 0.65, 28.82 ± 3.90; and to 1 with: 28.25 ± 0.77, 33.34 ± 2.06 both along and perpendicular to build direction, respectively. Statistical analysis revealed significant differences ($P < 0.05$) between the R_a values of along vs perpendicular measurements of Pattern 2 and 3. Figure 4.18 displays the wear tracks along and against (perpendicular) to the laser build direction. The pronounced irregular 'dents' on pattern 1 and 2 were measured to be 6.6 ± 0.15 mm and 3.9 ± 0 26 mm, respectively.

The surface roughness (R_a) of the as-ground control, and SLMed samples from the chosen six PPs were measured. The results in Figure 4.19 showed no statistical significance amongst them. The control pre- and post-thermal oxidation demonstrated the lowest R_a values of 0.94 ± 0.05 and 0.29 ± 0.05, respectively. All the SLMed samples demonstrated greater roughness measurements against (perpendicular to) the lasers BD. Along the BD, the Ti64 batch demonstrated the lowest R_a, followed by Ag5% witch 4.47 ± 3.18, 5.07 ± 1.52, respectively. This was consistent with its R_a against BD of 6.55 ± 4.42 and 6.62 ± 2.54, respectively. On the other hand, the Ag0.2% and Ag1% batches demonstrated higher R_a values of 8.66 ± 3.05 and 8.38 ± 6.98, respectively. Similarly, against BD both these batches' R_a values were also higher at 11.18 ± 4.31 and 13.72 ± 13.06, respectively. Post-thermal oxidation, each batch type decreased in roughness, with the lowest value of 2.46 ± 1.02 along BD being shown by batch Ag5%. Ag0.2% and Ti64 closely followed this with values at 2.47 ±1.15 and 2.51 ±

1.52, respectively. Ag1% demonstrated the roughest R_a of 3.53 ± 2.90. Against the BD post-thermal oxidation, Ag5% continued to demonstrate the lowest R_a of 5.55 ± 0.6. Differently, this was followed by Ag1%, Ag0.2% and Ti64, with 6.00 ± 2.10, 6.66 ± 2.28 and 7.78 ± 0.96.

After being ground with 400 silica carbide paper, the R_a of the batches pre-thermal oxidation decreased to 1.34 ± 0.76, 1.32 + 1.51, 1.24 ± 1.22 and 0.65 ± 0.42, for Ag0.2%, Ag5%, Ag1% and Ti64, respectively. Against BD, the difference in R_a was closer to that of along BD. Ti64, Ag0.2%, Ag1% and Ag5% exhibited values of 1.39 ± 0.99, 2.91 ± 1.69, 1.49 ± 0.51 and 1.50 ± 0.81. However, post-thermal oxidation, both the Ra of ground samples decreased even more to 0.80 ± 0.58, 042 ± 0.02, 0.59 ± 0.03, 0.97 ± 0.12 along BD for Ti64, Ag0.2%, Ag1% and Ag5%, respectively. In the same order of batches listed, the R_a values against BD increased to 1.64 ± 1.35, 1.58 ± 0.50, 1.10 ± 0.24 and 2.01 ± 0.60.

The depth roughness profiles evidently display the roughness of the sample batches starting with the control pre- and post-thermal oxidation. Figure 4.21 demonstrates the difference in depth profile of the control sample before and after thermal oxidation. Post-thermal oxidation, the control was rougher with oxide scales growing on its surface. Figure 4.22 displays the differences in the surface finish of six PPs, especially, PPs 5 and 6 exhibited higher boundary layers between island scan strategies to the general surface texture; these PPs had small a 1 spacing and high energy densities, as also shown by Figure 4.23 to Figure 4.25 After grinding the laser track grooves, a comparison 3D image can be seen with flatter surface features in Figure 4.26**.** However, after being ground the laser grooves can be seen flattened for Ag1% and Ag5%. Post-thermal oxidation, the oxide scales can be seen grown onto the surface of the samples before being ground for the Ti64 sample in Figure 4.27. However, with the batches doped with Ag rougher oxide scales on the ground samples were evident.

4.2.2 Surface composition & phases (EDX, XRD, XPS)

Surface composition, phases, crystal structure and elemental identification analyses were conducted and result displayed in this section.

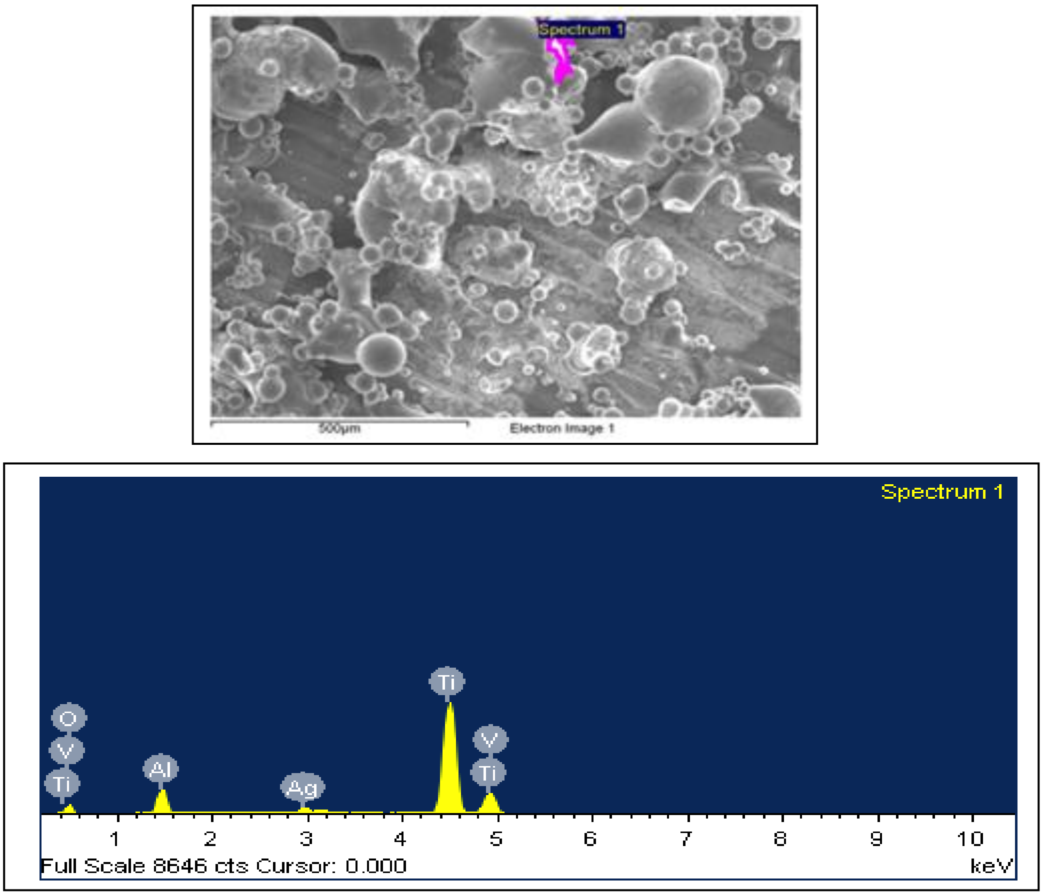

Figure 4.28 EDS point scan of the surface of Ag0.2% concentrates in a specific area.

Table 4-4 EDS elemental weight percentage of Ag0.2% surface

Elements	Weight percentage (wt. %)
Ag	1.24
O	25.26
Ti	60.31
Al	6.69
V	3.38

SLM Ti64 disk treated with 0.2 wt.% Ag + T.O: Blister

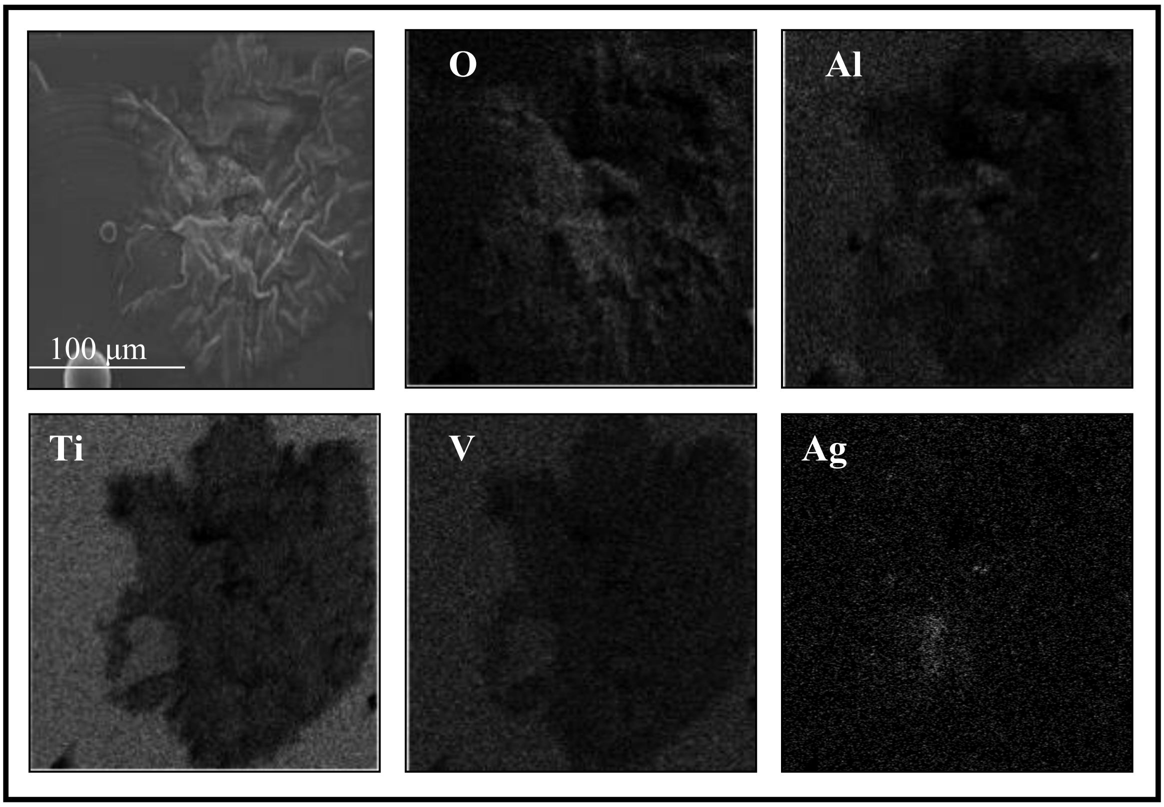

Figure 4.29 EDS elemental mapping of an oxide 'blister' formed on the surface of Ag0.2%”.

SLM Ti64 disk treated with 1 wt.% Ag + T.O: Blister

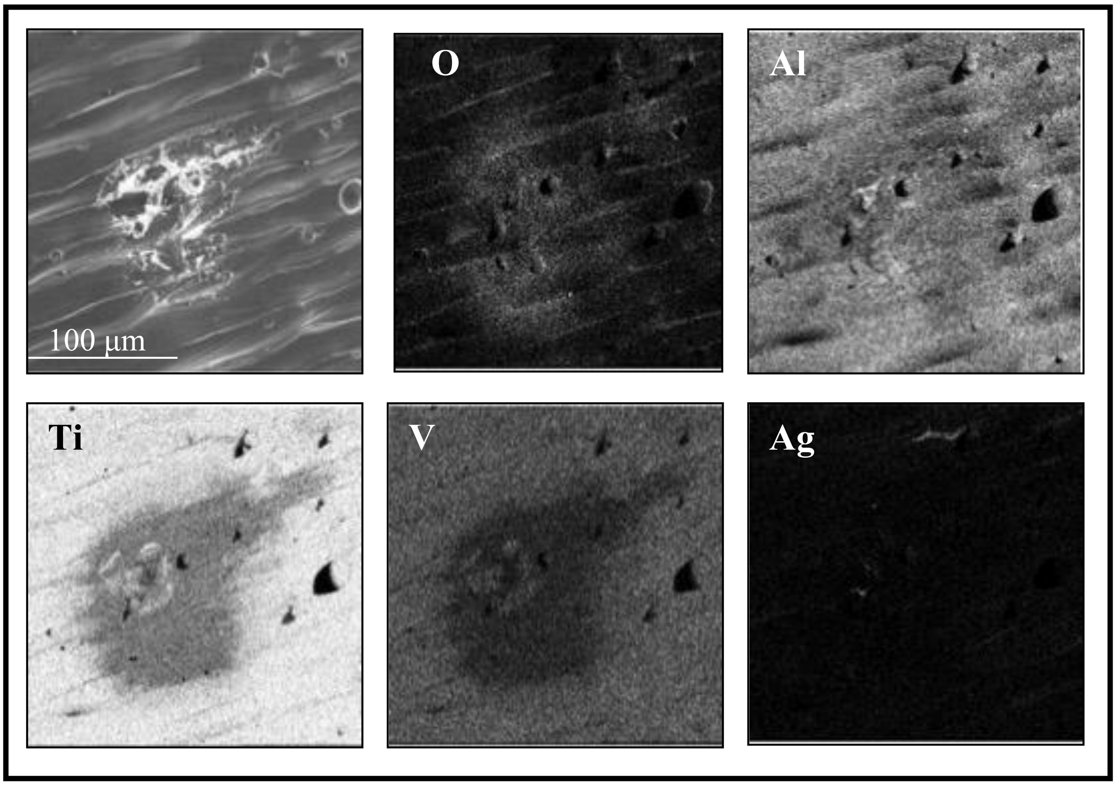

Figure 4.30 EDS elemental mapping of an oxide 'blister' formed on the surface of Ag1%”.

SLM Ti64 disk treated with 5 wt.% Ag + T.O: Blister

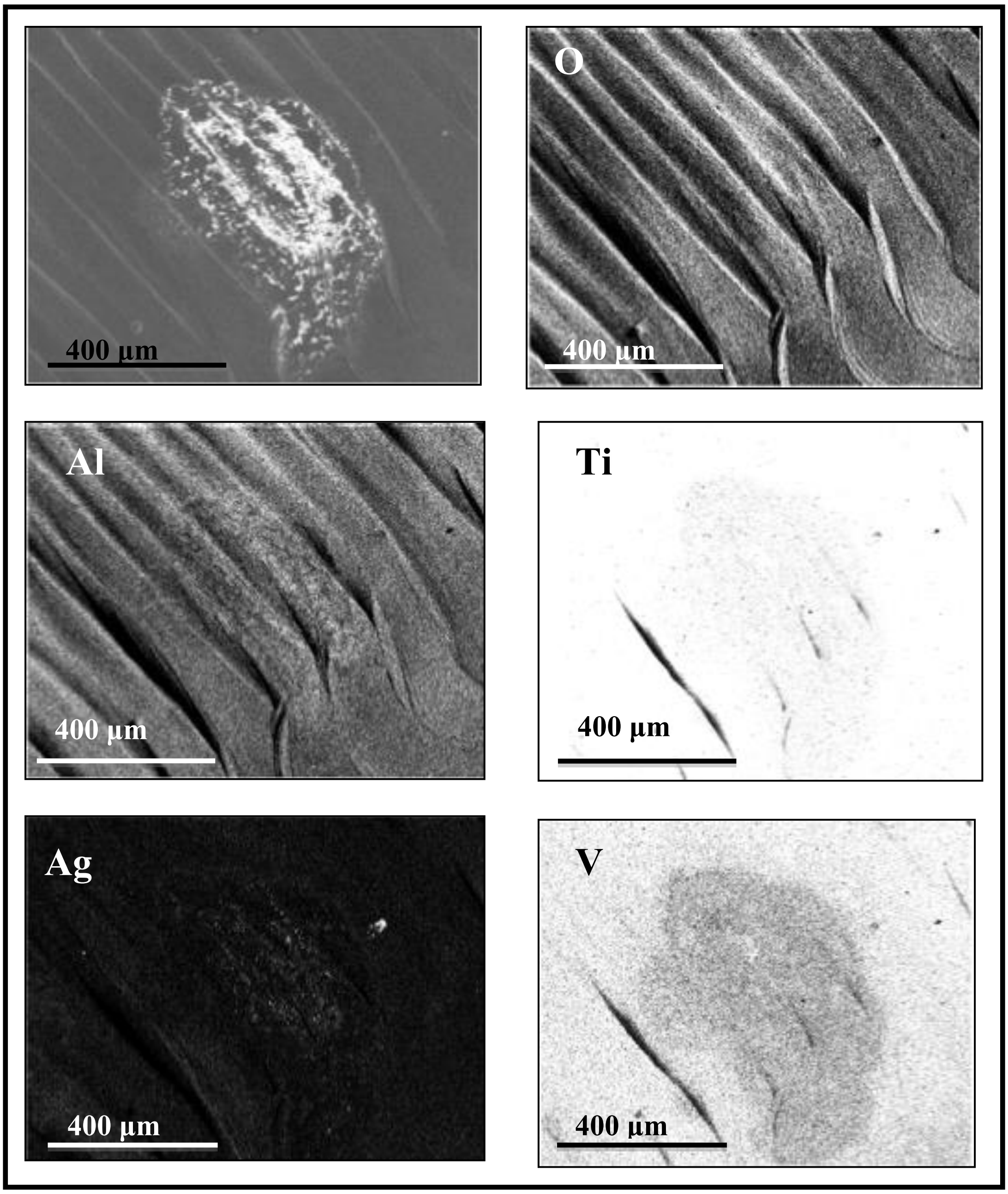

Figure 4.31 EDS elemental mapping of an oxide 'blister' formed on the surface of Ag5%”.

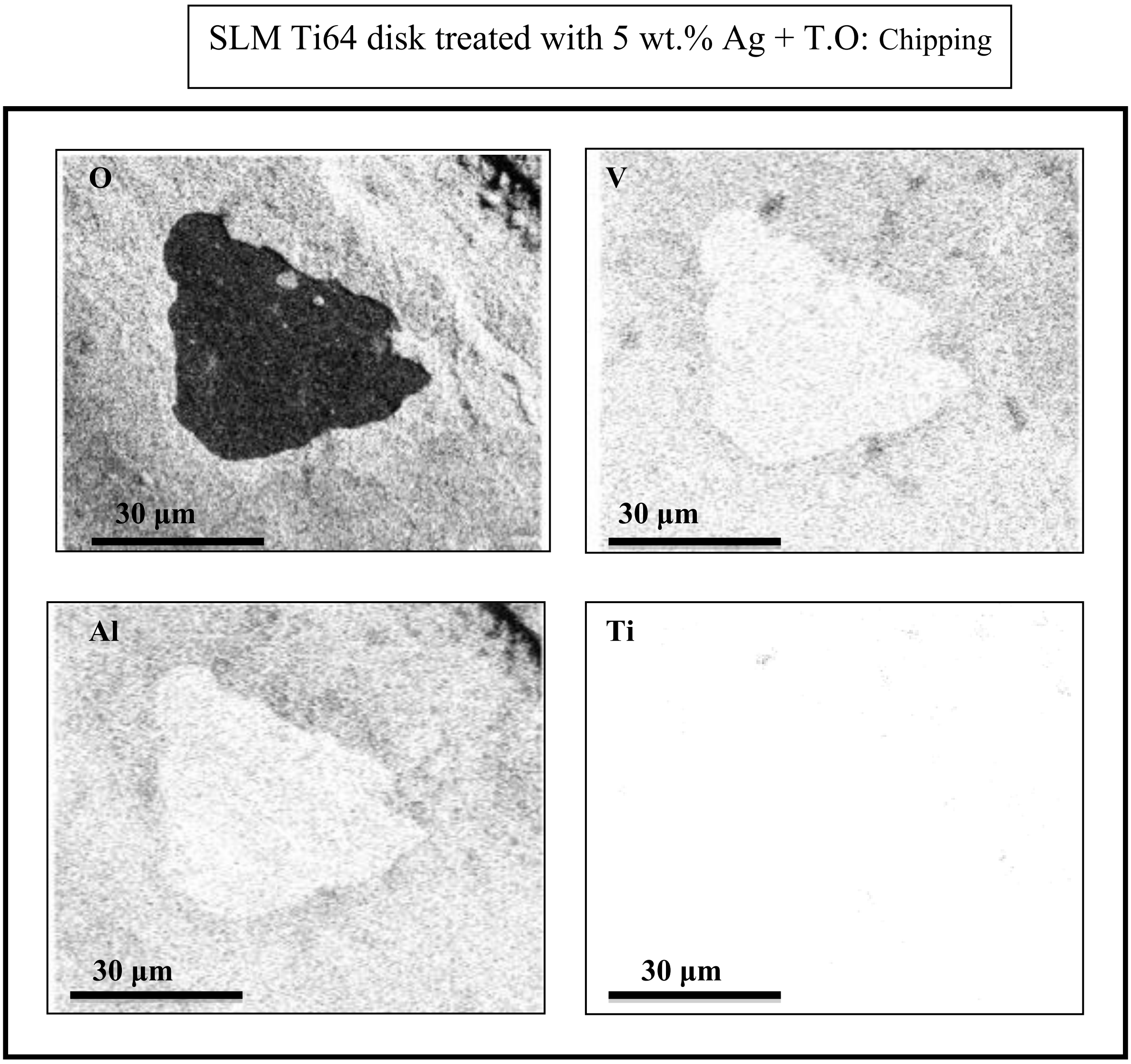

SLM Ti64 disk treated with 5 wt.% Ag + T.O: Chipping

Figure 4.32 EDS elemental mapping of a chipped area of the formed oxide layer on Ag5%”.

Phase identification by X-ray diffraction (XRD)

XRD analyses conducted to examine the crystalline phases present on the surface of the samples pre- and post thermal oxidation treatment and Ag alloying.

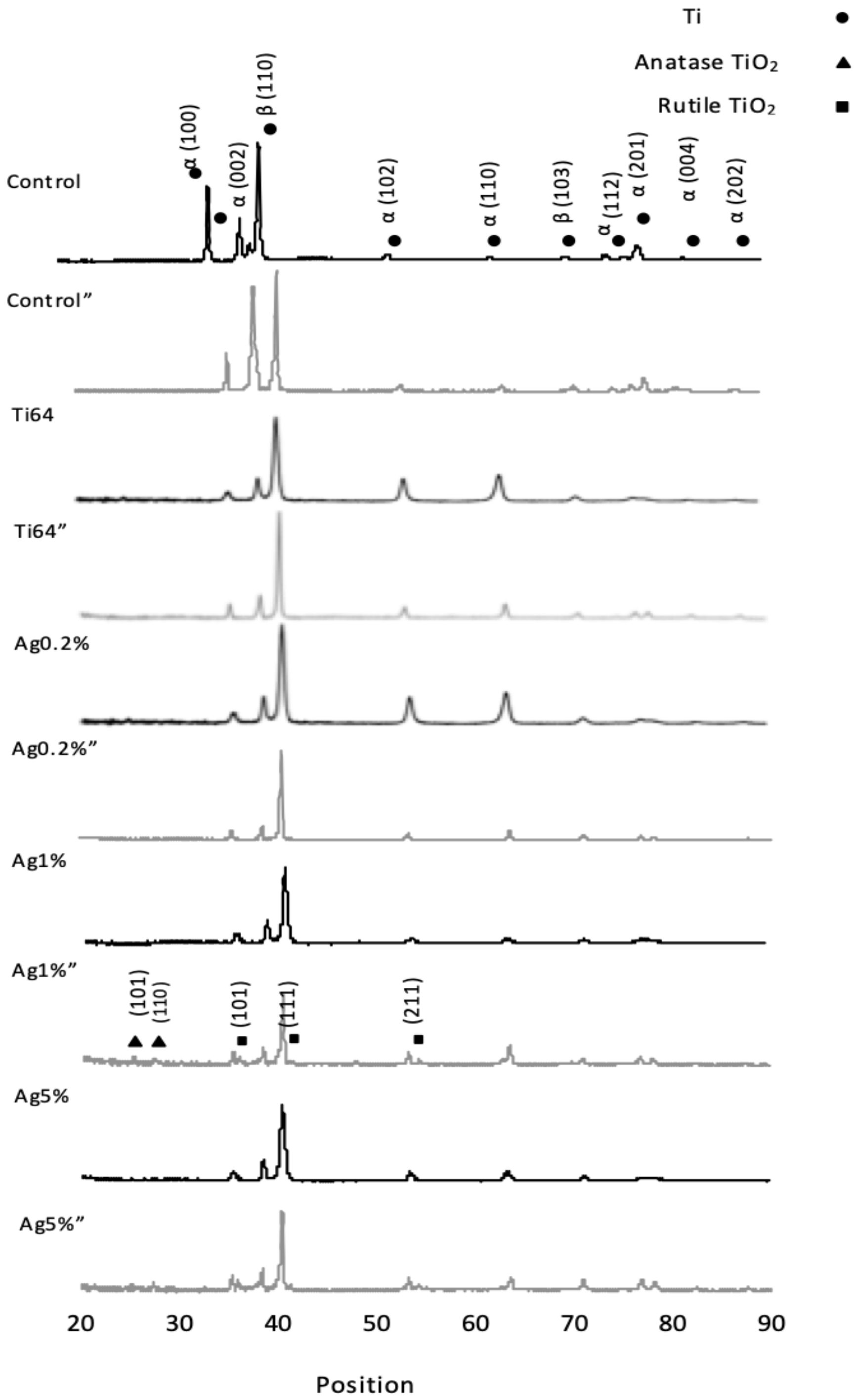

Figure 4.33 XRD analyses of all samples treatment types before and after thermal oxidation.

XPS analysis

XPS analysis demonstrating the elements present on the surface of an Ag1% sample.

Ag1%

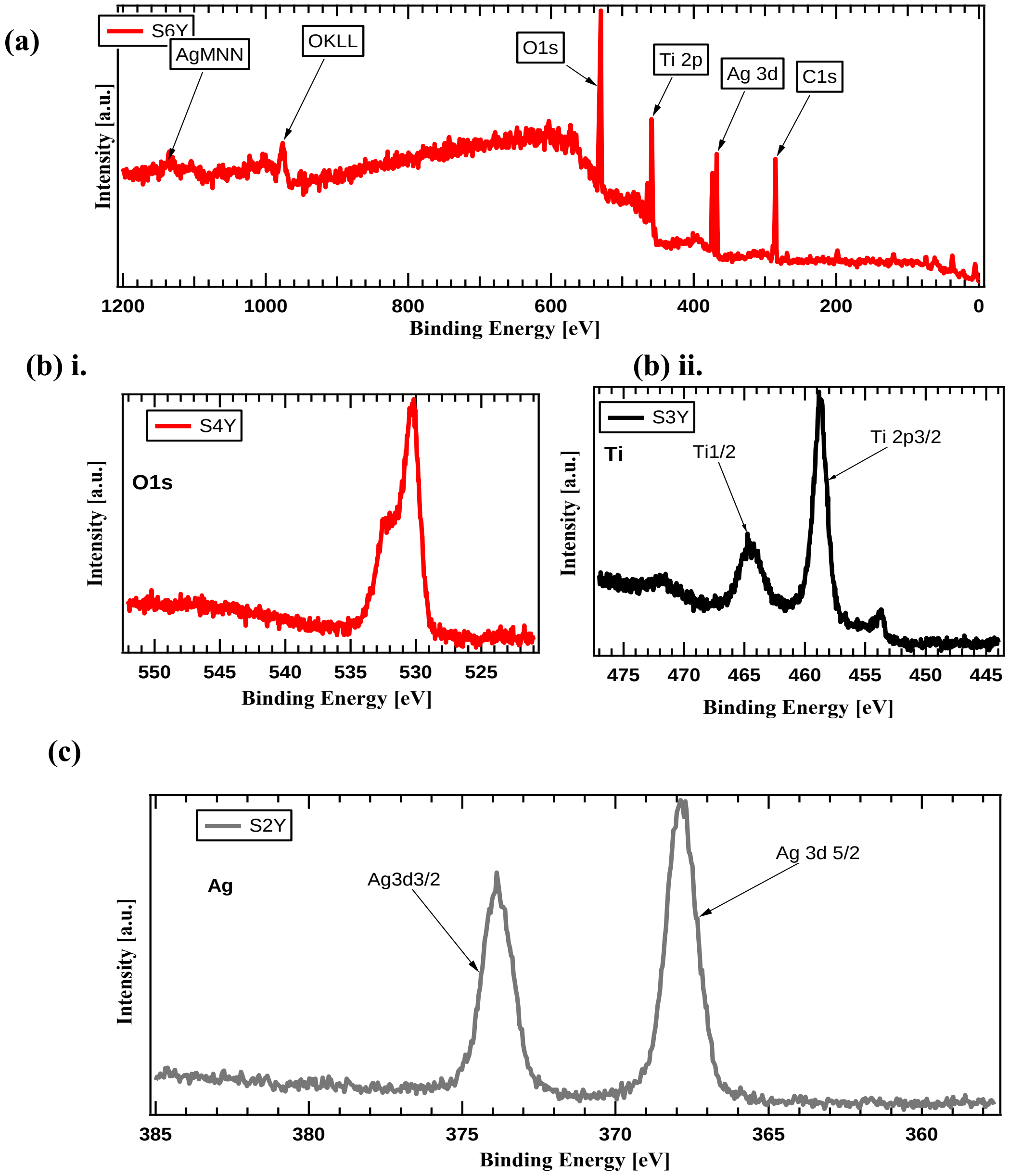

Figure 4.34 XPS study of Ag1%, a) illustrates Ag, O and Ti peaks found, while the other images are zoomed in images of the oxygen, titanium and silver peaks.

Figure 4.28 in an EDS of Ag 0.2% post-thermal oxidation; the lighter reflective areas on the sample surface were tested and demonstrating Ag content of 1.24 wt. %, and an O content of 25.26. The Ag content detected was higher than the weight percent doped into the surface SLM layer. More specifically, Figure 4.29 and Figure 4.30 displays the EDS elemental analyses carried on an exemplary Ag1 %" sample oxide blister. The EDS mapping demonstrated the presence of oxygen concentrated in the area of the blister, with a decrease in intensity of Ti as well as V more so than Al. Barely any silver can be seen on the surface mapping, but Figure 4.27 shows a small area concentrated in Ag for Ag0.2%. An even small section Ag was detected for Ag1%" Figure 4.30. However, analysis on Ag5%" depletion present. In the 'chipped' areas, Figure 4.32 previously described and seen during SEM surface morphology were confirmed in EDS analyses that the areas were discontinued oxide layer. There was a clear contrast was observed between oxygen found in a titanium oxide layer versus its subsurface bulk layer. Harmoniously, there were increased intensities of Al and V in the oxygen depleted area where the oxide layer had been chipped away.

XRD analyses conducted to examine the crystalline phases present on the surface of the samples pre- and post- thermal oxidation treatment and Ag alloying. Figure 4.33 displays XRD pattern collected for the characterisation of the crystalline Ti6Al4V material, and their atomic arrangements, to investigate the presence of any other crystalline phase structures. It can be seen, all samples treatment types show expected α-Ti peaks. With thermal oxidation and the formation of a thicker oxide layer, anatase TiO_2 and rutile TiO_2 peaks were displayed. The peak intensities of anatase and rutile TiO_2 were increasing with increase in weight percentage of Ag doping. No Ag was spotted via XRD analyses, which could be due to the negligible amount of Ag doped within the SLM layer for its crystalline phase structures to be detected. However, in Figure 4.34, the XPS study revealed the presence of Ti, O and Ag in

Ag1%. Ag $3d_{3/2}$ and Ag $3d_{5/2}$ were detected at biding energy (eV) of 374 and 368, respectively. The presence of Ag spotted in XPS confirms Ag is present in the SLM layer in its metallic state. Oxygen was detected at a binding energy of 531 eV, while Ti $2p_{1/2}$ and Ti $2p_{3/2}$ were detected at biding energies of 465 and 4601 eV, respectively.

4.2.3 Cross-sectional structure

Cross-section SEM images of samples pre and post treatments.

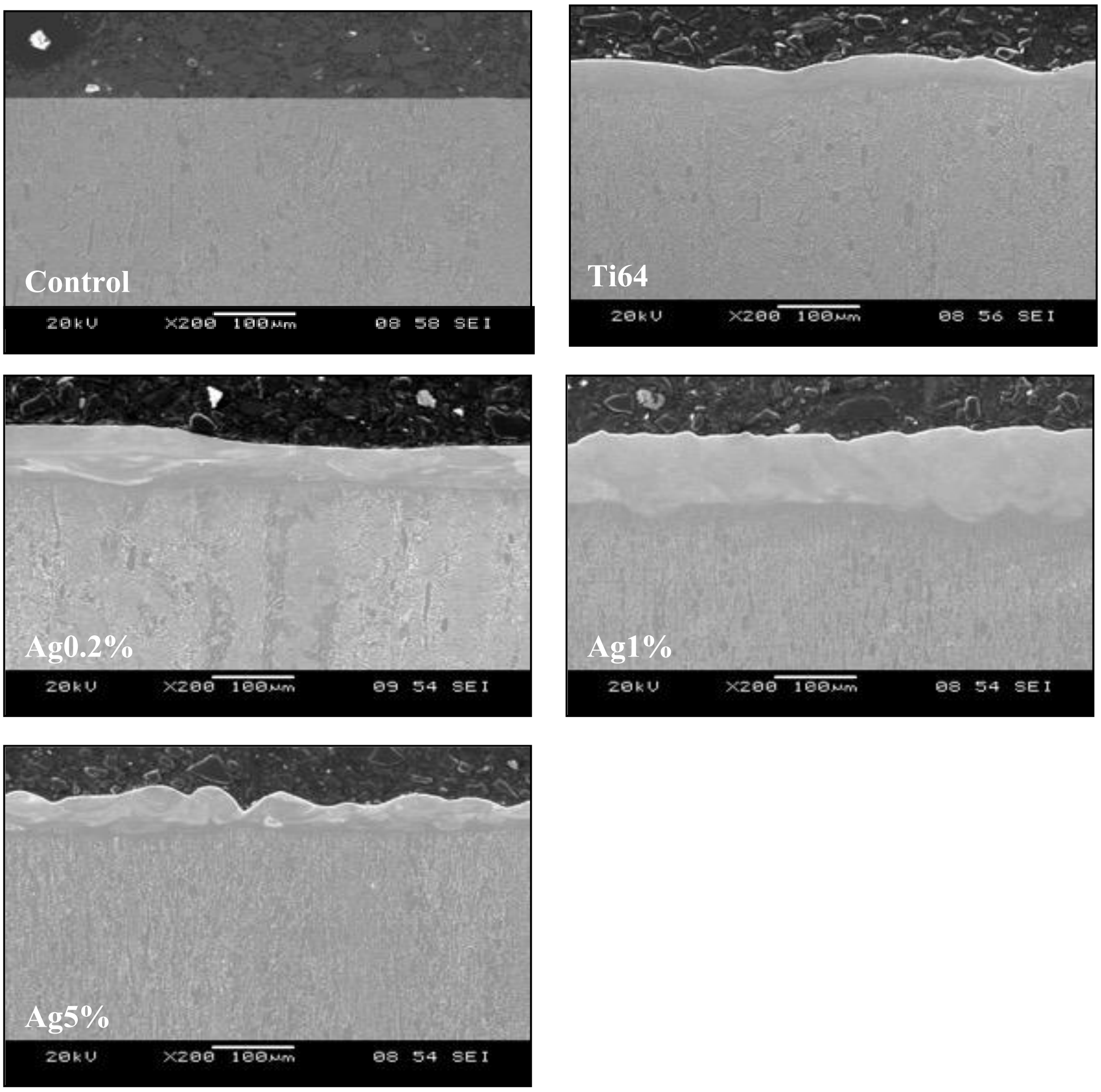

Figure 4.35 SEM cross-section of control and as-SLMed sample batches.

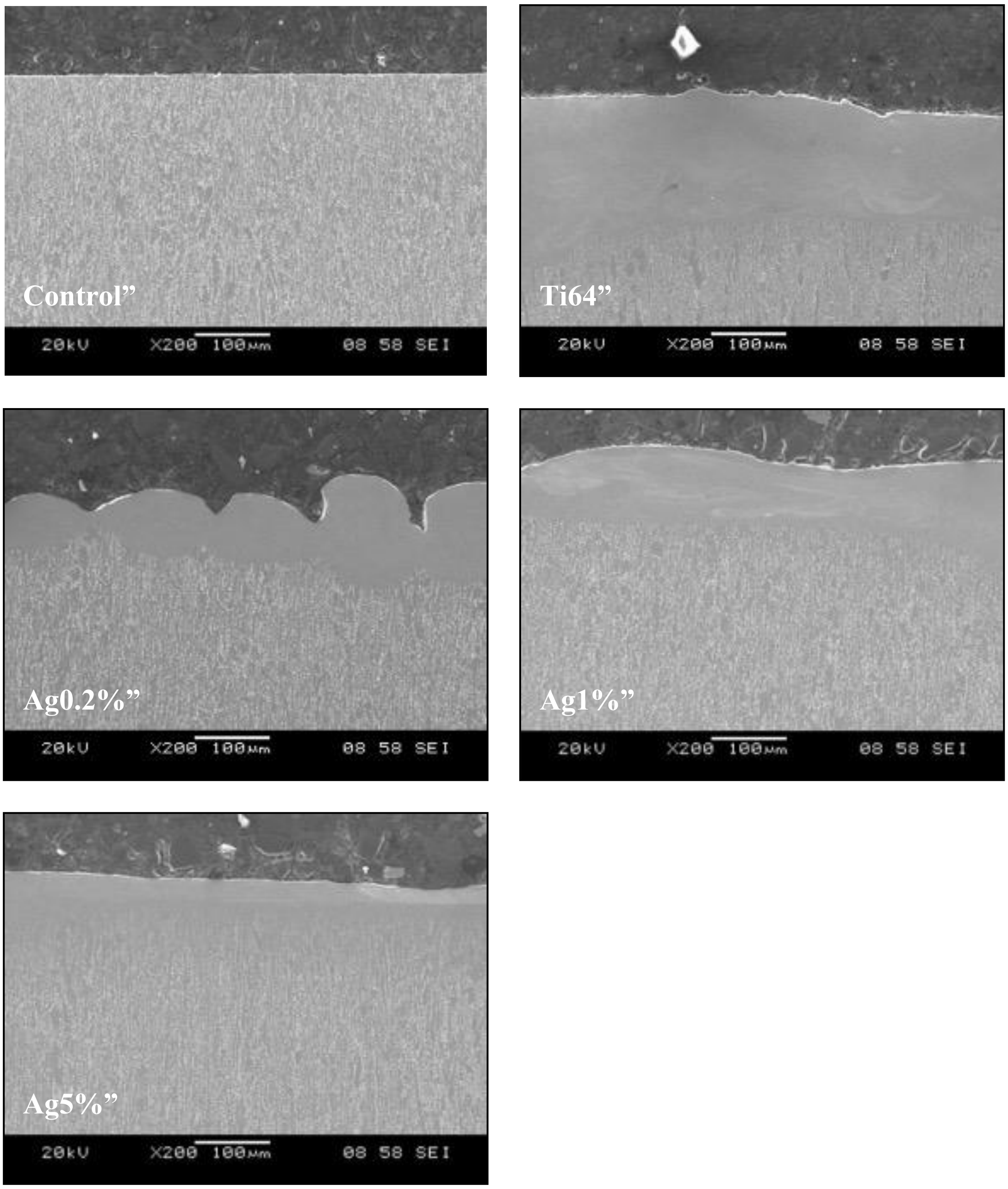

Figure 4.36 SEM cross-section of samples post thermal oxidation treatment. Very thin oxide layer can be seen on top of the SLM layer.

Higher magnification images of cross-section of different SLM batches, demonstrating the thickness of the SLM layer.

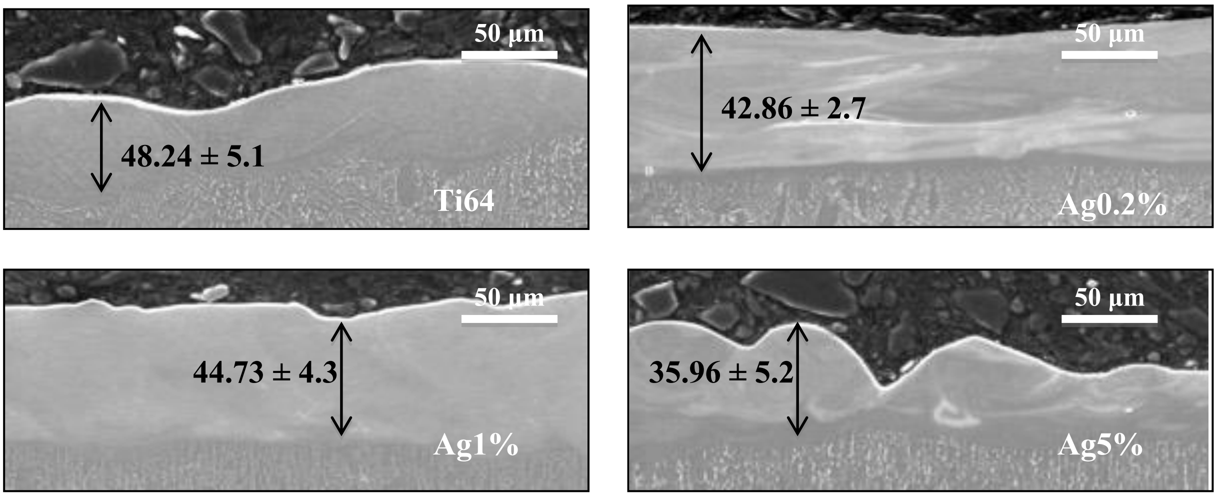

Figure 4.37 Cross-section morphology of as-SLMed samples.

SEM cross-sectional images of samples post-thermal oxidation treatment.

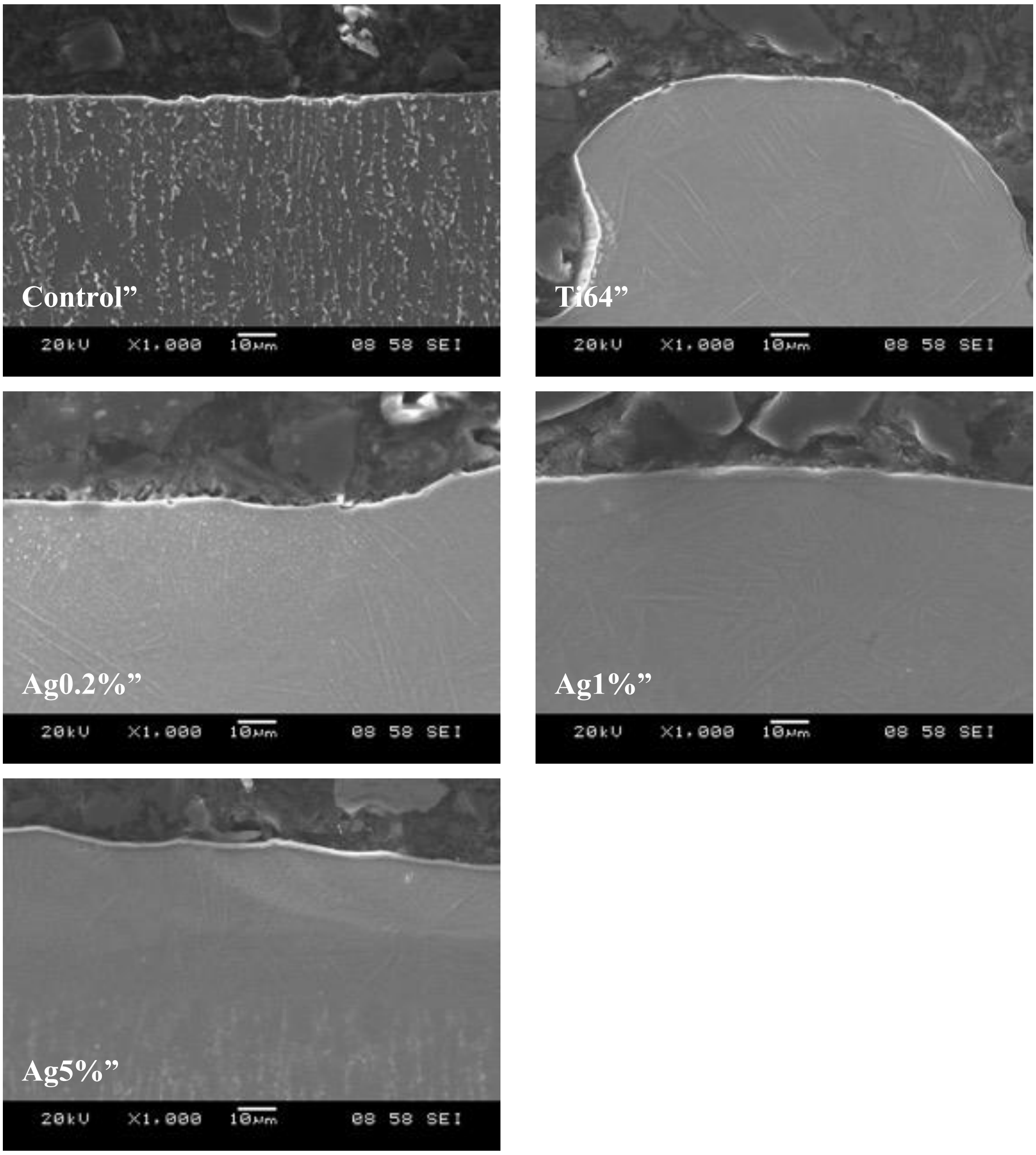

Figure 4.38 Cross-section morphology at a higher magnification of control and SLMed samples after thermal oxidation treatment.

EDS mapping of cross-sections of samples post-thermal oxidation.

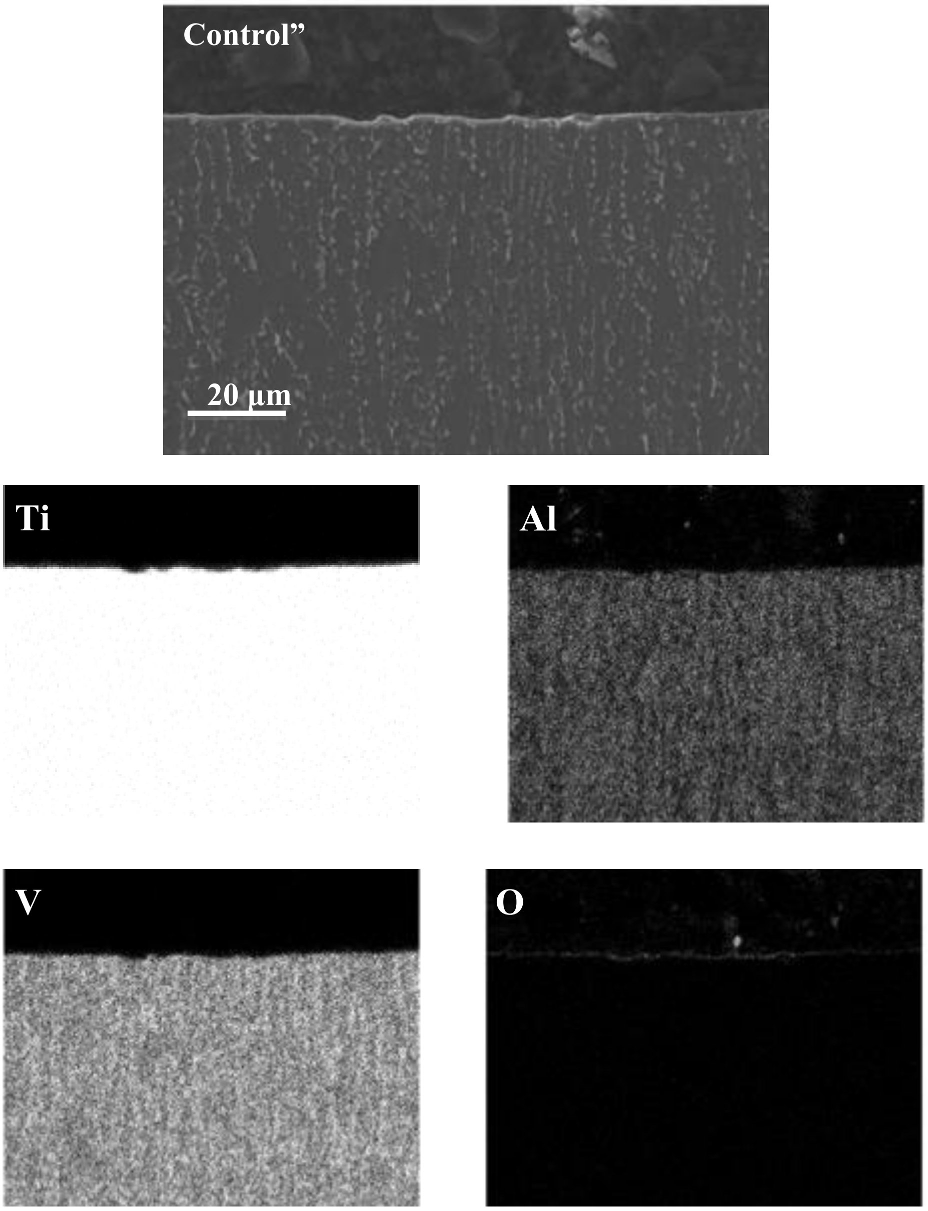

Figure 4.39 EDS mapping of cross-section control"

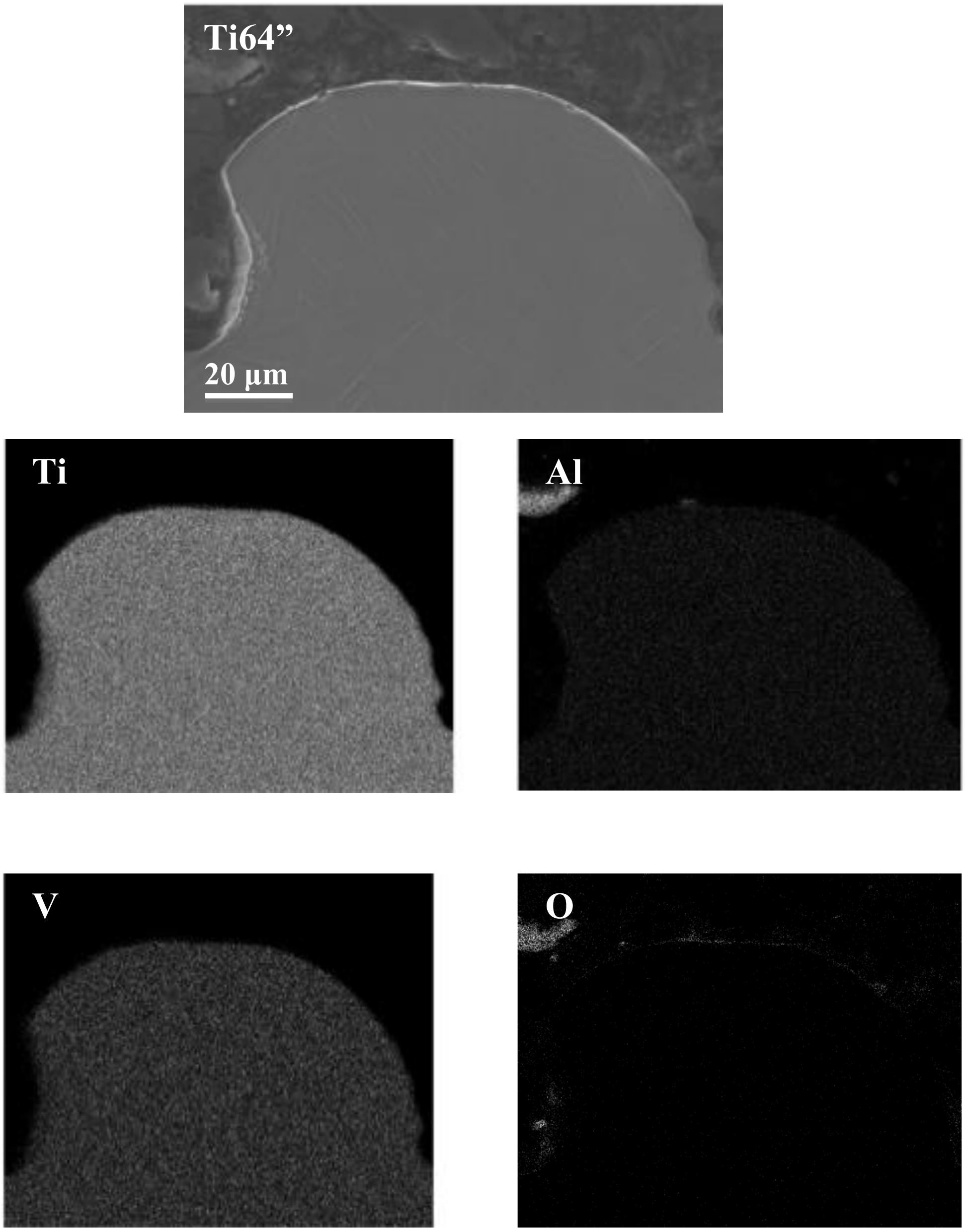

Figure 4.40 EDS mapping of cross-section Ti64"

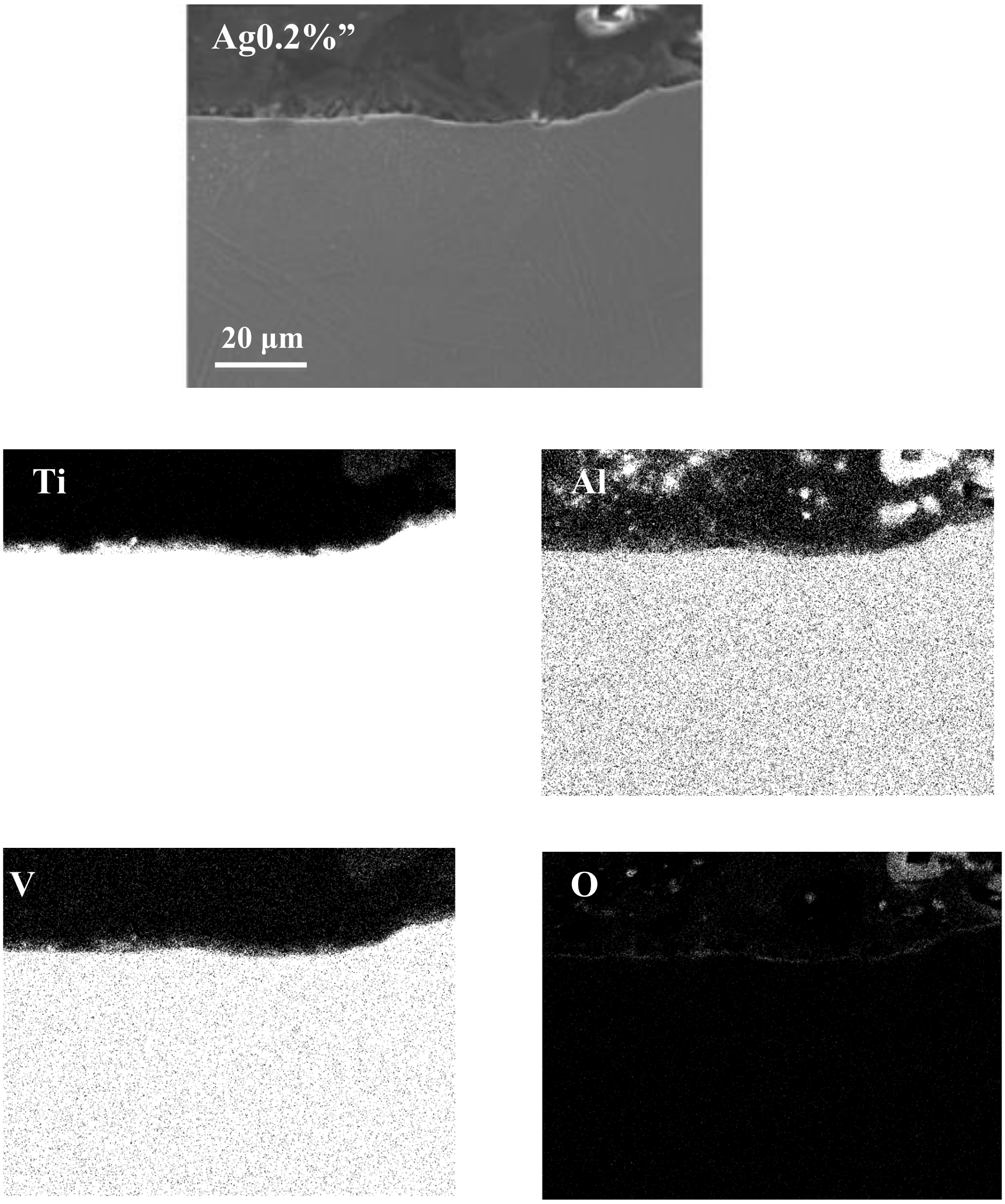

Figure 4.41 EDS mapping of cross-section Ag0.2%"

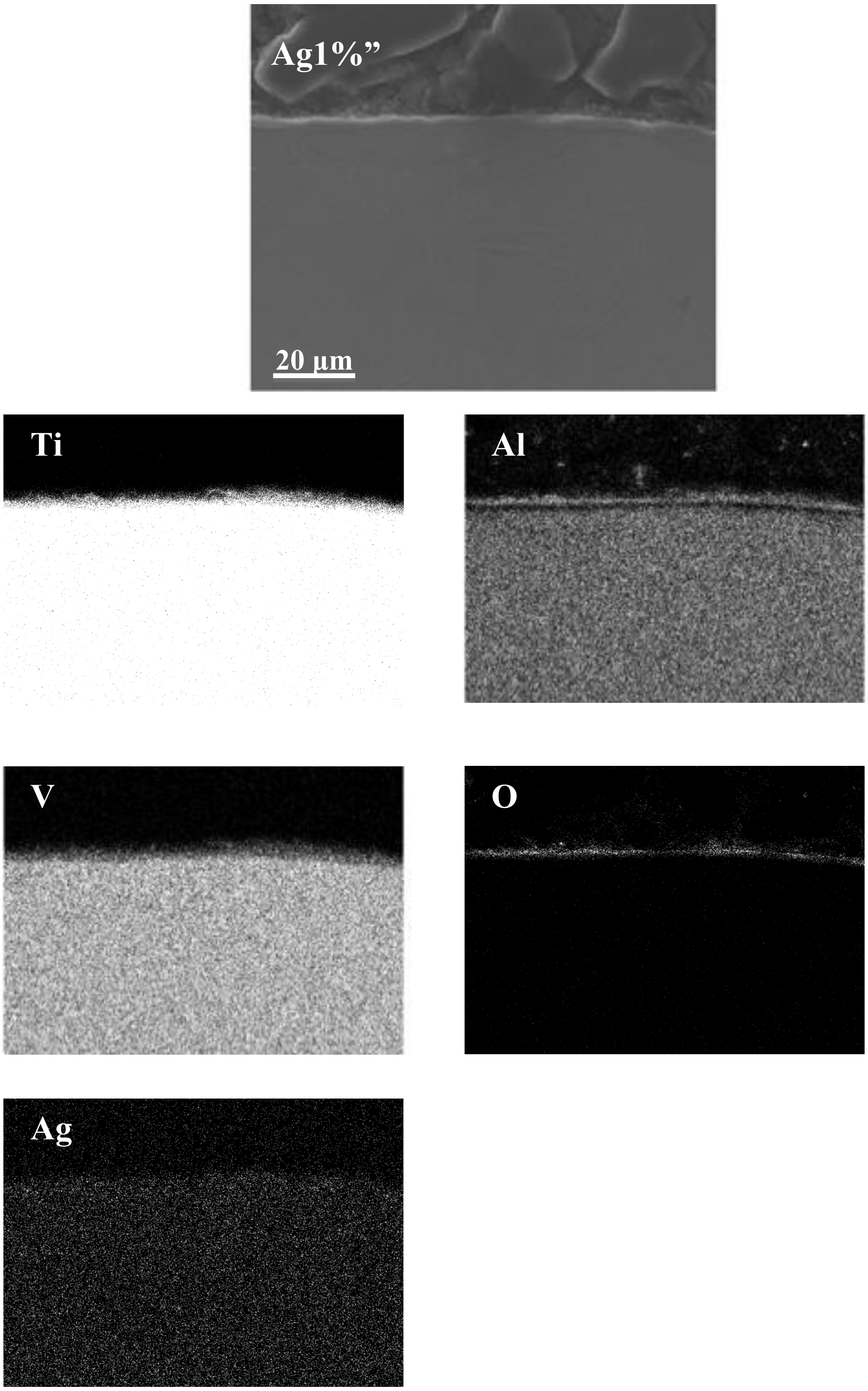

Figure 4.42 EDS mapping of cross-section Ag1%".

EDS point scans of the SLM and oxide layer post-thermal oxidation.

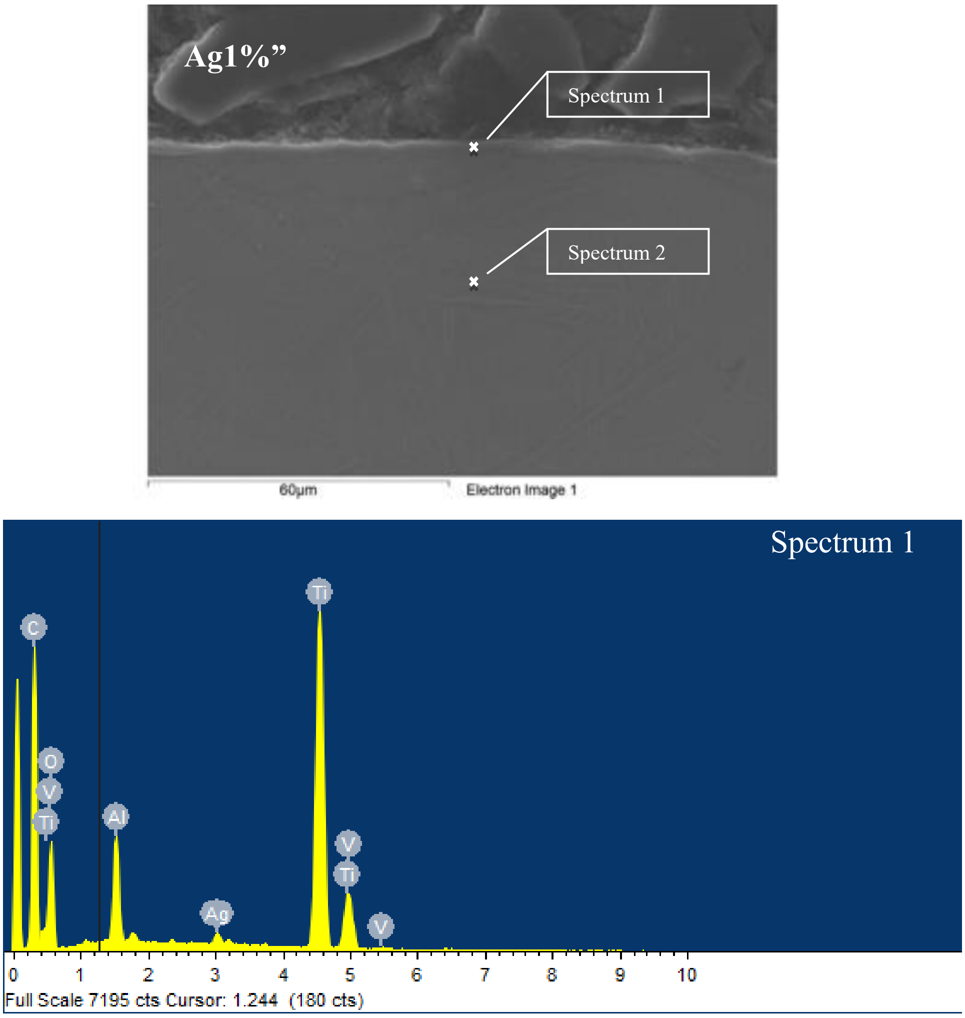

Figure 4.43 (a) Displays a cross-section image of the a Ag 1 Wt.%-doped Ti64 sample and spectrums 1 and 2 were point EDS scans, with (b) presenting EDS of spectrum 1.

Table 4-5 EDS elemental weight percent of point scans for Ag1%”

Elements (Wt.%)		
	Spectrum 1	**Spectrum 2**
Ti	24.59	89.91
Al	3.23	5.98
V	1.12	4.11
Ag	1.14	-

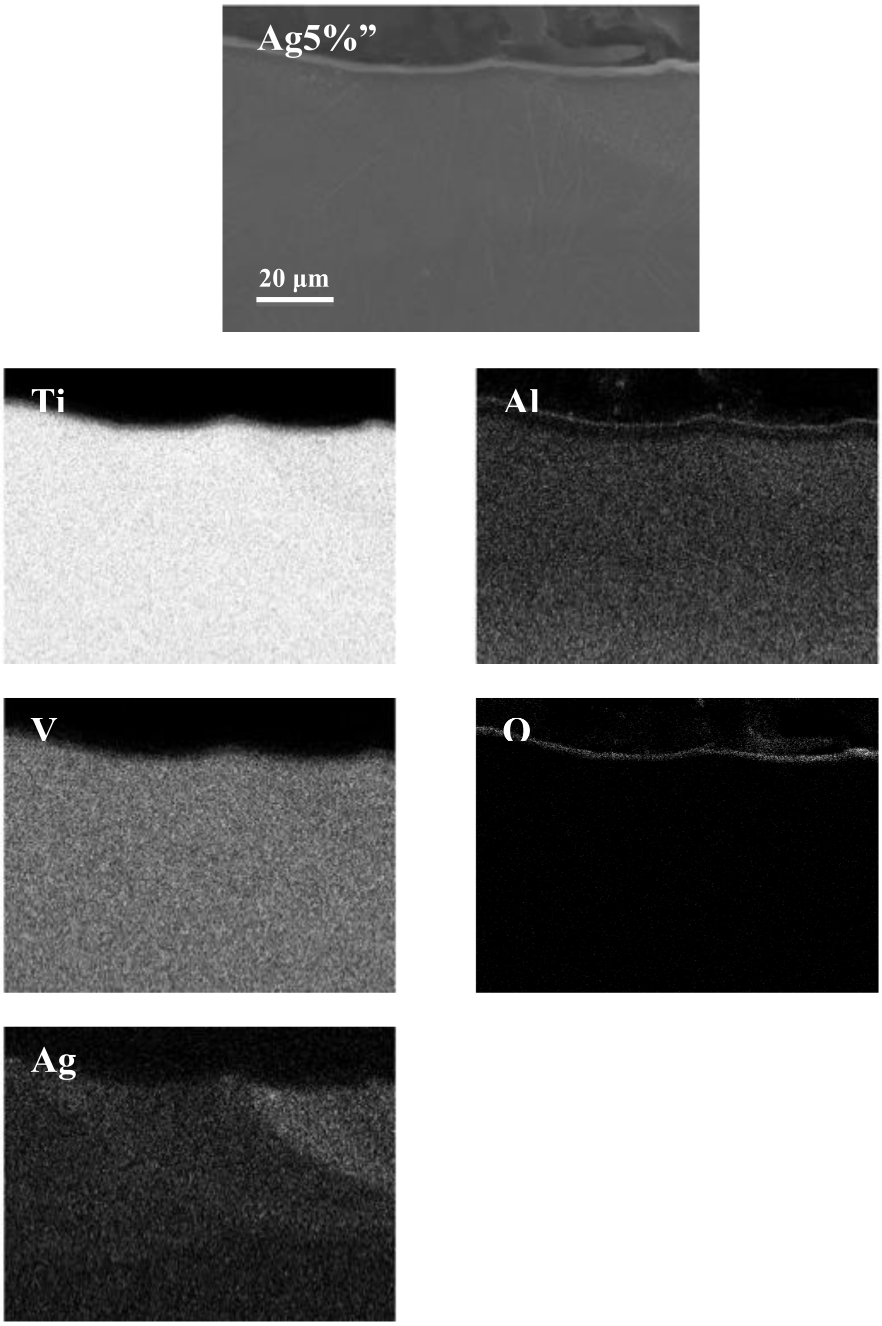

Figure 4.44 EDS mapping of cross-section Ag5%"

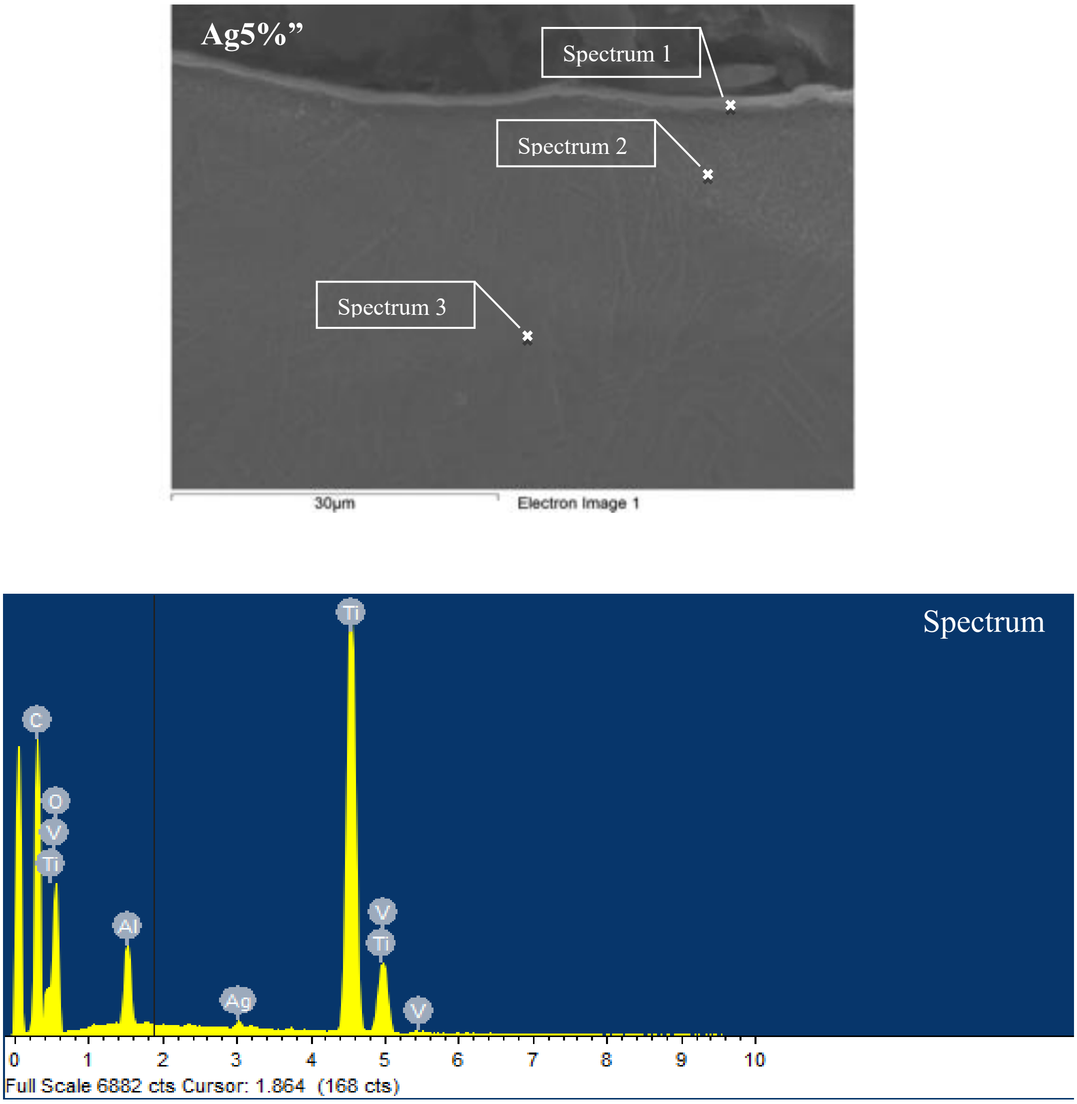

Figure 4.45 (a) Displays a cross-section image of the a Ag 5 Wt.%-doped Ti64 sample and spectrums 1 and 2 were point EDS scans, with (b) presenting EDS of spectrum 1.

Table 4-6 EDS elemental weight percent of point scans for Ag5%”

Elements	Weight (%)		
	Spectrum 1	**Spectrum 2**	**Spectrum 3**
Ti	26.11	84.46	86.19
Al	2.18	4.49	4.02
V	1.41	3.71	3.74
Ag	0.63	2.54	1.07
C	31.49	4.81	4.98

Higher magnification images and EDS mapping of the SLM layer displaying the presence of Ag.

Spreading of Ag in 1wt. % Ag-doped SLM layer

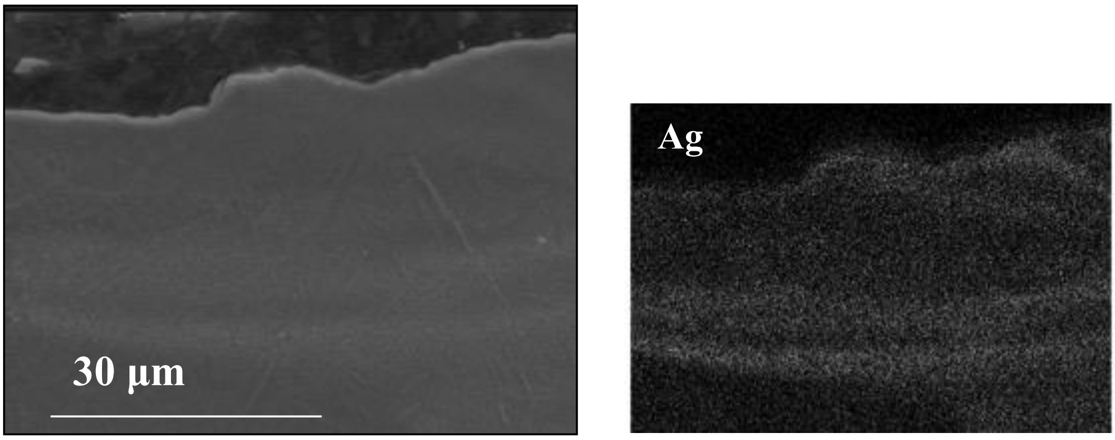

Figure 4.46 EDS mapping demonstrating Ag spread in the SLM layer of Ag1%".

Spreading of Ag in 5 wt. % Ag-doped SLM layer

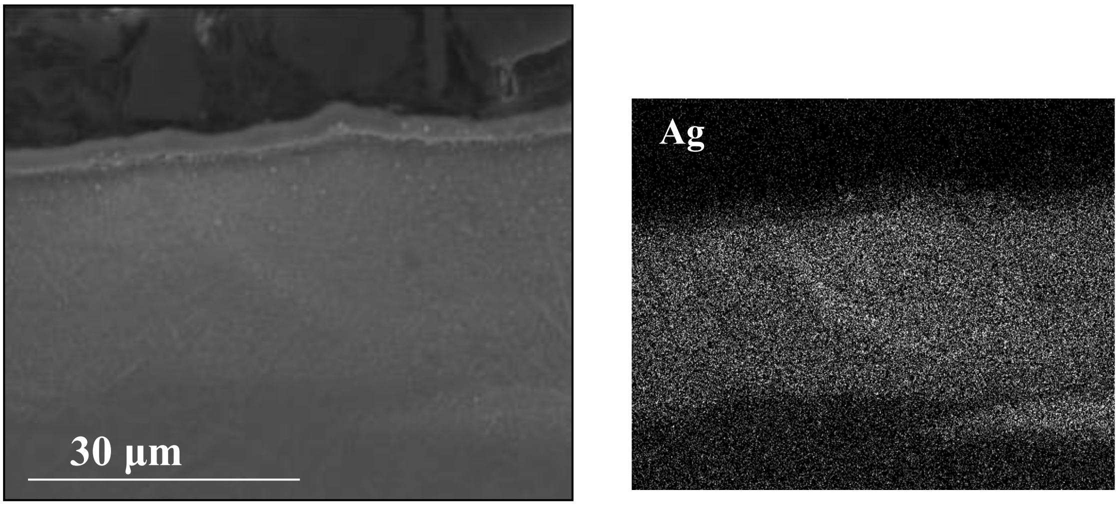

Figure 4.47 EDS mapping demonstrating Ag spread in the SLM layer of Ag5%".

Focused Ion Beam (FIB) SEM analysis

FIB analysis was conducted to get a site-specific analyses and SEM images of an oxide blister.

<u>Cross-section of Ag1%”</u>

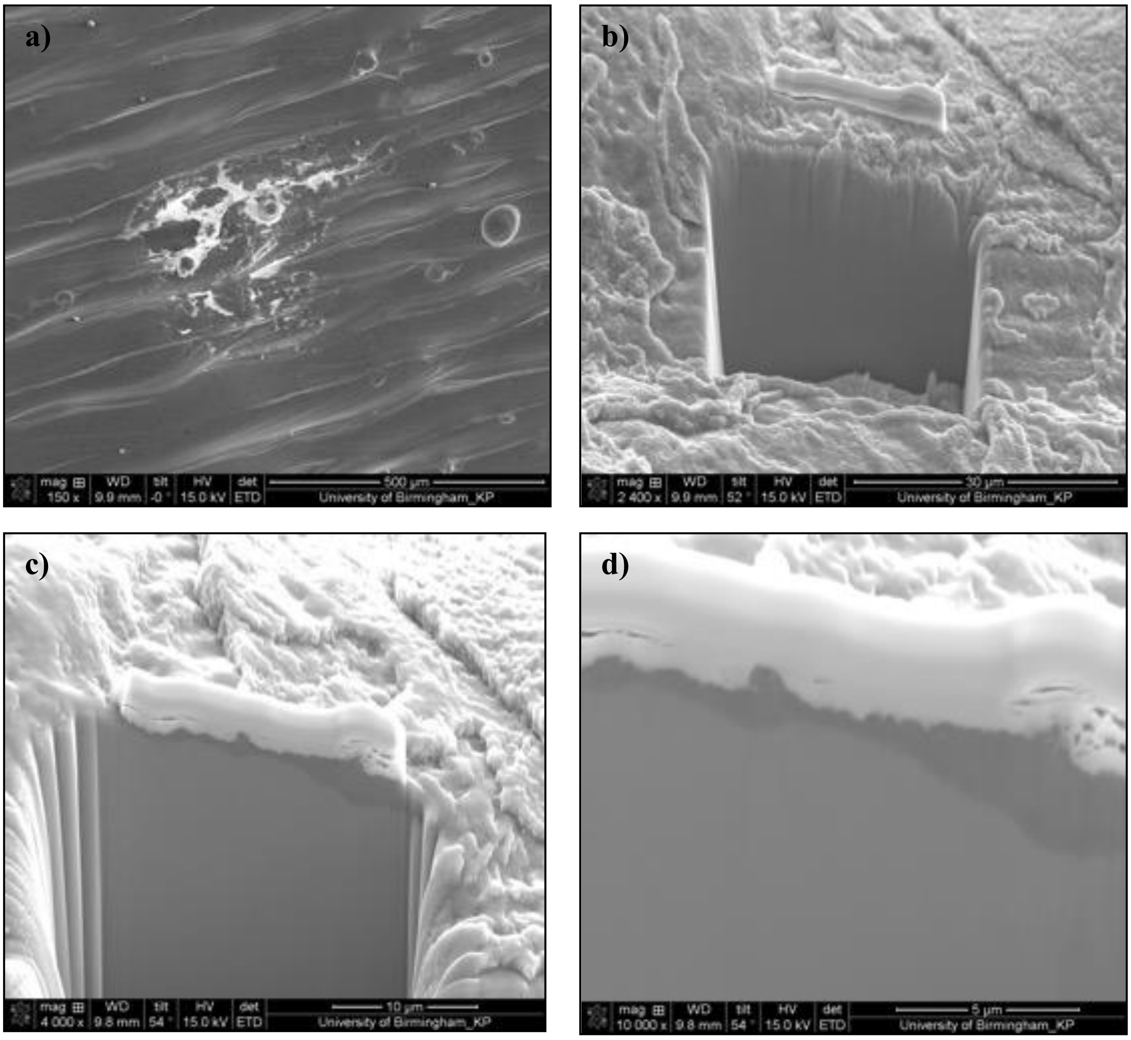

Figure 4.48 SEM images of cross-section created by an ion beam on a blister situated on Ag1% doped sample, (a) SEM images, (b) secondary electron (SE) image at a 52° tilt post Pt coating, (c) SE image post FIB milling and (d) a higher magnification of a cross section FIB milled trench.

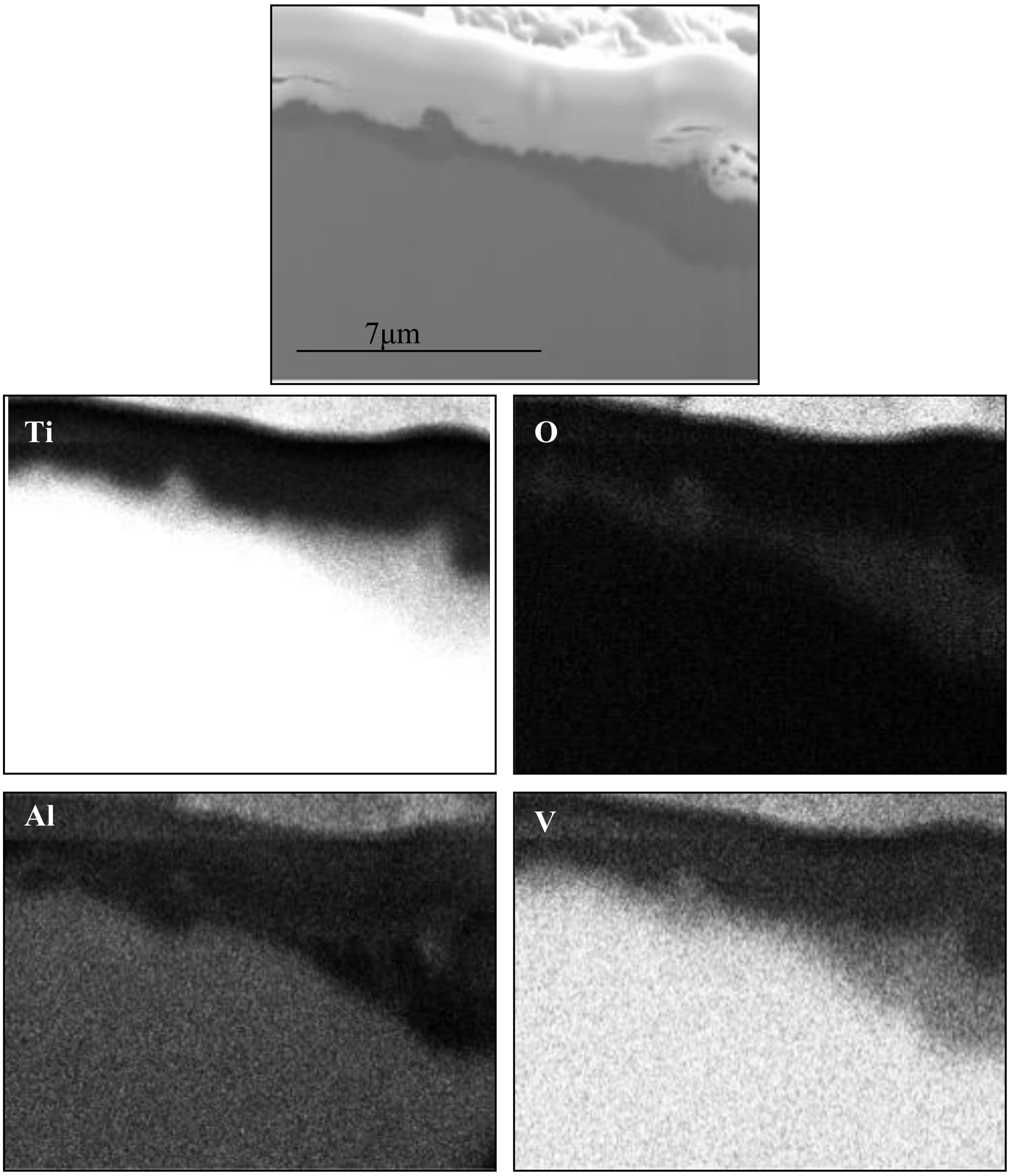

Figure 4.49 SEM and EDS elemental cross sectional mapping analyses of the post milled area on a Ag1% sample.

Figure 4.35 cross-sectional images of control and all different SLM treatment types i.e. Ti64, Ag1%, Ag2%, Ag5% demonstrates a different microstructure to the bulk material. The control does to demonstrate any SLM or oxide layer. Post-thermal oxidation, SLM layer on the treated samples the oxide layer was very thin Figure 4.36**.** Additionally, the surface grooves can be clearly seen in the cross section of the Ag5% in Figure 4.37. Furthermore, due to the limitations of the M2 SLM machine in Netshape not being able to spread powders at an even thickness the thickness of the SLM layer which in theory should have been 20 μm, resulted in layers that were were 48.24 ± 5.1, 43.85 ± 2.7, 44.73 ± 4.3 and 35.96 ± 5.2, for samples Ti64, Ag0.2%, Ag1% and Ag5%. This is demonstrated in Figure 4.37.

Post-thermal oxidation, very thin oxide layers can be spotted in Figure 4.38 at higher magnification. The Ag1% and Ag5% demonstrate the thickest oxide layer, furthermore, the α' martensite microstructure can be seen. To confirm the presence the oxide layer, EDS cross-sectional mapping studies were conducted, and Figure 4.39 demonstrated a thin oxygen rich film on top of the sample bulk material with a depletion in Ti, V and Al in the control. Similarly, Ti64" demonstrated some oxygen, but not a consistent film due to the roughness of the sample laser wear tracks. Ag0.2% also exhibited a thin oxygen rich film on top of the bulk material with a decrease in Ti intensity but with an even greater decrease of Al and V in the layer. Ag1%" and Ag5%" demonstrated the thickest oxygen rich film, with and an Al film above it, as well as concentrated in the bulk material, refer to Figure 4.42, and V was also depleted and Ti displayed the least depletion out of the three elements depleted in the oxygen rich layer. Some silver was also detected in the SLM layer. Point scan analysis in Figure 4.45 and Table 4-5 displayed the spectrum 1 of Ag1%" on the oxygen rich film but no oxygen was detected; however Ti was the highest element in detected in wt. % 24.59. Spectrum 2 of Ag1%", was pointed at the SLM bulk layer whereby a great weigh percent (89.91) of Ti was detected. 1.14 wt. % of Ag was detected within the oxygen rich film. Expectantly, Al and V were greater, 5.98 and 4.11 wt. % in the SLM bulk than in the layer, 3.23 and 1.12 wt.%, respectively. Similarly, Figure 4.42 demonstrated slightly thicker oxide layer in EDS mapping, with Al creating an additional film above the oxide layer. Ag was detected in uneven concentration along the SLMed layer. Ti and V behaved similarly to Ag1%. Figure 4.45 and Figure 4.5 demonstrated spectrum 1 of the oxygen rich layer that contained Ag, Ti, Al and V with no Ag being detected at 0.63, 26.11, 2.18 and 1.41 wt.%, respectively.

A greater wt.% of Ag at 2.54 was detected in the bulk layer that demonstrated high concentration of Ag in the EDS mapping compared to the Ag-depleted areas of the layer where Ag was detected to be at 1.07 wt.%. Additionally, Figure 4.46 and Figure 4.47 demonstrate the uneven spreading of Ag in the SLM layers of Ag1%" and Ag5%" samples. This correlates with the way in which the Ag powder agglomerated and was clumped even after 12 h of mixing.

The cross-section of the Ag1%" was analysed using a FIB-SEM to analyse the site-specific oxide 'blister' on the sample surface. Figure 4.48 (a) demonstrates the SEM surface of the site of interest. Figure 4.48 (b) is a Secondary electron image tilted at 52° of the site of interest after the protective Pt coating has been deposited and milling had begun. Figure 4.48 (c) reveals the tilted cross section of a FIB milled trench at the site of interest, through a blister and Figure 4.48 (d) is a higher magnification image displaying a very thin layer (<1 μm) that has grown on top of the SLMed layer.

Figure 4.49 demonstrates, EDS mapping of the cross section of the blister. The thin film that grew on top is rich in oxygen, depleted in Ti, Al, and V, but Ti is still significantly feasible in the layer. No Ag was detected in this cross-section.

4.3 Surface physical & chemical properties

4.3.1 Wettability and surface energy

Contact angles (°) was conducted to determine the substrate surface wettability with respect to water (^{w}).

Table 4-7 Water contact angle measurements

Sample types	Contact angle measurements
	Average water contact angle (WCA) (°)
As-polished control	54.77 ± 1.48
Pattern 1	0
Pattern 2	52.5 ± 7.16
Pattern 3	17.77 ± 14.23

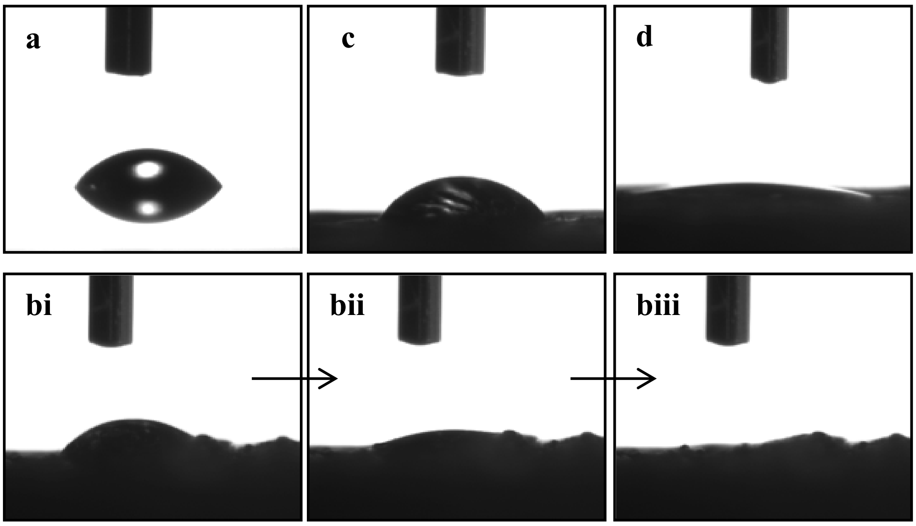

Figure 4.50 Droplet images of water on top of sample surfaces: a) as-polished control, b)pattern 1 demonstrates snapshots of the liquid droplet seeping into porous surface, c) pattern 2 and d) pattern 3.

Wettability and surface energy measurements are displayed below for all sample treatment types and conditions.

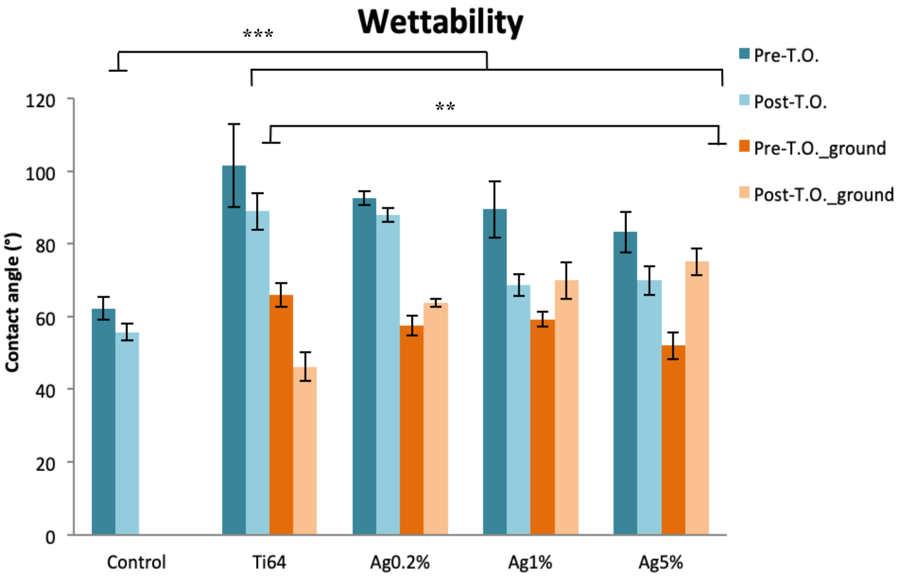

Figure 4.51 Wettability measurements using water were conducted 4 weeks after the samples were created under SLM and 2 weeks prior to being ground. *** P value < 0.001, ** P value < 0.01.

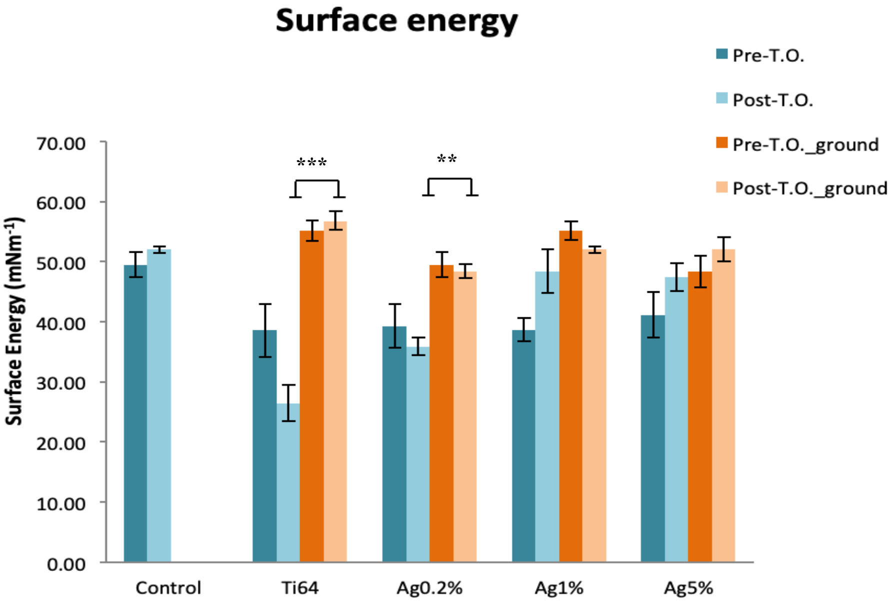

Figure 4.52 Average surface energy measurements of all samples types. ** P value < 0.01 and *** P value < 0.001.

Exemplary droplet images of water placed onto the surface of substrates of different conditions. The droplets reflected the hydrophobicity and hydrophilicity of substrate

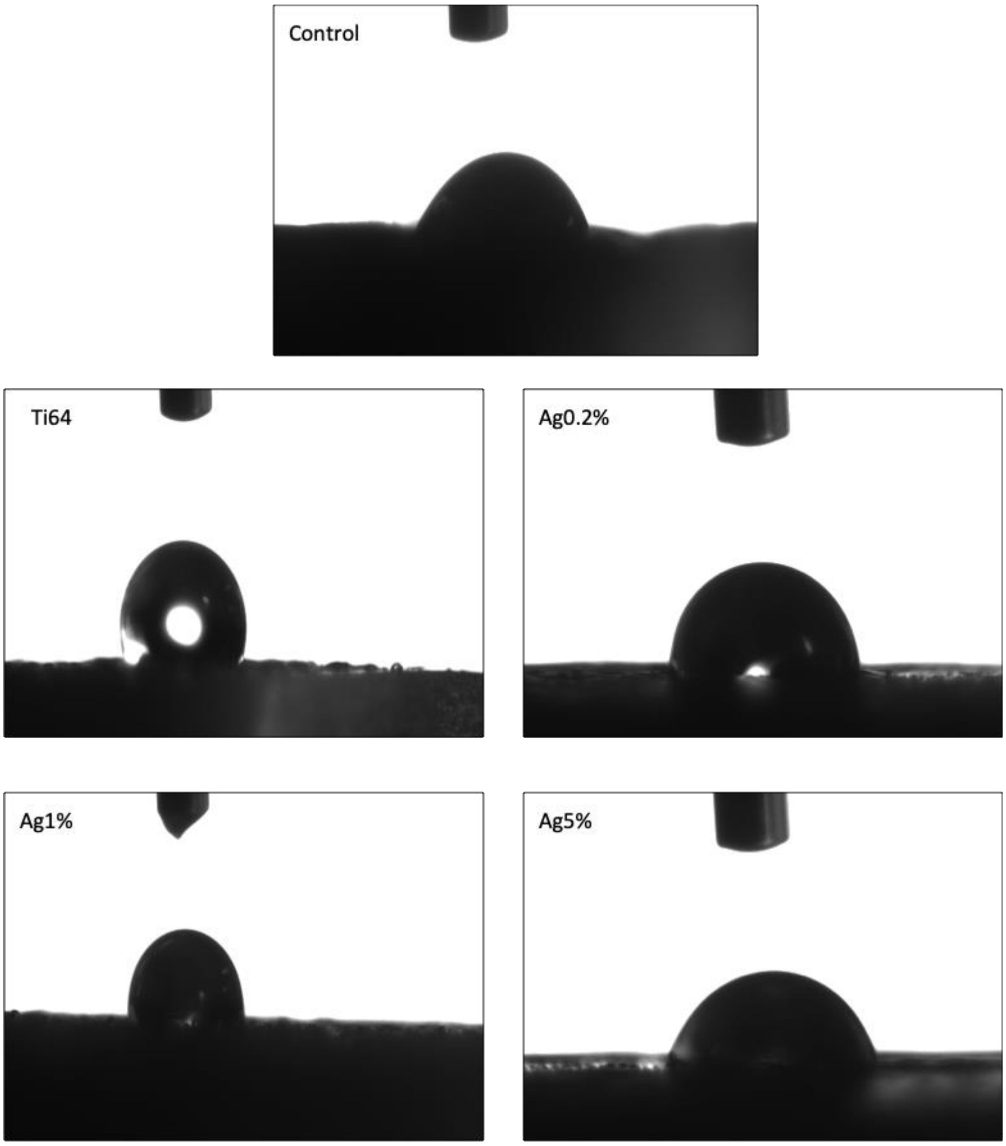

Figure 4.53 Droplet images of water on top of sample surfaces.

Contact angle (°) measurements were conducted to determine the alloys surface wettability with respect to water (^{w}). Table 4-7 presents the average water contact angle (WCA) of the as-polished control, Pattern 1, 2 and 3. The higher the contact angle the more hydrophobic the sample surface. The control sample demonstrated the highest water contact angle of 54.77 ± 1.48, followed by Pattern 2 and 3 at 52.5 ± 7.16 and 17.77 ± 14.23. Due to the porosity of Pattern 1, water droplet could not be contained on the surface of the sample; it seeped through the pores and Figure 4.50 (b) demonstrates an image time frame capture of the water droplet sinking into the sample. Pattern 2 demonstrated a similar contact angle to the control sample, but Pattern 3 was considerably lower.

Figure 4.51 depicts the wettability of the samples made using the six chosen parameters. The wettability of the ground control was 62.2 ± 3.1 after thermal oxidation the control became more hydrophilic with a WCA value of 55.7 ± 2.3. Statistical analysis determined a significant difference $P < 0.001$ between control and control”. The SLMed batches demonstrated higher WCAs of 101.6 ± 11.4, 92.6 ± 1.9, 89.6 ± 7.8 and 83.2 ± 5.6 for Ti64, Ag0.2%, Ag1% and Ag5%, respectively. With an increase in Ag wt.% there was a decrease in WCA. With respect to the previous order of listed batches, post- thermal oxidation these values reduced to 89 ± 5.0, 88 ± 2.0, 68.7 ± 3.0 and 69.9 ± 4.0. In general, there was a greater decrease after thermal oxidation for Ag1% and Ag5%, which could be due to the effects of oxide layer. Once the samples were ground using a 400 SiC paper finish the effects of roughness (the laser tracks) were reduced and the WCA reduced even more, with values more similar to ground control. In order of most hydrophobic to hydrophilic, Ti64 65.8 ± 3.3, Ag1% 59.2 ± 2.0, Ag0.2% 57.5 ± 2.8 and Ag5% 52.1 ± 3.7. After thermal oxidation of the ground samples, generally all the samples WCA increased except Ti64, which further reduced to 46.2 ± 4.0. While Ag0.2%, Ag1% and Ag5% increase in that particular order, with WCA values of 63.8 ± 1.0, 69.9 ± 5.0 and 75.1 ± 3.7. These values were closer to the thermally oxidised samples that were not ground. Both as-SLM and ground-SLMed Ag1% and Ag5% samples that underwent thermal oxidation demonstrates quite similar WCA. Generally thermal oxidation decreased WCA making samples more hydrophilic when compared to the as-SLMed samples. However, when the effects of roughness are minimised by grinding the surface of each as-SLMed sample, thermal oxidation generally renders the surface of the sample more hydrophobic, with the exception of Ti64. Additionally, a three-way anova was conducted and statistical differences were established within SLMed batch, with the exception of Ag5%, of $P < 0.01$ between the ground (blue coloured bars) and non-ground (orange coloured bars). Ag5% demonstrated a significant difference of $P = 0.032$ therefore a P value < 0.05 between its ground and non-ground groups. There was also a significant difference between as-SLMed its thermally oxidised equivalents $P < 0.01$.

SE is the difference in energy between the surface of a substrate and surface bulk atoms; it influences the wettability of a surface, which is the contact angle measurement of a spread of a liquid over a substrate surface. The investigations of the surface free energy (SE) of samples were conducted as it influences cell-biomaterial interactions. The control ample and Pattern 2 demonstrated similar SE values of 51.97 ± 0.57 and 55.49 ± 7.60, respectively; with Pattern 3 demonstrating the highest SE of 69.44 ± 5.60. SE of Pattern 1 could not be calculated as contact angle measurements could not be measured (Table 4-7). The surface energy of as-ground control was 49.41 ± 2.10 and after thermal oxidation this value increased to 52.91 ± 1.7, Figure 4.52. There was a general decrease for the as-SLMed samples, displaying SE values of 38.56 ± 4.41, 39.28 ± 3.60, 38.66 ± 1.90 and 41.15 ± 3.75 for Ti64, Ag0.2%, Ag1% and Ag5%. Post-thermal oxidation, Ah1% and Ag5% SLMed samples increased in SE to 48.39 ± 3.69 and 47.40 ± 2.28, respectively; while Ti64 and Ag0.2% decreased to 26.39 ±

3.03 and 35.90 ± 1.52. After the samples were ground, the as-SLMed samples increased in SE to 55.1 ± 1.8, 49.4 ± 2.1, 55.1 ± 1.5 and 48.3 ± 2.7, for Ti64, Ag0.2%, Ag1%, Ag5%. However, after thermal oxidation of ground samples, Ti64 and Ag5% further increased in SE to 56.77 ± 1.5 and 52.03 ± 2.0, respectively. On the other hand, Ag02% and Ag1% slightly decreased in SE to 48.38 ± 1.2 and 52.03 ± 0.6. In general, the higher SE lowers the WCA; thus, the high SE of the ground samples, corresponded to its low WCA rendered the sample surfaces more hydrophilic. The low SE demonstrated mostly in as-SLMed samples, also corresponded with the high WCA exhibited by the sample surfaces. However, in the case of as-SLMed samples that underwent thermal oxidation, Ti64 and Ag0.2% exhibited even lower SE than their as-SLMed counterparts however, the WCA of these two batches types were not higher. These results could be due to the prominent effect of surface roughness**.** Alternatively, the ground samples generally exhibited higher SE than the non-ground samples. These results corresponded with WCA measurements also generally being lower, thus more hydrophilic. Figure 4.53 demonstrate examples of droplets on as-SLMed surfaces. The rounder the water droplet the more hydrophobic the surfaces, these results were in accordance to the WCA of as-SLMed sample types. Furthermore, a three-way anova statistical analyses revealed significant difference $P < 0.01$ between the non-ground (blue coloured bars) and ground (orange coloured bars) within Ti64 and Ag0.2% batch types, respectively. With regards to the other batches, the difference in mean values amongst the different treatment types (pre- and post-thermal oxidation) evaluated within both the non-ground and ground samples, were not great enough to exclude the possibilities that the differences were based on random sampling variabilities.

4.3.2 Electrochemical corrosion

Table 4-8 Displays the average i_{corr} and E_{corr} values of all sample treatment types

Sample treatment type	i_{corr} x10^{-7} (Acm^2)		E_{corr} 10^{-1} (mV)	
Control	19.7	±0.01	-2.65	±0.03
Control”	1.20	±0.01	-0.50	±0.01
Ti64	1.96	±0.06	0.50	±1.93
Ti64”	1.92	±0.19	1.04	±5.09
Ag0.2%	110	±0.08	-0.50	±4.13
Ag0.2%”	18.0	±2.75	1.20	±2.55
Ag1%	100	±0.37	0.05	±1.26
Ag1%”	0.19	±0.21	1.05	±1.89
Ag5%	110	±0.05	-0.21	±3.08
Ag5%”	1.66	±0.71	0.98	±4.24

Electrochemical corrosion: Control vs Control”

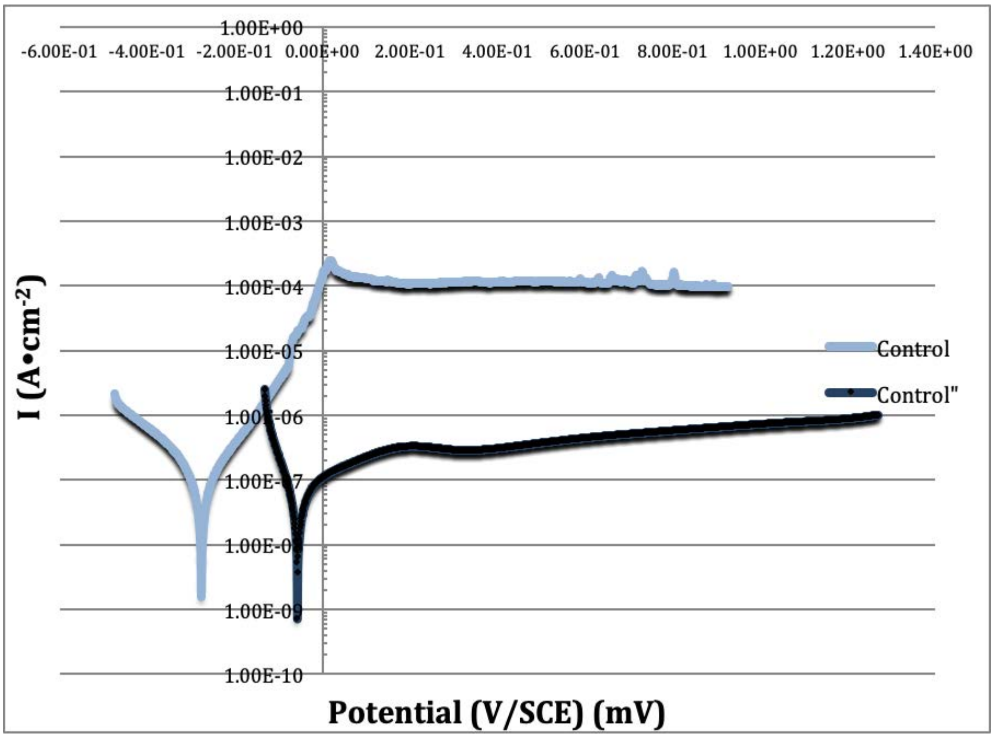

Figure 4.54 Potentiodynamic polarisation curve of as-ground control pre- and post-thermal oxidation.

Electrochemical corrosion: Ti64 vs Ti64”

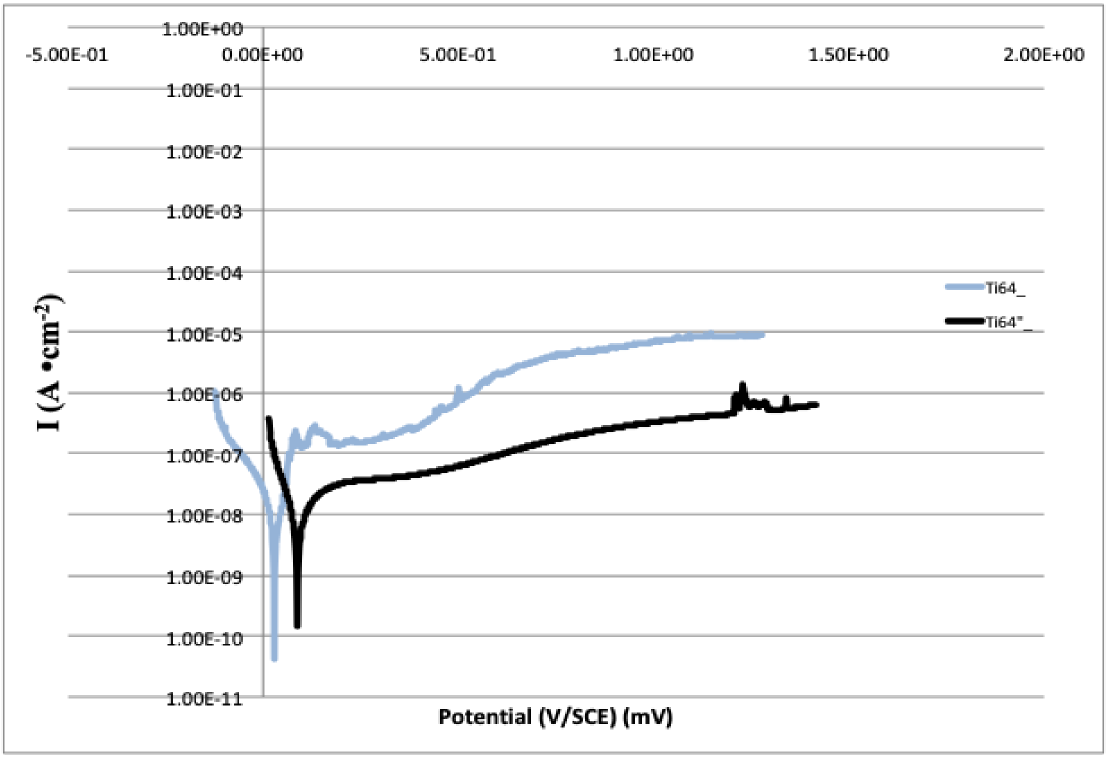

Figure 4.55 Potentiodynamic polarisation curve of Ti64 pre- and post-thermal oxidation.

Electrochemical corrosion: Ag0.2% vs Ag0.2%”

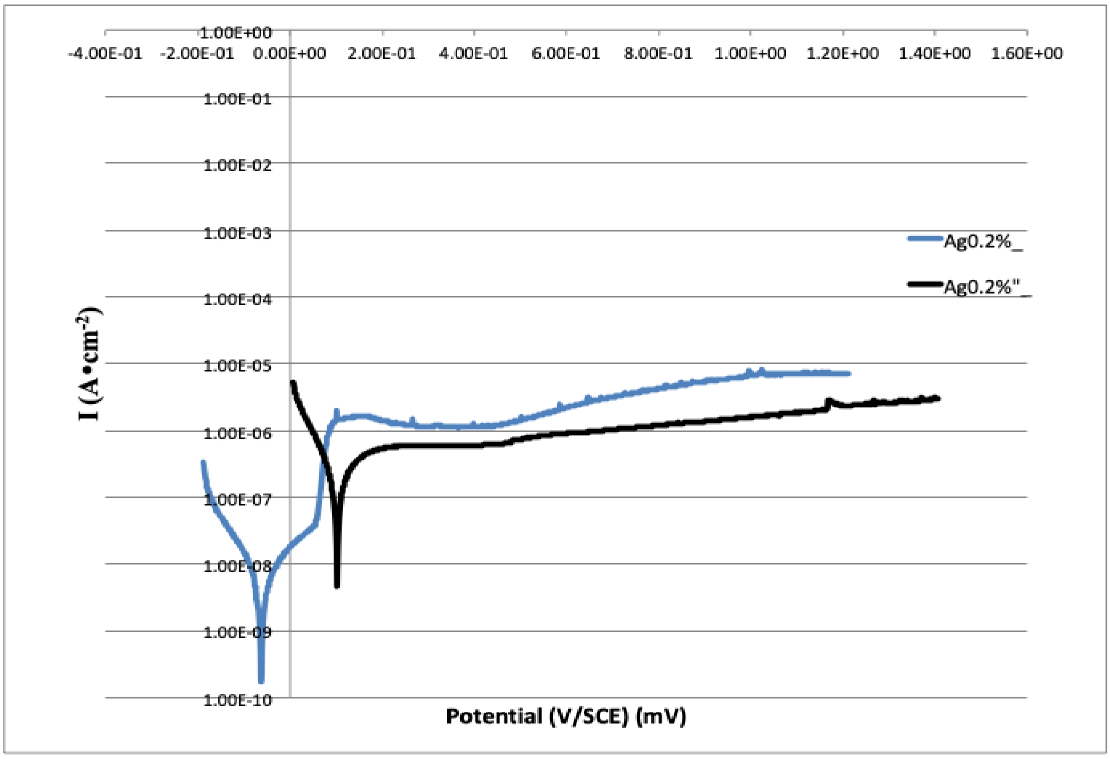

Figure 4.56 Potentiodynamic polarisation curve of Ag0.2% pre- and post-thermal oxidation.

Electrochemical corrosion: Ag1 vs Ag1”

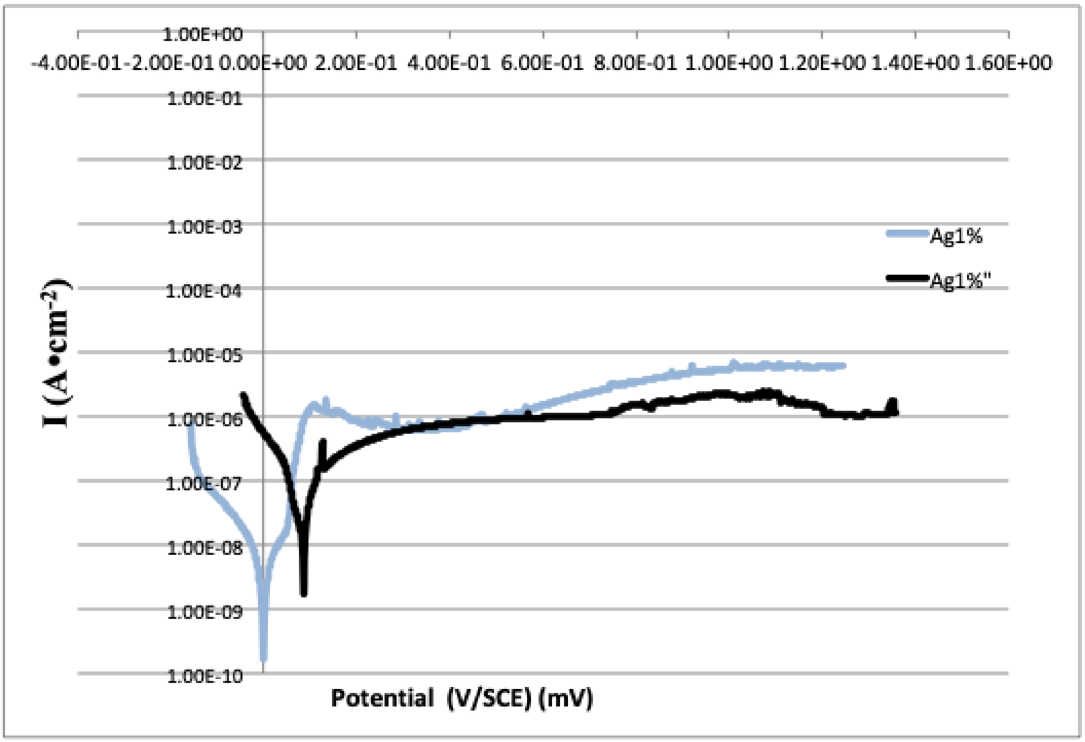

Figure 4.57 Potentiodynamic polarisation curve of Ag1% pre- and post-thermal oxidation.

Electrochemical corrosion: Ag5 vs Ag5”

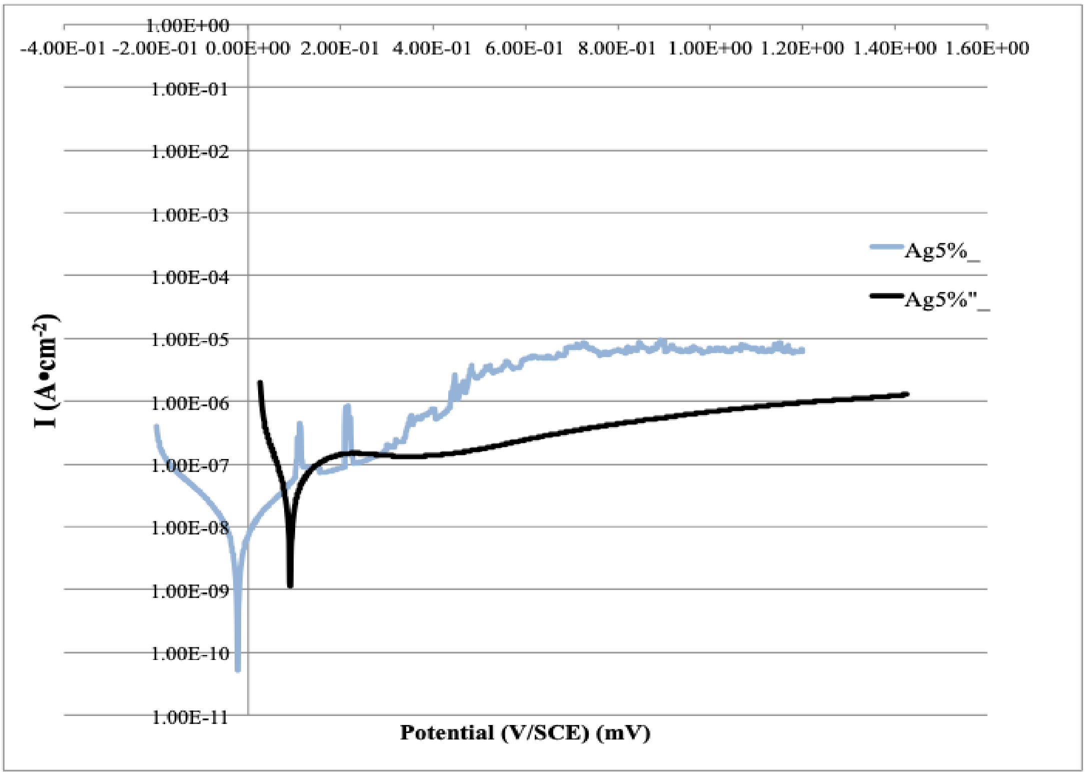

Figure 4.58 Potentiodynamic polarisation curve of Ag5% pre- and post-thermal oxidation.

SEM of samples post-electrochemical testing

SEM images of samples surfaces post electrochemical testing. Some images display the interface between the sample and the resin, whereby some crack growth were displayed.

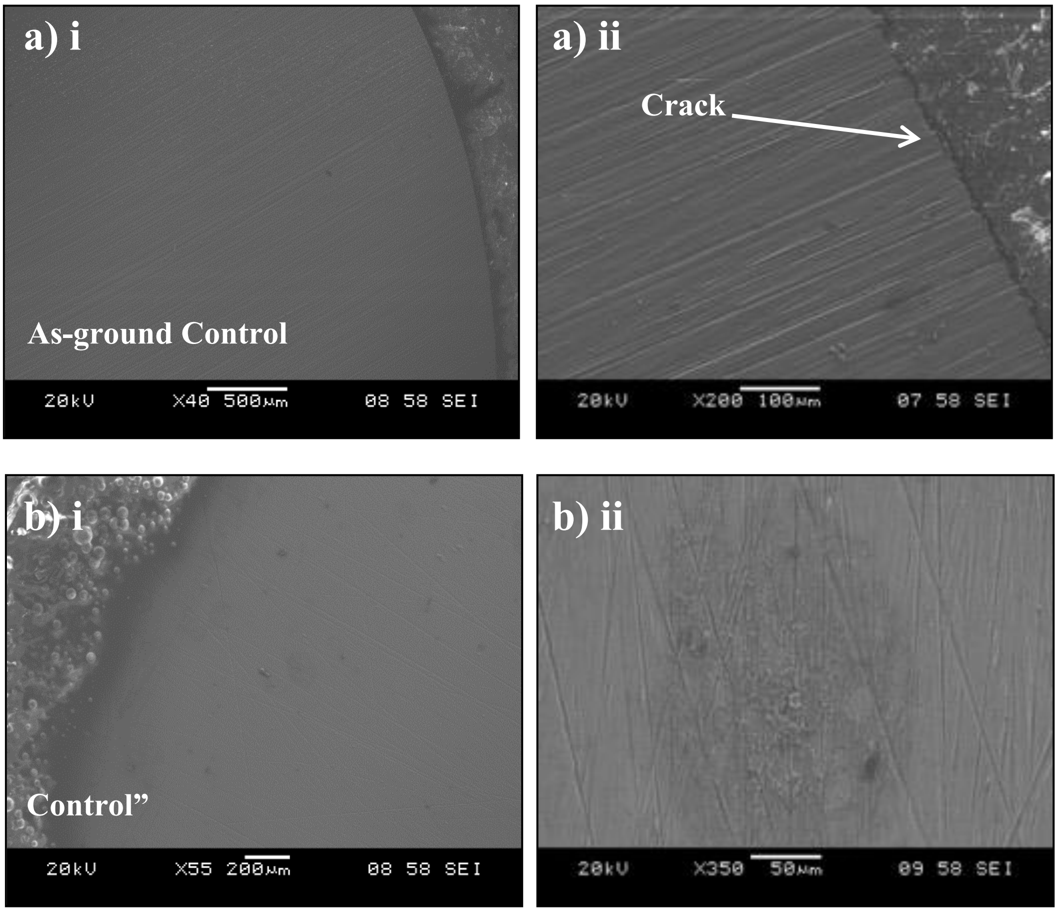

Figure 4.59 SEM surface images of control and thermally oxidised control after electrochemical testing. a (ii) demonstrates a crack between the sample and the resin. b (ii) demonstrates surface of titanium substrate with dehydrates salts from the Ringers solution on top.

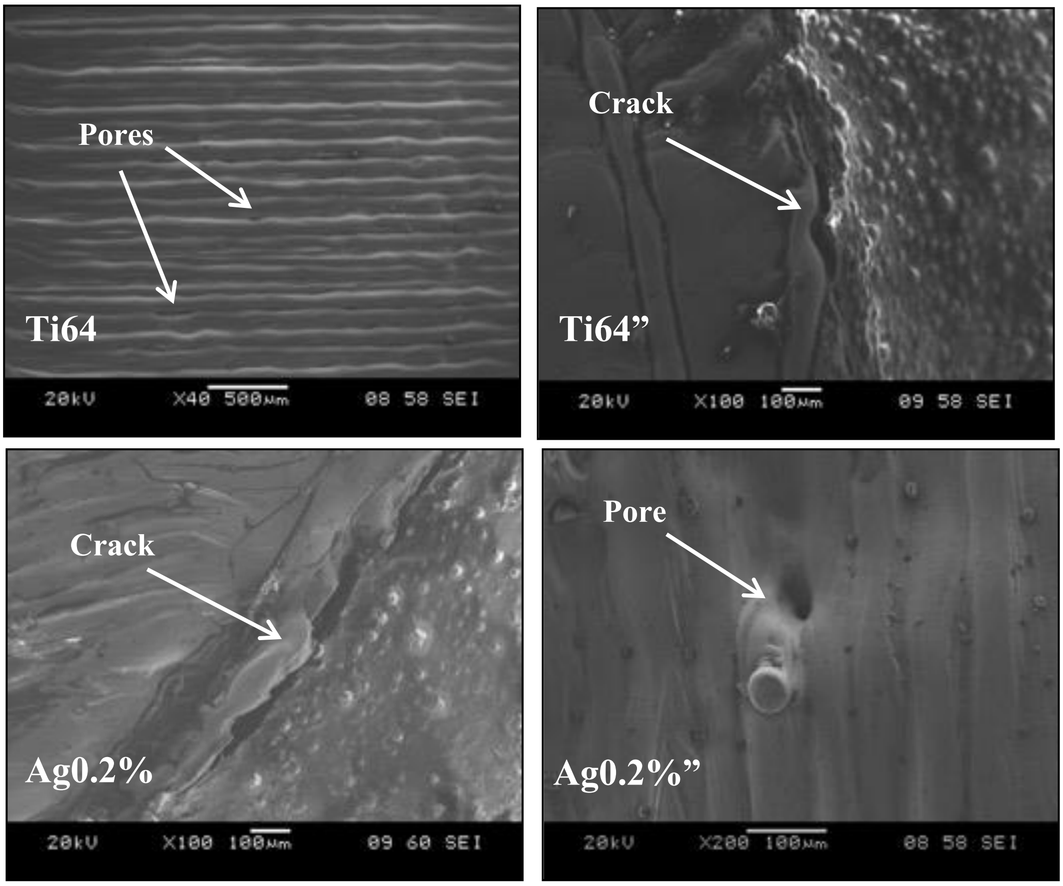

Figure 4.60 SEM surface images of control and thermally oxidised control after electrochemical testing.

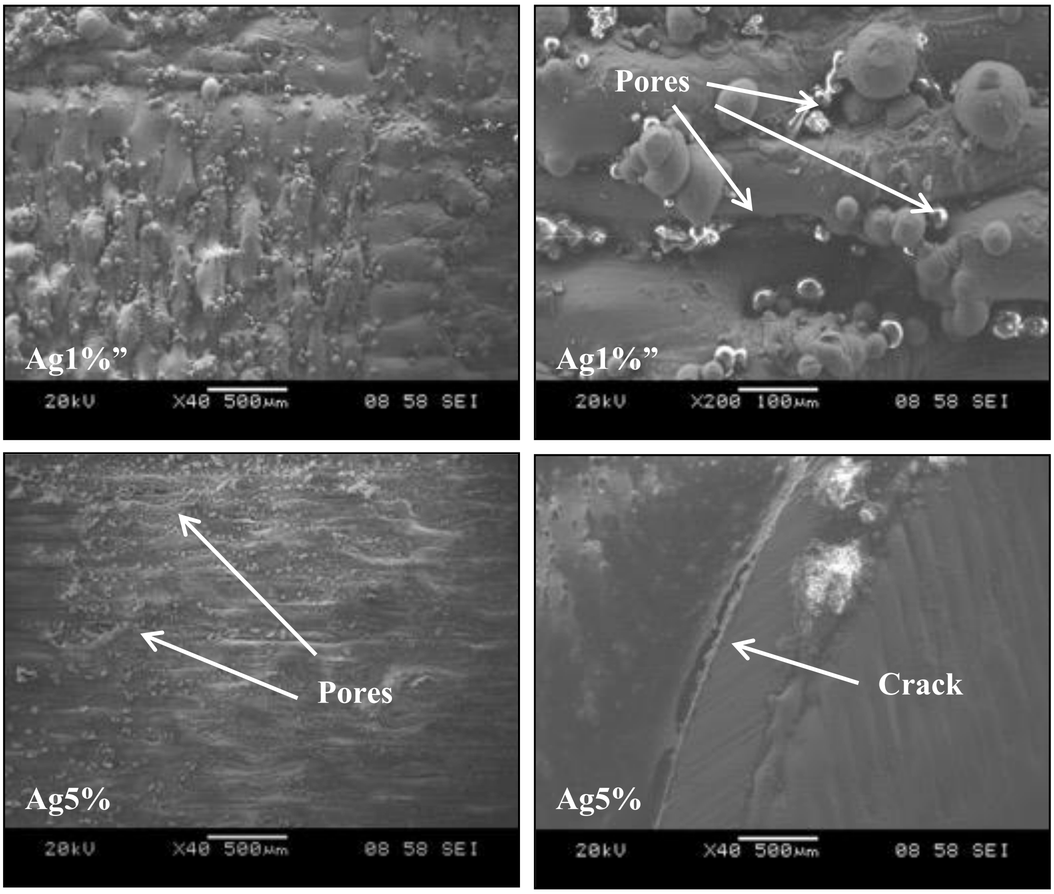

Figure 4.61 SEM surface images of control and thermally oxidised control after electrochemical testing.

The electrochemical corrosion studies were carried out by conducting potentiodynamic polarisation, to investigate the corrosion behaviour of the different sample batch types within Ringer's solution. With reference to Table 4-8, the as-ground control sample exhibited an i_{corr} (corrosion current density) ($x10^{-7}$) value of 19.7 ± 0.01, which decreased to 1.20 ± 0.01 after thermal oxidation. Alternatively, its E_{corr} (corrosion potential) ($x10^{-1}$) increased after thermal oxidation treatment from -2.65 ± 0.03 to -0.5 ± 0.01. This in turn relates to a decrease in the corrosion rate of the control" sample as a greater potential is required to initiate the corrosion of the material within Ringer's solution. Furthermore, Figure 4.54 displays the potentiodynamic polarisation curve for the as-ground control Vs its thermally oxidised counterpart (control"; it can be seen that in the anodic direction of the curve, passivation potential of the control" is lower than that of the as-ground control.

Additionally, a passive region is reached at a consistently lower current density. Aside from demonstrating a higher passivation potential and passive region, the as-ground control sample also demonstrated metastable pits, which repassivated. This could be explained by Figure 4.59 (a) ii which displays SEM surface analyses of the as-ground control and shows crack between the sample and resin interface where some of the Ringer's solution could have seeped in.

As for Ti64 samples, it presented corrosion density ($x10^{-7}$) of 1.96 ± 0.06 and an E_{corr} (10^{-1}) of 0.5 ± 1.93. After thermal oxidation treatment, i_{corr} ($x10^{-7}$) decreased to 1.92 ± 0.19 while the E_{corr} ($x10^{-1}$) increased to 1.04 ± 5.09, respectively. These results demonstrate that thermal oxidation of Ti64 resulted in a higher potential to initiate corrosion, thus the material became more corrosion resistance. With reference to Figure 4.55 the potentiodynamic curve of these samples (Ti64 Vs Ti64") shows that post- thermal oxidation, the passivation potential and passive region is decreased, rendering the sample less prone to corrosion. On both curves, metastable pits were recorded, which could be explained by Figure 4.60 that demonstrates SLM defect (i.e. pores) and cracks at the sample, resin interface. However, metastable pitting occurred at a much higher applied voltage for the post-thermal oxidation treated Ti64" than the as-SLMed Ti64.

Similarly, Ag0.2% revealed a lower i_{corr} ($x10^{-7}$) and higher E_{corr} ($x10^{-1}$) post-thermal oxidation, 18 ± 2.75 and 1.20 ± 2.55 from 110 ± 0.08 and -0.05 ± 4.13 pre-thermal oxidation, respectively. Likewise, to the Ti64 batch, Ag0.2% batch demonstrated a lower passivation potential and a high density of current in the passive region concluding the material became more corrosion resistant after oxidation. Moreover, metastable pits were also evident in Figure 4.56 thus upon further SEM analyses, boundary cracks and pores were found on the Ag0.2% and Ag0.2%" Figure 4.60. Once again, metastable pitting was delayed by the thermal oxidation treatment.

Ag1% sample batch also demonstrated improved corrosion resistance after undergoing thermal oxidation. Prior to the oxidation treatment, the samples presented i_{corr} ($x10^{-7}$) and E_{corr} ($x10^{-1}$) values of 100 ± 0.37 and 0.05 ± 1.26, respectively. After the treatment, the i_{corr} ($x10^{-7}$) decreased and E_{corr} ($x10^{-1}$) increased to 0.19 ± 0.21 to 1.05 ± 1.89, respectively. Thus, it is demonstrating that post-thermal oxidation the E_{corr} ($x10^{-1}$) lies at a higher potential thus rendering the material more corrosion resistant. Furthermore, the current density in the passive region was slightly lover with the Ag1%" than it non-oxidised counterpart. This can be seen in Figure 4.57 whereby additional metastable pits were apparent in both polarisation curves. This treatment type demonstrated the most metastable peaks, which could be explained by SEM analyses in Figure 4.61 that demonstrates the roughness and porous nature of the sample surface.

Lastly, Ag5% demonstrated current density ($x10^{-7}$) of 110 ± 0.05 prior to thermal oxidation, with an E_{corr} ($x10^{-1}$) of -0.21 ± 2.08. The current density reduced and the corrosion potential increased after thermal oxidation to 1.66 ± 0.71 and 0.98 ± 4.24, respectively. The passivation potential and passive region was a smoother transition in Ag5%" than Ag5% Figure 4.58, with the latter demonstrating metastable peaks which upon further SEM surface evaluation as shown in Figure 4.61 whereby cracks and pores were observed.

It can be concluded based on the above results that thermal oxidation treatment has ameliorated the corrosion tendency of all sample treatment types; accordingly, (Cao et al 2018) reported Ti6Al4V post-thermal oxidation demonstrated an increased corrosion potential with a decreased corrosion current density when tested within 0.9 wt.% NaCl solution (187). The researchers described that post-thermal oxidation, the TiO_2 rutile formed is a more thermodynamically stable structure, which acts a parting barrier between the substrate and the corrosive medium; consequently extending the time the corrosive medium encounters the substrate.

4.4 Mechanical and tribological performance

4.4.1 Cross-section nano-hardness measurements

Cross-section hardness measurements were taken of the bulk Ti6Al4V substrate, surface SLM surface layer post-thermal oxidation (SLM layer_TO), oxide layer formed on Ag1%” (Ag1%”_OL) and of the oxide layer formed on Ag5%” (Ag5%”_OL).

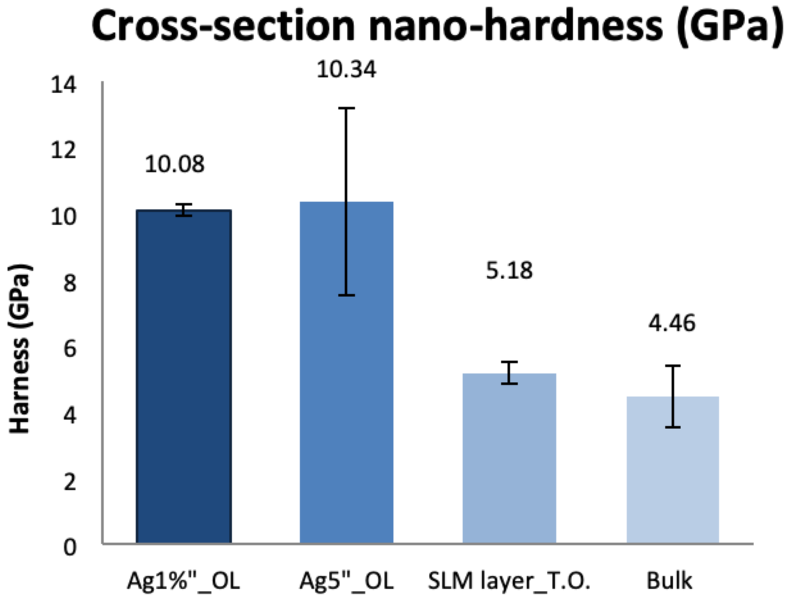

Figure 4.62 Average nano-indentation of cross-sectional hardness from the oxide layer (OL) to the bulk material.

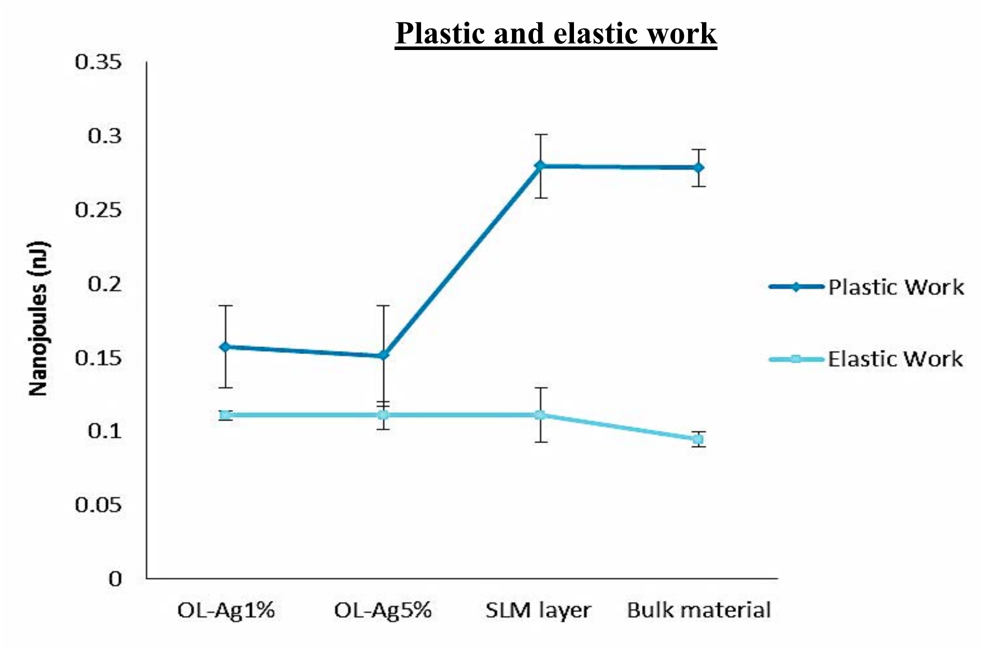

Figure 4.63 Average nano-indentation of cross-sectional plastic work and elastic work from the oxide layer to the bulk material. The plots are connected to better illustrate the relationship between the different batch types.

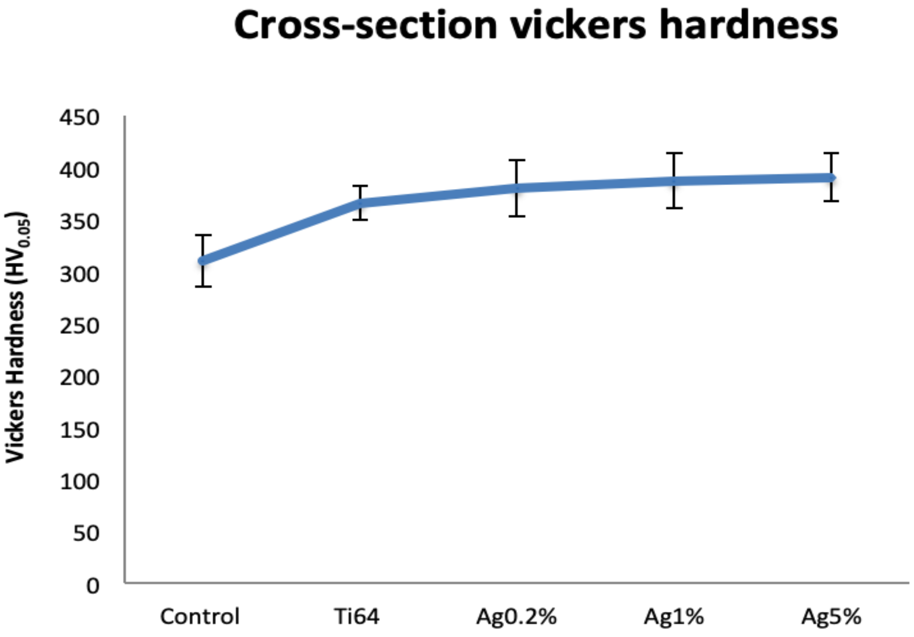

Figure 4.64 Cross-sectional Vickers hardness ($HV_{0.05}$) of samples pre-thermal oxidation. The plots are connected to better illustrate the relationship between the different batch types.

Cross-sectional nano-indentation hardness measurements of all batch types were tested at a load of 5 mN. The bulk Ti64 materials displayed a hardness (GPa) of 4.46 ± 0.93 and there was a slight increase of the hardness in the SLM bulk materials to 5.18 ± 0.33 Figure 4.62. Although the hardness difference is not significant if the experiment erros are taken into account, the slight increase average hardness could be related to the formation of self-quenching induced α' martensite see Figure 4.38.

However, the oxide layer hardness measured on the oxide layers of both Ag1% and Ag5% exhibited double the hardness (GPa) of the bulk or SLM layer, with values of 10.08 ± 0.18 and 10.34 ± 2.83, respectively. These values are in good agreement with the reported value of 10.5 ± 0.5 GPa (188). It seems that Ag has limited effect, if any, on the mechanical properties of the surface oxide layer.

Accordingly Figure 4.63 displays the plastic work and elastic work of the surface tested. The plastic and elastic work of the bulk materials and of the SLM layer were very similar with the bulk demonstrating lower elastic work (nJ), at 0.278 ± 0.026, 0.093 ± 0.01 and 0.278 ± 0.012, 0.094 ± 0.01, respectively. The oxide layer behaved similarly too, with Ag1% and Ag5% displaying plastic and elastic (nJ) work of 0.151 ± 0.03, 0.110 ± 0.01 and 0.157 ± 0.03, 0.111 ± 0.003, respectively. The plastic work of the oxide layers is much more lower than that of the bulk. Both the plastic and elastic work of Ag5%'s oxide layer was slightly lower.

Additionally, there was an increase in Cross-sectional Vickers Hardness measured at 0.05 kgf, on the SLMed layer with increasing Ag wt.% Figure 4.64. Ag5% demonstrated the highest hardness (GPa) value of 390.24 ± 22.89, followed by Ag1%, Ag0.2% and Ti64, 386.3 ± 26.61, 379.96 ± 27.24, 365.4 ± 16.25, respectively. The control demonstrated the lowest value of 309.54 ± 25.04. When these values are converted to GPa, they demonstrated of 3.03, 3.58, 3.73, 3.78, and 3.82 for the control, Ti64, Ag0.2%, Ag1% and Ag5%, respectively.

4.4.2 Coefficient of friction (CoF) measurements

Coefficient of friction (CoF) analysis was carried out on all samples conditions and treatment types.

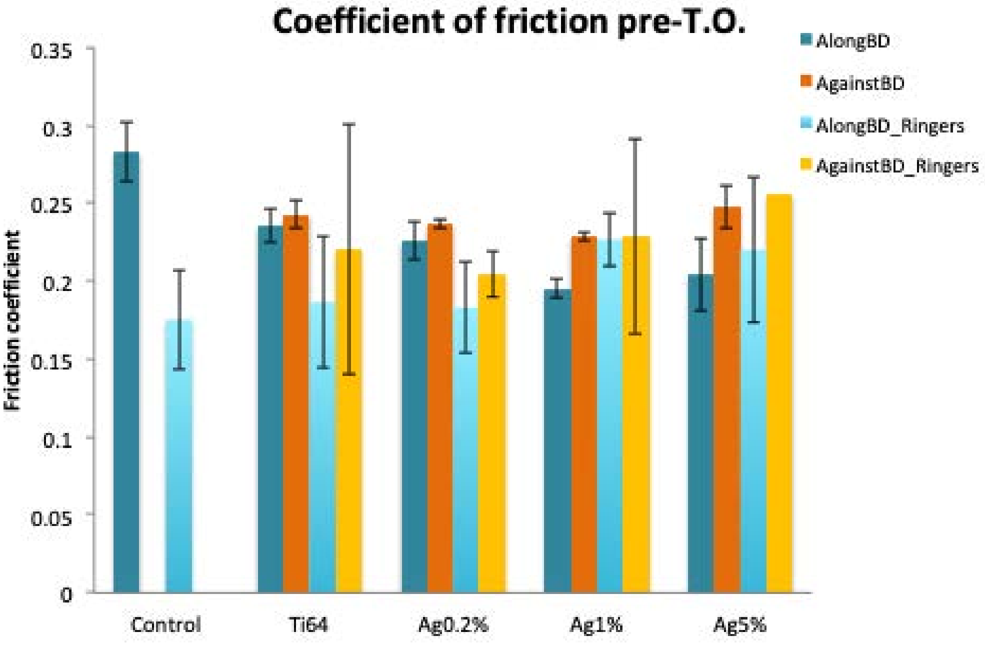

Figure 4.65 Coefficient of friction control and SLMed samples in air and Ringers

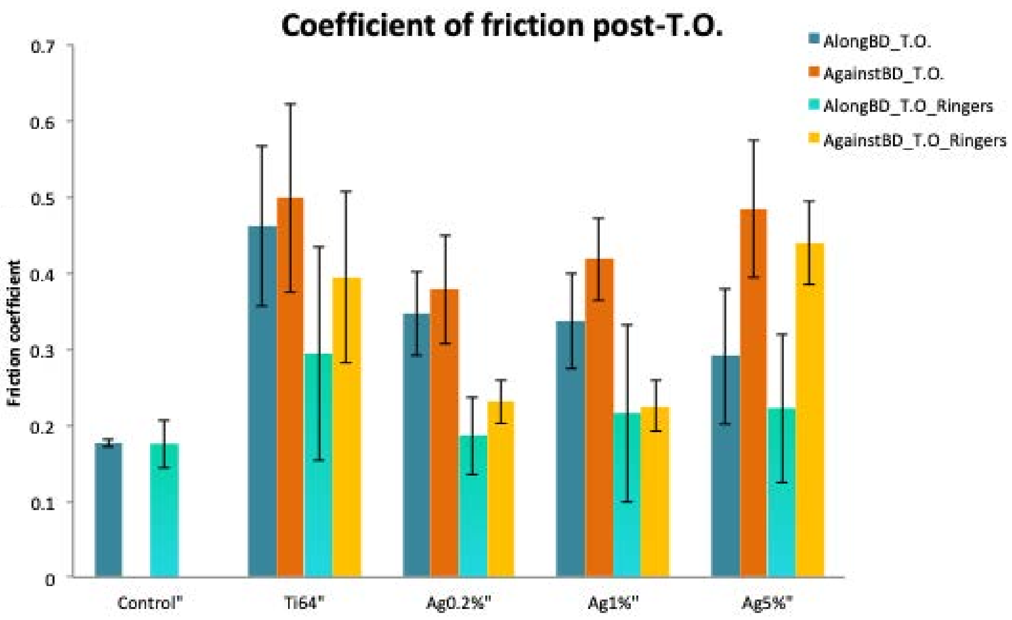

Figure 4.66 Coefficient of friction of control and SLMed samples post-thermal oxidation treatment in air and Ringer's solution.

The coefficient of friction (CoF) of the samples were measured using a load of 10 N and a tungsten carbide ball 8 mm in diameter along and against (perpendicular) the BD within air and with Ringer's solution at room temperature, at a track distance of 3 x 10^{-3} m, 1000 cycles at 5 mms^{-1}. CoF of the control sample decreased from 0.283 ± 0.02 when tested in air to 0.175 ± 0.03 when tested within Ringers solution Figure 4.65. The SLMed samples all demonstrated a greater CoF when tested against BD as opposed to along BD. Ti64, Ag0.2%, Ag1%, Ag5% all demonstrated values at 0.236 ± 0.01, 0.226 ± 0.01, 0.195 ± 0.01, 0.204 ± 0.02 along BD, respectively. These values increased to 0.243 ± 0.01, 0.237 ± 0.003, 0.229 ± 0.003 and 0.248 ± 0.02 against BD, respectively. The above observations indicate that the CoF is closely related to surface roughness as the roughness values decreased when measured along BD compared to against BD (Figure 4.19).

However, when tested within Ringer's solution, while the CoF of Ti64 and Ag0.2% demonstrated a decrease, the opposite is observed for samples containing relatively higher Ag content (i.e. Ag1% and Ag5%). Ag1% demonstrated values of 0.227 ± 0.02 and 0.229 ± 0.015, along and against BD within Ringers solution, respectively. The other sample batches, demonstrated the expected pattern of a greater decrease in CoF when tested along BD in Ringers than against BD. Ti64, Ag0.2%, Ag5% presented values at 0.187 ± 0.04, 0.18 ± 0.029, 0.22 ± 0.05, respectively. In a similar order to the batches previously mentions, against BD with Ringers values were 0.22 ± 0.22 ± 0.12, 0.21 ± 0.08, 0.255 ± 0.06. The above observations imply that while Ringers solution could play a lubricant role to reduce the CoF of Ti64 and Ag0.2%, negative effect on CoF was observed for the high Ag samples.

After thermal oxidation, the control sample demonstrated a lower CoF of 0.170 ± 0.005 when compared to that (0.283 ± 0.02) for the as-ground control without Ringers Figure 4.66. With Ringers, there was barely any change in the CoF after thermal oxidation at 0.175 ± 0.03.

With the SLMed sample batches that underwent thermal oxidation, all demonstrated a higher CoF values when measured against than along BD in both air and Ringers' solution. Ti64", Ag0.2%", Ag1%" and Ag5%" along BD were 0.467 ± 0.001, 0.346 ± 0.06, 0.336 ± 0.06, and 0.291 ± 0.09, respectively. When tested against BD, these values further increased to 0.498 ± 0.12, 0.379 ± 0.07, 0.418 ± 0.06, and 0.484 ± 0.09, respectively. With an increase in Ag wt. % there was an increase in CoF against the BD post-thermal oxidation. Within the Ringers' solution, the SLMed batches demonstrated a considerably lower CoF to its oxides counters parts tested in air. These values were reduced to 0.294 ± 0.14, 0.186 ± 0.05, 0.217 ± 0.17, and 0.223 ± 0.10, for Ti64", Ag0.2%", Ag1%" and Ag5%" along BD, respectively. As expected the CoF increased when tested against (perpendicular) to the laser BD, with the highest increase being with Ag5%" of 0.44 ± 0.05; an CoF value that was greater than is Ag5%" along BD without Ringers counter-part. The other batches, demonstrated an increased in CoF but not higher than their thermally oxidised counterparts without ringers. Ti64, Ag0.2%, Ag1% demonstrated values at 0.39 ± 0.11, 0.23 ± 0.03 and 0.225 ± 0.03, respectively. It is also evident with an increase in Ag wt. %, there is an decline in CoF when tested in air.

4.4.3 Wear-rates

The wear rate ($m^3N^{-1}m^{-1}$)of the different sample batches were tested pre- and post-thermal oxidation at two loads of 15 N and 30 N, using a Tungsten carbide (WC) 12 mm in diameter ball, at a track distance o 5 X 10^{-3} m for 1000 cycles at 5 mms^{-1} is compared in the figure below (Figure 4.67). It can be seen that the wear rate of all the samples increased with increasing the load from 15 N and 30 N, and that the post-thermal oxidation can effectively reduce the wear rate of all the samples tested.

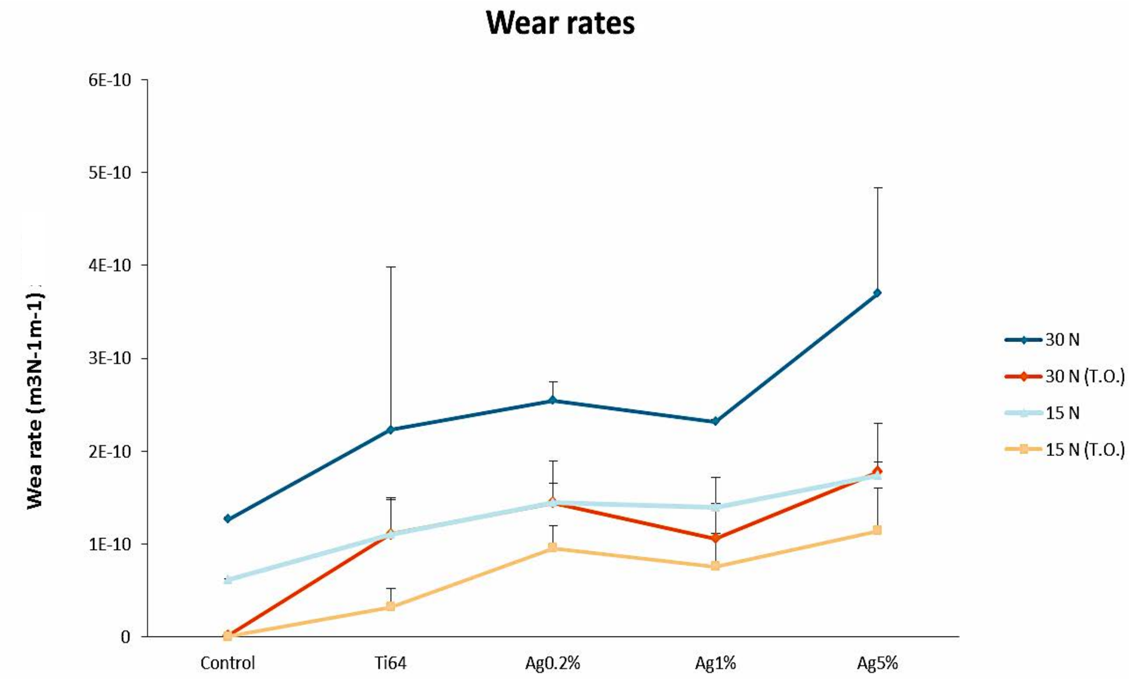

Figure 4.67 Average wear rates of all samples treatment types at 15 and 30 N pre and post-thermal oxidation. The plots are joined together to better illustrate the relationship between the different batch types.

Wear track at 15 N

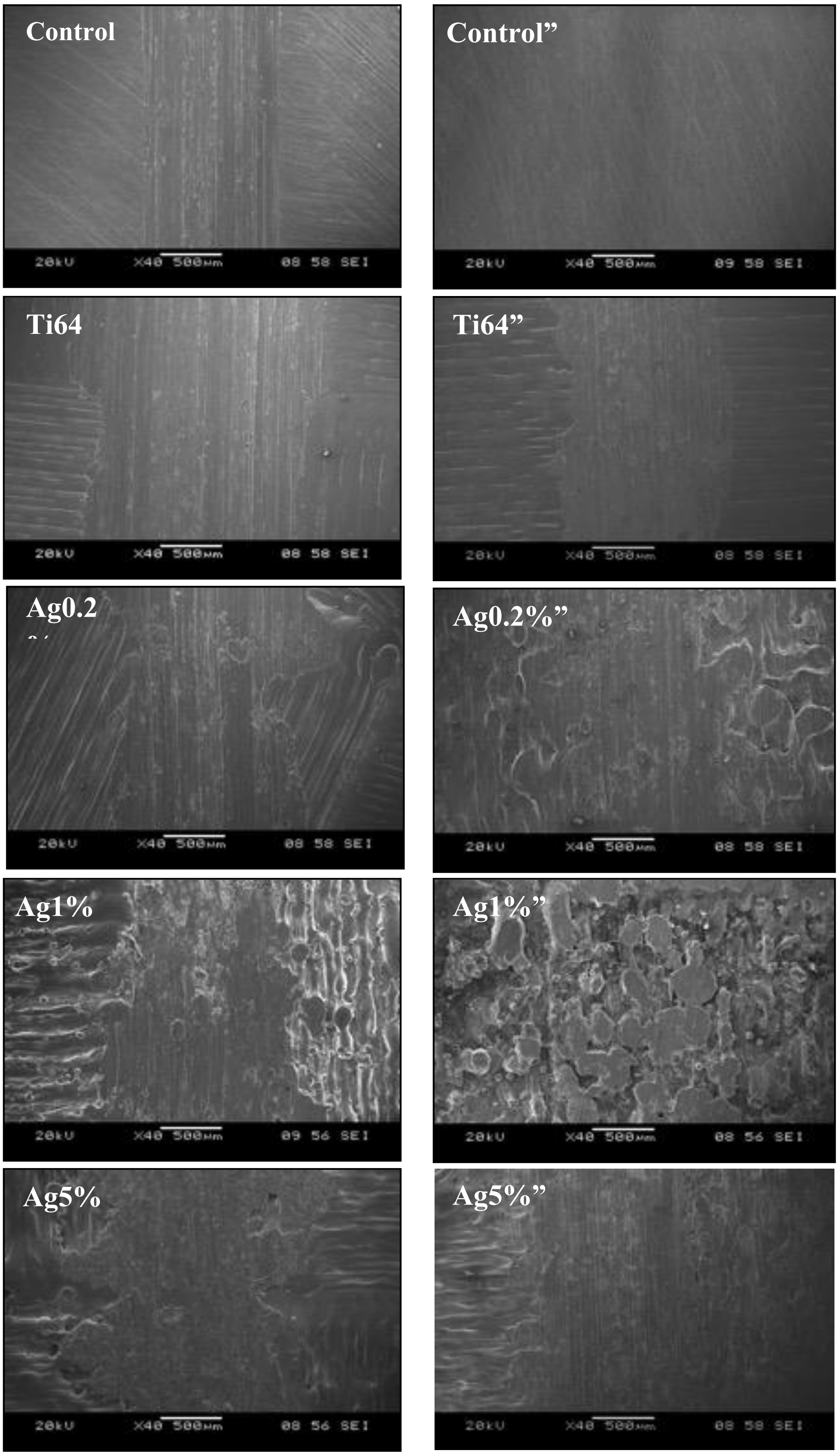

Figure 4.68 SEM surface morphology of wear tracks at a load of 15 N tested on all treatment types, pre and post-thermal oxidation.

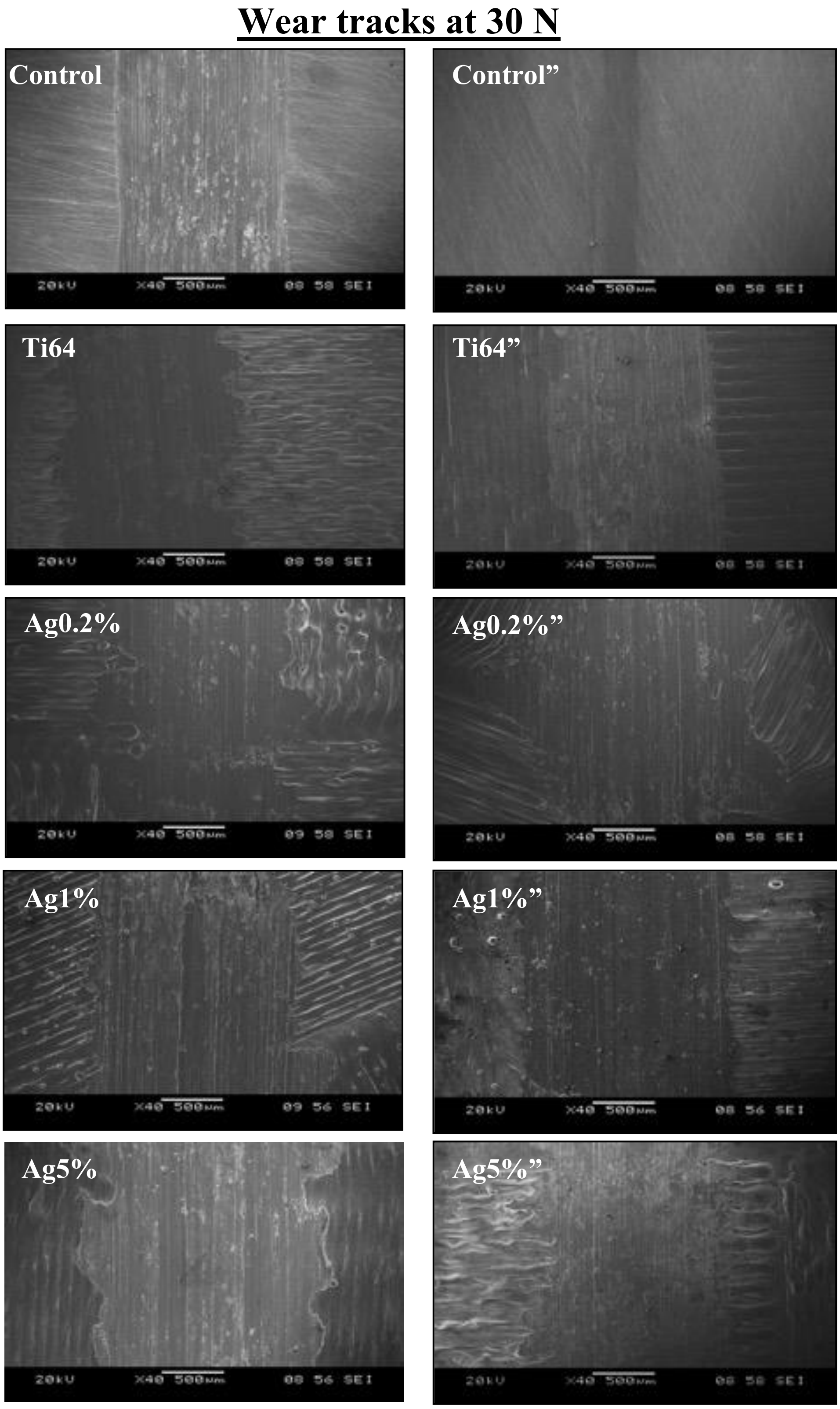

Figure 4.69 SEM surface morphology of wear tracks at a load of 30 N on all treatment types, pre and post-thermal oxidation.

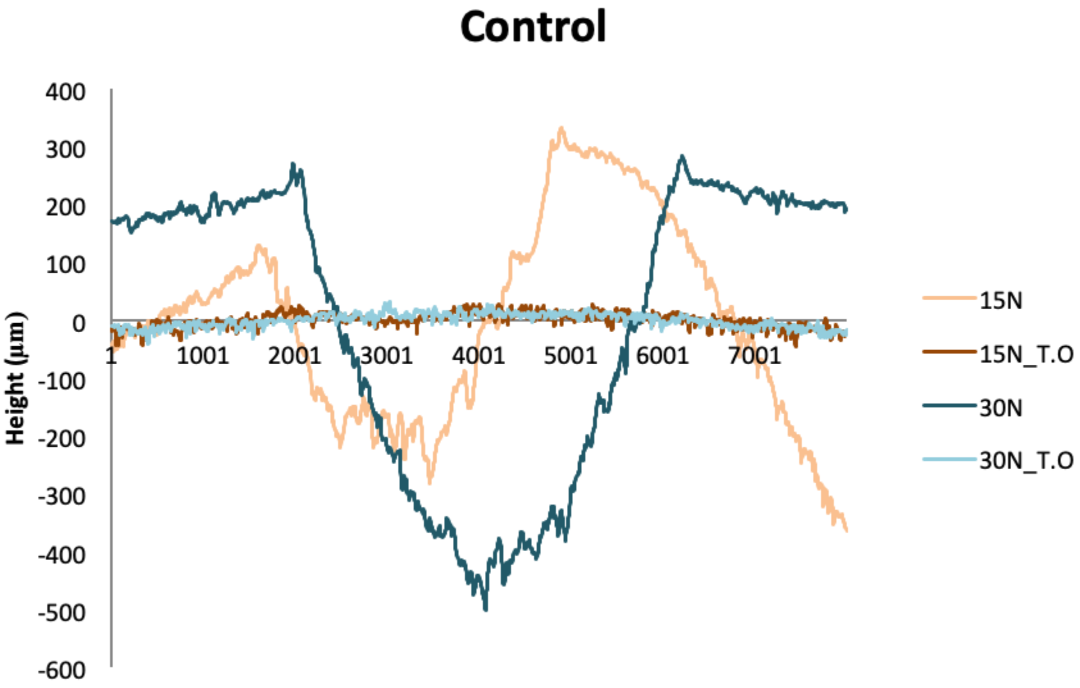

Figure 4.70 Cross-sectional wear track comparisons for control.

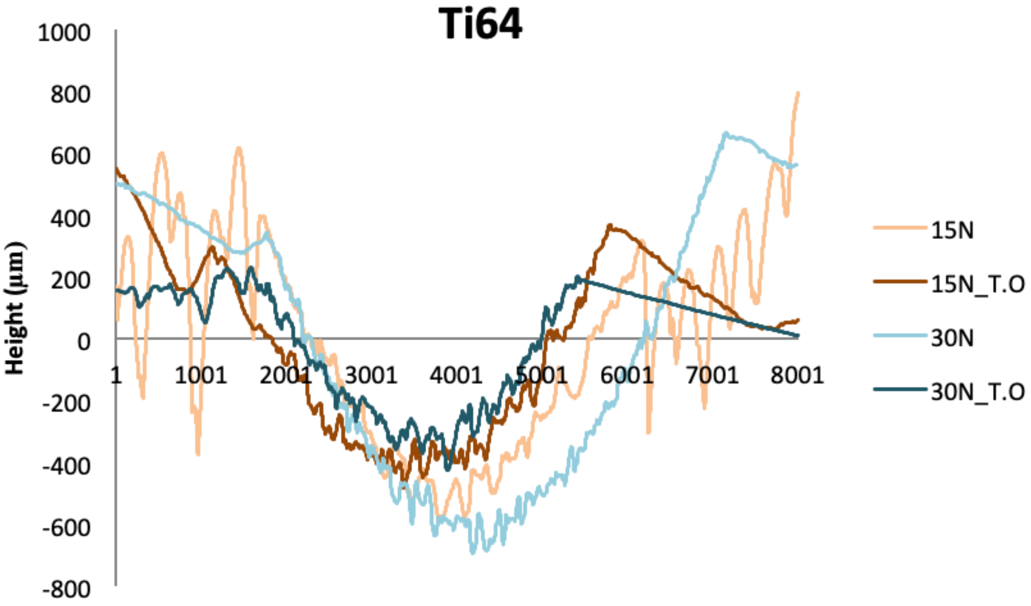

Figure 4.71 Cross-sectional wear track comparisons for Ti64.

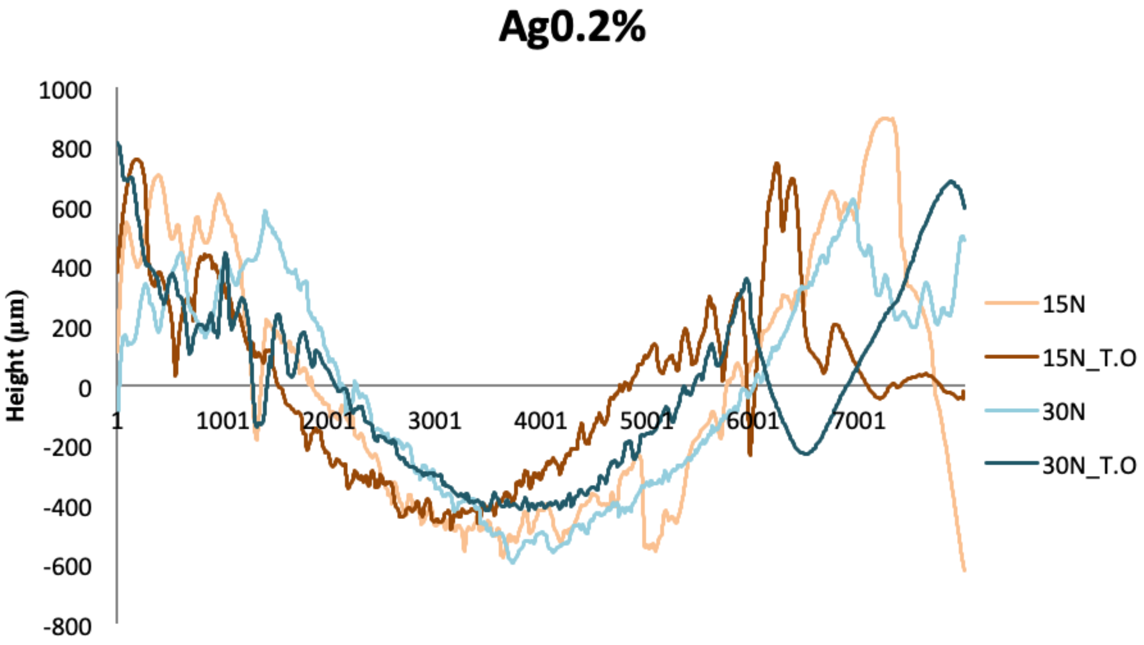

Figure 4.72 Cross-sectional wear track comparisons for Ag0.2%.

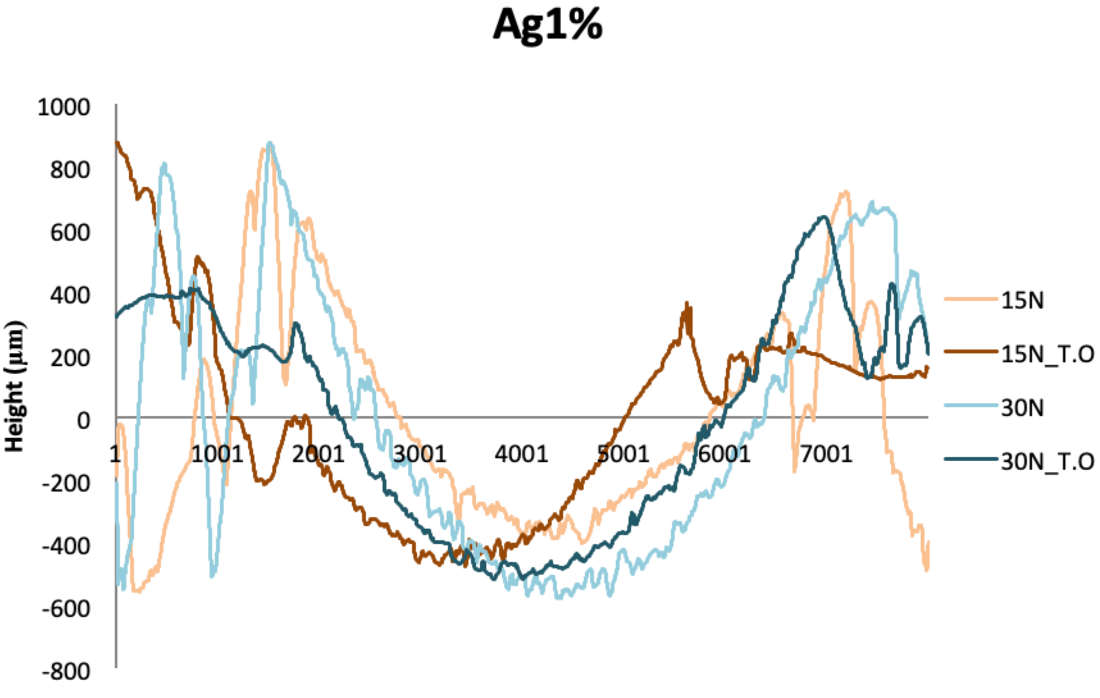

Figure 4.73 Cross-sectional wear track comparisons for Ag1%.

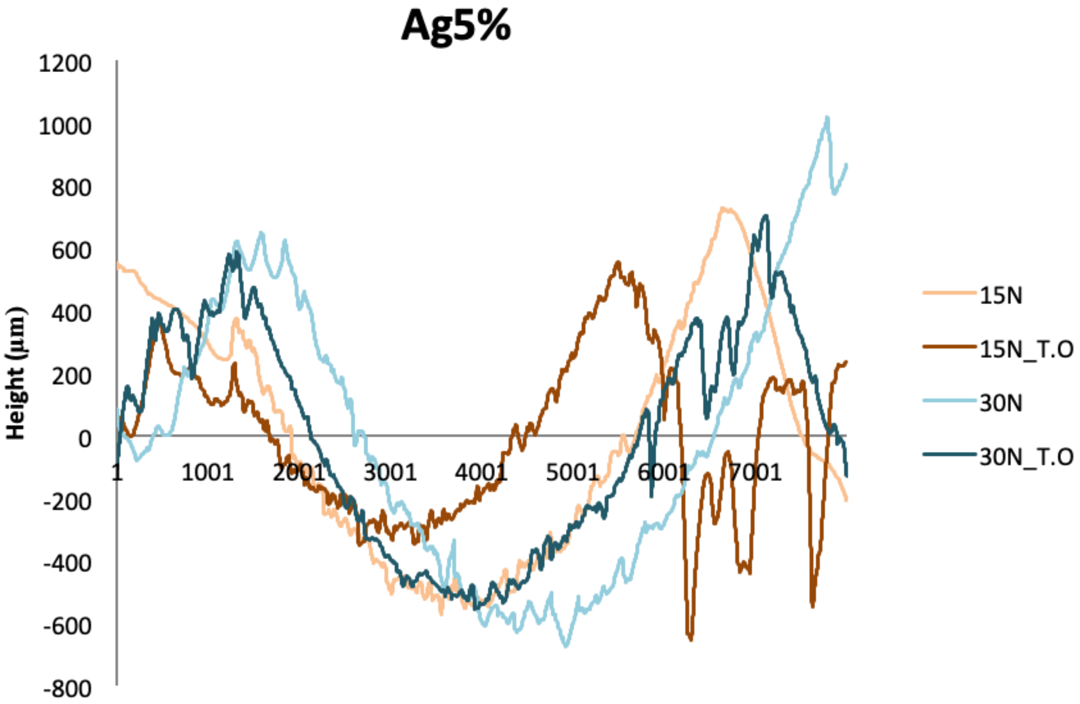

Figure 4.74 Cross-sectional wear track comparisons for Ag5%.

The comparison in the wear rate of the control pre- and post-thermal oxidation were evidently different for both loads Figure 4.67. After thermal oxidation the wear rate ($m^3N^{-1}m^{-1}$) decreased significantly to $3.37x10^{-13}$ ± 2.54 $x10^{-15}$ and to $1.38x10^{-12}$ ± 3.69 $x10^{-14}$ for 15 N and 30 N, respectively. These values were significantly reduced from $6.20x10^{-11}$ ± 6.43 $x10^{-13}$ and $1.27x10^{-10}$ ± 3.53 $x10^{-12}$, for 15N and 30N, respectively. With further analyses of Figure 4.68 and Figure 4.69 the differences in wear tracks can be seen. The as-ground control at both loads demonstrates severe wear as evidenced by the clear grooves and craters observed on the wear track surfaces (Figure 4.68 and Figure 4.69) and the fluctuations on the wear track profiles Figure 4.70. Therefore, two specific wear mechanisms may have operated during the wear process; strong adhesion or cold welding. These may have occurred between Ti64 and WC counter surfaces due to the lower hardness of Ti64, which consequently suffered severe plastic deformation; additionally, Ti demonstrates high chemical activity that leads to its strong tendency to adhesion. The relative motion of the WC ball caused peeling of debris (delamination of material) from Ti surface and thus bits of materials are removed by surface adhesion to the WC ball. This is evidenced by the white craters observed especially, from the wear tracks formed under a high load of 30N (Figure 4.69). The transferred Ti on the WC was worked hardened and acted a 3rd body debris which is an abrasive to form the observed parallel grooves, on the wear tracks (Figure 4.68 and Figure 4.69). In comparison the wear tracks formed on the pos-thermal oxidation treated samples are much smoother and narrower, and indeed the wear track can hardly be detected from the wear track profiles (Figure 4.70). This significantly reduced wear by two orders of magnitude should be attributed to the rutile oxide layer.

XRD analyses conducted to examine the crystalline phases present on the surface of the samples pre- and post-thermal oxidation treatment and Ag alloying XRD analyses conducted to examine the crystalline phases present on the surface of the samples pre- and post-thermal oxidation treatment and Ag alloying Figure 4.33. The wear rates ($m^3N^{-1}m^{-1}$) for as-SLMed Ti64 pre- and post-thermal oxidation were 1.09 x 10-10 ± 3.97 x 10^{-11}, 2.22 x 10^{-10} ± 1.75 x 10^{-10}, 3.23 x 10^{-11} ± 10.96 x 10^{-11} (15N_TO) and 11 x 10^{-10} ± 3.75 x 10^{-11} (30N_TO), respectively. Both wear rates reduced, therefore improved post-thermal oxidation. It is clear from Figure 4.67 that the wear rates of SLMed Ti64 is higher than that of the control under both 15N and 30N; this is also true even after thermal oxidation, although thermal oxidation can effectively reduced the wear of the SLMed Ti64.

These results were supported by examining the tracks in terms of wear morphologies (Figure 4.68 and Figure 4.69) and wear track profiles Figure 4.71. Compared with the wear tracks formed on the control samples, the wear track formed on SLMed Ti64 surfaces was much wider although both are characterised by sever adhesive wear. This could be attributed to the significant increase in surface roughness as an outcome of the laser process. For the thermally oxidised Ti64" samples, wear track demonstrated very fine parallel wear grooves that can clearly be observes in Figure 4.68 and Figure 4.69. This could be explained by the mechanism typical for thin hard coatings on rough surfaces. Whereby the WC ball slid on the Ti64" surface, stress concentrated and cracking in the thin and hard TiO_2 layer at the peaks of the asperities occurred; the wear hard debris of TiO_2 oxide would act as abrasives and produce fine parallel wear grooves this leading to abrasive wear.

With the addition of Ag to the as-SLMed samples, except Ag1%, the wear rate of the other two Ag containing samples (Ag0.2% and Ag5%) increased when compared to as-SLMed Ti64 (with no Ag). Ag1% performed the bet with the lowest rates in comparison to Ag0.2% and Ag5% under similar treatment and test conditions.

Firstly, at a load of 15N prior to thermal oxidation, Ag1% exhibited a wear rate ($m^3N^{-1}m^{-1}$) of $1.39x10^{-10} \pm 3.277x10^{-11}$, closely followed by Ag0.2% at $1.44x10^{-10} \pm 2.05x10^{-11}$ and lastly Ag5%" with $1.73x10^{-11} \pm 1.45x10^{-11}$. Compared with the wear rate of as-SLMed Ti64 ($1.09x10^{-10} \pm 3.97x10^{-11}$), the wear rate of all threes Ag containing samples is generally, higher but the difference is not significant if the experimental errors are taken into account. This is supported by the observation of their wear track morphologies. As shown in Figure 4.68 and Figure 4.69, the wear tracks of the as-SLMed samples are all characterised by severe plastic deformation and adhesion. However, the Ag containing samples showed more severe adhesive wear.

It is commonly believed that Ag is a solid lubricant and could be used to reduce friction and wear of most materials. However, it should be indicated that the maximum solid solubility of

Ag in Ti has been reported to be 10.3 wt.% (189), hence Ag should exists in solid solution of Ti and Ag. This has been confirmed by XPS studies that either pure Ag not Ti-Ag intermetallic (Ti_2Ag and TiAg) could be identified (Figure 4.34).

When the load was increased to 30N, a significant increase in wear rate was observed, which was also evident in the Figure 4.69 SEM wear track images. More severe adhesion and plastic deformation of the material surface occurred when compared with the 15N tested surfaces. Among all the as-SLMed samples, at 30N, Ti64 performed the best, closely followed by Ag1% with values of $2.28x10^{-10} \pm 1.74x10^{-10}$, and $2.31x10^{-10} \pm 1.05x10^{-12}$, respectively. Figure 4.69 displays the plastic deformation and adhesive wear mechanism that occurred in both Ti64 and Ag1%. Ag0.2% presented wear rates of $2.54x10^{-10} \pm 1.93x10^{-11}$, while Ag5%" performed the worst with the highest wear rate of $3.69x10^{-10} \pm 1.13x10^{-10}$. Figure 4.68, the wear track of Ag5% displays very different wear track morphology as evidenced by the large contrast between the wear track and the adjacent surfaces. The relatively dark surface layer seemed to have been removed. This is most probably that under 30N severe adhesive wear occurred to the Ag5% sample and the wear debris was smeared onto the surface and work hardened by the reciprocating sliding of the WC ball. Due to the relatively rough and thin built layer (Figure 4.37) the contact stress could reach the interface between the SLMed layer and the substrate. Under the repeated alternating shear stress, cracks would initiate and propagate along the interface. Eventually, the surface layer was delaminated from the surface via delaminate wear mechanism (190).

However, after the thermal oxidation treatment the wear rate significantly reduced, especially for Ag1%" sample. Among all the post-thermal oxidation treated as-SLMed samples, Ti64" and Ag1%" demonstrates similar wear rates of $1.10x10^{-10} \pm 3.74x10^{-11}$ and $1.05X10^{-10} \pm 5.51X10^{-12}$, respectively. Ag1%" marginally performed better than the Ti64" batch type. The

Ag1%” displays wear that occurred on the peask and asperities of the highest grooves and features of the surface. At 30N post-thermal oxidation, Ag0.2%” outperformed Ag5%” with wear rates of $1.44x10^{-10} \pm 44.4x10^{-11}$ and $1.77x10^{-10} \pm 5.19x10^{-11}$. However, it should be pointed out that post-thermal oxidation can effectively address the severe delamination wear of the Ag5%” sample mainly due to the reduced adhesion tendency of Ag5%” sample due to the formation of a rutile layer. Wear track profile can also be seen Figure 4.70 to Figure 4.74, and for each one, the thermally oxidised treated samples outperformed its counterparts.

4.5 Microbiological behaviour

4.5.1 Antimicrobial test

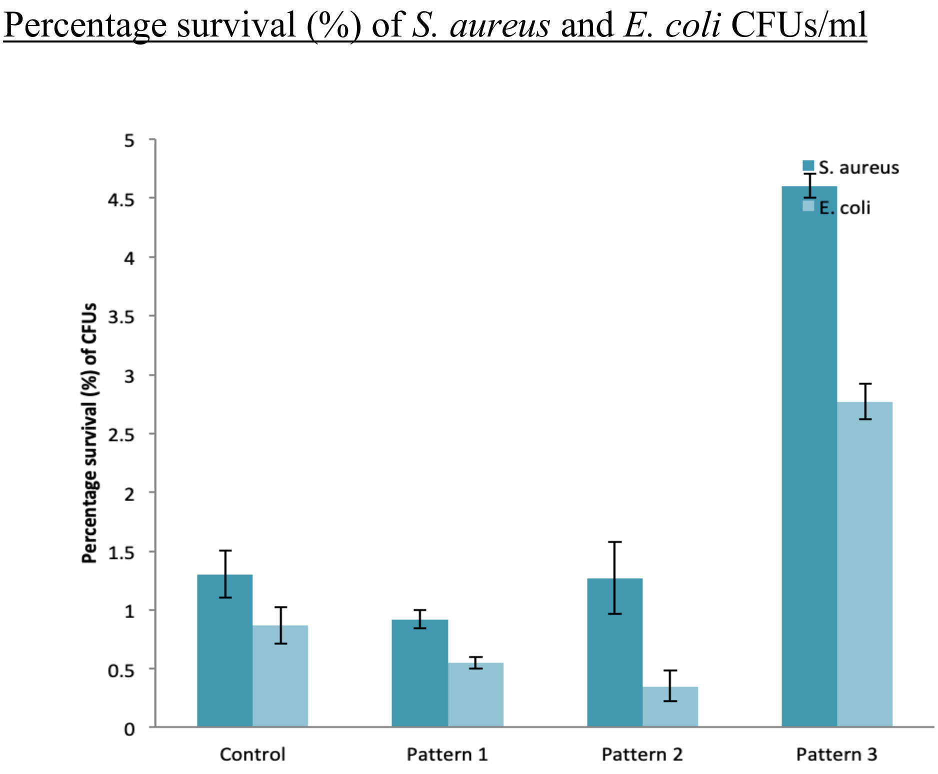

Figure 4.75 Percentage *S. aureus* and *E. coli* bacterial survival attachment of CFUs/ml on the surface of as-polished control and SLMed patterns 1, 2 and 3.

Percentage survival (%) of *S. aureus* and *E. coli* CFUs/ml

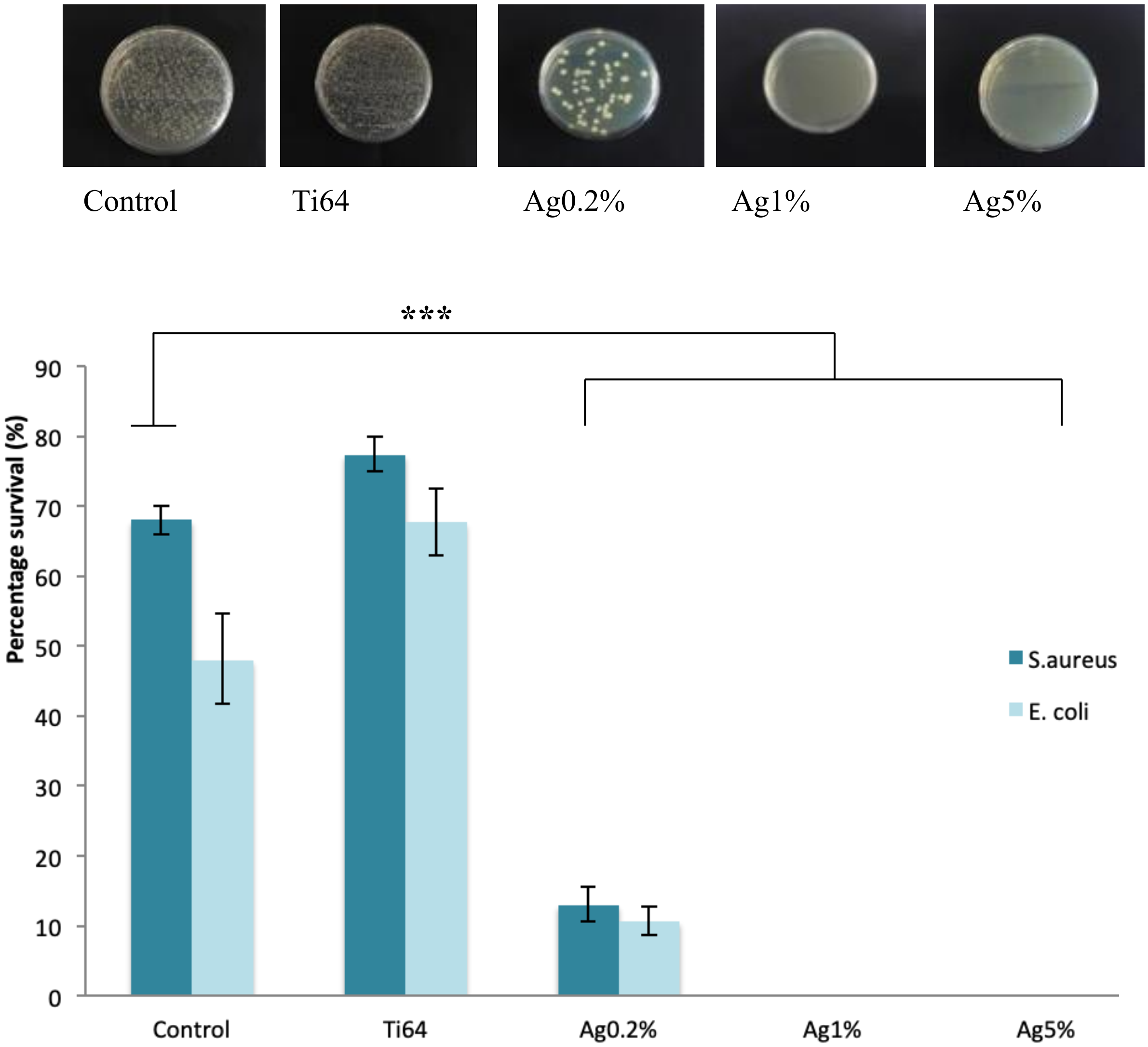

Figure 4.76 Percentage *S. aureus* and *E. coli* bacterial attachment of CFUs/ml on the surface of as-ground control and SLMed samples. *** P values of < 0.001.

LIVE/DEAD STAINING

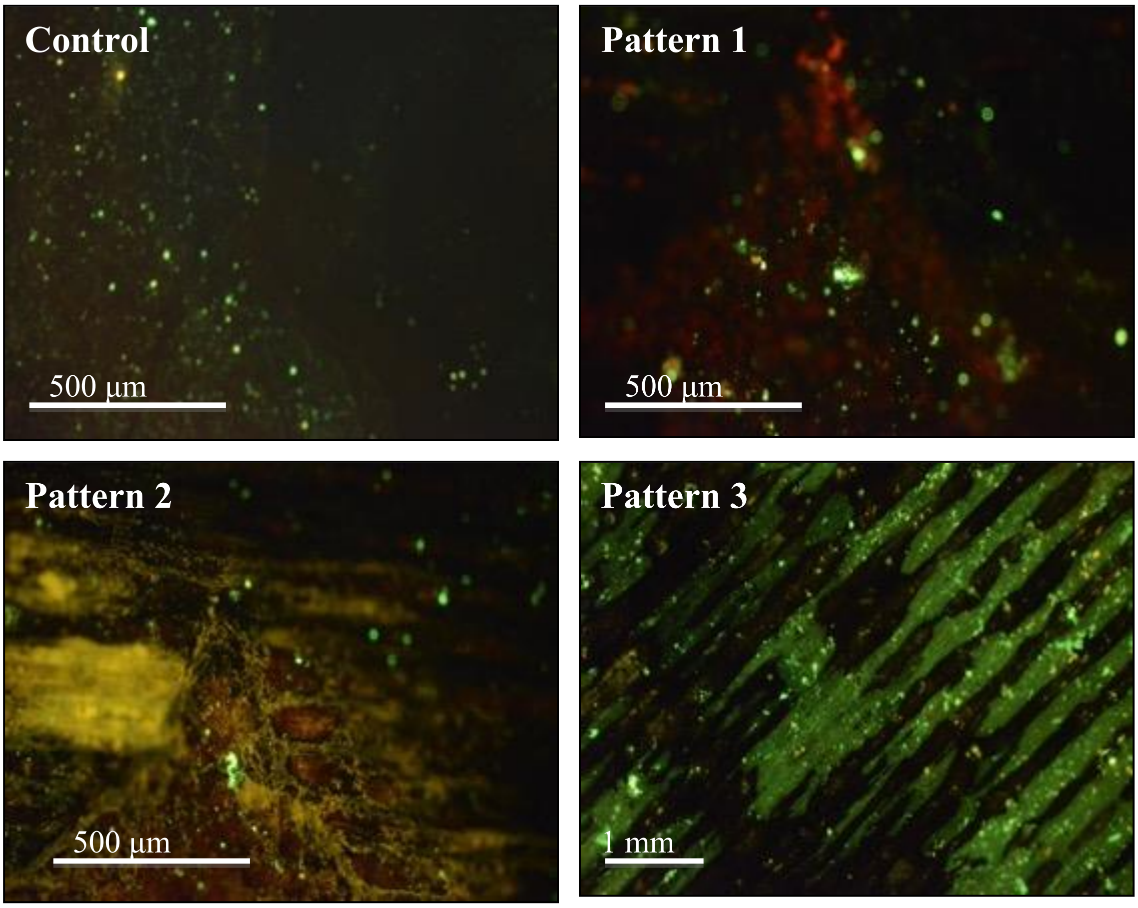

Figure 4.77 Live/dead staining of as-polished control, Pattern 1, Pattern 2 and Pattern 3. Green are live bacteria while red are dead.

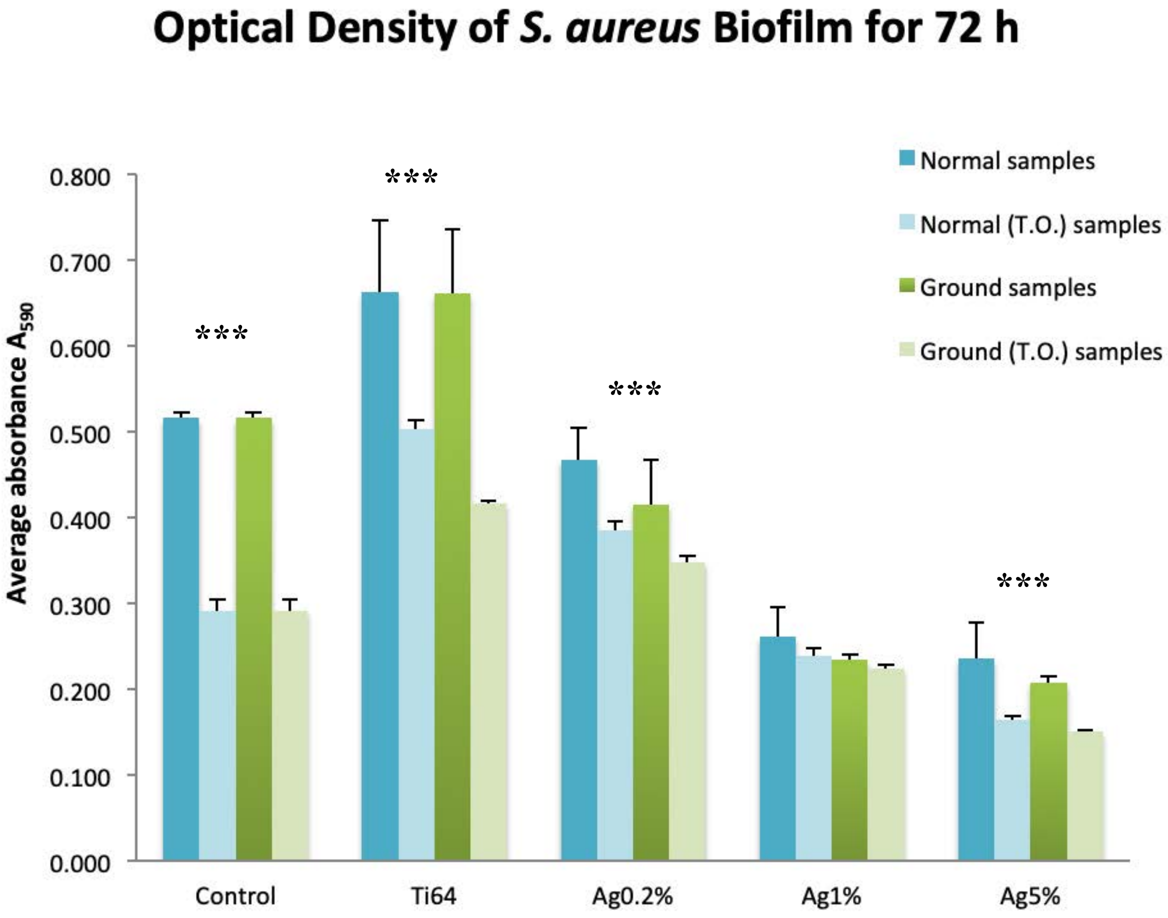

Figure 4.78 The optical density of a biofilm formation test during 72 h using S. aureus for control and SLM'ed sample treatment types pre and post-thermal oxidation, including each sample's ground counter part. *** P values < 0.001.

Control

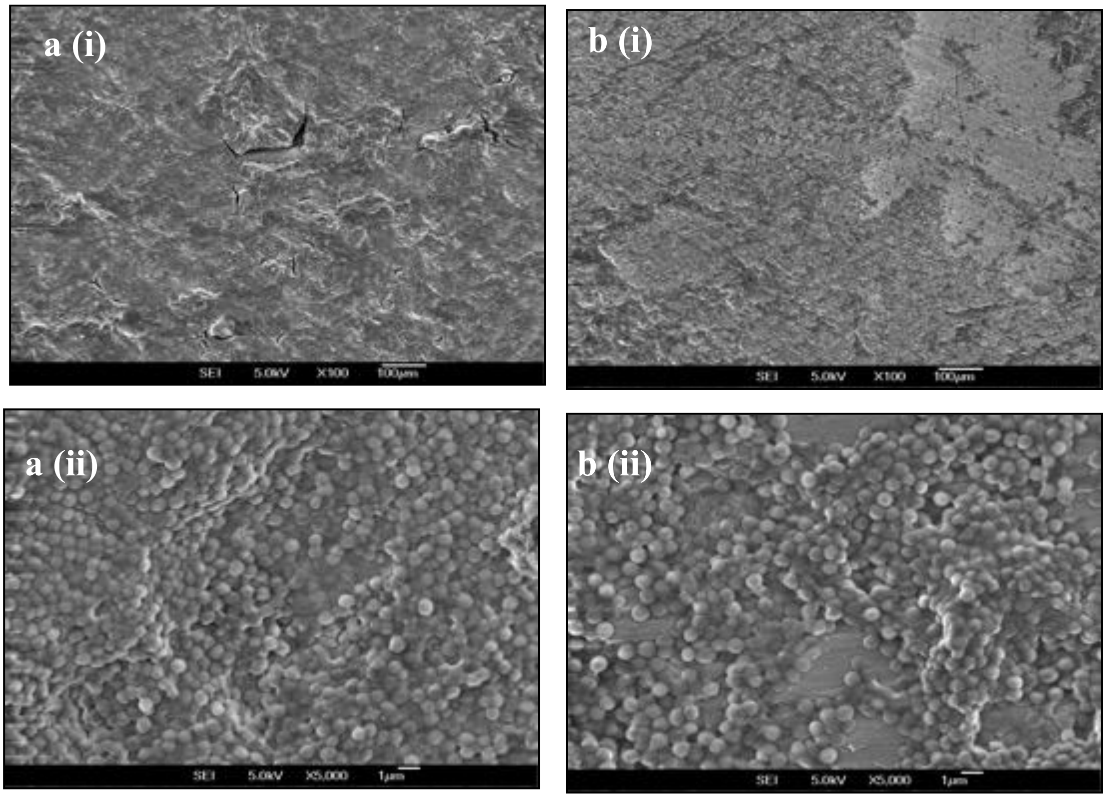

Figure 4.79 SEM surface images control pre-thermal oxidation a (i) and a higher mag image a (ii), and post-thermal oxidation b (i) and a higher image b (ii). The biofilm test was conducted using *S. aureus* for 72 h.

Ti64

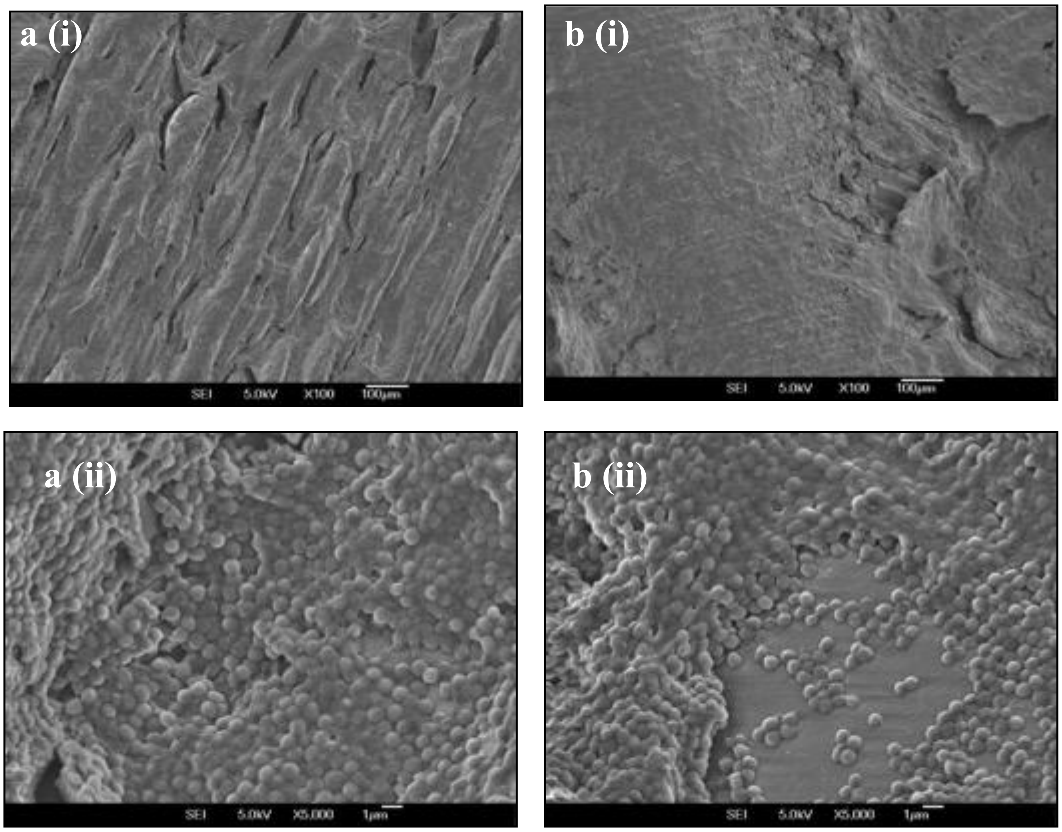

Figure 4.80 SEM surface images Ti64 pre-thermal oxidation a (i) and a higher mag image a (ii), and post-thermal oxidation b (i) and a higher image b (ii). The biofilm test was conducted using *S. aureus* for 72 h.

Ag0.2%

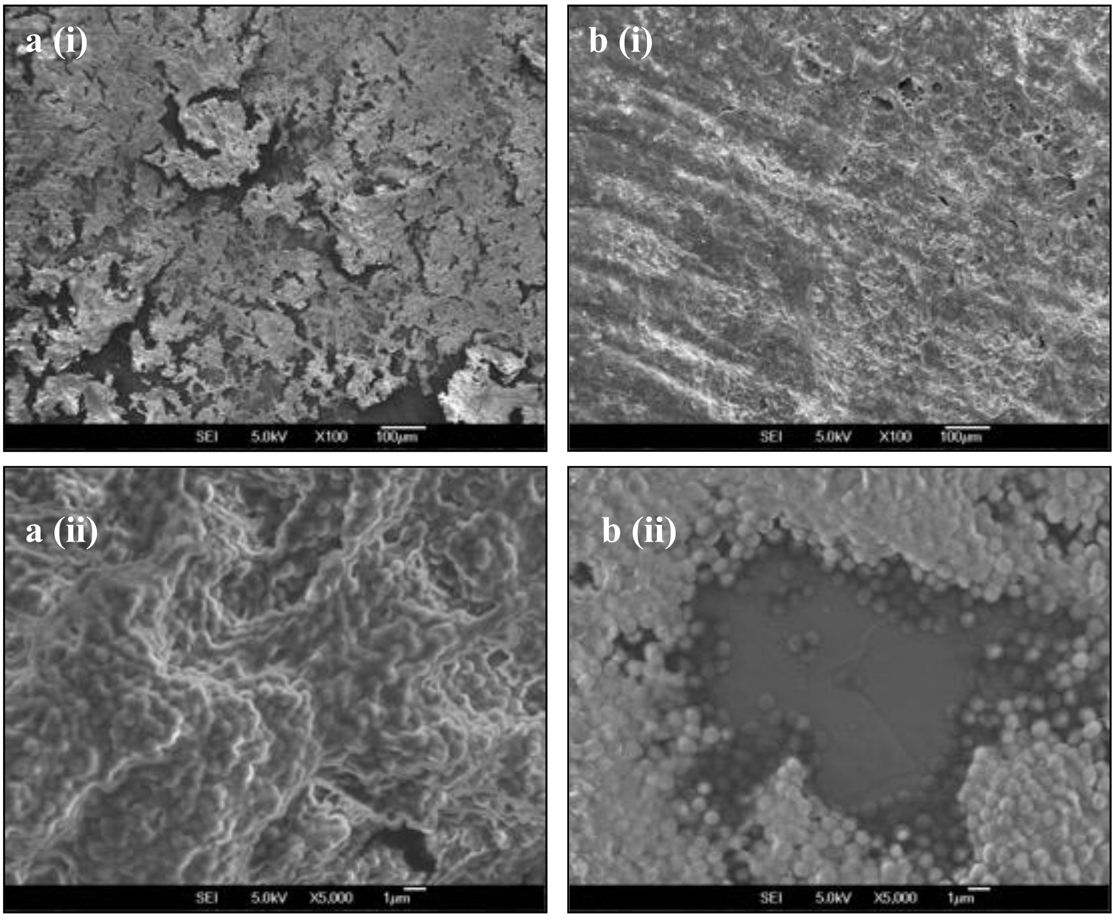

Figure 4.81 SEM surface images Ag0.2% pre-thermal oxidation a (i) and a higher mag image a (ii), and post-thermal oxidation b (i) and a higher image b (ii). The biofilm test was conducted using *S. aureus* for 72 h.

Ag1%

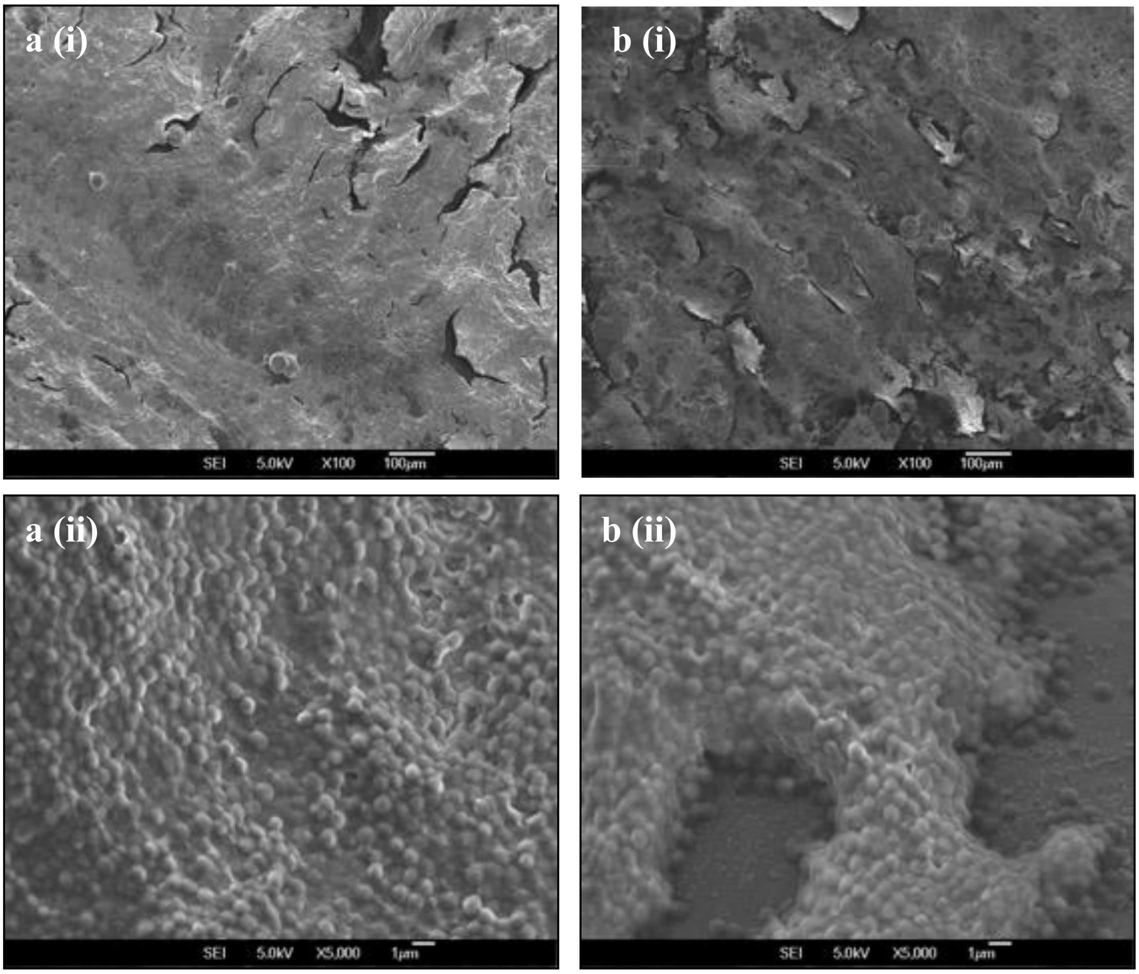

Figure 4.82 SEM surface images Ag1% pre-thermal oxidation a (i) and a higher mag image a (ii), and post-thermal oxidation b (i) and a higher image b (ii). The biofilm test was conducted using *S. aureus* for 72 h.

Ag5%

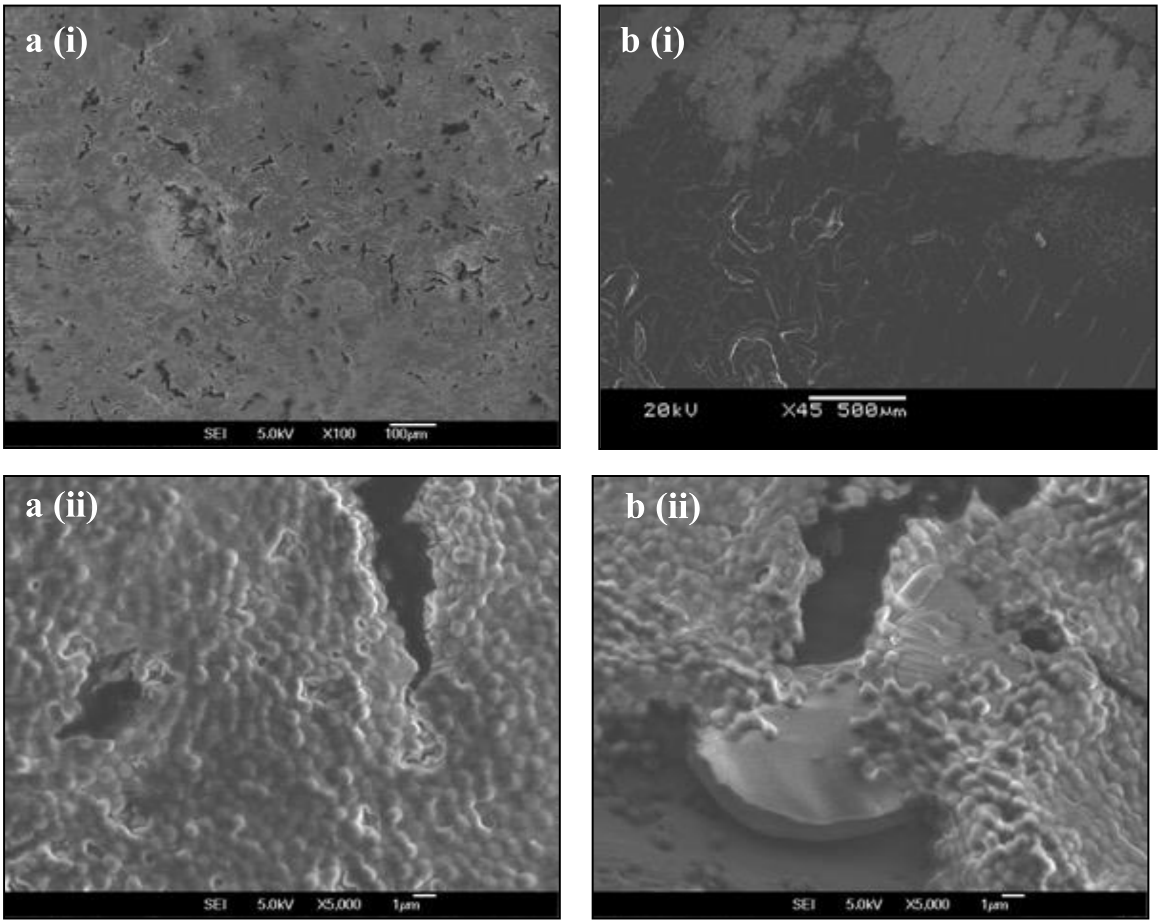

Figure 4.83 SEM surface images Ag5% pre-thermal oxidation a (i) and a higher mag image a (ii), and post-thermal oxidation b (i) and a higher image b (ii). The biofilm test was conducted using *S. aureus* for 72 h.

Ground samples

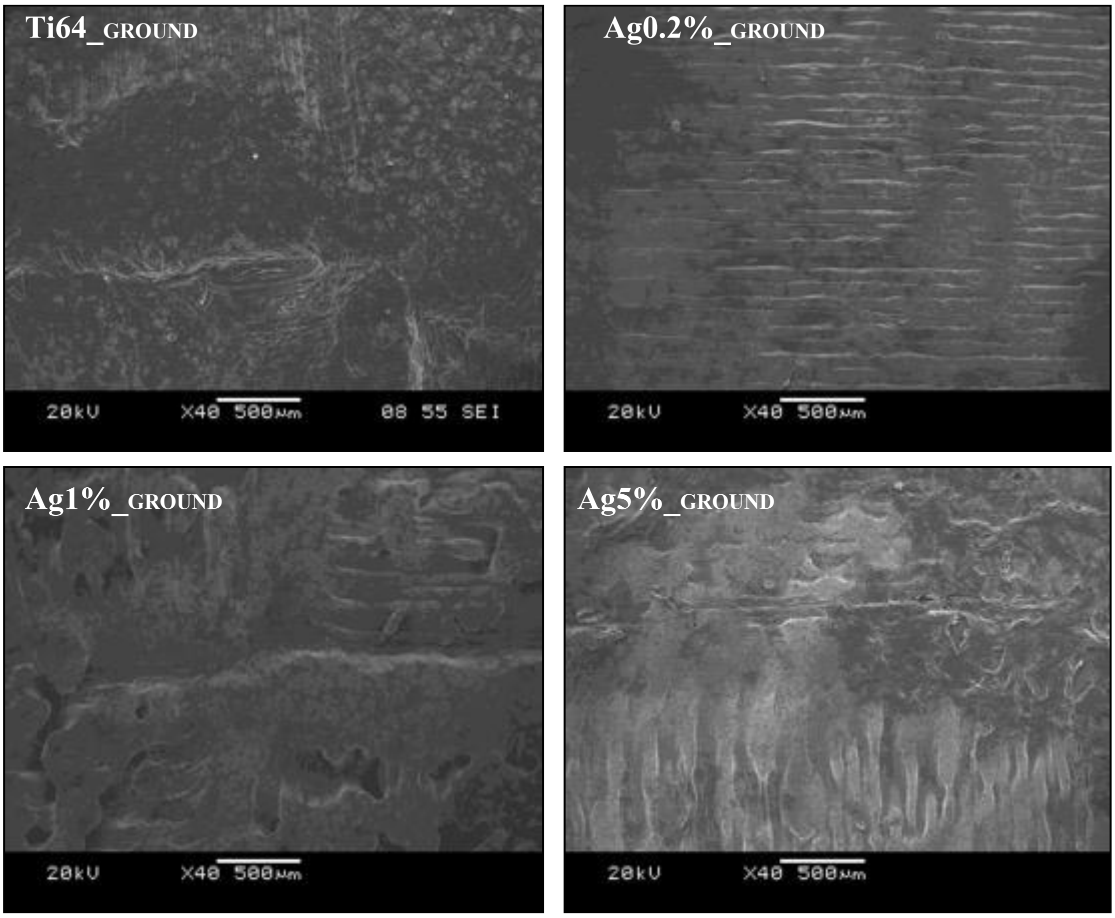

Figure 4.84 SEM surface images of ground samples after the biofilm test using *S. aureus* for 72 h were carried out.

4.5.2 Cell culture

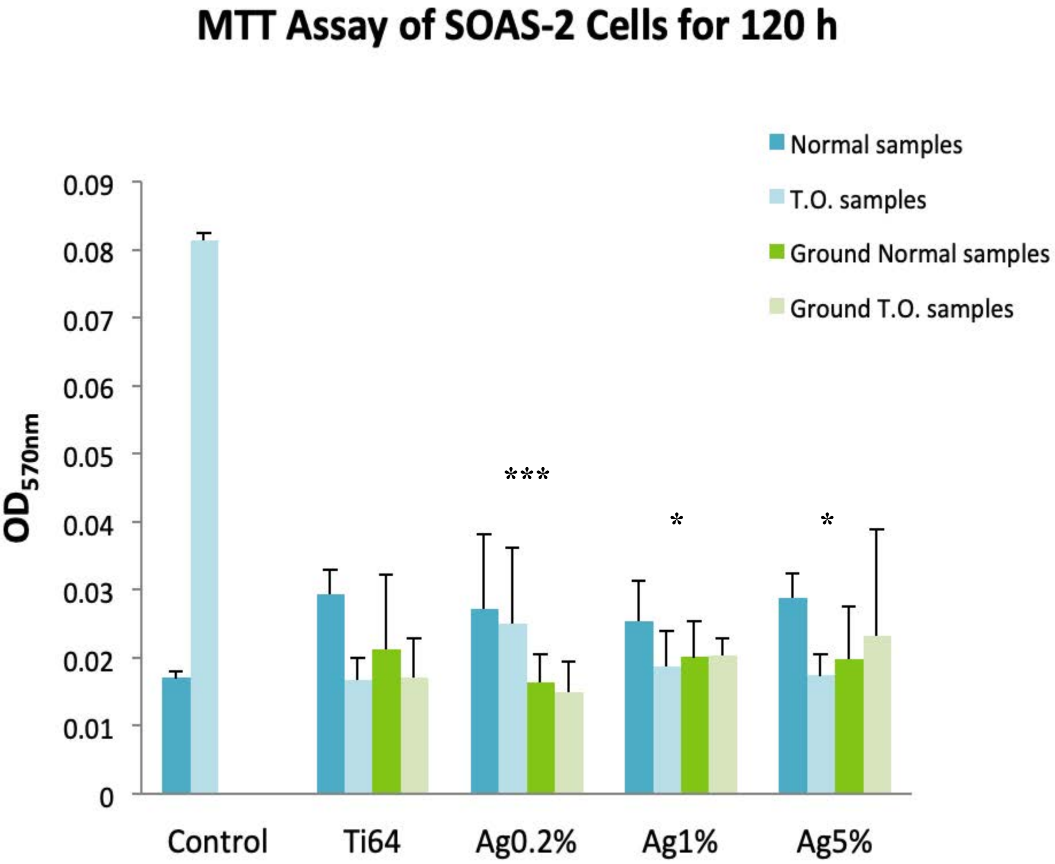

Figure 4.85 MTT assay of SOAS-2 cell growth on the surface of samples from all treatment types for 120 h. * $P < 0.05$ and *** < 0.001.

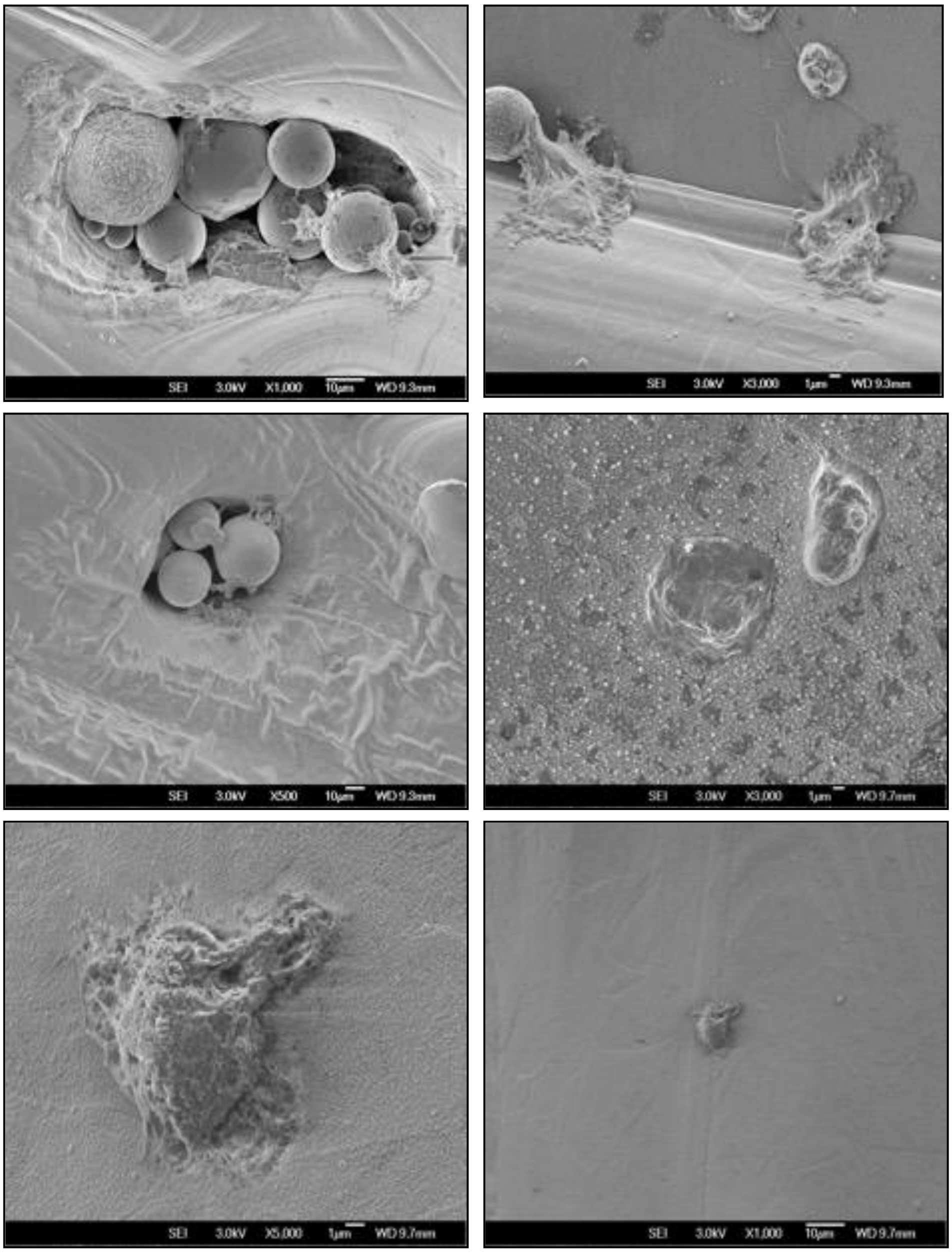

Figure 4.86 SEM images of SOAS-2 cells on surfaces of SLMed samples.

The antibacterial performance of all sample types were evaluated on Gram-positive *S. aureus* NCTC 6571 and *E. coli* NTCT 10418, Figure 4.75. The percentage survivals of colony forming units (FCUs) per ml were compared to the 103 concentration of bacteria suspension incubated for 6 h. Generally, Pattern 1 demonstrated a consistently low percentage bacterial survival of 0.86 ± 0.12, 1.13 ± 0.2 for *E. coli* and *S. aureus*, respectively. This was then followed by Pattern 2 with 1.27 ± 0.21, 0.17 ± 0.13; control with: 0.86 ± 0.15, 1.13 ± 0.2; and Pattern 3 with : 2.83 ± 0.15, and 4.6 ± 0.1, for *E. coli* and *S. aureus*, respectively.

Figure 4.76 showed what the percentage survivals of colony forming units (CFU's) per ml were, compared to the 10^4 concentrations of bacteria suspension incubated for 4 h. When cell attachment was conducted with both *E. coli* and *S. aureus* on the as-ground control, it demonstrated a percentage survival of 48 ± 2.00 and 68 ± 6.55 CFUs, respectively. However, the Ti64 batch generally presented higher attachment to *E. coli* and *S. aureus* than the control with percentage survival of 67.6 ± 2.51 and 77.3 ± 4.72. Comparing the Ag doped samples; Ag0.2% performed the worse with a bacterial percentage survival of 10.7 ± 2.51, and 13 ± 2 for *E. coli* and *S. aureus*, respectively. Ag1% and Ag5% resulted in no survival of CFU's. The agar plates display the CFU's images when the experiment was conducted. More units can be observed on the control and Ti64 sample compared to the Ag0.2%. However Ag1% and Ag5% there were none.

A biofilm formation analysis was conducted on samples with all treatment types. The titanium discs were immersed in S. aureus and culture 72 h to form a biofilm. The final optical density (OD) measurements after crystal violet staining were measured at an absorbance at 590 nm (Figure 4.78). The results revealed Ag5% and Ag1% presented the lowest optical densities across all treatment conditions from as-SLMed ground, as-SLMed thermal oxidation as well as the ground thermally oxidised samples; there were further depicted by Figure 4.79 as less biofilm covered the control", a significant difference between the controls was detected at a P value < 0.01. The lower the absorbance, the less biofilm attachment occurred on to the surface of the discs. The second best treatment bath was the Ag1%. Generally, in both samples, the thermally oxidised counterparts performed better with values of 0.15 ± 0.001 and 0.224 ± 0.004, for Ag5% and Ag1%, respectively (Figure 4.81 and Figure 4.83). There were significant difference in the pre- Vs the post-thermal oxidised samples within batch type Ti64, Ag0.2% and Ag5% of $P < 0.001$. In general, the ground samples performed better than the non-ground, with significant differences of $p < 0.001$ within batches Ti64 and Ag0.2% Figure 4.84. Subsequently, the control" performed in close relation to the Ag1% and significantly better than its as-ground counterpart. Figure 4.81 demonstrated that Ag0.2% then performed better than Ti64 with the thermally oxidised samples outperforming in both batch types. In all treatment types, the as-SLMed samples underperformed compared to its ground or oxidised equivalent. Lastly, Ti64 Figure 4.82 performed the worst across the board with the highest absorbance. Similar to bacterial attachment, with an increase in Ag content there was a decrease in the reduction of bacteria attachment and formation. Generally, SEM images of *S. aureus* cell attachment of samples pre- and post-thermal oxidation displays a biofilm scale grown onto surfaces.

Figure 4.84 demonstrates biofilm attachment on the ground samples. It can be evidently seen there is less biofilm attachment in comparison to other sample treatment types. Furthermore, Figure 4.77, displays live/dead stain of as-polished control, pattern 1, 2 and 3. It was evident that more bacteria survived based on the fluorescent green dye colour on pattern 3 due to macro-features. There was also a bacterial preferential alignment along BD. Fluorescent green dye can also be seen on the polished control sample, however, red colour is indicative of 'dead' bacterial cells.

The MTT assay, demonstrates the performance of the material in promoting SOAS-2 Cell attachments and growth. The MTT assay measures the cell's metabolic activity, the greater the metabolic activity the higher the optical density, which was measured at a wavelength of 570 nm. Cell attachment was conducted for 120 h (Figure 4.85). Evidently, control" outperformed all the other samples significantly. The normal SLMed sampled performed better than their alternate equivalents. In contrast to its bacterial behaviour, thermally oxidised SLM'ed samples specifically Ag1%" and Ag5%" underperformed within their batch type. The results demonstrate a significant difference between treatment types of as-SLMed vs post-thermal oxidation samples of $P < 0.005$. Meanwhile the ground thermally oxidised counterparts performed better followed by normal (as-SLMed) ground samples. There was also an overall significant difference between treatment types non-ground vs ground of $P < 0.001$. Ag0.2% demonstrated a different pattern of behaviour, with ground samples presenting lower OD in comparison to its non-ground counterparts with ground T.O. performing the worst. Figure 4.86 demonstrates images of SOAS-3 cells attachment onto the surface of sample surfaces. Cells can be seen, spread out mostly with a preferential growth inside pores and crevices.

5 DISCUSSION

Ti6Al4V is the most popular and most researched titanium alloy employed for medical applications. However, as previously explained titanium exhibits poor tribology (refer to section 2.2.5 of literature review). Thermal oxidation is one of the surface engineering methods employed for the growth of harder titanium oxide layer that in turn betters the wear resistance of titanium.

Within this study, the effects of thermal oxidation (TO) and selective laser melting (SLM) of Ti6Al4V were observed on the corrosion, hardness and wear surface characteristics of the alloy. SLM was employed to dope the surface of Ti6Al4 Ag in an attempt to also tackle issues faced with infection. SLM was the chosen processes for Ag deposition, as previously conducted work; refer to Error! Reference source not found.**,** demonstrated frailer attachment of Ag. Thus, this research, aims to ameliorate both the antibacterial and wear characteristics of Ti6Al4V.

5.1 Corrosion behaviour

When a titanium implant is placed into the body (surrounded by extracellular fluids) it immediately experiences electrochemical interactions with bodily chemical compounds. Thus, it becomes susceptible to corrosion. Corrosion could cascade into implant failure, for example its been reported to accelerate the fatigue fracture of a metal implants. Corrosion could also cause the release of metallic ions into the body, which could be carcinogenic, toxic or lead to other adverse effects (191).

All sample batches, as-SLMed pre- and post-thermal oxidation underwent an electrical corrosion test, via potentiodynamic polarisation test. Firstly, in Table 4-8 when a comparison between the as-ground control and Ti64 as-SLMed samples are conducted, it was evident that the latter sample although, being rougher with laser track configuration, presented higher corrosion potential (E_{corr}) at a lower current density (i_{corr}). The improvement in corrosion resistance, post-SLM could be attributed to a passive oxide protective layer formed on the surface of the Ti64 post-treatment. In agreement to these findings by Sui et al (2019), whom concluded that the SLM Ti6Al4V demonstrated better corrosion resistance than the wrought control due to the formation of thin passive oxide layer consisting of TiO, Al_2O_3 revealed by XPS analyses. The authors also suggested that a more hydrophobic surface enhances corrosion resistance. Accordingly, the as-SLMed Ti64 demonstrated hydrophobic (WCA of 101.6 ± 11.4 °), while the as-ground control was deemed hydrophilic (WCA of 62.2 ± 3.1 °). The idea that SLM layers exhibited a protective passive oxide layer was further supported by the Figure 4.55 in comparison to Figure 4.54.

These figures demonstrate that prior to thermal oxidation, Ti64 reached passivation (hence the dip in its current density), before the control, as a passive oxide layer was protecting the SLM surface from corrosion. The ensuing increase in current density was a testament to the breakdown of this thin layer. Contrary, the presence of less α' martensitic Ti-phase, and more β- phase Ti phases was reported to improve titanium's corrosion resistance (192). This report was not in accordance with the findings of this research, as a comparison between the control and as-SLMed Ti64, demonstrated the latter performed better and contained α' martensites Figure 4.37.

The inclusion of Ag within the SLM layer, established that Ag had a detrimental effect in the corrosion resistance of Ti64. Compared to as-SLMed Ti64, Ag containing SLMed samples presented higher corrosion density values. With increasing Ag wt. %, there was a general reduction in corrosion resistance, thus corrosion occurred earlier. Additionally, Figure 4.56 to

Figure 4.58 shows the potentiodynamic polarisation curves of Ag treated samples pre-thermal oxidation. There was an increase in the frequency and severity of metastable pits with increased Ag wt. % doping. However, once these samples underwent thermal oxidation, the ceramic conversion to form TiO_2 layer remedied the adverse effects of Ag. The Ag doped as-SLMed samples, demonstrated similar corrosion potential behaviour to the as-SLMed Ti64, post-thermal oxidation; not significant differences shown. The potentiodynamic polarisation curves of these samples Figure 4.55 to Figure 4.58 display no pitting; with general better passivation potential and region. The effects of thermal oxidation on the improvement of corrosion resistance was more obviously demonstrated by the comparison of the control, Figure 4.54, the corrosion potential, (E_{corr}) increased while corrosion current density (i_{corr}) decreased post-thermal oxidation. With better passivation and zero pitting being detected. These results were in accordance with Cao et al. (2018) (187). But generally, SLM increased corrosion density.

Taking into account experimental limitations (such as the bonding between the resin and the metal substrate), which potentially influenced the initiated metastable peaks, thermal oxidation demonstrated a greater effect on improving the corrosion resistance of titanium discs than Ag. But together, the combining effects of Ag and thermal oxidation, which promoted the growth of an oxide layer, resulted in Ag5%" performing the best within all SLMed samples. No pits, lower passivation potential and region were observed (Figure 4.58).

5.2 Effects of roughness, silver alloying and thermal oxidation.

The use of different process parameters (PPs) influenced the morphology of the samples as evident in Figure 4.13. Typical balling effects of SLM process were also observed (Figure 4.11and Figure 4.13), with a noticeable difference in the morphology of PP 5 and PP 6 due to its high energy density inputs (J/mm^3) of 101.01 and 303.03, at small a1 spacings of 0.3, and 0.1 respectively. By minimising the a1 spacing, different morphological surface compositions were evident. A difference in depth profile of the roughness of samples can be seen in a difference in depth profile of the roughness of samples can be seen in Figure 4.21 to Figure 4.25 where the SLM effects of PPs 5 and 6 can be observed. PP 6 resulted in finer laser track width with a glossier, smoother surface finish (Figure 4.22 to Figure 4.25) while PP5 produced rough protrusions, and pores as a result of a slight increase in a1 spacing. In both PPs the following laser scan overlapped the previous, thus re-melting molten powder. The high energy densities used, could cause keyhole effects, whereby the material is evaporated, bubbles and splattered forming a keyhole shaped vapour cavity upon which adjacent molten `metal falls back into the cavity to close it up. The keyhole effect could not be viewed in cross-sectional analyses as the entire surface of the discs underwent SLM. Additionally, one of the limitations of the M2 machine was the inconsistency in powder bed thickness. Theoretically, a layer's thickness of 20 μm is achievable, but practical cross-section analyses demonstrated a variation in thicknesses (Figure 4.37). The variation in SLM powder thickness influenced surface roughness (R_a), which in turn influenced cell adhesion and wear behaviour. It can be concluded that the variations in layers thickness were due to two contributing factors: (i) powder spread (including the difficulty of spreading fine Ag powder with poor flowability) and (ii) key-hole effect. These limitations influenced the average R_a of all sample batch types (i.e. Ti64, Ag0.2%, Ag1% and Ag5%) (Figure 4.19). Thus, the individual effects of PPs were not taken into account, but rather the comparisons made were between SLMed batches, which each included all six parameters. Over all, the roughness measurements displayed no significant differences (Figure 4.19).

The R_a measurements against BD were expectantly higher than along BD, due to the fact that roughness was measured perpendicular to the laser track grooves. However, Ag1% generally demonstrated a higher R_a values. Samples were also ground, for antibacterial test purposes to study the effects of Ra, and a depth profile of exemplary samples were shown in Figure 4.26.

A site specific cross-section of an oxide blister on Ag1%", was studied using a FIB-SEM (Figure 4.48) and it revealed nano-meter thick layer which after EDS mapping (Figure 4.49) demonstrated layer rich in oxygen and depleted in Al, V, and Ti; this study confirmed that the 'blisters' were oxide initiation points. It is well known that during thermal oxidation, oxygen diffuses into the substrate reacting with titanium to form TiO_2 (117). As oxygen diffuses inward, aluminium has been reported to diffuse outwardly forming Al_2O_3, which could explain the thin films of Al on the oxide layer shown in Figure 4.42 and Figure 4.44. However, this alternate growth of Al_2O_3 has been reportedly detected on the XRD after 100 h of thermal oxidation (117). With reference to the XRD results in this thesis, Figure 4.33 there was no Al_2O_3 spotted as thermal oxidation was only conducted for 4 h.

In addition, the Ag1% and Ag5% revealed oxides layers that were 'chipped'. When EDS elemental mapping was conducted on one of the chipped area, Figure 4.36 and Figure 4.32, on Ag5%", a depletion in O was evident, while greater intensities of Al, V and Ti was detected from the sub-surface SLMed area. There was an increase in oxide layer thickness, from control to Ag5%, Figure 4.38, with increasing Ag content. . Ag has demonstrated catalytic effects on oxide layer growth during thermal oxidation; these findings, Figure 4.39 to Figure 4.45, have also been confirmed by previous works, refer to Error! Reference source not found.. In the agreement to these findings, Ag NPs were reported to promote the formation of rutile TiO_2 from anatase by decreasing the transition temperature to 600 °C. It was explained that initially, Ag NP agglomerated into larger clusters post-annealing, which took up the space so anatase unit cells are motivated to change to more thermodynamically stable rutile (193).

5.3 Tribological performance

The hardness measurements of the sample were measured via cross-section nano-indentation due to the very rough surface features. It was possible to measure the hardness of oxide layers of the Ag1% and Ag5%, which demonstrated double the hardness (GPa) (Figure 4.62), than the SLM layer post-thermal oxidation. Overall, the hardness of all SLM and bulk layer increased with thermal oxidation treatment. Post thermal oxidation the 10.08 ± 0.18 and 10.34 ± 2.83 GPa of Ag1%' and Ag5%" oxide layer hardness were similar to the literature (188). The increase in Ag wt. % pre-thermal oxidation in the as-SLMed samples increased the cross-sectional hardness of the layer due to the Ag effects of solid solution strengthening. This report was in accordance with Han *et al.*, 2014, demonstrated insignificant effects on the hardness of the oxide layer (194).

Commonly, an increase in hardness results in better wear resistance, however, in other cases corrosion could be a factor that assists the wear of an implant (188). Corrosion-wear could not be measured in this research due to time limitations. Only the coefficient of friction was measured using Ringer's solution. But the wear tests that were conducted to measure wear rates were done in air.

Firstly, the coefficient of friction (CoF) of the samples were analysed in air and in Ringer's solution, as Ti6Al4V implants would be lubricated with bodily fluids once inserted in the body. There was a considerable decrease in CoF with the as-ground control when tested in Ringer's solution in comparison to air. Similarly, an overall regression in CoF was observed in the SLMed samples batches when tested in Ringer's solution, especially when measured along BD. General testing of CoF in Ringer's solution resulted in lowered values, pre- and post-thermal oxidation.

When the control sample underwent thermal oxidation, there was a decrease in CoF, but negligible differences were witnessed in the measurements conducted in air or Ringer's solution Figure 4.66. The ceramic conversion on the surface of the substrate (formation of TiO_2 layer) caused reduced plasticity, thus reducing adhesive wear tendencies generated under plastic contact (Figure 4.63). This surface modification behaviour was apparent in the wear behaviour of the control, Figure 4.67 and Figure 4.69, when tested under 15 N and 30 N. The wear profile in Figure 4.69 illustrated the lack of wear. However, when a comparison is made to pre-thermal oxidation, two wear mechanisms can be identified on the surface of as-ground control; this sample exhibited lower hardness and greater CoF. As the control underwent adhesive wear whereby material transferred from the surface of the control to the harder WC ball. The debris transferred, would get trapped under the sliding surfaces, and result in a roughened material- to material surface contact points that concludes in the abrasion of the remaining material surface (127). The effect of these wear mechanisms were heightened with 30 N load.

Generally, as-SLMed samples demonstrated increased CoF, especially when measured against BD in air (Figure 4.64). These increases were due to the increased R_a and laser track configuration, as well as hardness which all acted as a resistant barrier generating stresses against the motion of the WC ball, hence the greater CoF values (Figure 4.19, Figure 4.62). More specifically, there was a gradual increase in CoF (along and against BD) with increasing Ag wt.%, which could be due to the increase in the hardening of the SLM layer as a consequence of Ag solid solution strengthening (Figure 4.65). The increasing in hardness, increased the stresses experienced during sliding, and the WC ball experienced greater difficulty in ploughing through the laser track configuration resulting in increased CoF (Figure 4.65). An experiment conducted on a range of Cp Ti-*x*Ag alloys containing 5, 10, 15, and 20 wt.% Ag were conducted, the Vickers hardness demonstrated in increase in material hardness with increasing Ag content credited to (i) the solid solution strengthening of the α-Ti, and the changes in microstructure from α-Ti to α' martensite phase (194).

However, the wear rate of Ag1% performed considerably better than Ag5% which could be attributed to the effects of Ag5%'s higher R_a, as a limiting factor of the M2 SLM process. The higher roughness values, resulted in wear occurring at the peaks and asperities of the highest grooves and ploughing and chipping away the inconsistent OL, which was more evident in Figure 4.68, additionally, the general low thickness values of Ag5% eventually resulted in contact stress reaching the interface of the SLM and bulk layer, which is 'softer' therefore would wear quicker (Figure 4.35, Figure 4.37 and Figure 4.69).

Contrary to the effects of the post-thermally oxidised control, SLMed samples that underwent thermal oxidation resulted in an even greater increase in CoF. Which supports the formations of an even harder surface layer, Figure 4.62, which when aligned to the grooves of the laser track, increased the stresses and work required for the WC ball to plough. However, a considerable difference was witnessed with Ringers solution, which helped improve the effects of thermal oxidation but only along BD. Against the BD, there was an increase in CoF with increasing Ag wt.%, it can reasoned that the effects oxide layer which grew thicker with increasing Ag wt. % doping, proved more difficult for the WC ball to plough through.

The wear rates recorded for Ag5% were the highest in comparison to other same types including the control There was decreasing trend in wear rate after thermal oxidation, for 15 N and 30 N for all samples types (Figure 4.67). However, Ag5% demonstrated high CoF and severe adhesive wear (Figure 4.69**)**; two deep wear grooves were evident on the Ag5% before thermal oxidation. After oxidation, the lower thickness in SLM layer recorded of SLM cross-section of the Ag5% (Figure 4.37**)** meant that the sample generally experienced a combined effect of (i) delamination wear and weaker bonded oxide layer on the SLM layer, and (ii) contact stress reaching the bulk material, which has a lower hardness value. Before explaining the delamination wear mechanism, the formation of TiO_2 hard layer must first be explain via solid solution strengthening. The idea being a harder oxide layer grown onto the surface of Ti6Al4V occurs due to the diffusion of oxygen into the titanium alloy lattice structures. Oxygen atoms alter the lattice parameters of the existing alloy matrix, thus producing a hardening effect due to size misfits (195). Oxygen was reported to demonstrate more lattice strain on hcp Ti towards its *c* direction than the *a* thus, changing the c/a ratio of hcp Ti causing restricted dislocation motion, hence increased hardness (196).

Now during the delamination wear, the material at the surface (in this case TiO_2) exhibits low dislocation density. This means during sliding motion, load applied by the harder WC ball to the oxide surface (softer material) results in dislocations in the oxide layer being driven into the subsurface layer (softer material) (191). The Young's modulus of Ti6Al4V has been reportedly in the range of 105-116 GPa dependent on interstitial elements (**107**). While anatase and rutile were reported to demonstrate higher modulus of 170 and 260 GPa, respectively (197). The WC ball employed for wear testing has been reported to exhibit modulus between 600-686 GPa (198). As sliding continued, stresses increase and dislocation densities build up within the oxide layer's sub-surface eventuating in crack formation and shearing. Eventually, with enough crack being formed, shear deformation can link the crack together producing more favourable thin sheet like wear particles as opposed to spherical particles. Some of these wear debris (thin sheets) can become entrapped between the sliding surfaces, and so break into smaller particles which can be smeared back into the surface layer. The occurrence of delamination is not exclusive to the formation of any other wear mechanism (191). Figure 4.44 and Figure 4.45 demonstrate the oxide layer grown onto the surfaces of the SLM layer Ag5% and Ag1%". The boundaries between the oxide layer and SLM layer were evident, thus it can be suspected that poor bonded layer, encouraged delamination wear. In addition, the chipped oxide layer area's were exposed area's which could initiate delamination wear, Figure 4.32.

Generally, more severe adhesion and plastic deformation was evident on non-thermally oxides samples. These wear mechanisms were heightened when the load was doubled. The control post-thermal oxidation resulted in the most ameliorated wear rates, which was attributed to its lowered R_a and reduced influence of laser track surface configuration. The effects of SLM configuration on wear were evident, as asperities heights affected the rates of wear and CoF. Thermal oxidation has proved to be a useful tool in improving wear rate, however, more experiments must be conducted to optimise the oxidation temperature, time, with the correct weight. % of Ag added within the ideal SLM process parameters. In addition, the effects of Ag as a solid lubricant were not evident in this research when melted into the alloy, its effects could be more effective treated onto the surface as oppose to within.

However, its effects could have also been overshadowed by laser track roughness configurations, as the CoF results are greatly influenced by mechanical interactions.

5.4 Biological behaviour

The surface topography of an implant is a key influence on cellular adhesion; generally, rougher surfaces provide greater surface areas that favour both native and pathogenic cell adhesions. However due to conflicting reports, sole surface roughness cannot permit accurate predictions on the attachment behaviour of bacterial cells. For example, Whitehead and Verran (2006) reported that coccal micro-organism with similar-sized topographical features as the substrate surface onto which they were tested, resulted in higher cell retention in comparison to the substrates smoother and rougher counterparts (199). Contrarily, Hsu et al., (2013) have reported significant bacterial adhesion on smooth-surfaced substrates, thus the surface topography of a sample needs to be considered as a whole; this means considering the specific characteristics of a surfaces' physical features (200). There are many conflicting results on the effects of roughness on bacterial adherence; however, bacterial adhesion is not only affected by surface roughness, but also rather the physiochemical properties of the sample surface, such as wettability, surface energy etc. Roughness has been reported to affect the wettability of a surface, which could explain the contradictory deductions that surface roughness has on the anti-fouling behaviour of the sample. Additionally, surfaces could have similar roughness results (i.e. height variations) but demonstrate completely different topographical features (i.e. different configurations such as grooves, pits etc) (35,36). In this study, there are ensuing physical configuration and surface chemistry effects of SLM, Ag, and thermal oxidation.

After SLM, the titanium powders formed titanium discs with varying physical configurations, due to varying surface patterns (Figure 4.6). All SLMed samples seemed rougher than the control, which was polished to a mirror- like finish, and this was further confirmed by R_a measurements (Figure 4.17). Pattern 1 exhibited the highest R_a, which could be due its generally porous surface irregularities (Figure 4.10), as its surface was covered in random micro-pores, and lacked any organised structural consistency aside from the pronounced diamond-shaped dips. There are reposts whereby porous surfaces have resulted in higher infections rates due to a preferential adherence an colonisation of bacteria compared to non-porous surfaces. In this study, the random porous micro-features found on Pattern 1 overall demonstrated the lowest percentage bacteria survivals of both E. coli and S. aureus (Figure 4.75). Pattern 1 performed the best out all the other samples regardless of its increased surface area for bacterial attachment. The pores based on Figure 4.11 a) ii can be mostly seen to be micro-sized hence big enough for *E. coli* (rod-like bacterium approximately 2 x 1 µm in size) and *S. aureus* (round-shaped 0.5 to 1.5 µm in diameter) to fit into (201). Thus the porosity of the pattern could favour bacterial adhesion and its proliferation, as the bacteria have a greater surface area (attachment within the porous matrix) than less porous counterparts. Additionally, the porous nature of the sample could also provide a protective barrier, during the bacterial attachment test. Thus the antifouling results deduced from pattern 1 are not clear as to whether it was the effects of attachment as a result of increased surface area within pores, or more so the ineffective detachment of cells during vortexing as a result of the porous matrix which trapped bacteria (Figure 4.77) (36). The live/dead stain for Pattern 1 demonstrated green (live) and viable bacteria dotted around in the irregular diamond-shaped dips, with more red (dead) dotted in other areas. This supports the theory that the porous matrix could harbour bacteria.

On the contrary, Pattern 3 (Figure 4.10) consisted of macro-features due to the employed island scanning strategy; consequently, this resulted in a significantly rougher R_a perpendicular to the laser beam BD in comparison to the measurements taken along BD. Ribeiro et al (2012) reported that bacteria adhered more to grooved and braided surfaces compared to their smooth counter parts (202). Agreeably, when the comparison is made between the control and pattern 3, it can be seen that the latter sample demonstrated a considerably higher percentage bacterial survival. This was due to bacterial aligning themselves along the macro-morphological grooved lines of the island scanning strategy surface of Pattern 3 (Figure 4.77**)**. As cells respond to topographical features is dependent on cell size and geometry, and *S. aureus* and *E. coli* are of micron scale, the macro-features found on Pattern 3 may have promoted stronger interlocking adhesions. This is phenomenon is best described by Lorenzeti et al., 2014, who reported a decrease in bacterial cell attachment with decreasing peak-to-peak distances on differently treated commercially pure titanium (cpTi) discs (201). For example, when presented with titanium discs with peak-to-peak surface width distances of 5, 3, and 0.4 µm, two *E. coli* bacteria could theoretically lie within the 5 µm peak-to-peak gap, while only one can lie within the 3 µm, gap and none within the 0.4 µm,gap (Figure 5.1). Subsequently, the cpTi discs with the highest peak-to-peak width can potentially "hide" and "protect" the bacteria from any external forces; in addition, it provided maximal contact area between bacteria/titanium-surface resulting in an interlocking adhesion. Contrarily, the cpTi discs with the lowest peak-to-peak width did not allow sufficient contact area for interlocking adhesion, but the *E. coli* did form weaker "contact-points" adhesion. Consequently, these discs demonstrated ~50% less bacterial attachment compared to the discs with the highest peak-to-peak width.

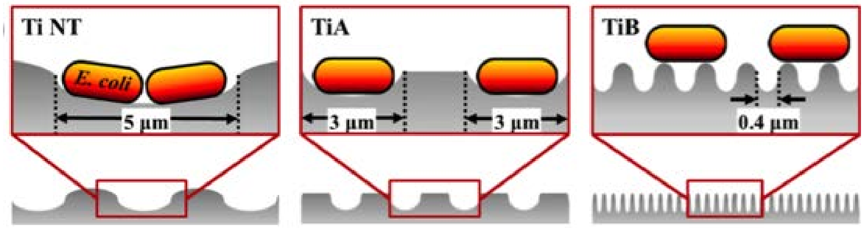

Figure 5.1 A height Vs distance profile of differently treated CP-Ti discs (201).

Pattern 2 (Figure 4.10) consisted of both micro- (diamond-like dips) and macro-features (island scanning strategy), hence it significantly also presented a difference in R_a along versus perpendicular to laser beam BD. This pattern demonstrated an overall percentage survival rate of both bacteria closer to that of Pattern 1 than 3. It displayed a percentage survival lower than the smooth control which could be resultant effects of the regular micro diamond-like dips. Regarding the diamond-like dips, their wear tracks are displayed in Figure 4.18 for pattern 1 and 2. There is a hardly a difference in the dip depth in Pattern 1, as it can be seen that along vs perpendicular to laser beam BD, a diamond-like dip of ~6.6 ± 0.15 mm, respectively. However, there is a larger difference the Pattern 2 which revealed depths of ~3.9 ± 0.26 mm. In both patterns, the wear track perpendicular to laser BD was wider; this could be due to the diamond shape of the dips.

Limited amount is known on the wettability of bone tissues but it has a been reported by Bruschi et al., 2014 and Gittens et al., 2014 that a high SE enhances cell interactions as it promotes protein adsorption (8,55). However there are numerous contradicting reports on the effects of hydrophilic and hydrophobic surfaces. Generally, bacteria with hydrophobic properties prefer hydrophobic surfaces vice versa. *S. aureus* and *E. coli* have been reported to be attracted to hydrophilic surface characteristics (48,203).

The control sample demonstrated a similar WCA to pattern 2 (hydrophilic) despite its considerate differences in roughness (R_a) (Table 4-7) (Figure 4.50). These samples also demonstrated similar SE's of 51.97 ± 0.57 and 55.49 ± 7.60 mN/m, respectively; these results mean the surface tension forces acting on the substrates were unable to overcome that of the deposited water droplet (72 mN/m) which resulted in a coalesce spherical droplet (Figure 4.50) (203). Pattern 2 resulted in complete absorbance of the liquids placed onto its due to its interconnecting porous channels. However, Pattern 3 had a considerably lower average WCA of 17.77 ± 14.23, the highest SE of 69.44 ± 5.60 mN/m, deeming the surface even more hydrophilic than the control or Pattern 2. In accordance to *S. aureus* and *E. coli* preferring hydrophilic surfaces, Pattern 3 demonstrated the greatest percentage bacterial survival. Although there are contradicting reports on the influence of implant surface wettability on bacterial adhesion, generally hydrophobic surfaces are preferentially employed as they have been mostly identified to adsorb more proteins for reasons not fully elucidated.

The low reproducibility of the depths of the dips by the SLM machine was evident in pattern 1 and 2 samples (Figure 4.18) was a limiting factor of the M2 SLM machine, in addition to the lack of validation as to the effects porosity on cell attachment and detachment, meant the SLM island scan strategy on pattern 3 was the preferred chosen pattern for further analyses in this research.

Some samples were ground to remove the effects of laser tracks to be tested on pathogenic and native cells. No general trend was spotted with regards to the effects of Ag on R_a, this could be attributed to inconsistent powder spread. The high standard deviation was a testament to the great variation in data. After grinding, the difference in surface roughness could be seen with exemplary depth profile images (Figure 4.26). Flatter laser tracks were evident. The flatter surfaces after grinding were to minimise the effects of laser track on pathogenic and SAOS-2 cell attachments. Evidently, Figure 4.78 demonstrates the significant differences of $P < 0.001$ between the treatment types of ground vs non-ground samples within batch Ti64.

The as-SLMed Ti64 exhibited a higher WCA (°) and lower SE (mN/m) of 101.6 ± 11.4 and 38.56 ± 4.41 compared to as-ground control WCA (°) of 62.2 ± 3.1 and SE (mN/m) 49.41 ± 2.10. It must be noted that the SLM process resulted in a considerable increase in WCA of sample surfaces. Correspondingly, Wysocki et al (2018), reported a similar high (> 90 °) for as-SLMed CPTi (204). In addition to the increase in WCA, the SLM process also resulted in a considerable increase in R_a due to the laser track grooves. With these differences in surface characteristics, the as-ground control outperformed the as-SLMed Ti64 with lower OD in the biofilm growth. When the as-SLMed Ti64 was ground to minimise the effects its surface configuration, there was a great reduction in WCA closer to that of the as-ground control, rendering the sample hydrophilic. Surface roughness has been reported to influence the wettability of a surface (36). However, the biofilm test determined a negligible difference between ground Ti64 and as-SLMed Ti64, despite the latter demonstrating higher R_a values (increased surface area for bacteria attachment) Figure 4.79 to Figure 4.84.

Therefore, the synergetic effects of the hydrophilic nature of ground Ti64 with its surface topography (although minimised) encouraged to biofilm growth. The laser track configuration still provided an increased surface area for *S. aureus* attachment, as grinding mainly reduced the effects of heightened peaks (Figure 4.26). For these reasons, the ground Ti64 with lowered R_a value considerably performed worse than as-ground control.

With increase in Ag wt.% there was a general decrease in WCA, eventually falling into the hydrophilic regions (WCA < 90 °) with Ag1% and Ag5%. However, all as-SLMed batches presented WCAs higher than the as-ground control. The increasing affect of Ag also demonstrated in a decreasing OD values, thus decrease in biofilm attributed to Ag's bactericidal characteristics. When the Ag doped SLMed samples were ground, there was an evident decrease in WCA, negligibly lower than as-SLMed Ti64. Thus, yet again demonstrating the influence of roughness upholds on wettability. The ground Ag doped samples performed better than their non-ground equivalents, due to decreased roughness despite their more hydrophilic character, which *S. aureus* is reported to favour (48,203)**.** Therefore decrease in surface area for bacterial attachment of ground Ag samples prevailed over its favoured hydrophilic character.

Wang *et al.*, 2016 reported a decrease in WCA after heat treatment of SLM-printed Ti6Al4V disk. When the biofilm formation test was conducted, it revealed considerable decrease in biofilm formation (lower OD) (205). This was in accordance to the results in this thesis, as thermal oxidation decreased the WCA of as-SLMed samples. Additionally the control post-thermal oxidation also demonstrated a reduction in WCA favouring S aureus attachment but demonstrating significantly lower ($P < 0.001$) lower biofilm OD values. These results are attributed to the reported bactericidal effects of titanium dioxide. Anatase has been reported to exert photo-catalytic bactericidal behaviour, while rutile has been reported to be bio-inert (91,92).

The cross-sectional analyses confirmed the increase in oxide layer thickness with increasing Ag wt. %, as shown in Figure 4.38. Ag1%" and Ag5%" both demonstrated oxide layer < 1 µm, but were thicker than Ag0.2%", Ti64" and Control". There was an overall decrease in surface roughness (R_a) of the samples, refer to Figure 4.20. However, Ag5%" demonstrated a considerable higher R_a when measured along BD compared to the other samples, due to its initial rougher surfaces. But there was a general decline of roughness when measured against

BD, attributed to the increasing oxide layer thickness, which smoothed the effects of the laser grooves; specifically, Figure 4.15 c) demonstrates the oxide layers scales grown onto the sample surface. Figure 4.27 display the 3D depth profile of samples post-thermal oxidation; the formations of micro-scales on the laser grooves were evidently covering the surface of the samples. Even after being ground, the ground surfaces displayed oxide growth on its surfaces. The was also an overall decrease in ground samples R_a post-thermal oxidation compared to non-thermally oxidised counterparts.

As depicted by Figure 4.77, post-thermal oxidation resulted in significant decrease in biofilm OD measurements, insinuating better antibacterial behaviour, credited to the addition of an oxide layer. When the effects of SLM roughness are not taken into account, a greater decrease in OD results was demonstrated by the control" Vs control. There were insignificant differences, exhibited by as-SLMed and ground SLM batches pre- and post-thermal oxidation. These results suggest laser track configuration were fairly prominent (Figure 4.22). More specifically, ground as-SLMed Ti64" demonstrated the greatest difference in OD reduction in comparison to its non-ground Ti64" counterpart. These samples also demonstrated WCA reduction after being ground, Figure 4.51. There have been reports that thermal oxidation renders sample surface super hydrophilic, but after aging (3 weeks later) the surfaces have been shown to become more hydrophobic. This change in wettability has been attributed due to loss of OH- groups which attract water molecules (206). This explains the hydrophilic nature of ground Ti64" in comparison to the control", as the control was measured 4 week post-thermal oxidation, while ground samples were measured 2 weeks post-thermal oxidation. However, with increasing Ag there was an increase in the WCA of the ground SLMed samples, that eventually surpassed that of the control". This trend was not evident in their non-ground counterpart, which could have been influenced by surface topography. The growth of TiO_2 layer rendered the surface of the ground samples more hydrophobic and the as-SLMed samples more hydrophilic Figure 4.51.

Therefore, it can be concluded that TiO_2 layer grown within this research was hydrophilic in nature, but the different times at which the samples were measured must be taken into account. However, thermal oxidation displayed a greater effect in reducing OD of *S. aureus* biofilm than the sole effects grinding (reducing roughness), as thermal oxidation, also reduced roughness while producing an antibacterial TiO_2 layer. Even when the ground samples contained Ag, their as-SLMed thermally oxidised counter parts still outperformed them. It can be concluded from these results that with TiO_2 and Ag demonstrated bactericidal behaviour, thermal oxidation exhibited a greater influence in reducing biofilm than Ag; with the only difference being that the thermal oxidation process produced an antibacterial TiO_2 layer while also reducing the R_a (surface area) for bacteria attachment. The optimal, parameter in biofilm test was the ground Ag5%" sample type.

Krasowska and Sigler, 2014 reported on the changes bacterial cells can exert in phenotype thus becoming more hydrophobic and hydrophilic in nature in an attempt to adapt to environmental changes (207). The authors suggested the best way to avoid bacteria growth on implant surfaces was to avoid bacteria attachment in the first place. Therefore, strong antifouling characteristics are ideal. Figure 4.76 demonstrates a Japanese spread plate method, which depicted bacterial cell attachment, hence percentage survival. The results evidently, suggest, a significant difference of $P < 0.001$ between the control and all other Ag doped as-SLMed samples. The concentration of *S. aureus* and *E. coli* deposited onto sample surfaces was 10^4, and these samples were incubated for 4 h. These results demonstrated inhibition parameters for Ag0.2%. Ag1% and Ag5% demonstrated zero CFUs. The control sample performed better than the as-SLMed Ti64 due to the SLMed sample exhibiting greater R_a (surface area) for bacterial cell contact.

The antifouling mechanisms of Ag are still to be understood. However, Ag has been reported to release Ag^+ ions upon bacterial contact that penetrate the bacteria cell wall, inhibit cell functions, and permeate cell eventuating in cell death (see section 2.1.2 of literature review) (64,67). There was a general trend of *S. aureus* bacteria percentage survival being greater than E. coli (Figure 4.75 and Figure 4.76).

In agreement with these findings, Qing *et al.*, 2018 reported that AgNPs had a greater effect on gram-negative (e.g. *E. coli*) than gram-positive (*S. aureus*) due the latter exhibiting thicker cell walls of 30 nm, compared to the former at 3-4 nm thick (208).

As for cell growth, all sample treatment types, underwent a cell culture test, whereby SAOS-2 cells (sarcoma osteogenic) were cultured onto the samples for 120 h. A considerable difference was noticed in the performance of the control Vs control". The MTT assay, which measures the metabolic activity of the SAOS-2 cells revealed post-thermal oxidation with a smoother surface promoted cell attachment and cell growth. Similarly, all as-SLMed treated samples demonstrated considerably less metabolic activity than the control" (Figure 4.85). It could be deduced that when the topographical features (R_a) caused by the laser grooves could be too great for the cell's filopodia to notice, the effects of roughness are negated. However when the control samples were observed, prior to thermal oxidation the sample exhibited a R_a of 0.94 ± 0.05, and after thermal oxidation, it decreased to 0.29 ± 0.05. Osteoblast SAOS-2 have been reported to demonstrate preferential growth on rougher surfaces (209). However, within this research, the effects of thermal oxidation were greater than that of roughness, as the control" outperformed the as-ground control. Agreeably, Vandrovcova *et al.*, 2014, concluded greater SAOS-2 cell proliferation and differentiaition on CpTi stream oxidised with air at 600 °C for 1 h than those heated at 165 °C in an autoclave for 12 h (210). The former demonstrated rutile phases, and the authors suggested that the cell differentiation was a resultant effect of the negatively charged sites on the TiO_2 phase. TiO_2 contains OH- groups which has been reported to be more optimal for osseointeergration, as its hydrophillicity enhances amino acids, proteins and ions in tissue fluids to react promoting osteoblast attachment (205). However, there are differences in the behaviour of cpTi and Ti6Al4V (210); the combining release of Ti and Al ions in Ti6Al4V resulted in "deleterious" effects on human osteoblast proliferation and differentiation. The authors concluded, a protective oxide layer significantly reduced these effects, and so was necessary for the biocompatibility and bioinertness of Ti6Al4V (211). This report further supports the performances in metabolic activity of the as-ground control vs control" **(**Figure 4.85**)**.

However, the SLM process has had a great effect on cell metabolic activity. A report by Wysocki et al. (2018) concluded that higher energy density (maximum of 45 J/mm^3) lead to reduced cell adhesion and proliferation (204). Within this research, the energy density parameters far exceeded 45 J/mm3. The authors also stated that presence of TiO_2, from as-SLMed samples; there was a general decline in the intensity of TiO_2 with increasing energy density from a range of 8 to 45 J/mm^3. It was concluded that higher WCA (80 to 100 °) were also apparent, and thus needed to be reduced for the promotion of cell responses. Accordingly, Figure 4.51 and Figure 4.53 display the high WCA observed in this experiment. However, post-thermal oxidation, the samples demonstrated even lower metabollic activity, despite an overall decrease in WCA for all as-SLMed batches, which could be due to thermal oxidation treatment temperature. When Ni-Ti was thermally oxidised treated at 400 °C, there was increased calcium phosphate formation than those treated at 600 °C. The desired calcium phosphate has been reported to be more likely to spark biological activity of cells (207). A better suited comparison of Ti64Al4V previously mentioned (211), thermally treated Ti6Al4V at 700 °C and 500 °C, the former presented enhanced human osteoblasts attachment but at a cost of imparing cell proliferation and viability. Futhermore, the effects of metals vary with varying cells. In this study, the control" demonstrated a much lower WCA (°) of 55 ± 2.3, than Ti64" 89.0 ± 5.0. Similarly, there was a considerable difference in SE (mN/m) values with control" being considerably higher than Ti64", 52.91 ± 1.7, and 26.39 ± 3.03, respectively. A decrease in SE was also determined post-chemical and thermal treatment of the as-SLMed CpTi , which the authors attributed to the changes in stoichiometry and internal stresses. In regards to the SOAS-2 cells, higher SE and lower WCA (more hydrophilic) were favoured pre-Ag doping.

When grinding minimised the effects of R_a, ground Ti64 performed better than its ground Ti64" counterpart, as the ground Ti64 exhibited high WCA (°) of 65.8 ± 3.3 than Ti64" at 46.2 ± 4.0. However, the SE (mN/m) of ground Ti64" was greater than that of ground Ti64 56.77 ± 1.5 and 55.1 ± 1.8. This similar, trend was observed for Ag0.2%. Contrarily, Ag1% and Ag5% resulted in its ground thermally oxidised counterpart outperforming the as-SLMed ground equivalent which could be a resultant effect of significant oxide layer growth, reported to be more negatively charged thus triggering cell attachment. An increase in Ag also resulted in an increase in WCA (Figure 4.51). When the sole effects of Ag are isolated without thermal oxidation and minimized effects of R_a, the differences in WCA and SE were not significant. However, the effects of Ag post-thermal oxidation including laser track grooves, demonstrated a general decreasing WCA trend with increasing Ag content. Accordingly, there was an overall increase in SE with increasing Ag content. These effects, led to a decrease in

SAOS-2 cell metabolic activity with increasing Ag, thus concluding the cells favoured higher WCA and lower SE.

The general behaviour of SOAS-2 cells on SLMed parts would need to be futher investigated. The increasing in Ag with minimised laser track configuration effects resulted in increased oxide layer which proved to ameliorate the mettabolic activity of the cells. It can be concluded, that different treatment types, had a general positive effect in promoting SOAS-2 cell growth (Figure 4.86).

6 CONCLUSION

Within this thesis, SLM has been explored as method of integrating silver into Ti6Al4V surface. Subsequently, the effects of thermal oxidation treatment on the silver doped SLMed Ti6Al4V has been explored and investigated. The key findings are summarised as follows:

6.1 Corrosion behaviour

1. SLM ameliorated the corrosion behaviour of Ti6Al4V by producing a thin protective passive oxide layer. However, by adding Ag to Ti6Al4V via SLM, the corrosion resistance was reduced, as shown by the increasing corrosion density values. There was also an increase in the frequency of metastable pitting with increasing silver.
2. Thermal oxidation remedied the effects of Ag on corrosion behaviour of the titanium alloy. Post-thermal oxidation, Ag-doped samples presented similar corrosion potential behaviour to that of SLMed Ti64. Heat treatment lowered the passivation potentials and regions, which were more clearly emphasized when comparing the control vs control" samples. Corrosion density (i_{corr}) decreased while the corrosion potential (E_{corr}) increased.

6.2 Tribological performance

3. When the CoF of the samples were studied, as-SLMed samples generally demonstrated an increased CoF in comparison to the control. The process evidently increased the roughness of the sample surfaces and resulted in laser grooves. These grooves, made it harder for the WC ball to plough through, thus increased stresses and increased CoF.

4. With increasing in Ag wt. %, there was a general increase in CoF measured against BD as a result of Ag solid solution hardening of SLM surfaces.
5. When tested in Ringer's solution, there was a decrease in CoF, as the solution lubricated the sliding interface. This effect was mostly pronounced in the control samples.
6. Thermal oxidation was essential in decreasing wear rates when tested at both 15 N and 30 N.
7. Post-thermal oxidation, an increase in CoF was evident due to the growth of a harder TiO_2 surface layer. Although there was a decrease in roughness post- oxidation treatment, the oxide layer was not thick enough to completely flatten the surface. But rather the oxide layer grown was in alignment to the grooves, which provided an even greater resistance for the WC ball to plough through. This effect was evident in CoF against BD of oxidised samples in Ringer's solution.
8. The wear rates of SLMed treated samples were greater than the control, which was attributed to its roughness.
9. The reported solid lubrication characteristics of Ag were not apparent in this study, as wear rates did not decrease with increasing Ag wt.%. However, Ag 5% in all treatment types and test conditions presented the highest wear rates due to its generally thinner SLM layer; the WC ball probably wore into the SLM and bulk interface. This was a limiting factor of the M2 SLM machine.
10. After thermal oxidation, Ag5%" experienced delamination wear, but Ag1% performed considerably better. The effects of its higher roughness impacted its performance, as peaks and asperities were worn away first which ploughed into the surface before contact with the bulk SLM layer.

11. Severe adhesion and plastic deformation were the two wear mechanisms apparent in this study. Overall, the effects of SLM were unfavourable to wear resistance due to its surface configuration, however thermal oxidation was instrumental to improving its behaviour.

6.3 Biological behaviour

12. Throughout the study, surface topography (laser grooves) played a vital role in corrosion, wear and finally on cell attachment. There was an evident preferential alignment of *S. aureus* cells along the laser grooves when observed via live or dead staining.
13. Rougher surfaces usually result in increased contact area for bacterial attachment. The SLM process (no Ag) increased surface roughness as a result of laser grooves. Thus, bacteria attachment.
14. In comparison to the control, the SLM process led to increased WCA. This increased roughness as the dominant factor in increasing in increase bacterial attachment and biofilm growth.
15. When the roughness was minimised by grinding the surface of these samples, the WCA reduced thus, the surface went from hydrophobic to hydrophilic.
16. With increasing Ag content there was a decrease in bacterial attachment, thus improved antifouling character, and decrease in biofilm growth.
17. The thermal oxidation process not only improved the corrosion resistance of the SLMed samples, and hardened the SLM surface layer, it also demonstrated antimicrobial properties against biofilm growth. The oxidation treatment demonstrated

greater influence on the reduction of biofilm compared to Ag, as the thermal oxidation process was bactericidal while also having reduced surface area for bacteria attachment by reduced surface roughness.

18. The incremental increase of Ag, led to an increase in antifouling character and lower OD, thus biofilm growth. No trend was spotted in the bioactive nature of silver, but it promoted SOAS-2 cell growth generally better than the control.
19. The thermally oxidised control, displayed the best SOAS-2 cell metabolic activity, therefore it improved bioactivity of the titanium alloy.

Overall in response to SLM, adding Ag was beneficial in considerably reducing bacterial attachment and biofilm growth, but at the detriment of its corrosion and wear behaviour. However, when these samples underwent heat treatment, wear and corrosion behaviours were improved, and the samples maintained their antimicrobial properties.

6.4 Future Work

The present project has shown that alloying Ti6Al4V with Ag via SLM can improve the alloy's antifouling behaviour, and thermal oxidations bettered the alloys corrosion and wear performances. However, based on these results the following future work studies are suggested:

- Cross-sectional and EDS analyses of wear tracks to view the depth and effects of wear.
- SLM modelling, to predict the optimal SLM process parameters, silver content that would be ideal for investigated thermal oxidation time and temperature.

- Modelling of the current SLM parameters used could also be conducted to depict the actual temperature of the laser during melting, and a comparison of the actual Ag wt. % vs the wt. % post-SLM taking into account the vaporisation temperatures of Ag could be investigated.
- Different thermal oxidation treatment temperatures and times could be investigated to compare the growth of TiO_2 layer, its wear behaviour and bioactivity.
- Stress measurements could also be conducted on the SLM samples and hot isostatic pressing (HIP) treatment can be done to investigate its influence on wear and biological behaviour.

7 REFERENCES

1. Latham KJ. Human Health and the Neolithic Revolution: an Overview of Impacts of the Agricultural Transition on Oral Health, Epidemiology, and the Human Body. Nebraska Anthropol [Internet]. 2013;28:95–102.
2. Ayre C, Scally AJ. Critical values for Lawshe's content validity ratio: Revisiting the original methods of calculation. Meas Eval Couns Dev. 2014;47(1):79–86.
3. Wells K, Hamede RK, Jones ME, Hohenlohe PA, Storfer A, McCallum HI. Individual and temporal variation in pathogen load predicts long-term impacts of an emerging infectious disease. Ecology. 2019;100(3):1–27.
4. Alberts B. Molecular Biology of the Cell. 4th ed. Albert, B., Johnson, A., Lewis J et al, editor. New York: New York : Garland Science, c2002; 2002.
5. Craig ENL, Chan- EM, Gellert M, Lambowitz AM, Rice PA, Sandmeyer SB, et al. June 2017 NEW BIOLOGICAL BOOKS 203. 2017;00(June):8153.
6. Humphreys H. Infection—Microbiology and Management, 3rd edn. Clin Microbiol Infect [Internet]. 2007;13(10):1038.
7. Plachouras D, Kärki T, Hansen S, Hopkins S, Lyytikäinen O, Moro ML, et al. Antimicrobial use in European acute care hospitals: results from the second point prevalence survey (PPS) of healthcare-associated infections and antimicrobial use, 2016 to 2017. Eurosurveillance. 2018;23(46).
8. Manley G. Public Access NIH Public Access. 2013;71(2):233–6.
9. Lenzer J. Centers for Disease Control and Prevention: protecting the private good? BMJ. 2015;350(May):h2362.
10. Haque M, Sartelli M, Mckimm J, Abu Bakar M. Infection and Drug Resistance Dovepress Health care-associated infections-an overview. 2018;2321–33.
11. PHE. UK Standards for Microbiology Investigations Investigation of orthopaedic implant associated infections. 2016;1–35.
12. World health organization. WHO Global Health Observatory (GHO) . 2019.
13. Weist K, Monnet DL, Goossens H, Coignard B, Catry B, Suetens C, et al. The European Centre for Disease Prevention and Control (ECDC) pilot point prevalence survey of healthcare-associated infections and antimicrobial use. Eurosurveillance. 2017;17(46).
14. Chang B, Frendl G. Nosocomial infections. Essent Clin Anesth Rev Keywords, Quest Answers Boards. 2015;5(1):494–8.

15. Mackley A, Baker C, Bate A. Raising standards of infection prevention and control in the NHS. 2018;(May):1–23.

16. Centers for Disease Control and Prevention. Antibiotic Resistance Threats. Centers Dis Control Prev. 2013;22–50.

17. CDC. Detect and protect against antibiotic resistance. 2014.

18. Aujla RS, Bryson DJ, Gulihar A, Taylor GJ. Trends in orthopaedic antimicrobial prophylaxis in the UK between 2005 and 2011. Ann R Coll Surg Engl. 2013;95(7):495–502.

19. Ratner BD, Hoffman AS, Schoen FJ, Lemons JE. Biomaterils Science. 1996. 864 p.

20. Hermawan P, Pranowo HD, Kartini I. Physical characterization of Ni(II) doped Tio_2 nanocrystal by sol-gel process. Indones J Chem. 2011;11(2):135–9.

21. Smeets R, Henningsen A, Jung O, Heiland M, Hammächer C, Stein JM. Definition, etiology, prevention and treatment of peri-implantitis - a review. Head Face Med. 2014;10(1):1–13.

22. Knetsch MLW, Koole LH. New strategies in the development of antimicrobial coatings: The example of increasing usage of silver and silver nanoparticles. Polymers (Basel). 2011;3(1):340–66.

23. World Health Organization. WHO Staticical inFORMATION system (WHOSIS). 2011.

24. Kumar S, Narayanan TSNS, Raman SGS, Seshadri SK. Thermal oxidation of CP-Ti: Evaluation of characteristics and corrosion resistance as a function of treatment time. Mater Sci Eng C [Internet]. 2009;29(6):1942–9.

25. Oldani C, Dominguez A. Titanium as a Biomaterial for Implants. Recent Adv Arthroplast. 2012;

26. Elias CN, Lima JHC, Valiev R, Meyers MA. Biomedical applications of titanium and its alloys. Jom. 2008;60(3):46–9.

27. Park CH, Son Y Il, Lee CS. Constitutive analysis of compressive deformation behavior of ELI-grade Ti-6Al-4V with different microstructures. J Mater Sci. 2012;47(7):3115–24.

28. Dong H, Bell T. Enhanced wear resistance of titanium surfaces by a new thermal oxidation treatment. Wear. 2000;238(2):131–7.

29. Bhushan B. Boundary Lubrication and Lubricants. Introd to Tribol. 2013;501–23.

30. Walkelin R. Tribology: The friction, lubrication, and wear of moving parts. Mater Sci Eng C. 1974;

31. Zhecheva A, Sha W, Malinov S, Long A. Enhancing the microstructure and properties of titanium alloys through nitriding and other surface engineering methods. Surf Coatings Technol. 2005;200(7):2192–207.

32. Darouiche RO. Infections Associated with Surgical Implants. N Engl J Med. 2004;351(2):193–5.

33. Otto M. Staphylococcal biofilms. In: Romeo, T. (ed.) Bacterial biofilms (current topics in microbiology and immunology). Springer-Verlag. 2008;207–28.

34. Geetha M, Singh AK, Asokamani R, Gogia AK. Ti based biomaterials, the ultimate choice for orthopaedic implants - A review. Prog Mater Sci [Internet]. 2009;54(3):397–425.

35. Nouri A, Wen C. Introduction to surface coating and modification for metallic biomaterials [Internet]. Surface Coating and Modification of Metallic Biomaterials. Elsevier Ltd; 2015. 3–60 p.

36. Cheng Y, Feng G, Moraru CI. Micro-and nanotopography sensitive bacterial attachment mechanisms: A review. Front Microbiol. 2019;10(FEB):1–17.

37. Navarro E, Baun A, Behra R, Hartmann NB, Filser J, Miao AJ, et al. Environmental behavior and ecotoxicity of engineered nanoparticles to algae, plants, and fungi. Ecotoxicology. 2008;17(5):372–86.

38. Widmer AF. New Developments in Diagnosis and Treatment of Infection in Orthopedic Implants. Clin Infect Dis. 2002;33(s2):S94–106.

39. Dhir S. Biofilm and dental implant: The microbial link. J Indian Soc Periodontol. 2013;17(1):5.

40. Percival SL, Suleman L, Vuotto C, Donelli G. Healthcare-associated infections, medical devices and biofilms: risk, tolerance and control. J Med Microbiol [Internet]. 2015;64(Pt 4):323–34.

41. Trampuz A, Zimmerli W. Diagnosis and treatment of infections associated with fracture-fixation devices. Injury. 2006;37(2 SUPPL.):59–66.

42. van der Mei HC, van den Dungen JJAM, Grainger DW, Jutte PC, Busscher HJ, Schultz MJ, et al. Biomaterial-Associated Infection: Locating the Finish Line in the Race for the Surface. Sci Transl Med. 2012;4(153):153rv10-153rv10.

43. Gallo J, Kolár M, Novotný R, Riháková P, Tichá V. Pathogenesis of prosthesis-related infection. Biomed Pap Med Fac Univ Palacky Olomouc Czech Repub. 2003;147(1):27–35.

44. Moriarty TF, Kuehl R, Coenye T, Metsemakers W-J, Morgenstern M, Schwarz EM, et al. Orthopaedic device-related infection: current and future interventions for improved prevention and treatment. EFORT Open Rev [Internet]. 2016;1(4):89–99.

45. Geetha M, Singh AK, Asokamani R, Gogia AK. Ti based biomaterials, the ultimate choice for orthopaedic implants - A review. Prog Mater Sci. 2009;54(3):397–425.

46. von Eiff C, Jansen B, Kohnen W, Becker K. Infections Associated with Medical Devices. Drugs. 2005;65(2):179–214.

47. Norowski PA, Bumgardner JD. Biomaterial and antibiotic strategies for peri-implantitis. J Biomed Mater Res - Part B Appl Biomater. 2009;88(2):530–43.

48. Sousa C, Teixeira P, Oliveira R. Influence of Surface Properties on the Adhesion of Staphylococcus epidermidis to Acrylic and Silicone . Int J Biomater. 2009;2009:1–9.

49. Hart KM, Hyrenbach KD. Biofilms: Survival Mechanisms of Clinically Relevant Microorganisms. Clin Microbiol Rev. 2002;15(2):167–89.

50. Gallo J, Holinka M, Moucha CS. Antibacterial surface treatment for orthopaedic implants. Vol. 15, International Journal of Molecular Sciences. 2014. 13849–13880 p.

51. Murray A, Lead IPC, Williams M, Nurse IPC. Director of infection prevention and control (DIPC) annual report annual work programme April 2012 to March 2013. The DIPC annual report for Dudley and Walsall Mental Health NHS Partnership Trust. 2013;(July).

52. Guideline C. Infection: prevention and control of healthcare-associated infections in primary and community care Clinical Guideline Methods, evidence and recommendations Commissioned by the National Institute for Health and Clinical Excellence Infection Prevention.

53. Bratzler DW, Dellinger EP, Olsen KM, Perl TM, Auwaerter PG, Bolon MK, et al. Clinical practice guidelines for antimicrobial prophylaxis in surgery. Am J Heal Pharm. 2013;70(3):195–283.

54. Le Guéhennec L, Soueidan A, Layrolle P, Amouriq Y. Surface treatments of titanium dental implants for rapid osseointegration. Dent Mater. 2007;23(7):844–54.

55. Bruschi M, Steinmüller-Nethl D, Goriwoda W, Rasse M. Composition and Modifications of Dental Implant Surfaces. J Oral Implant. 2015;2015:1–14.

56. Panwisawas C, Perumal B, Ward RM, Turner N, Turner RP, Brooks JW, et al. Keyhole formation and thermal fluid flow-induced porosity during laser fusion welding in titanium alloys: Experimental and modelling. Vol. 126, Acta Materialia. 2017. p. 251–63.

57. Kim JS, Kuk E, Yu KN, Kim JH, Park SJ, Lee HJ, et al. Antimicrobial effects of silver nanoparticles. Nanomedicine Nanotechnology, Biol Med. 2007;3(1):95–101.

58. Turner DA, Girgin M, Alonso-Crisostomo L, Trivedi V, Baillie-Johnson P, Glodowski CR, et al. Anteroposterior polarity and elongation in the absence of extra-embryonic tissues and of spatially localised signalling in gastruloids: mammalian embryonic organoids. Development. 2017;144(21):3894–906.

59. Arya V, Komal R, Kaur M, Goyal A. ewsletter Arya et al . Silver anoparticles as a Potent Antimicrobial Agent : A Review Arya et al . 2011;124(47):118–24.

60. Senjen R. Nano and biocidal silver : extreme germ killers present a growing threat to public health. Earth. 2009;(June):1–47.

61. Lara HH, Ayala-Núñez N V., del Turrent LCI, Padilla CR. Bactericidal effect of silver

nanoparticles against multidrug-resistant bacteria. World J Microbiol Biotechnol. 2010;26(4):615–21.

62. Chen YH, Hsu CC, He JL. Antibacterial silver coating on poly(ethylene terephthalate) fabric by using high power impulse magnetron sputtering. Surf Coatings Technol [Internet]. 2013;232:868–75.

63. Kwakye-Awuah B, Williams C, Kenward MA, Radecka I. Antimicrobial action and efficiency of silver-loaded zeolite X. J Appl Microbiol. 2008;104(5):1516–24.

64. Woo KJ, Hye CK, Ki WK, Shin S, So HK, Yong HP. Antibacterial activity and mechanism of action of the silver ion in Staphylococcus aureus and Escherichia coli. Appl Environ Microbiol. 2008;74(7):2171–8.

65. Dakal TC, Kumar A, Majumdar RS, Yadav V. Mechanistic basis of antimicrobial actions of silver nanoparticles. Front Microbiol. 2016;7(NOV):1–17.

66. Fuhrmann GF, Rothstein A. The transport of Zn2+, Co2+ and Ni2+ into yeast cells. BBA - Biomembr. 1968;163(3):325–30.

67. Raffi M, Mehrwan S, Bhatti TM, Akhter JI, Hameed A, Yawar W, et al. Investigations into the antibacterial behavior of copper nanoparticles against Escherichia coli. Ann Microbiol. 2010;60(1):75–80.

68. Schreurs WJA, Rosenberg H. Effect of silver ions on transport and retention of phosphate by Escherichia coli. J Bacteriol. 1982;152(1):7–13.

69. Yamanaka M, Hara K, Kudo J. Bactericidal Actions of a Silver Ion Solution on. Appl Environ Microbiol. 2005;71(11):7589–93.

70. Poulter N, Donaldson M, Mulley G, Duque L, Waterfield N, Shard AG, et al. Plasma deposited metal Schiff-base compounds as antimicrobials. New J Chem. 2011;35(7):1477–84.

71. Noyce JO, Michels H, Keevil CW. Potential use of copper surfaces to reduce survival of epidemic meticillin-resistant Staphylococcus aureus in the healthcare environment. J Hosp Infect. 2006;63(3):289–97.

72. Grass G, Rensing C, Solioz M. Metallic Copper as an Antimicrobial Surface. Appl Environ Microbiol. 2011;77(5):1541–7.

73. Steindl G, Heuberger S, Springer B. Antimicrobial effect of copper on multidrug-resistant bacteria. Wiener Tierärztliche Monatsschrift – Vet Med Austria. 2012;99:38–43.

74. McDevitt CA, Ogunniyi AD, Valkov E, Lawrence MC, Kobe B, McEwan AG, et al. A molecular mechanism for bacterial susceptibility to Zinc. PLoS Pathog. 2011;7(11).

75. Francolini I, Vuotto C, Piozzi A, Donelli G. Antifouling and antimicrobial biomaterials: an overview. Apmis. 2017;125(4):392–417.

76. Radin S, Ducheyne P. Controlled release of vancomycin from thin sol-gel films on

titanium alloy fracture plate material. Biomaterials. 2007;28(9):1721–9.

77. Privett BJ, Youn J, Hong SA, Lee J, Han J, Shin JH, et al. Antibacterial fluorinated silica colloid superhydrophobic surfaces. Langmuir. 2011;27(15):9597–601.

78. Hogan S, Stevens NT, Humphreys H, O'Gara JP, O'Neill E. Current and Future Approaches to the Prevention and Treatment of Staphylococcal Medical Device-Related Infections. Curr Pharm Des. 2014;21(1):100–13.

79. Mendonça G, Mendonça DBS, Aragão FJL, Cooper LF. Advancing dental implant surface technology - From micron- to nanotopography. Biomaterials. 2008;29(28):3822–35.

80. Mendonça G, Silveira Mendonça DB, Fernandes-Neto AJ, Neves FD. Management of fractured dental implants: A case report. Implant Dent. 2009;18(1):10–6.

81. Kulkarni GU, Radha B. Metal nanowire grating patterns. Nanoscale. 2010;2(10):2035–44.

82. Subramani K, Ahmed W. Titanium Nanotubes as Carriers of Osteogenic Growth Factors and Antibacterial Drugs for Applications in Dental Implantology [Internet]. First Edit. Emerging Nanotechnologies in Dentistry. Elsevier Inc.; 2012. 103–111 p.

83. S. K, Oh S, J. C, Ji S. Biomaterials and Biotechnology Schemes Utilizing TiO2 Nanotube Arrays. Biomater Sci Eng. 2012;(September 2011).

84. Pye AD, Lockhart DEA, Dawson MP, Murray CA, Smith AJ. A review of dental implants and infection. J Hosp Infect [Internet]. 2009;72(2):104–10.

85. Prathapachandran J, Suresh N. Management of peri-implantitis. 2012;9(5).

86. Niinomi M. Biologically and Mechanically Biocompatible Titanium Alloys. Mater Trans. 2008;49(10):2170–8.

87. Gázquez MJ, Bolívar JP, Garcia-Tenorio R, Vaca F. A Review of the Production Cycle of Titanium Dioxide Pigment. Mater Sci Appl. 2014;05(07):441–58.

88. Bordbar H, Yousefi AA, Abedini H. Production of titanium tetrachloride (TiCl4) from titanium ores : A review. Polyolefins J. 2017;4(2):149–73.

89. Hanaor DAH, Sorrell CC. Review of the anatase to rutile phase transformation. J Mater Sci. 2011;46(4):855–74.

90. Kaur M, Singh K. Review on titanium and titanium based alloys as biomaterials for orthopaedic applications. Mater Sci Eng C [Internet]. 2019;102(December 2018):844–62.

91. Allen NS, Mahdjoub N, Vishnyakov V, Kelly PJ, Kriek RJ. The effect of crystalline phase (anatase, brookite and rutile) and size on the photocatalytic activity of calcined polymorphic titanium dioxide (TiO2). Polym Degrad Stab [Internet]. 2018;150(January):31–6.

92. Haider AJ, Jameel ZN, Al-Hussaini IHM. Review on: Titanium dioxide applications.

Energy Procedia [Internet]. 2019;157:17–29.

93. Zhang J, Matsuura H, Tsukihashi F. Processes for Recycling. Vol. 3, Treatise on Process Metallurgy. Elsevier Ltd.; 2014. 1507–1561 p.

94. Lutjering, Gerald., Williams JC. Titanium. 2nd ed. Berlin: Springer Berling, Heidelberg New York; 2007.

95. Nie JF. Physical Metallurgy of Light Alloys [Internet]. Fifth Edit. Vol. 1, Physical Metallurgy: Fifth Edition. Elsevier; 2014. 2009–2156 p.

96. Gammon J. MetallographyandMicrostructuresofTitanium.., Gammon et al. (2004)pdf.pdf.

97. Zhecheva A, Malinov S, Sha W. Microstructure and microhardness of gas nitrided surface layers in Ti–8Al–1Mo–1V and Ti–10V–2Fe–3Al alloys. Surf Eng. 2005;21(4):269–78.

98. Sidambe AT. Biocompatibility of advanced manufactured titanium implants-A review. Materials (Basel). 2014;7(12):8168–88.

99. Leyens, C and Peters M, editor. Titanium and Titanium Alloys: Fundamental and Applications. Germany: WILEY-VCH Verlag GmBH & Co. KGaA, Weinteim; 2003.

100. Kolli R, Devaraj A. A Review of Metastable Beta Titanium Alloys. Metals (Basel). 2018;8(7):506.

101. Froes FH. Principles of Beta Transformation and Heat Treatment of Titanium Alloys. Titan - Phys Metall Process Appl. 2015;

102. Petersen R. Titanium Implant Osseointegration Problems with Alternate Solutions Using Epoxy/Carbon-Fiber-Reinforced Composite. Metals (Basel). 2014;4(4):549–69.

103. Yuhua L, Chao Y, Haidong Z, Shengguan Q, Xiaoqiang L, Yuanyuan L, et al. New Developments of Ti-Based Alloys for Biomedical Applications. Vol. 7, Materials. 2014. p. 1709–800.

104. James R, Wanhill H, Barter S, Science D. Executive summary Fatigue of β processed and β heat-treated titanium alloys A contribution to the DSTO - NLR joint programme of Damage Tolerance and Durability assessment of beta annealed Ti-6Al-4V plate. 2012;

105. Boyer, R., Welsch, G and Collins EW, editor. Materials Properties Handbook: Titanium Alloys. 1st Ed. United States of America: ASM international ; 1994.

106. Paridah M., Moradbak A, Mohamed A., Owolabi F abdulwahab taiwo, Asniza M, Abdul Khalid SH. We are IntechOpen , the world ' s leading publisher of Open Access books Built by scientists , for scientists TOP 1 %. Intech. 2016;i(tourism):13.

107. Dong H, editor. Surface engineering of light alloys. Woodhead Publishing Limited; 2010.

108. Liu X, Chu PK, Ding C. Surface modification of titanium, titanium alloys, and related

materials for biomedical applications. Mater Sci Eng R Reports. 2004;47(3–4):49–121.

109. Costa A, Miranda R, Quintino L, Yapp D. Analysis of beam material interaction in welding of titanium with fiber lasers. Mater Manuf Process. 2007;22(7):798–803.

110. Aleksander L. Welding of titanium alloy by different types of lasers. Arch Mater Sci Eng. 2012;58(2):209–18.

111. Lisiecki A. Welding of titanium alloy by different types of lasers. Arch Mater Sci Eng. 2012;58(2):209–18.

112. [20834799 - Advances in Materials Science] Weldability of Titanium and its Alloys - Progress in Joining., Ranatowski (2008).pdf.

113. Havlík P, Kouřil J, Foret R, Dlouhy I, Enzinger N, Wiednig C. Evaluation of Weldability of Titanium Alloy Ti-6Al-4V and Aluminum Alloy 6061 Produced by Electron Beam Welding. Vol. 879, Materials Science Forum. 2016. p. 714–9.

114. Veiga C, Davim JP, Loureiro AJR. Review on machinability of titanium alloys: The process perspective. Rev Adv Mater Sci. 2013;34(2):148–64.

115. Dandekar CR, Shin YC, Barnes J. Machinability improvement of titanium alloy (Ti-6Al-4V) via LAM and hybrid machining. Int J Mach Tools Manuf [Internet]. 2010;50(2):174–82.

116. Ugarte A, M'Saoubi R, Garay A, Arrazola PJ. Machining behaviour of Ti-6Al-4V and Ti-5553 alloys in interrupted cutting with PVD coated cemented carbide. Procedia CIRP [Internet]. 2012;1(1):202–7.

117. Guleryuz H, Cimenoglu H. Oxidation of Ti-6Al-4V alloy. J Alloys Compd. 2009;472(1–2):241–6.

118. Kumar S, Sankara Narayanan TSN, Ganesh Sundara Raman S, Seshadri SK. Thermal oxidation of Ti6Al4V alloy: Microstructural and electrochemical characterization. Mater Chem Phys. 2010;119(1–2):337–46.

119. Revankar GD, Shetty R, Rao SS, Gaitonde VN. Wear resistance enhancement of titanium alloy (Ti-6Al-4V) by ball burnishing process. J Mater Res Technol [Internet]. 2017;6(1):13–32.

120. Nosonovsky M. Entropy in tribology: In the search for applications. Entropy. 2010;12(6):1345–90.

121. Totten, G and Liang H, editor. Mechanical tribology : materials, characterization, and applications. 1st ed. New York: New York : Marcel Dekker, 2004.; 2004.

122. Zeng H, editor. Polymer adhesion, friction, and lubrication. Canada: John Wiley & Sons, Inc. Hoboken, New Jersey; 2013.

123. Venkatachalam S, Liang SY. Effects of Ploughing Forces and Friction Coefficient in Microscale Machining. J Manuf Sci Eng. 2007;129(2):274.

124. Zmitrowicz A. Wear patterns and laws of wear – a review. J Theor Appl Mech.

2006;44(2):219–53.

125. Bowden, P and Tabor D, editor. The friction and lubrication of solids. England: Oxford : Clarendon Press, 1950; 1950.

126. Bruce R, editor. Handbook of lubrication and tribology: Volume II theory and design. United stated of America: Taylor & Francis Group, LLC; 2012.

127. Dong H. Surface engineering of light alloys: Aluminium, magnesium and titanium alloys. Surface Engineering of Light Alloys: Aluminium, Magnesium and Titanium Alloys. 2010. p. 1–662.

128. Kumar D, Deepak KB, Muzakkir SM, Wani MF, Lijesh KP. Enhancing tribological performance of Ti-6Al-4V by sliding process. Tribol - Mater Surfaces Interfaces [Internet]. 2018;12(3):137–43.

129. Kenneth G Budinski. Tribological properties of titanium alloys. Wear. 1991;151(2):203–17.

130. Feng, C; Khan T. The effect of quenching medium on the wear behaviour of a Ti-6Al-4V alloy. J Mater Sci. 2008;43(2):788–92.

131. Hadke, S; Khatirkar, RK; Shekhawat, SK; Jain, S; Sapate S. Microsctructure evolition and abrasive wear behavior of Ti-6Al-4V alloy. J Mater Eng Perform. 2015;24(10):3969–81.

132. Wilson, S; Alpas A. Wear mechanism maps for metal matrix composites. Wear. 1997;212(1):41–9.

133. Pürçek G, Savaskan, T; Küçükömergoglu, T; Murphy S. Dry sliding friction and wear properties of zinc-based alloys. Wear. 2002;11(12):894–901.

134. Collings E w. The physical metallurgy of Titanium Alloys. American society for metals. USA; 1984.

135. Suh NP. The delamination theory of wear. Wear. 1973;25(1):111–24.

136. Venkataraman B SG. The sliding wear behaviour of Al-SiC particulate composites-II. The characterisation of subsurface deformation and correlation with wear behaviour. Acta Mater. 1996;44(2):461–73.

137. Astarita A, Durante M, Langella A, Montuori M, Squillace A. Mechanical characterization of low-pressure cold-sprayed metal coatings on aluminium. Surf Interface Anal. 2013;45(10):1530–5.

138. Chaubey S, Kumar A, Singh D, Habib S. The apicoplast of Plasmodium falciparum is translationally active. Mol Microbiol. 2005;56(1):81–9.

139. Yaszemski, M., Trantolo, D., Lewandrowski, K., Hasirci, V., Altobelli, D., Wise D, editor. Tissue engineering and novel delivery systems. Taylor & Francis Inc, CRC Press Inc; 2003.

140. Vanhegan IS, Malik AK, Jayakumar P, Ul Islam S, Haddad FS. A financial analysis of

revision hip arthroplasty. J Bone Joint Surg Br [Internet]. 2012;94-B(5):619–23.

141. Billi F, Campbell P. Nanotoxicology of metal wear particles in total joint arthroplasty: a review of current concepts. J Appl Biomater Biomech [Internet]. 2010;8(1):1–6.

142. Mediaswanti K, Wen C, Ivanova EP, Berndt CC, Malherbe F, Thi V, et al. A Review on Bioactive Porous Metallic Biomaterials. J Biomimetics Biomater Tissue Eng. 2013;18(1):1–8.

143. Chauhan SR, Dass K. Dry Sliding Wear Behaviour of Titanium (Grade 5) Alloy by Using Response Surface Methodology. Vol. 2013, Advances in Tribology. 2013. p. 1–9.

144. Basu B, Sarkar J, Mishra R. Understanding friction and wear mechanisms of high-purity titanium against steel in liquid nitrogen temperature. Metall Mater Trans A Phys Metall Mater Sci. 2009;40(2):472–80.

145. Viswanadham, R.K., Rowcliffe, D.J., Gurland J, editor. Science of Hard Materials. 1st ed. New York: Plenum Press, New York; 1983.

146. Buckley DH. Surface films and metallurgy related to lubrication and wear. Prog Surf Sci. 1982;12(1):1–153.

147. Miyoshi K, Wu RLC, Lanter WC. Friction and wear of diamondlike carbon on fine-grain diamond. Tribol Lett. 1997;3(2):141–5.

148. Kossowsky R, editor. Surface Modeling Engineering, Volume 1. 1st ed. Florida: CRC Press Inc. ; 1989.

149. Buckley DH, Miyoshi K. Tribological Properties of Structural Ceramics. 2012. 293–365 p.

150. Li LH, Kong YM, Kim HW, Kim YW, Kim HE, Heo SJ, et al. Improved biological performance of Ti implants due to surface modification by micro-arc oxidation. Biomaterials. 2004;25(14):2867–75.

151. Murr, Lawrence E., Edwin Martinez KNA, Gaytan SM, Jennifer Hernandez, Diana A. Ramirez PWS, Medina F, Wicker RB. Fabrication of Metal and Alloy Components by Additive Manufacturing: Examples of 3D Materials Science. J Mater Res Technol [Internet]. 2012;42–54.

152. S. Izman, M. R. Abdul-Kadir MA, E.M. Nazim, R. Rosliza AS and MAH. Surface modification techniques for Biomedical grade of titanium alloys Oxidation, carburization and ion implantation processes. Intech. 2012;i:31.

153. Daoud WA, Xin JH. Low Temperature Sol-Gel Processed Photocatalytic Titania Coating. J Sol-Gel Sci Technol [Internet]. 2004;29(1):25–9.

154. Arango S, Peláez-Vargas A, García C. Coating and Surface Treatments on Orthodontic Metallic Materials. Coatings. 2012;3(1):1–15.

155. Ewald C, Kuhn S, Kalff R. Pyogenic infections of the central nervous system

secondary to dental affections - A report of six cases. Neurosurg Rev. 2006;29(2):163–6.

156. K.L. Choy. Chemical vapour deposition of coatings. Prog Mater Sci. 2003;48:57–170.

157. Raoufi M, Mirdamadi S, Mahboubi F, Ahangarani S, Mahdipoor MS, Elmkhah H. Effect of active screen plasma nitriding pretreatment on wear behavior of TiN coating deposited by PACVD technique. Appl Surf Sci [Internet]. 2012;258(20):7820–5.

158. Biro E, Vignier S, Kaczynski C, Mcdermid JR, Lucas E, Embury JD, et al. Predicting Transient Softening in the Sub-Critical Heat-Affected Zone of Dual-Phase and Martensitic Steel Welds. ISIJ Int. 2013;53(1):110–8.

159. Liu S, Shin YC. Additive manufacturing of Ti6Al4V alloy: A review. Mater Des [Internet]. 2019;164:107552.

160. Attallah MM, Jennings R, Wang X, Carter LN. Additive manufacturing of Ni-based superalloys: The outstanding issues. Vol. 41, MRS Bulletin. 2016. p. 758–64.

161. Turner RP, Panwisawas C, Sovani Y, Perumal B, Ward RM, Basoalto HC, et al. Linking a CFD and FE analysis for Welding Simulations in Ti-6Al-4V. Proceedings of the 10th International conference on Trends in Welding Research. 2016. p. 960–3.

162. Liu S, Shin YC. Additive manufacturing of Ti6Al4V alloy: A review. Vol. 164, Materials and Design. 2019.

163. T. DebRoy, H.L. Wei, J.S. Zuback, T. Mukherjee, J.W. Elmer, J.O. Milewski, et al. Additive manufacturing of metallic components – Process, structure and properties. Vol. 92, Progress in Materials Science. 2018. p. 112–224.

164. Li Y, Jia G, Cheng Y, Hu Y. Additive manufacturing technology in spare parts supply chain: a comparative study. Int J Prod Res [Internet]. 2017;55(5):1498–515.

165. Hu D, Mei H, Kovacevic R. Improving solid freeform fabrication by laser-based additive manufacturing. Proc Inst Mech Eng Part B J Eng Manuf. 2002;216(9):1253–64.

166. Bi G, Gasser A, Wissenbach K, Drenker A, Poprawe R. Identification and qualification of temperature signal for monitoring and control in laser cladding. Opt Lasers Eng. 2006;44(12):1348–59.

167. D. D. Gu*1 W. Meiners2, K. Wissenbach2 and R. Poprawe2 2. Laser additive manufacturing of metallic components: materials, processes and mechanisms. International Materials Reviews. 2012.

168. Uhlmann E, Lypovka P, Hochschild L, Schröer N. Influence of rail grinding process parameters on rail surface roughness and surface layer hardness. Wear [Internet]. 2016;366–367(August):287–93.

169. Dilip JJS, Zhang S, Teng C, Zeng K, Robinson C, Pal D, et al. Influence of processing parameters on the evolution of melt pool, porosity, and microstructures in Ti-6Al-4V alloy parts fabricated by selective laser melting. Prog Addit Manuf. 2017;2(3):157–67.

170. El-Sayed, Mahmoud; Ghazy, Mootaz; Yehia, Youssef; Essa K. Optimization of SLM Process Parameters for Ti64 Medical Implants [Internet]. University of Birmingham; 2018.

171. Bi Zhang; Yongtao Li; Bai Q. Defect formation mechanism in selective laser melting: A review. Chin J Mech Eng. 2017;30:515–27.

172. Hanzl P, Zetek M, Bakša T, Kroupa T. The influence of processing parameters on the mechanical properties of SLM parts. Vol. 100, Procedia Engineering. 2015. p. 1405–13.

173. Basoalto H, Brooks JW, Qiu C, Panwisawas C, Ward M, Basoalto HC, et al. On the role of melt flow into the surface structure and porosity development during selective laser melting PhD project View project development during selective laser melting [Internet]. Vol. 96, Acta Materialia. 2015. p. 72–9.

174. Gong H, Gu H, Zeng K, Dilip JJS, Pal D, Stucker B, et al. Melt Pool Characterization for Selective Laser Melting of Ti-6Al-4V Pre-alloyed Powder. Solid Freeform Fabrication Symposium. 2014. p. 256–67.

175. Kasperovich G, Haubrich J, Gussone J, Requena G. Erratum: Corrigendum to "Correlation between porosity and processing parameters in TiAl6V4 produced by selective laser melting" (Materials and Design (2016) 105 (160–170)). Mater Des. 2016;112:160–1.

176. Sames WJ, List FA, Pannala S, Dehoff RR, Babu SS. The metallurgy and processing science of metal additive manufacturing. Vol. 61, International Materials Reviews. 2016. p. 315–60.

177. Wroe J. Introduction to Additive Manufacturing Technology: A Guide for Designers and Engineers [Internet]. European Powder Metallurgy Association. 2015.

178. Characterisation of pre-alloyed Ti-6Al-4V powders form EIGA and PREP Process and mechanical properties of HIPed Powder compacts., Guo et al. (2017).pdf.

179. Yang, Jingjing; Yu, Hanchen; Yin, Jie; Gao, M; Wang Z. Formation and control of martensite in Ti64 alloy produced by SLM., Yang et al (2016).pdf. 2016;

180. Microstructure, static properties, and fatigue crack growth mechanism in Ti64 fabricated by AM□ LENS and EBM., Zhai et al. (2016).pdf.

181. Sun P, Fang ZZ, Zhang Y, Xia Y. Review of the Methods for Production of Spherical Ti and Ti Alloy Powder. Vol. 69, Jom. 2017. p. 1853–60.

182. King WE, Gibbs JW, Gallegos GF, Castillo VM, Rubenchik AM, Kamath C, et al. Observation of keyhole-mode laser melting in laser powder-bed fusion additive manufacturing. Vol. 214, Journal of Materials Processing Technology. 2014. p. 2915–25.

183. Song K, Lee J, Choi SO, Kim J. Interaction of surface energy components between solid and liquid on wettabilit. Polymers (Basel). 2019;11(3).

184. Saji VS, Choe HC. Electrochemical corrosion behaviour of nanotubular Ti-13Nb-13Zr alloy in Ringer's solution. Corros Sci [Internet]. 2009;51(8):1658–63.

185. SUZUKI K, TAKANO T, TAKEMOTO S, UEDA T, YOSHINARI M, SAKURAI K. Influence of grade and surface topography of commercially pure titanium on fatigue properties. Dent Mater J. 2017;37(2):308–16.

186. Christensen GD, Simpson WA, Younger JJ, Baddour LM, Barrett FF, Melton DM, et al. Adherence of coagulase-negative staphylococci to plastic tissue culture plates: A quantitative model for the adherence of staphylococci to medical devices. J Clin Microbiol. 1985;22(6):996–1006.

187. Cao L, Wan Y, Yang S, Pu J. The tribocorrosion and corrosion properties of thermally oxidized Ti6Al4V alloy in 0.9 wt.% NaCl physiological saline. Coatings. 2018;8(8).

188. Dong H, Mukinay T, Li M, Hood R, Soo SL, Cockshott S, et al. Improving tribological and anti-bacterial properties of titanium external fixation pins through surface ceramic conversion. J Mater Sci Mater Med. 2017 Jan 1;28(1).

189. Liu Y, Wang G, Cao W, Xu H, Huang Z, Zhu D, et al. Brazing ZrB2-SiC ceramics to Ti6Al4V alloy with TiCu-based amorphous filler. J Manuf Process [Internet]. 2017;30:516–22.

190. P. Suh N. The delamination theory of wear. Wear. 1973;25(1):111–24.

191. Kirmanidou Y, Sidira M, Drosou ME, Bennani V, Bakopoulou A, Tsouknidas A, et al. New Ti-Alloys and Surface Modifications to Improve the Mechanical Properties and the Biological Response to Orthopedic and Dental Implants: A Review. Biomed Res Int. 2016;2016.

192. Sui, Qingxuan; Li, Peizhen; Wang, Kunlun; Yin, Xiaotian; Liu, Linggyu; Zhang Y. E ff ect of Temperature on the Corrosion Behavior of Physiological Solution. 2019;1–17.

193. Mosquera AA, Albella JM, Navarro V, Bhattacharyya D, Endrino JL. Effect of silver on the phase transition and wettability of titanium oxide films. Sci Rep. 2016;6(April):1–14.

194. Han MK, Hwang MJ, Won DH, Kim YS, Song HJ, Park YJ. Massive transformation in titanium-silver alloys and its effect on their mechanical properties and corrosion behavior. Materials (Basel). 2014;7(9):6194–206.

195. Fleischer R. Substitutional solid solution hardening of titanium. J Chem Inf Model. 1987;21(9):1083–985.

196. Oh JM, Lee BG, Cho SW, Lee SW, Choi GS, Lim JW. Oxygen effects on the mechanical properties and lattice strain of Ti and Ti-6Al-4V. Met Mater Int. 2011;17(5):733–6.

197. Gheewala I, Smith R, Kenny SD. Nanoindentation and nanoscratching of rutile and anatase TiO2studied using molecular dynamics simulations. J Phys Condens Matter. 2008;20(35).

198. aZoM materials. Ti6Al4V wear resistance. 2019.

199. Whitehead KA, Verran J. The effect of surface topography on the retention of microorganisms. Food Bioprod Process. 2006;84(4 C):253–9.

200. Hsu LC, Fang J, Borca-Tasciuc DA, Worobo RW, Moraru CI. Effect of micro- and nanoscale topography on the adhesion of bacterial cells to solid surfaces. Appl Environ Microbiol. 2013;79(8):2703–12.

201. Lorenzetti M, Dogša I, Stošicki T, Stopar D, Kalin M, Kobe S, et al. The influence of surface modification on bacterial adhesion to titanium-based substrates. ACS Appl Mater Interfaces. 2015;7(3):1644–51.

202. Ribeiro M, Monteiro FJ, Ferraz MP. Infection of orthopedic implants with emphasis on bacterial adhesion process and techniques used in studying bacterial-material interactions. Biomatter. 2012;2(4):176–94.

203. Lin C, Tang P, Zhang W, Wang Y, Zhang B, Wang H, et al. Effect of superhydrophobic surface of titanium on staphylococcus aureus adhesion. J Nanomater. 2011;2011.

204. Wysocki B, Idaszek J, Zdunek J, Rożniatowski K, Pisarek M, Yamamoto A, et al. The influence of selective laser melting (SLM) process parameters on in-vitro cell response. Int J Mol Sci. 2018 Jun 1;19(6).

205. Wang M, Wu Y, Lu S, Chen T, Zhao Y, Chen H, et al. Fabrication and characterization of selective laser melting printed Ti–6Al–4V alloys subjected to heat treatment for customized implants design. Prog Nat Sci Mater Int [Internet]. 2016;26(6):671–7.

206. Patel SB, Hamlekhan A, Royhman D, Butt A, Yuan J, Shokuhfar T, et al. Enhancing surface characteristics of Ti-6Al-4V for bio-implants using integrated anodization and thermal oxidation. J Mater Chem B. 2014;2(23):3597–608.

207. Krasowska A, Sigler K. How microorganisms use hydrophobicity and what does this mean for human needs? Front Cell Infect Microbiol. 2014;4(AUG):1–7.

208. Qing Y, Cheng L, Li R, Liu G, Zhang Y, Tang X, et al. Potential antibacterial mechanism of silver nanoparticles and the optimization of orthopedic implants by advanced modification technologies. Int J Nanomedicine. 2018;13:3311–27.

209. Anselme K, Bigerelle M. Role of materials surface topography on mammalian cell response. Int Mater Rev. 2011;56(4):243–66.

210. Vandrovcova M, Jirka I, Novotna K, Lisa V, Frank O, Kolska Z, et al. Interaction of human osteoblast-like Saos-2 and MG-63 cells with thermally oxidized surfaces of a titanium-niobium alloy. PLoS One. 2014;9(6).

211. Saldaña L, Barranco V, García-Alonso MC, Vallés G, Escudero ML, Munuera L, et al. Concentration-dependent effects of titanium and aluminium ions released from thermally oxidized Ti6Al4V alloy on human osteoblasts. J Biomed Mater Res - Part A. 2006;77(2):220–9.

212. Chrzanowski W, Abou Neel EA, Armitage DA, Knowles JC. Surface preparation of bioactive Ni-Ti alloy using alkali, thermal treatments and spark oxidation. J Mater Sci Mater Med. 2008;19(4):1553–7.